



MONASH
University

**Particle Scale Modeling of Mixing and Segregation of
Particles Mixtures in Liquid Fluidized Beds of
Spherical and non-Spherical Particles**

by

Esmail Abbaszadeh Molaei

A thesis submitted for the degree of
Doctor of Philosophy
at Monash University
Department of Chemical Engineering

Supervisors:

Dr. Zongyan Zhou

Prof. Aibing Yu

January 2018

This page is intentionally blank.

Copyright notice

© Esmail Abbaszadeh Molaei (2018).

Under the Copyright Act 1968, this thesis must be used only under the normal conditions of scholarly fair dealing. In particular no results or conclusions should be extracted from it, nor should it be copied or closely paraphrased in whole or in part without the written consent of the author. Proper written acknowledgement should be made for any assistance obtained from this thesis.

I certify that I have made all reasonable efforts to secure copyright permissions for third-party content included in this thesis and have not knowingly added copyright content to my work without the owner's permission.

This page is intentionally blank.

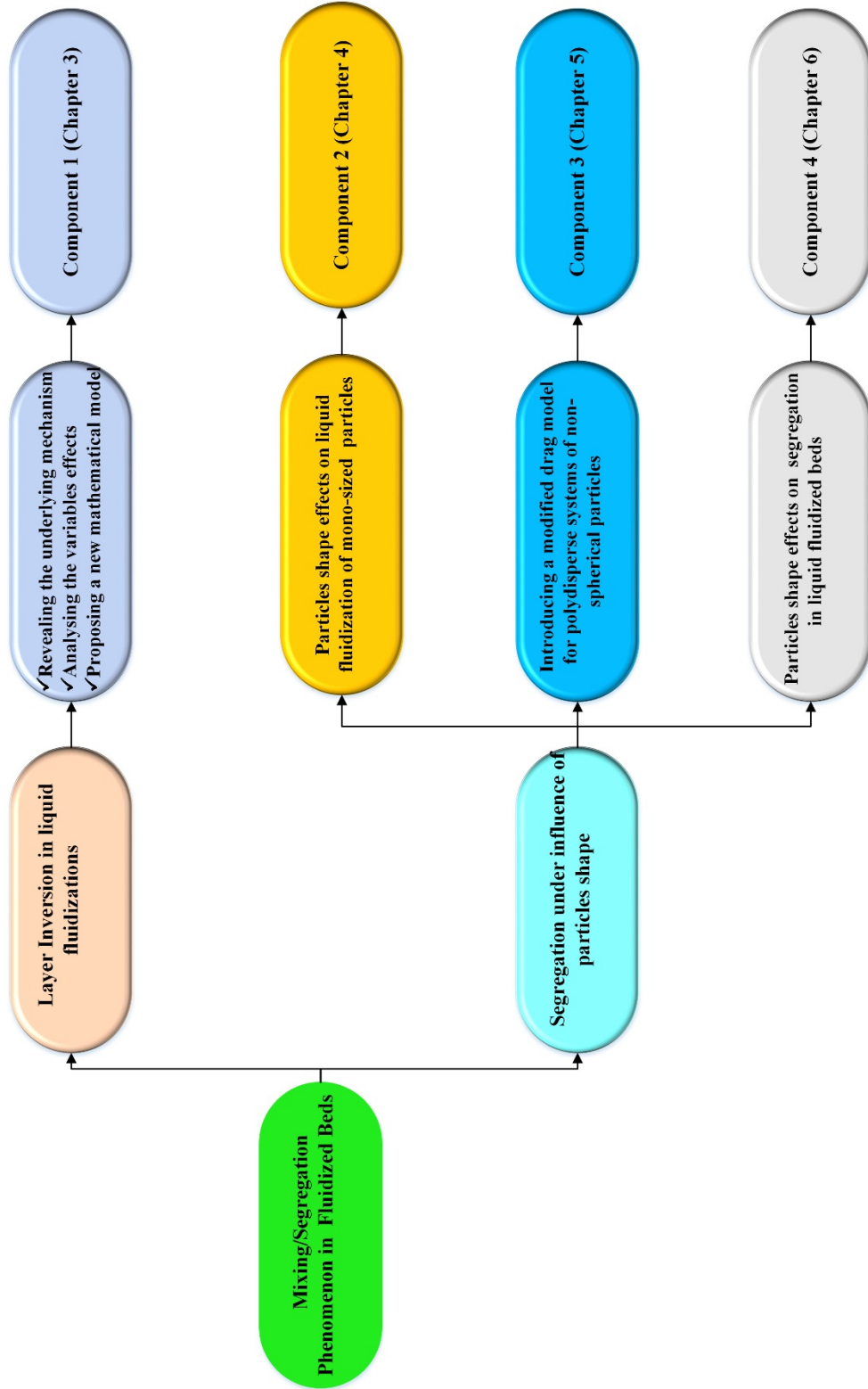
In memory of my father

and

To my mother for her ongoing love and support

This page is intentionally blank.

Thesis at a Glance



This page is intentionally blank.

Abstract

In most of the multiphase operations in the fluidized beds, the properties of the particles, i.e. size, density, and shape can differ from each other either from the beginning of the operations or they may change during the process because of attrition, coalescence or chemical reactions. The differences in particles properties can result in segregation or mixing phenomena in fluidized beds. Segregation is a popular phenomenon for granular materials and can be observed in various particulate systems due to the property differences. In this thesis, two types of segregation phenomenon were chosen to investigate. The first one is called layer inversion phenomenon and the second one is segregation under influence of particles shape.

In terms of layer inversion phenomenon, even though substantial studies have been conducted, limited efforts are made to explain the segregation mechanisms behind this peculiar phenomenon. Therefore, there is a need to elucidate the fundamentals for the occurrence of layer inversion. In principle, the motion of particles is governed by forces acting on them, including particle-particle, particle-wall, and particle-fluid interaction forces. Thus, the layer inversion must be controlled by these interactions, and quantifying these interaction forces is crucial to reveal the segregation mechanism. Unfortunately, these interaction forces are difficult to measure experimentally. This difficulty, however, can be overcome by the combination of Computational Fluid Dynamics and Discrete Element Method (CFD-DEM). Therefore, the aim of the first part of the thesis was to use this approach to address what causes layer inversion and provide a thorough explanation of this phenomenon. The force analysis revealed that the particle-fluid interaction force is responsible for the occurrence of the layer inversion phenomenon. The particle-fluid force value on the large particle is greater than the particle-fluid force on small

particle at low velocity, hence the large particles are observed at the top of the bed at low liquid velocity. With increasing the liquid velocity, the particle-fluid force on large particle decreases and at the same time the particle-fluid force on the small particles increase until they intersect each other at the inversion velocity. Therefore, small and large particles receive same amount of particle-fluid force, and there is not any driving force to segregate the particles, resulting in well mixing condition in the bed. On the other hand, at higher velocity the particle-fluid force on the small particles is bigger than that of large particles and this leads to observing small particles at the top of the bed and large particles at the bottom section. Furthermore, the comparison of different drag force correlations revealed that Di Felice (1994) drag model failed to predict the inversion phenomenon while Rong et al. (2014) drag model predicted the inversion velocity with the best accuracy. In regards to the effects of different parameters on the inversion velocity, it was found that with increasing the particles size ratio, particles density ratio, and liquid velocity the inversion phenomenon happens at higher liquid velocity; however, with increasing the liquid density and liquid temperature the inversion velocity decreases. Finally, a mathematical model was proposed to predict the inversion velocity. The new mathematical model predicted the inversion velocity with average error of 14% which is consistent with the best available model in the literature. On the other hand, the maximum error of the new model is just 34% while the maximum error of other models is at least 150%. Therefore, in this regard it can be noted that the new model is more reliable in term of the range of prediction of the inversion velocity.

In the second part of the thesis, the particles shape effects on fluidized beds behaviour and also on the mixing/segregation phenomenon was studied. In spite of substantial studies on the hydrodynamics of liquid fluidized beds of spherical particles, the effects of particles shape on the solid-liquid flow behaviour are still less reported and the answers to some fundamental questions

such as how and why particle shape affects flow phenomena are not clear, and hence still poorly understood. In the simulations, ellipsoidal particles were used as they can represent a wide range of particle shapes from oblate to prolate particles. It was observed that particles shape significantly affects the solid flow behaviour in liquid fluidizations of mono-sized particles. The spherical particles exhibited highest minimum fluidization velocity while the oblate and prolate particles had less minimum fluidization velocity. A uniform pressure gradient distribution was observed for spherical particles confirming their uniform expansion in the bed while changing the particles shape from spherical to oblate or prolate ones distorted the pressure gradient distribution. For the oblate and prolate particles, a maximum pressure gradient happened somewhere between the bottom and middle of the bed. Force analysis as well as particles orientation and terminal velocity analysis revealed that the changes of particle orientations is responsible for the entrainment phenomenon.

A modified drag force correlations was proposed for the mixtures of polydisperse systems of non-spherical particles. There has been no such a drag model so far. The modified drag force provides more consistent results with experiments than the drag model developed based on mono-sized particles. The analysis of mixtures of spheres and ellipsoids in gas fluidized beds showed that the minimum fluidization velocity of spheres decreases when a second component in the shape of oblate or prolate particles are introduced into the spheres. Adding ellipsoids to spheres causes segregation phenomenon, and it reduces the mixing index. The reason behind the bad quality of mixing under influence of particles aspect ratio was found to be the effects of particles aspect ratio on the particle-fluid interaction force. On the other hand, according to analysis of mixtures of spheres and ellipsoids it was found that particles shape clearly affects the mixing and segregation phenomenon in liquid fluidized beds. Increase in liquid superficial

velocity results in decreasing the mixing index. Nonetheless, for the mixtures of spheres and oblate particles, the mixing index remains constant after specific liquid velocity. The reason behind the segregation due to particle shape effect was found to be the role of the particles shape on the amount of the drag force that a particle receives when particle shape varies. The oblate and prolate particle have larger projected area compared to spherical particles and this leads to receiving larger drag force than that of spherical and hence a driving force is created and segregation happens.

Declaration

This thesis contains no material which has been accepted for the award of any other degree or diploma at any university or equivalent institution and that, to the best of my knowledge and belief, this thesis contains no material previously published or written by another person, except where due reference is made in the text of the thesis.

Signature: _____



Print Name: Esmaeil Abbaszadeh Molaei

Date: 10/01/2018

This page is intentionally blank.

Acknowledgment

First of all, I must thank my primary supervisor Dr. Zongyan Zhou whose knowledge guided me when I was confused, whose compliments encouraged me when I was disappointed, and whose ideas inspired me when I was desperately looking for answers. I also would like to thank him for spending an immense amount of time in polishing and perfecting my manuscripts as well as this thesis.

I would like to express my sincere gratitude to my co-supervisor, Prof. Aibing Yu, for giving me the all help and guidance.

I give my many thanks to Dr. Ruiping Zou who not only as SIMPAS group manager provided all the most facility and decent environment needed for undertaking the research but also provided me with her advice over the duration of my candidature.

Appreciation also goes to fellow researchers and staffs in SIMPAS (Lab for Computer Simulation and Modelling of Particulate Systems) based both in Melbourne and Sydney for their companionships during this journey.

I also wish to express my gratitude to the staffs in the Department of Chemical Engineering, particularly Lilyanne Price and Jill Crisfield for their help during my study. Special thanks to Ms Jane Moodie for teaching a range of programs and courses that have improved my academic writing skills.

I would like to acknowledge the financial support from Monash University and University of New South Wales as well as Funding from the Australian Research Council Industrial Transformation Research Hubs Scheme. Without these funding, the research would not have been possible. Thanks go to the National Computational Infrastructure (NCI) supported by the Australian Government for facilitating the computational section of the research.

Last but not least, I would like to express my biggest thanks to my family who loves, supports, and believes me at every stage of my life. Without you, I couldn't achieve any success in my life including accomplishing this thesis.

This page is intentionally blank.

Contents

THESIS AT A GLANCE	V
ABSTRACT	VII
DECLARATION	XI
ACKNOWLEDGMENT	XIII
CONTENTS	XV
LIST OF FIGURES	XIX
LIST OF TABLES	XXV
CHAPTER 1 INTRODUCTION	1
CHAPTER 2 LITERATURE REVIEW	8
2.1 OVERVIEW	8
2.2 LAYER INVERSION PHENOMENON	8
2.2.1 <i>Introduction</i>	8
2.2.2 <i>Experimental Works and Physical Models</i>	10
2.2.3 <i>Numerical Simulations</i>	20
2.3 PARTICLE SHAPE EFFECTS ON THE MIXING AND SEGREGATION PHENOMENON	22
2.3.1 <i>Introduction</i>	22
2.3.2 <i>Non-Spherical Particles Description</i>	24
2.3.3 <i>The Role of Particles Shape on Fluidizations</i>	26
2.3.3.1 <i>Particle Shape Effects in Gas-Solid Fluidized Beds</i>	26
2.3.3.1.1 <i>Experimental works</i>	26
2.3.3.1.2 <i>Numerical Simulations</i>	33
2.3.3.2 <i>Particle Shape Effects in Liquid-Solid Fluidized Beds</i>	38
2.4 COMPUTATIONAL MODELING OF FLUIDIZED BEDS.....	39
2.4.1 <i>Governing Equations for Solid Particles in CFD-DEM</i>	44
2.4.2 <i>Governing Equations for Fluid Phase in CFD-DEM</i>	47
2.5 SUMMARY AND OBJECTIVES	48
CHAPTER 3 INVESTIGATION OF CAUSES OF LAYER INVERSION AND PREDICTION OF INVERSION VELOCITY IN LIQUID FLUIDIZATIONS OF BINARY PARTICLE MIXTURES	50
3.1 OVERVIEW	50
3.2 INTRODUCTION.....	50
3.3 MODEL DESCRIPTIONS.....	54
3.3.1 <i>Governing equations for particle phase</i>	54
3.3.2 <i>Governing equations for liquid flow</i>	57
3.3.3 <i>Coupling methodology</i>	58

3.4	SIMULATION CONDITIONS.....	58
3.5	RESULTS AND DISCUSSION.....	60
3.5.1	<i>Layer inversion phenomenon.....</i>	60
3.5.2	<i>Force analysis.....</i>	63
3.5.3	<i>Comparison of different drag force models.....</i>	70
3.5.4	<i>Effects of particle and fluid properties on inversion velocity.....</i>	73
3.5.5	<i>A new mathematical model for prediction of inversion velocity.....</i>	78
3.6	SUMMARY	83

CHAPTER 4 CFD-DEM MODELLING OF SOLID FLOW CHARACTERISTICS IN LIQUID FLUIDIZATIONS OF ELLIPSOIDAL PARTICLES85

4.1	OVERVIEW	85
4.2	INTRODUCTION.....	85
4.3	MODEL DESCRIPTIONS	87
4.3.1	<i>CFD-DEM governing equations for ellipsoids.....</i>	88
4.3.2	<i>Particle-particle and particle-fluid interaction forces.....</i>	89
4.3.3	<i>Particle-particle contact detection and particle orientation</i>	92
4.3.4	<i>CFD-DEM coupling methodology.....</i>	93
4.4	SIMULATION CONDITIONS	94
4.5	RESULTS AND DISCUSSIONS	96
4.5.1	<i>Flow patterns</i>	96
4.5.2	<i>Pressure drop.....</i>	98
4.5.3	<i>Bed expansion.....</i>	103
4.5.4	<i>Force analysis.....</i>	108
4.5.5	<i>Particle orientation analysis.....</i>	113
4.5.6	<i>Summary</i>	118

CHAPTER 5 A MODIFIED DRAG MODEL FOR MULTICOMPONENT MIXTURES OF NON-SPHERICAL PARTICLES120

5.1	OVERVIEW	120
5.2	INTRODUCTION.....	120
5.3	MODEL DESCRIPTIONS	123
5.3.1	<i>Drag model for mixtures of non-spherical particles.....</i>	123
5.4	SIMULATION CONDITIONS.....	127
5.5	RESULTS AND DISCUSSION.....	131
5.5.1	<i>Validations of the modified drag model.....</i>	131
5.5.2	<i>Mixing behaviour under influence of particles shape.....</i>	137
5.5.3	<i>Relations of mixing index to forces acting on particles.....</i>	140
5.6	SUMMARY	145

CHAPTER 6 MIXING AND SEGREGATION CHARACTERISTICS OF BINARY MIXTURES OF ELLIPSOIDAL PARTICLES IN LIQUID FLUIDIZATIONS146

6.1	OVERVIEW	146
6.2	INTRODUCTION.....	147
6.3	MODEL DESCRIPTIONS AND SIMULATION CONDITIONS	147
6.4	RESULTS AND DISCUSSION.....	149
6.4.1	<i>Flow patterns and mixing quality</i>	149
6.4.2	<i>Mixing index</i>	157

6.4.3	<i>Force Analysis</i>	159
6.5	SUMMARY	165
CHAPTER 7 CONCLUSIONS AND RECOMMENDATIONS FOR FUTURE WORK ..		167
7.1	CONCLUSIONS	167
7.2	RECOMMENDATIONS FOR FUTURE WORK	171
REFERENCES		173

This page is intentionally blank.

List of figures

Figure 1-1. A picture of layer inversion phenomenon (Escudié et al., 2006b).	3
Figure 2-1. A descriptive demonstration of the layer inversion phenomenon (Escudié et al., 2006b).....	9
Figure 2-2. Variations of the bulk density of small and large particles with liquid superficial velocity (Epstein and LeClair, 1985).	11
Figure 2-3. A simplified picture of the layer inversion phenomenon (Gibilaro et al., 1986).	13
Figure 2-4. Change of bulk density of monocomponent bed with liquid velocity (Moritomi et al., 1982).....	13
Figure 2-5. Solid concentration relationships for the system water/zirconia/copper (Gibilaro et al., 1986).....	15
Figure 2-6. Bulk density evaluations for the illustrative example of Figure 2-5 (Gibilaro et al., 1985).....	17
Figure 2-7. a comparison between Gibilaro et al. (1986) model and experiments (Gibilaro et al., 1986).....	17
Figure 2-8. Snapshots showing bed inversion in liquid fluidized bed for PB:GB volume ratio 0.54:0.46 with increasing superficial liquid velocity: (a)18.2mm/s, (b)28.1mm/s, (c) slightly greater than 33.1mm/s, (d) 38.2mm/s, (e) 43.1mm/s. Inversion was observed at 33.1 mm/s (Chun et al., 2011).....	20
Figure 2-9. Snapshots of flow patterns in liquid fluidization for different liquid superficial velocities (Zhou and Yu, 2009).....	22
Figure 2-10. Various non-spherical particulate systems in nature and industry (Zhong et al., 2016).....	23
Figure 2-11. Various particle shapes with different aspect ratio (Yovanovich et al., 1995).....	24
Figure 2-12. Schematic of (a) prolate ($b > a$) and (b) oblate ($b < a$) ellipsoidal particles (picture from Gan, 2015).....	26
Figure 2-13. Photographs of the seed particles used (Liu and Litster, 1991).	27
Figure 2-14. U_{mf} / U_{mf-sph} of plate-like particles vs. Zingg factor (Liu et al., 2008).....	28
Figure 2-15. Physical properties of irregular particles used in Shao et al., 2013.....	29
Figure 2-16. Pressure drop versus superficial gas velocity in the bed (Shao et al., 2013).....	29
Figure 2-17. Mixing behaviour of wood pelletW1 at different superficial gas velocities (Shao et al., 2016).....	32
Figure 2-18. Comparison of simulated flow patterns with experiments at different superficial gas velocity: (a) $U_f = 0.5$ m/s, (b) $U_f = 1.0$ m/s, (c) $U_f = 1.5$ m/s, and (d) $U_f = 2.0$ m/s (Zhong et al., 2009).....	35

Figure 2-19. Non-dimensionalised friction factor against Reynolds number for 4 and 8 mm volume equivalent diameter particles. Lift-off pressures are shown by the dotted diagonal lines. Post-fluidisation the average friction factor follows this line, as expected. The Ergun curve, shown as a solid black line, shows excellent agreement with our spherical simulations (Hilton et al., 2010).....36

Figure 2-20. Comparison of snapshots of solid flow patterns observed in the experiments (the top figures) and CFD–DEM simulations (the bottom figures) when the gas superficial velocity is 3.0 m/s (Zhou et al., 2011).36

Figure 2-21. Effect of aspect ratio on the minimum fluidization velocity (Figure 2-21).37

Figure 2-22. Experimental (left column) and numerical results (right column) for mixtures of 7mm spheres as the bottom component and 7mm spheres (a-b), 5mm× 6mm× 6mmcubes (cd), 4 mm × 4 mm × 11 mm elongated cuboids (e-f) or 2 mm × 9 mm × 10 mm plates (g-h) as the top component (Vollmari et al., 2017).38

Figure 2-23. Dynamic pressure gradient profiles for the three particle shapes: (a) Spheres, $U = 0.316\text{m/s}$, (b) discs, $U = 0.251\text{m/s}$, (c) rods, $U = 0.316\text{m/s}$ (Escudié et al., 2006a).39

Figure 2-24. The linear-spring-dashpot contact force model.45

Figure 2-25: The comparison of the non-contact force (Zhu et al., 2007).47

Figure 3-1. Snapshots (a-f) of flow patterns in liquid fluidized beds at different liquid superficial velocities U_0 : (a) 0 cm/s; (b) 0.34 cm/s; (c) 0.6 cm/s; (d) 1.0 cm/s; (e) 1.5 cm/s; and (f): 1.7 cm/s. Six inset figures at the left top: temporal variations of the mean height of each of the species at different liquid superficial velocities.....61

Figure 3-2. Variations of the mean-normalized height of each component with liquid velocity; (b) variations of normalized bottom layer height with liquid velocity (the left-bottom inset is a schematic diagram of the definition of different bed heights introduced by Jean and Fan (1986)).63

Figure 3-3. Snapshots displaying the spatial distribution of particle-fluid interaction forces at steady state conditions at different liquid superficial velocities: (a) drag force, (b) pressure gradient force, and (c) total particle-fluid interaction force.64

Figure 3-4. Probability density function of normalized forces on particles at different liquid superficial velocities on small particles ((a), (b), (c)); and large particles ((d), (e), (f)).65

Figure 3-5. The variation of the mean forces on both large and small particles in the vertical direction: the top row is particle-fluid interaction force; the middle row is the particle-particle interaction force; and the bottom row is the particle-wall (including side and bottom walls) interaction force. Figures from the left to the right are corresponding to different liquid velocities: (a) 0.34 cm/s, (b) 1.0 cm/s, and (c) 1.7 cm/s. Note that the time-axis in the figures is on a logarithmic scale.68

Figure 3-6. Variations of temporal-spatial mean forces with liquid superficial velocity for both large (represented by circles) and small particles (represented by triangles): (a) the total particle-fluid interaction force, and (b) the drag force and pressure gradient force.69

Figure 3-7. Snapshots of flow patterns in solid-liquid fluidized beds for different drag force models at different liquid superficial velocities: (a) Cello et al. (2010); (b) Di Felice (1994); (c)

Rong et al. (2014); and (d) Yin and Sundaresan (2009). All snapshots are coloured based on drag force values.71

Figure 3-8. Probability density function of the drag force and the pressure gradient force predicted by different drag models ($U_0 = 0.34\text{m/s}$): (a) and (c) for small particles; (b) and (d) for large particles.73

Figure 3-9. (a) The effect of particles size ratio on the inversion velocity; (b) the effect of density size ratio on the inversion velocity; (c) variations of particle-fluid force ratio with liquid superficial velocities at different particles size ratio; and (d) variations of particle-fluid force ratio with liquid superficial velocities at different particle density ratio.....75

Figure 3-10. (a) The effect of liquid viscosity on the inversion velocity; (b) the effect of liquid density size ratio on the inversion velocity; (c) variations of particle-fluid force ratio with liquid superficial velocities at different liquid viscosity; and (d) variations of particle-fluid force ratio with liquid superficial velocities at different liquid density.....76

Figure 3-11. The effects of operating temperature on the inversion velocity.....78

Figure 3-12. The comparison of inversion velocity predicted by the model and measured experimentally.....80

Figure 3-13. (a) Comparison of the mean errors of different models; and (b) comparison of the maximum and minimum mean errors of different models.....82

Figure 4-1. Illustrations of spheroids with different aspect ratios (AR): (a) oblate spheroid with $AR = 0.5$, and (b) prolate spheroid with $AR = 2$. The vector OA is used to represent particle orientation (O - particle mass centre; A - polar apex).....96

Figure 4-2. Particle configurations for different aspect ratios: (I) $AR = 0.28$, (II) $AR = 1.0$, and (III) $AR = 3.5$. For each aspect ratio, liquid superficial velocities used are: (a) 0.1 m/s, (b) 0.15 m/s, (c) 0.2 m/s, (d) 0.225 m/s, (e) 0.251 m/s, (f) 0.275 m/s, (g) 0.316 m/s, (h) 0.325 m/s, and (i) 0.47 m/s.....97

Figure 4-3. Effect of aspect ratio on the pressure drop variation with time and its corresponding standard deviation: (a) Spherical particles ($AR = 1$), (b) oblate particles ($AR = 0.28$), (c) prolate particles ($AR = 3.5$); and (d) variations of standard deviation with liquid superficial velocities for different particle shape.....98

Figure 4-4. The effect of aspect ratio on the transition velocities from particulate fluidisation to turbulent fluidisation..... 100

Figure 4-5. Dimensionless pressure drop variations as a function of liquid superficial velocities: (a) Oblate spheroids ($AR \leq 1.0$), and (b) prolate spheroids ($AR \geq 1.0$)..... 101

Figure 4-6. Effect of particle aspect ratio on the minimum fluidization velocity..... 101

Figure 4-7. Time-averaged pressure gradient variations along the bed height for oblate (a, d), spherical (b, e), and prolate (c, f) particles at two different liquid superficial velocities: (a-c) 0.1 m/s, and (d-f) 0.251 m/s..... 103

Figure 4-8. Transient bed expansion for different particle aspect ratios at two different liquid superficial velocities: (a) 0.1 m/s, and (b) 0.251 m/s..... 104

Figure 4-9. Time-averaged local voidage variations along the bed height for oblate (a, d), spherical (b, e), and prolate (c, f) particles at two different liquid superficial velocities: (a-c) 0.1 m/s, and (d-f) 0.251 m/s.	105
Figure 4-10. Bed expansion variations with liquid superficial velocities and aspect ratios: (a) oblate particles (AR=0.28), (b) spherical particles (AR=1), (c) prolate particles (AR=5.33), and (d) effects of aspect ratio on the bed expansion at different liquid superficial velocities.	106
Figure 4-11. Richardson-Zaki's equation parameters as a function of aspect ratio: (a) extrapolated velocity U_e , and (b) expansion index (n).	107
Figure 4-12. Effects of particle aspect ratio on the force probability density distribution at liquid superficial velocity of 0.251m/s: top two figures - drag force, middle two figures - pressure gradient force, and bottom two figures - particle-particle interaction force. Note that in the left column (a-c) are oblate particles, and in the right column (d-f) are prolate particles.	109
Figure 4-13. Effect of particle aspect ratio and liquid superficial velocities on spatial-temporal averaged forces: (a) drag force and (b) pressure gradient force.	110
Figure 4-14. Time-averaged variations of different variables with bed height at liquid superficial velocity of 0.251 m/s: (a) drag force, (b) pressure gradient force, (c) particle-fluid interaction force, (d) particle vertical velocity, (e) particle-particle interaction force, (f) particle-wall interaction force, and (g) total force acting on particles. The red dash line – bed interface height for ellipsoids at AR = 3.5, brown dash line – bed interface height for spheres, and green dash line – bed interface for ellipsoids at AR = 0.28.	112
Figure 4-15. Variations of particle orientation with time for various aspect ratios at two different liquid superficial velocities: (a) 0.1 m/s, and (b) 0.251 m/s.	114
Figure 4-16. Effects of particle aspect ratio and liquid superficial velocities on the bed average orientation angle.	115
Figure 4-17. Effect of liquid superficial velocities on the particle orientation angle distributions with bed height when $U_0 = 0.251$ m/s: (a) AR = 0.28, (b) AR = 1.0, and (c) AR = 3.5.	116
Figure 4-18. Effect of particle orientation on the terminal velocity of ellipsoidal particles.	117
Figure 5-1. Sampling size effects on mixing index for two extreme conditions of well-mixed bed and fully segregated bed; (a) binaries of oblate (AR=0.25) and spheres, (b) binaries of two identical spheres, (c) binaries of prolate (AR=3.5) and spheres.	131
Figure 5-2. Particles configurations predicted with (a) modified drag force model (Eq. (5-3)) (b) drag model for mono-sized drag model at different times and at the gas velocity of 2.4 m/s.	133
Figure 5-3. Comparison between the mixing index of beds simulated by modified drag model (Eq. (7)) and drag model for mono-size particles (Eq. (12)); (a) binaries of two spheres with the same size and density, (b) binaries of oblate particles (AR=0.25) and spheres.	135
Figure 5-4. The pressure drop variations as a function of liquid superficial velocities: (a) mono particles with different aspect ratios, (b) binaries with AR (1, 0.25), (c) binaries with AR (1, 0.5), (d) binaries with AR (1, 2).	137
Figure 5-5. Particles configurations predicted for different binaries at an equilibrium state at the gas velocity of 2.4 m/s.	138

Figure 5-6. The effects of gas velocity on the mixing behavior of different mixtures: (a) AR(1, 0.25), (c) AR(1,1), and (e) AR(1,3.5); The required time to reach steady-state mixed condition as a function of gas velocity for different mixtures: (b) AR(1, 0.25), (d) AR(1,1), and (f) AR(1,3.5).	139
Figure 5-7. The total particle-fluid force distributions in three different mixtures: (a) AR(1,0.25), (b) AR(1,1), (b) AR(1,3.5); $U_0 = 2.4$ m/s.	142
Figure 5-8. The effects of the aspect ratio of the added component to the spheres on the mixing index and particle-fluid force ratio at $U_0 = 2.4$ m/s.	142
Figure 5-9. Variations of temporal-spatial mean forces with the aspect ratio of the added component for both components: (a) added component (ellipsoids), and (b) spheres at $U_0 = 2.4$ m/s.	143
Figure 6-1. Solids configurations for binary mixtures of oblate particles and spheres: (I) AR(1,0.25), (II) AR(1,0.8) at different liquid velocities: (a) 0 m/s; (b) 0.09 m/s; (c) 0.13 m/s; (d) 0.16 m/s; (e) 0.19 m/s.	151
Figure 6-2. Solids configurations for different binary mixtures: (I) AR(1, 1), (II) AR(1, 1.13), and (III) AR(1, 2) at different liquid velocities: (a) 0 m/s; (b) 0.09 m/s; (c) 0.13 m/s; (d) 0.16 m/s; (e) 0.19 m/s.	152
Figure 6-3. Effects of particle initial configurations on the mixing index of binary mixtures: (a) mixture of AR(1, 1); and (b) mixture of AR(1, 0.8).	154
Figure 6-4. Variation of the volume fraction of spheres along the bed height for different binaries at different liquid superficial velocities.	155
Figure 6-5. Mixing index variations with time for different liquid superficial velocities and different mixtures: (a) AR(1, 0.5); (b) AR(1, 0.8); (c) AR(1, 1.13); and (d) AR(1, 1.2).	156
Figure 6-6. The effects of liquid superficial velocity on the temporal-spatial averaged mixing index of different binaries of ellipsoids and spheres: (a) binaries of oblate particles and spheres, (b) binaries of prolate particles and spheres.	158
Figure 6-7. Mixing index variation with respect to the aspect ratio of added ellipsoids to spheres at different liquid velocities.	159
Figure 6-8. The snapshots of particles configuration at steady state conditions coloured by different forces when $U_0 = 0.09$ m/s: (a) drag force, (b) pressure gradient force, and (c) particle-particle force; (d) particles velocity field coloured and sized by vertical velocity. Note that the top row is for the mixture of AR (1, 0.8), the middle row is for the mixture of AR(1,1) and the bottom row is for the mixture of AR(1,2).	161
Figure 6-9. Spatial-averaged forces variations with time for different binaries: first row: binary of oblate particles (AR=0.8) and spheres, second row: binary of identical spheres, binary of oblate particles (AR=0.8) and spheres, binary of prolate particles (AR=2) and spheres. Note that right column presents the drag force, pressure gradient force, and particle-fluid force and left column shows the particle-particle interaction force and the particle-wall interaction force.	164
Figure 6-10. Mixing index, drag force ratio, and projected area ratio as a function of the aspect ratio of the added ellipsoids when $U_0 = 0.09$ cm/s.	165

This page is intentionally blank.

List of tables

Table 2-1. Particle properties used in Vollmari et al., 2016.....	31
Table 2-2. Size and shapes of particles used in Hilton et al., 2010.....	35
Table 2-3. Equations to calculate forces and torques acting on the particle i	44
Table 3-1. Equations to calculate forces and torques acting on the particle i	55
Table 3-2. Drag force models assessed in the present work	56
Table 3-3. Parameters used in the present simulations.	58
Table 3-4. Inversion velocities predicted by different drag force models.	73
Table 3-5. Different mathematical model for prediction of the inversion velocity.	80
Table 4-1. Equations to calculate forces and torques acting on the particle i	90
Table 4-2. Parameters used in the present simulations.	95
Table 5-1. Parameters used in the present simulations.	127
Table 6-1. Parameters used in the present simulations.	148

This page is intentionally blank.

Chapter 1 Introduction

Fluidization is the phenomenon that all particles are fluidized/suspended in the bed. In industries, fluidization is carried out in Fluidized Bed Reactors. The main advantage of fluidized beds is that when the fluids pass through the particles, particles are vigorously agitated. This results in no temperature gradients in the bed even in the situation with highly exothermic or endothermic reactions. The fluid-like flow of particles provides handling of solids easy. In addition, the circulating of particles between two fluidized bed reactors provides a possible condition to transport or import heat out or into the large reactors. The application of fluidized beds in various industries such as chemical, food, mining, petroleum, and energy industries have increased in the past decades. The fluidizations are also used in the polymerization of olefins, drying of starch and combustion of coal (Kunii and Levenspiel, 1991). Other applications of fluidized beds are particle classifications, backwashing of down-flow granular filters, in situ fluidized washing of soils, crystal growth, leaching and washing, adsorption and ion exchange, flocculation, electrolysis, and liquid-fluidized bed heat exchangers (Epstein, 2002).

In most of the multiphase operations in the fluidized beds, the properties of the particles, i.e. size, density, and shape can differ from each other either from the beginning of the operations or they may change during the process because of attrition, coalescence or chemical reactions. The differences in particles properties can result in segregation or mixing phenomena in liquid fluidized beds. Segregation is a popular phenomenon for granular materials and can be observed in various particulate systems due to the property differences and/or other characteristics such as surface roughness, resilience, and electrostatic properties (Caulkin et al., 2010; Lozano et al.,

2015; Ottino and Khakhar, 2000). Segregation can significantly affect the quality of manufactured products, but it can also be used to separate materials. It represents a challenging research area in granular research, and more research is required to understand this phenomenon.

Therefore, the chief aim of the thesis is to investigate two types of segregation occurring in the fluidized beds using a combination of Computational Fluid Dynamics (CFD) and Discrete Element Method (DEM). The first segregation phenomenon is layer inversion phenomenon in solid-liquid fluidized beds, and another one is a segregation under influence of particles shape.

In the first part of the thesis, the layer inversion phenomenon in liquid fluidisations is comprehensively studied. In the layer inversion, the fluidization system contains a binary mixture of particles in which small particles are denser than large particles. At low liquid velocities, the two species form distinct layers with the smaller and denser particles at the bottom while the larger and lighter particles at the top. At high liquid velocities, however, the two layers are inverted. Smaller particles move to the top, and larger particles are located at the bottom. This peculiar phenomenon, as shown in Figure 1-1, plays an important role in fluidized bed solid classifiers or biological reactors (Di Renzo et al., 2011). Substantial studies have revealed that the inversion velocity depends on many variables such as mixture compositions, size/density ratio, and fluid properties (Escudié et al., 2006b). Some investigators (Epstein and LeClair, 1985; Hancock, 1936) assumed that for a specific binary, the inversion velocity did not depend on the overall compositions of the two species. However, Moritomi et al. (1982) experimentally found that the layer inversion can be achieved by not only varying liquid superficial velocity but also changing proportions of a binary mixture in a constant velocity. These observations have made a clear picture of layer inversion for later investigators (Gibilaro et al., 1986; Jean and Fan, 1986).

More than 20 models have been proposed in the literature to predict the layer inversion phenomenon behaviour in liquid-solid fluidized beds (for example, Epstein, 2005; Gibilaro et al., 1986; Patwardhan and Tien, 1985; Funamizu and Takakuwa, 1995; Moritomi et al., 1986; Jean and Fan, 1986; Gibilaro et al., 1986).

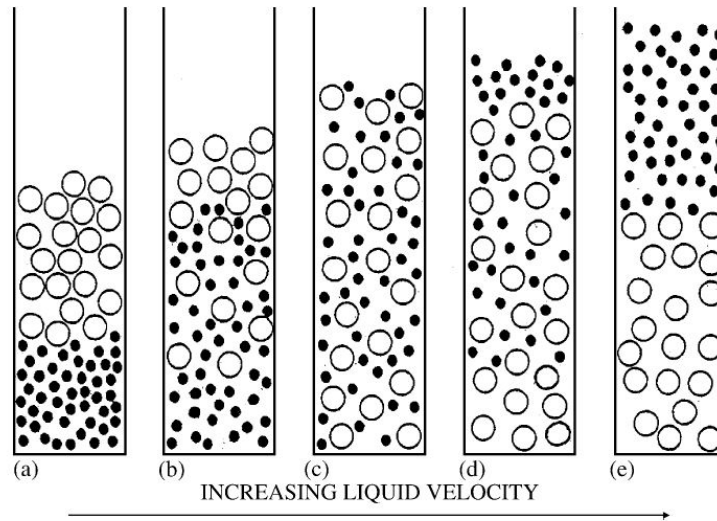


Figure 1-1. A picture of layer inversion phenomenon (Escudié et al., 2006b).

Despite a large number of experimental investigations on layer inversion in liquid fluidized beds, only a few researchers have put their efforts to numerically study this phenomenon. Generally speaking, there are two approaches to model liquid fluidized beds: continuum approach (e.g. so-called Eulerian-Eulerian approach or two-fluid model (A. Howley and J. Glasser, 2002; Reddy and Joshi, 2009; Syamlal and O'Brien, 1988)) and discrete approach (e.g. so-called Lagrangian-Eulerian or discrete element method (Di Renzo et al., 2011; Malone et al., 2007; Mukherjee and Mishra, 2007; Vivacqua et al., 2012; Zhou and Yu, 2009)). Particularly, as discrete approach such as CFD-DEM can provide some fundamental concepts of the flow at a particle scale, it has been verified as one of the most effective approaches to study the

fundamental behaviour of particle-fluid systems (Zhu et al., 2007, 2008). Such an approach has been used by some investigators to study layer inversion phenomenon (for example, Di Renzo et al., 2011; Mukherjee and Mishra, 2007; Vivacqua et al., 2012; Zhou and Yu, 2009; Malone et al., 2007).

Even though substantial studies have been conducted, limited efforts are made to explain the segregation mechanisms behind this peculiar phenomenon. Therefore, there is a need to elucidate the fundamentals for the occurrence of layer inversion. In principle, the motion of particles is governed by forces acting on them, including particle-particle, particle-wall, and particle-fluid interaction forces (Zhu et al., 2007 and 2008). Thus, the layer inversion must be controlled by these interactions, and quantifying these interaction forces is crucial to reveal the segregation mechanism. Unfortunately, these interaction forces are difficult to measure experimentally. This difficulty, however, can be overcome by the CFD-DEM. Therefore, the aim of this part of the project is to use this approach to address what causes layer inversion and provide a thorough explanation of this phenomenon. Different drag models have also been compared to examine their applicability in generating layer inversion phenomenon. In addition, parametric studies are conducted to figure out the impacts of particle and liquid properties on the inversion velocity. Finally, a mathematical model based on force balance criterion is proposed to predict the inversion velocity.

In the second part of the thesis, the effect of particles shape on the hydrodynamics and segregation/mixing phenomenon in fluidized beds, particularly in liquid fluidizations, are investigated. To gain an understanding of liquid fluidisation behaviour, most studies, either experimentally or numerically, have focused on solid flow behaviour with mono-sized particles or mixtures with different particle sizes or densities. Mono-sized spherical particles make

Chapter 1 Introduction

homogenous fluidized beds (Johnson, 1949; Wilhelm and Kwauk, 1948), and the bed expansion can be described by Richardson and Zaki (1954) correlation. Apart from homogenous/particulate flow regimes, other flow regimes such as wavy (Didwania and Homsy, 1981), aggregative/turbulent (Didwania and Homsy, 1981; Wilhelm and Kwauk, 1948, slugging Lettieri et al., 2006), and bubbly (Didwania and Homsy, 1981) regimes can also be observed in liquid fluidized beds. Moreover, introducing a second or third component with a different size or density causes more complicated flow structures. Extensive efforts have been made in this direction to understand the principles of liquid fluidized beds of multicomponent mixtures of spherical particles (Di Felice, 1995; Didwania and Homsy, 1981; Escudié et al., 2006b; Gibilaro et al., 1986; Moritomi et al., 1982; Van Duijn and Rietema, 1982). As a result, various models have been proposed to quantify the solid-liquid fluidized bed characteristics (Asif, 2004; Escudié et al., 2006b; Moritomi et al., 1982).

In spite of substantial studies on the hydrodynamics of liquid fluidized beds, the effects of particles shape on the solid-liquid flow behaviour are still less reported. Except for two physical experiments (Barghi et al., 2003; Escudié et al., 2006a), the previous studies considered particles as spheres, and few studies have been remarked on liquid fluidization of non-spherical particles. However, particles are generally irregular in most of processes (Escudié et al., 2006a) such as ore beneficiations using liquid-solid fluidized beds separator (Tripathy et al., 2017). The observations show that particle shape can cause different flow behaviour in liquid fluidizations rather than that observed for ideal spherical particles. However, the answers to some fundamental questions such as how and why particle shape affects flow phenomena are not clear, and hence still poorly understood. Therefore, firstly, CFD-DEM is used to examine the effects of particle shape on the flow characteristics in liquid fluidizations of mono-sized particles. Then, the effects of particles shape on the segregation and mixing phenomenon in binary mixtures of both gas-fluidized beds

Chapter 1 Introduction

and liquid fluidized beds are studied. So far, only limited studies are conducted to use CFD-DEM approach for the mixing behaviour of multi-component mixtures of non-spherical particles in fluidized beds. One main reason is that a proper drag force model for a multi-component mixture of non-spherical particles is still not available. Many drag models, so far, have been proposed for a binary mixture of spherical particles and systems with mono-sized non-spherical particles. However, these drag models are not recommended to be used for mixtures of non-spherical particles. This fact was also highlighted by Vollmari et al. (2017) who found noticeable differences between experimental and numerical predictions of mixing index for spheres and elongated cuboids mixtures as well as spheres and plates. They attributed such discrepancies to the lack of drag force model for polydispersity systems of spherical and non-spherical particles.

Therefore, in the thesis, an effort is made to propose a drag force model, which considers different shapes in multi-component mixtures, by the combination of Rong et al. (2014), Hölzer and Sommerfeld (2008), and Rong et al. (2015) drag model. The mixing indices predicted by the new drag model and a mono-sized drag force model are compared with experimental data obtained in gas-fluidized beds. Then the new modified drag model is employed to study the segregation/mixing phenomenon under influence of particles shape in gas-solid fluidized beds and liquid-solid fluidized beds.

Therefore, this thesis is organised into seven chapters; the overview of each chapter is summarized below.

Chapter 1 (Introduction) contains a complete introduction of the thesis including a brief background for the motivation of this thesis, the research aims and an outline of the thesis structure.

Chapter 1 Introduction

Chapter 2 (Literature Review) provides a comprehensive literature survey on the following areas: layer inversion phenomenon in liquid fluidizations, particles shape effects on the hydrodynamics of mono-sized fluidized beds, the mixing and segregation under influence of particles shape.

Chapter 3 demonstrates a comprehensive analysis of layer inversion phenomenon in liquid fluidized beds using CFD-DEM model.

Chapter 4 studies solids flow characteristics in liquid fluidizations of mono-sized ellipsoidal particles in order to study the effects of particles shape on the hydrodynamics of fluidized beds of mono-sized systems.

Chapter 5 introduces a modified drag model which is applicable to multicomponent systems of non-spherical particles. The new modified drag correlation is validated with experimental data from gas-fluidized beds, then the mixing/segregation phenomenon in gas fluidized beds is investigated.

In Chapter 6, the particles shape effects on the mixing characteristics of binary mixtures in liquid fluidizations are studied.

Chapter 7 summarizes the major findings of this thesis, and recommendations are presented for the future work.

Chapter 2 Literature review

2.1 Overview

This thesis focuses on a peculiar segregation/mixing phenomenon occurring in solid-liquid fluidized beds so called the layer inversion and the particles shape effects on the behaviours of fluidized beds, particularly the segregation and mixing phenomenon under influence of particles shape. Literature available on these subjects will be discussed here, followed by the thesis objectives.

2.2 Layer Inversion Phenomenon

2.2.1 Introduction

Solid-liquid fluidized beds have been employed in industries since the 16th century when Agricola (1556) separated solids with different sizes (Di Felice, 1995). Thereafter, the applications of liquid fluidizations have been increased in many areas such as particle classification, backwashing of granular filters, crystal growth, leaching and washing, adsorption and ion exchange, electrowinning, self-cleaning heat exchangers, and bioreactors due to high-efficient liquid-solid contact, favourable mass and heat transfer, high operation flexibilities, and reduced back mixing of phases (Epstein, 2005). Particle classifications in liquid fluidizations can be occurred by size, density or shape. Particles with the same shape and different size or density make the stratified bed with larger or denser particles at the bottom and smaller or less dense ones at the top. Depending on the difference between the particle size or density, two layers might be separated sharply or make mixing zones at the interface. The mixing zones can be along the whole bed regarding the composition of the binary (Di Felice, 1995). On the other hand, when

particles in a binary mixture differ in both size and density, the mixing and segregation patterns in the bed get complicated.

Liquid fluidization of a specific binary mixture differing in both size and density causes an interesting phenomenon. When a binary mixture with specific characteristics in which smaller particles are denser than the larger ones is fluidized, at low velocities the smaller denser particles are observed in the bottom of bed while the larger ones stay at the top of the bed. However, at high velocities these two separated layers are inverted. This phenomenon, as shown in Figure 2-1, is called the layer inversion. Velocity at which two species are uniformly distributed in the bed and above which the inversion of layers occurs is named the inversion velocity. In other words, in velocities lower or larger than inversion velocity, two layers are observed while at the inversion velocity two species are homogeneously mixed throughout the whole bed. This peculiar phenomenon plays an important role in fluidized bed solid classifiers or biological reactors (Di Renzo et al., 2011).

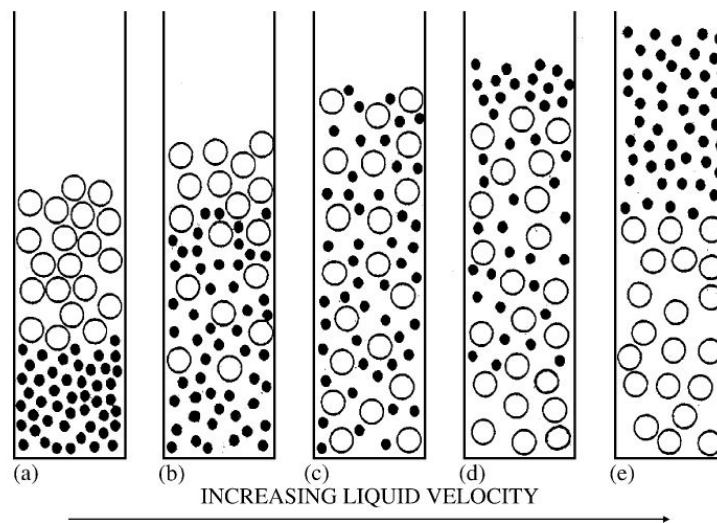


Figure 2-1. A descriptive demonstration of the layer inversion phenomenon (Escudié et al., 2006b).

Chapter 2 Literature Review

In terms of particle classification or particle sorting operation, when large particles are denser it is expected to observe the large particles at the bottom of the operating bed at a wide range of fluidization velocity. However, for the specific mixture, as mentioned above that small particles are denser than large particles, large and small particles can be observed at the bottom or top or mixed along the bed depending on the liquid superficial velocity; top bed rich in large particles at low velocity and small particles rich in the bottom at high velocity. Therefore, the ignorance and unawareness of this inversion can result in unexpected separation, and knowing about this phenomenon helps the bed column operator to select the appropriate velocity for separation or mixing purposes. On the other hand, from the mixing point of view, the inversion point is the optimum operating condition. For example, if it is required to increase the heat transfer rate in a bed with chemically active particle species 1, one option can be adding species 2 with chemically inert properties. Therefore, one can find a species 2 with a specific characteristic which meets the criteria for inversion layer and then chooses a velocity around the inversion point velocity as an operating condition that the bed shows perfectly mixing behaviour. This indeed results in extending the surface of species 1 and increasing the heat transfer coefficient.

The previous works on the study of layer inversion can be classified into two groups: experimental works and physical models, and numerical simulations. Here, these two groups are discussed.

2.2.2 Experimental Works and Physical Models

From the first time that the layer inversion was observed by Hancock (Hancock, 1936) to the late of twenty century almost no investigations had been carried out in this area. However, since early 80th of the twenty century, this peculiar phenomenon has come to the centre of investigators' attention either experimentally or numerically. A simplified picture of layer inversion (Epstein

Chapter 2 Literature Review

and LeClair, 1985) was based on elementary stability considerations, which states the species with a higher bulk density of monocomponent bed settle to the bottom. Therefore, the inversion velocity is readily determined when the bulk densities of two monocomponent beds are equal, as displayed in Figure 2-2. This ideal and simplified model describes two distinct layers at low and high velocities and a mixed bed at inversion velocity as shown in Figure 2-3. Thus it predicts sudden inversion of layer at a velocity which leads to inverting two layers. This description of the phenomenon also does not consider the volume fraction of each component as an effective factor on the inversion point.

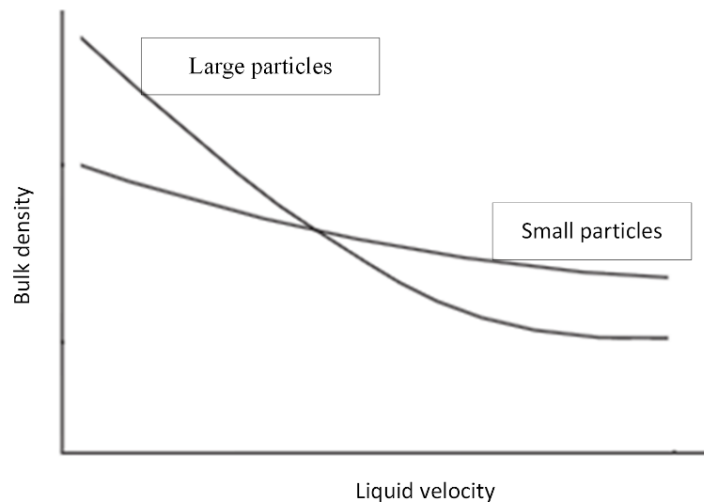


Figure 2-2. Variations of the bulk density of small and large particles with liquid superficial velocity (Epstein and LeClair, 1985).

However, the experiments of Moritomi et al. (1982) made a more realistic picture of inversion phenomenon. In their work, the effects of particle size ratio and mixture compositions on layer inversion were systematically investigated in liquid fluidized beds. They found that the intersection point of bulk densities of each monocomponent may not give the correct inversion velocity. For example, the bulk density of pure beds of 100 g of glass beads with average diameter of 163 μm and 30 g and 50 g of hallow char with average diameter of 775 μm were

Chapter 2 Literature Review

calculated based on the bulk density equations proposed, which is given as: $\rho_b = \varepsilon\rho_f + (1 - \varepsilon)\rho_p$; where ρ_b is the bulk density of monocomponent bed, ε is the void fraction of the bed, ρ_f is the density of fluid, and ρ_p is the density of particle. These bulk density variations with liquid velocity are presented in Figure 2-4. As it can be seen from this figure, the bulk density of 30 g and 50 g of hollow char are similar as the bed bulk density of hollow char does not depend on its weight. As a result, a mixture of 30 g hollow char and 100 g activated carbon and a mixture of 50 g hollow char and 100 g activated carbon give only one intersection. Moritomi et al. (1982), therefore, concluded that for binaries with different compositions, the bulk density variations with liquid density is the same, so the bulk density concept is not an appropriate model to predict the inversion point. Furthermore, it was found that the lower part of two layers consisted of both components with a composition that was independent of overall bed composition and solely depended on the liquid velocity. Therefore, five flow patterns were encountered as the liquid superficial velocity was increased (as illustrated in Figure 2-1). It was observed that small particles in the mixture expand with the liquid velocity in the same manner as its monocomponent bed while the height of the top layer of large particles increases till inversion velocity and then starts to decrease. They kept both particles types weights constant to study the effect of size ratios. The inversion velocity decreased with increasing large particles diameter for a constant small particles diameter. The inversion velocity, however, increased with increasing small particles diameter for a constant large particles diameter. In terms of the effect of binary compositions on inversion phenomenon, it was found that loading more large particles to the constant amount small particles caused an increase in inversion velocity. Nonetheless, the layer inversion always occurred when two bulk density curves of monocomponent beds intersected.

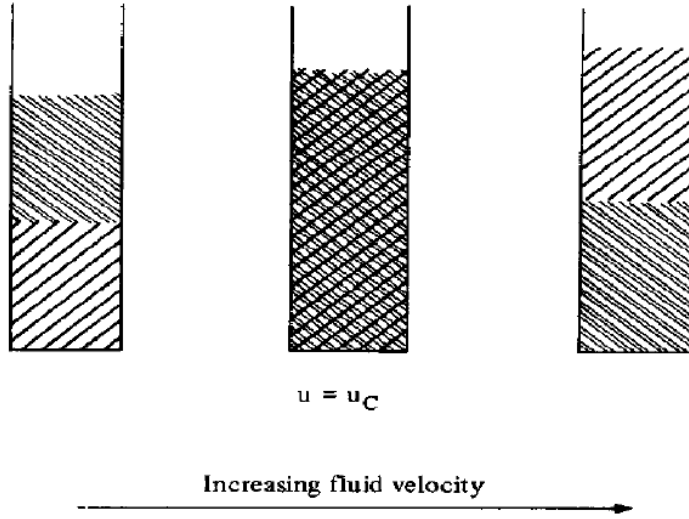


Figure 2-3. A simplified picture of the layer inversion phenomenon (Gibilaro et al., 1986).

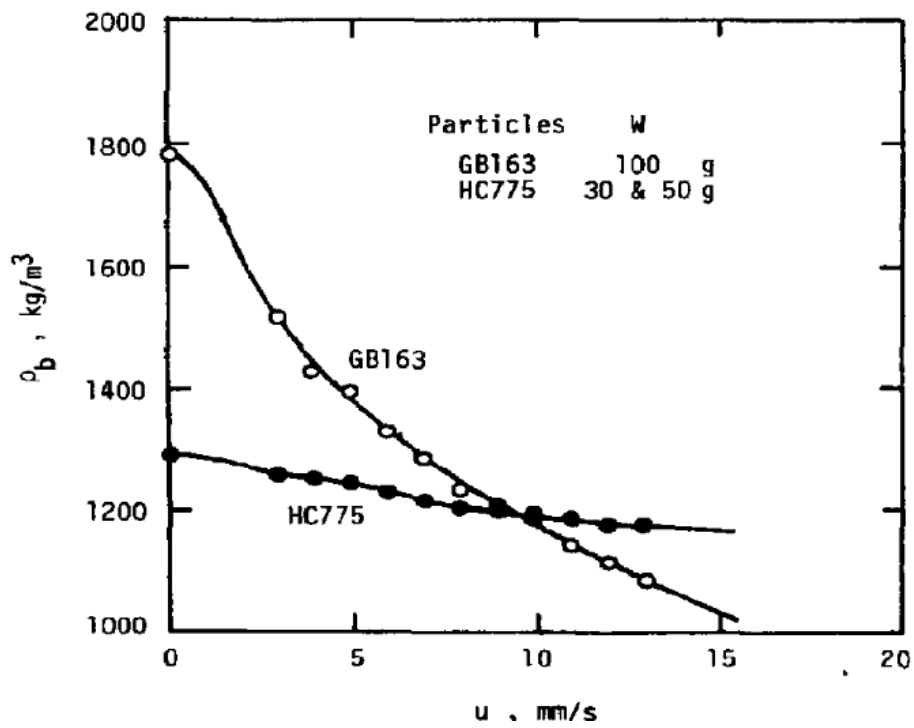


Figure 2-4. Change of bulk density of monocomponent bed with liquid velocity (Moritomi et al., 1982).

Chapter 2 Literature Review

The more realistic picture of the layer invasion created by Moritomi et al. (1982) was later confirmed by many investigators (Gibilaro et al., 1986; Jean and Fan, 1986; Matsuura and Akehata, 1985). Van Duijn and Rietema (1982) employed the momentum equations of a two-phase flow to develop criteria based on the concept of bulk density in order to calculate the inversion velocity. They found that the inversion velocity is only dependent on the solid and liquid properties, which is actually in contrary to the observations of Moritomi et al. (1982).

Epstein et al. (1985) proposed a model based on bulk density concept to study the layer inversion. In their model, they assumed that segregation degree of a binary mixture depends on the difference between the bulk densities of two components when each species is fluidized separately at the same given liquid superficial velocity. They used the criteria that at the inversion point the bulk densities of the two species beds are the same to determine the inversion velocity and corresponding void fraction. The correlation of Richardson-Zaki (Richardson and Zaki, 1954) was employed to calculate the void fraction of each monocomponent beds since the void fraction of each species was required to calculate the bed bulk densities. The predicted inversion velocities were in satisfactory agreement with experiments for some binaries; however, the significant differences were also observed. That was attributed to assuming identical Richardson-Zaki indices for the two species. The necessary and sufficient conditions were also proposed based on their model for the occurrence of solids layer inversion which is given as: $\varepsilon_{mf} < \varepsilon_{c1} < \varepsilon_{c2} < 1$; where ε_{mf} is minimum fluidization porosity, ε_{ci} is voidage of species i at the critical(inversion) velocity. In this model, the properties of liquid and solids are only considered, so the model does not explain the effect of the binary compositions on the predicting of the inversion point. In addition, this model is also constrained to the assumption that two particles have the identical flow regimes which might not be always right.

Chapter 2 Literature Review

A model based on settling velocity of each component, which uses a concept of apparent porosity to take into account the particle-particle interaction, was developed (Patwardhan and Tien, 1985) to predict the inversion velocity of binary mixtures. They modified the particle settling velocity correlation proposed by Masliyah (1979) in the way that they replaced the particle diameter with the average particle diameter. The authors then assumed the criterion that at the inversion point, large and small particles have the same settling velocity to calculate the inversion point. This model showed reasonable agreements with sedimentation observations, but poor agreements with the data of fluidizations were observed. Their model also did not consider the fact that the bed compositions affect the inversion velocity.

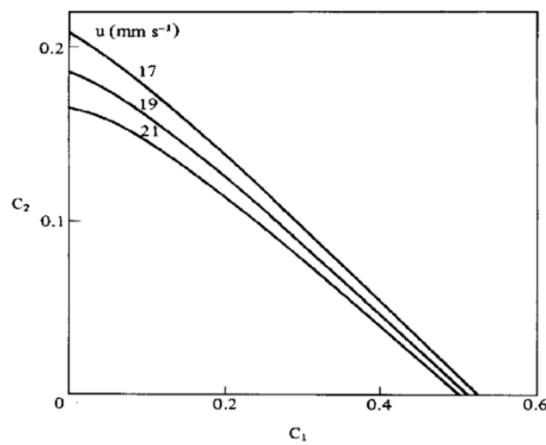


Figure 2-5. Solid concentration relationships for the system water/zirconia/copper (Gibilaro et al., 1986).

The effective voidage model was applied to a binary mixture in liquid fluidized beds to interpret the layer inversion phenomenon (Bhattacharya and Dutta, 2002). They also employed the concept of settling velocity to predict the inversion velocity similar to the work of Patwardhan and Tien (1985) with this difference that they assumed the average diameters of neighbouring particles, calculated from the Sauter mean diameter, and the test particle had its

Chapter 2 Literature Review

own size. The model reliability was verified by comparing the model prediction with 19 inversion velocities measured in experiments, and overall, a good agreement was found.

Gibilaro et al. (1986) proposed complete segregation model to predict the bed expansion characteristics of a binary mixture. They equated a pressure drop constraint relationship by equalling the pressure drop calculated from modified Ergun equation (Foscolo and Gibilaro, 1984; Gibilaro et al., 1985) and the pressure drop from bed weight at a given liquid superficial velocity. Therefore, the solution of this equation for a liquid velocity gave the all possible concentration pairs which could exist at the mixed layer (an example is illustrated in Figure 2-5). They assumed that the mixed layer composition corresponded to the pair that made the maximum bulk density (as shown in Figure 2-6), and the velocity in which the composition of the pair equalled to the overall bed composition was considered as the inversion velocity. They also treated the mixed layer as a mono-component bed with specifying an average diameter. Their model made good agreements with experimental measurements. However, as displayed in Figure 2-7, the authors found that the model was suffering from predicting a sharp fall in height of mixed zones after inversion point, which that was smoother in experiments. They attributed the discrepancies to ignoring the random mixing effects of particles in the model, which this effect could result in mixing between two layers.

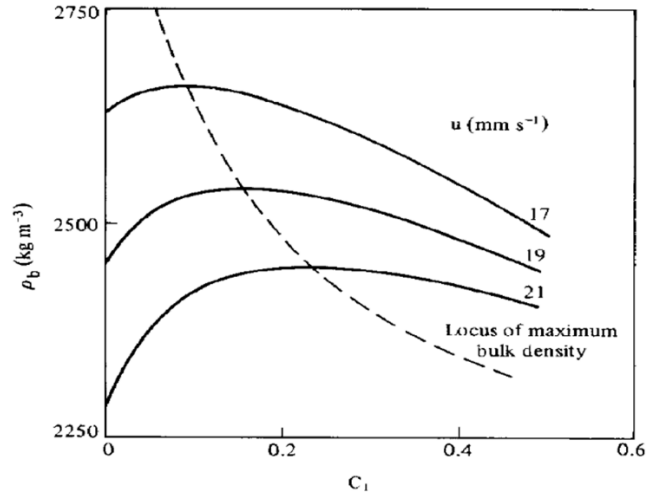


Figure 2-6. Bulk density evaluations for the illustrative example of Figure 2-5 (Gibilaro et al., 1985).

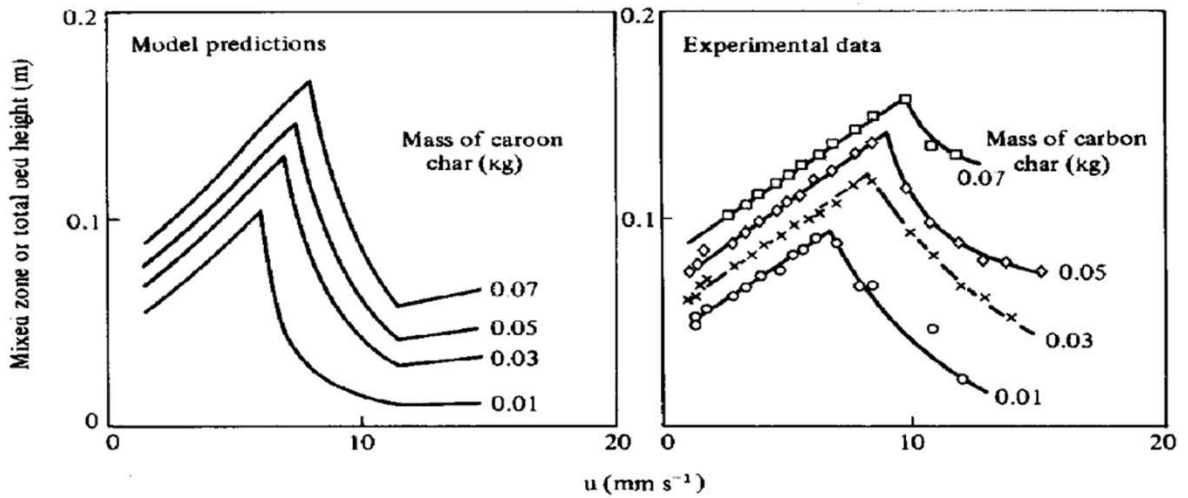


Figure 2-7. a comparison between Gibilaro et al. (1986) model and experiments (Gibilaro et al., 1986).

Epstein (2005) modified the complete segregation model of Gibilaro et al. (1986) by adopting the bed expansion equation as a combination of Di Felice (1994) and Schiller and Naumann (1933) model correlations. Jean and Fan (1986) carried out Experimental studies to

Chapter 2 Literature Review

characterize the occurrence of layer inversion phenomenon. A new criterion based on "particle segregation velocity" was proposed to determine the inversion velocity. Using all experimental data from their work, Moritomi et al. (1982), and Matsuura and Akehata (1985) works, it was found that the model predicted the inversion velocity within about 3% error based on experimental bed voidage, and 19% error based on voidage calculated from the serial model. They also developed criteria to determine if the layer inversion will occur for a given set of the binary particle. According to their criteria, the layer inversion occurs if and only if:

$$\rho_{b2} > \rho_{b1} \text{ at } U_0 = U_p \leq \max\{U_{mf1}, U_{mf2}\} \quad (2-1)$$

and

$$U_{e1} > U_{e2} \quad (2-2)$$

where ρ_{bi} is the bulk density of the particle i , U_0 is liquid superficial velocity, U_{mfi} is the minimum fluidization velocity of the component i , and U_{ei} is an extrapolated velocity in the U_0 vs. ε_i plot as the bed voidage approaches 1.

Moritomi et al. (1986) developed a model based on applying force balance for each component and using unit cell model for defining the voidage function to calculate the drag force on a particle in a mixed layer. The presented unit cell model fairly predicted the monocomponent bed expansion, but almost failed to predict the voidage and mixing index for the case of uniformly mixed bed.

A model based on force balance relationships of each particle was also developed by Funamizu and Takakuwa (1995) to obtain the volume fraction of each species in the mixed layer of liquid fluidization of binary mixtures beyond the laminar flow. In the model, they introduced a

Chapter 2 Literature Review

new description of drag force coupled with Richardson-Zaki correlation which resulted in the calculation of the mixed layer compositions. The velocity at which the mixed layer composition equalled to the overall bed composition was assumed to be the inversion velocity. As discussed by the authors, the application of the model far away the inversion point might lead some discrepancies in the results due to the random mixing effects of particles, which causes the mixing of particles between two layers. Another issue raised in this work about the application of the model was that despite the fact that the model could predict the volume fractions of the mixed layer and the monocomponent layer, the order and thickness of the layer were not predictable by the model.

Generally speaking, more than 20 models have been proposed in the literature to predict the layer inversion phenomenon behaviour, particularly the inversion velocity. Escudié et al. (2006) compared these models using available experimental data. It was found that there were uncertainties in their comparisons because, in some experiments, the temperature had not been reported or specified exactly. Nonetheless, the best model calculated the inversion phenomenon properties within $\pm 14\%$ errors.

Regarding the review in the area of study of layer inversion phenomenon done by Escudié et al. (2006), most of the experimental research had been applied in a small column. So, there was a need to study large beds since the scale up to large liquid fluidized beds had already not been explored. To reach this aim, some researchers have provided some experimental data in large liquid fluidized bed (210 mm semi-cylindrical column(Chun et al., 2011) and 190mm cylindrical column (Vivacqua et al., 2012)). Chun et al. (2011) observed the inversion phenomenon by increasing the liquid velocity as described, as shown in Figure 2-8. They found that introducing a gas co-currently with the liquid causes inversion velocity to decrease. Vivacqua et al. (2012)

concluded decreasing the temperature enhanced mainly the expansion behaviour of the smaller particles, and this can play an important role in intensifying the segregation of the two species. Layer inversion phenomenon in gas-liquid fluidized beds was also studied experimentally by Rim et al. (2013, 2014). The authors found that in gas-liquid co-current upflow, the superficial liquid velocity at the layer inversion point decreases as the superficial gas velocity increases. Recently, Tripathy et al. (2017) conducted experiments to study the iron ore and quartz misplacement in a liquid fluidized bed separator. They performed qualitative and quantitative evaluations of the particles misplacement. It was observed that there was a critical mean particle size ratio that inversion started and misplacement was highest; and the particle misplacement increased with the increase of operating superficial velocity, static bed height and overflow height.

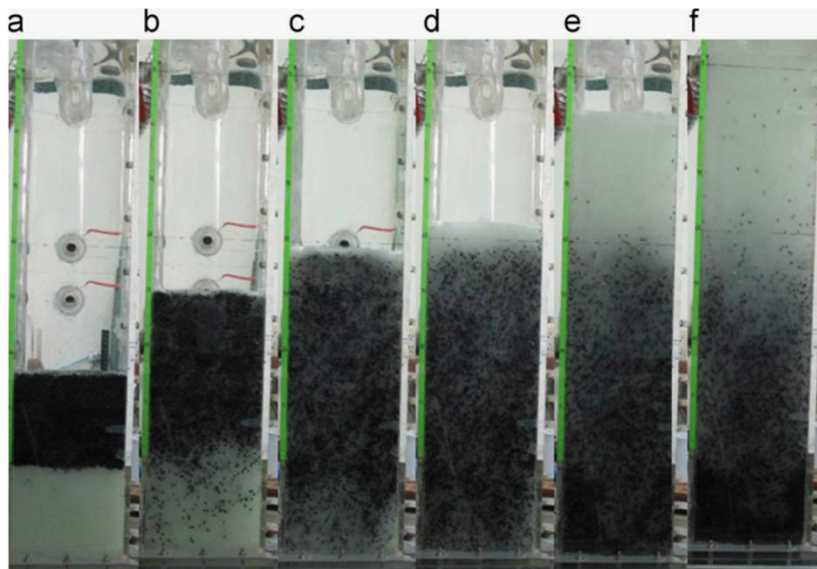


Figure 2-8. Snapshots showing bed inversion in liquid fluidized bed for PB:GB volume ratio 0.54:0.46 with increasing superficial liquid velocity: (a)18.2mm/s, (b)28.1mm/s, (c) slightly greater than 33.1mm/s, (d) 38.2mm/s, (e) 43.1mm/s. Inversion was observed at 33.1 mm/s (Chun et al., 2011).

2.2.3 Numerical Simulations

Despite a large number of experimental investigations on layer inversion in liquid fluidized beds, only a few researchers have put their efforts to numerically study this phenomenon.

Chapter 2 Literature Review

Generally speaking, there are two approaches to model liquid fluidized beds: continuum approach (e.g. so-called Eulerian-Eulerian approach or two-fluid model (A. Howley and J. Glasser, 2002; Reddy and Joshi, 2009; Syamlal and O'Brien, 1988)) and discrete approach (e.g. so-called Lagrangian-Eulerian or discrete element method (Di Renzo et al., 2011; Malone et al., 2007; Mukherjee and Mishra, 2007; Vivacqua et al., 2012; Zhou and Yu, 2009)). Particularly, as discrete approach such as CFD-DEM can provide some fundamental concepts of the flow at a particle scale, it has been verified as one of the most effective approaches to study the fundamental behaviour of particle-fluid systems (Zhu et al., 2007, 2008). Such an approach has been used by some investigators to study layer inversion phenomenon (for example, Di Renzo et al., 2011; Mukherjee and Mishra, 2007; Vivacqua et al., 2012; Zhou and Yu, 2009; Malone et al., 2007).

Mukherjee and Mishra (2007) combined DEM approach with a simplified fluid model to investigate the layer inversion, but they just qualitatively observed this phenomenon. Zhou and Yu (2009) used the combined CFD-DEM approach to reproduce the layer inversion behaviour. They applied a method to adapt the monodisperse drag force model (Di Felice, 1994) for the binary mixtures. They qualitatively reproduced the phenomenon, as shown in Figure 2-9, with good agreement with experiments. Malone et al. (2007) also combined CFD and DEM to figure out the parameters that affect the layer inversion phenomenon, but no comparison with experimental data was performed. They compared their simulation results with some models from literature and concluded that the discrepancies should be further investigated in the future. Di Renzo et al. (2011) utilized a new drag force model which was developed for polydisperse systems (Cello et al., 2010), and found that the comparison between experimental data from literature and their simulation results were satisfactory. Experimental and numerical studies were also conducted by Vivacqua et al. (2012) to analyse the factors such as temperature, bed aspect

ratio on inversion phenomenon in a binary liquid fluidized bed. The results were found in a reasonable agreement with experimental measurements.

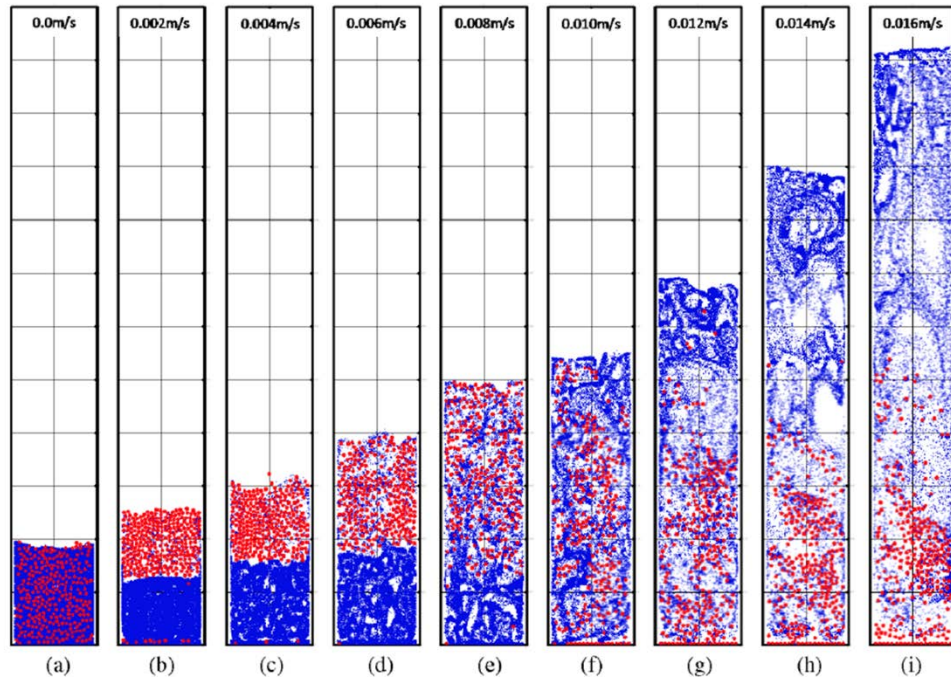


Figure 2-9. Snapshots of flow patterns in liquid fluidization for different liquid superficial velocities (Zhou and Yu, 2009).

2.3 Particle shape effects on the Mixing and Segregation Phenomenon

2.3.1 Introduction

Particles are mostly non-spherical in nature and engineering practices. A picture of diverse applications of non-spherical particles in different areas is presented in Figure 2-10. It is reported (Zhong et al., 2016) that at least 70 % of the raw materials are in non-spherical shapes in various industries such as pharmaceuticals (Freireich et al., 2011, Freireich et al., 2015), agriculture (Ren et al., 2012; Shao et al., 2014), energy (Abbaspour-Fard, 2004; Kruggel-Emden et al., 2012),

Chapter 2 Literature Review

mining (Adema et al., 2010; Peacey, 1979), environment (Paterson et al., 2004), and geological engineering (Knuth et al., 2012). A better understanding of the non-spherical particulate system behaviours improves the design and control of industrial processes. However, these behaviours are more complicated than spherical particles in many processes such as packing (Hidalgo et al., 2009), compaction (Delaney et al., 2015), conveying (Njobuenwu and Fairweather, 2015), or fluidization (Zhou et al., 2011). In this project, the main focus is on the effects of particles shape in fluidized beds. In this project, gas-solid fluidized beds and liquid-solids fluidized beds are studied. Therefore, the literature survey on this topic will be presented here; but first, some background on the non-spherical definitions are given.



Figure 2-10. Various non-spherical particulate systems in nature and industry (Zhong et al., 2016).

2.3.2 Non-Spherical Particles Description

Generally speaking, non-spherical particles can be classified into regular (e.g., ellipsoids, cones, disks; see Figure 2-11) and irregular (non-symmetric rough surfaces) shaped particles. In this work, ellipsoidal particles are used as they can represent a wide range of particle shapes from oblate to prolate particles. The aspect ratio and the sphericity are considered as the most common shape factors to describe ellipsoids shape (Pourghahramani and Forsberg, 2005).

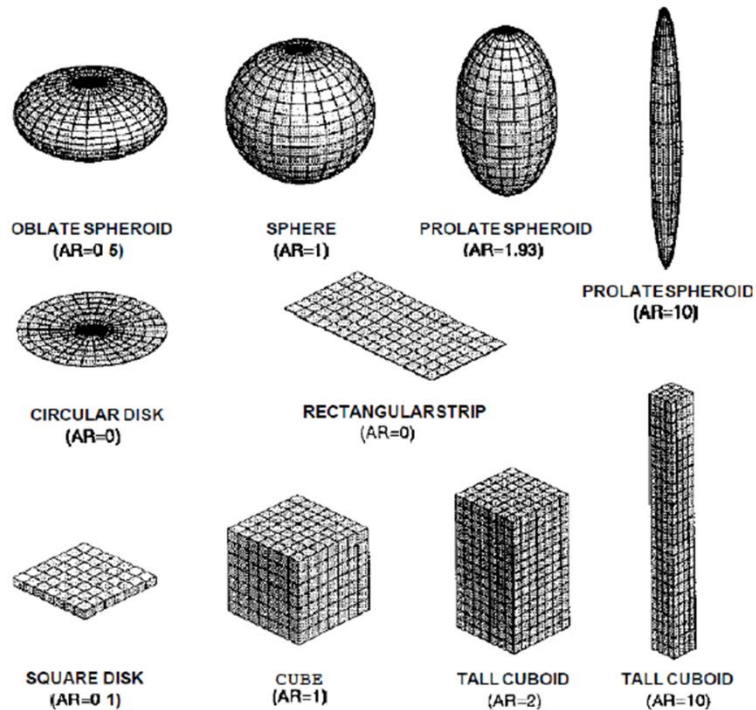


Figure 2-11. Various particle shapes with different aspect ratio (Yovanovich et al., 1995).

The aspect ratio is a factor that depends on the orientation. Spherical particles exhibit the aspect ratio of 1 regardless of the orientation while particles with other shapes can have aspect ratio smaller or larger than one. The high and low values of aspect ratio represent an irregularity

Chapter 2 Literature Review

of a particle shape. For the regular ellipsoid shaped particles shown in Figure 2-12, the aspect ratio is defined as (Loth, 2008):

$$AR = \frac{b}{a} \quad (2-3)$$

where b and a are the parallel and normal diameters, which, respectively, correspond to the semi-minor and semi major axis lengths. When $AR=1$, the geometry becomes sphere. Ellipsoidal are categorized as oblate ($AR < 1$) and prolate ($AR > 1$) shapes. Oblate particles become a circular disk when $AR \rightarrow 0$, and for the prolate particles, the shape approach to a needle shape when $AR \rightarrow \infty$. The effective diameter (d) of an ellipsoid is given as:

$$d = aAR^{1/3} = bAR^{-2/3} \quad (2-4)$$

Another shape descriptor of ellipsoidal is sphericity. Sphericity is combination of geometric shape and surface smoothness. The Wadell sphericity is defined as:

$$\phi = \frac{\Delta S_s}{\Delta S_r} \quad (2-5)$$

where ΔS_s is the surface area of a spherical particle with the same volume as the real particle and ΔS_r is the surface of the real particle. It is believed that a sphere will have a sphericity value of 1 if the surface asperities are negligible; however, a sphere with detectable surface asperities and particles of any other shapes could also have sphericity values greater than one. Particles of the same geometric shape but different surface smoothness will have different sphericity values and particles with the same surface smoothness but different geometric shape will also possess different sphericity values (Gan, 2015).

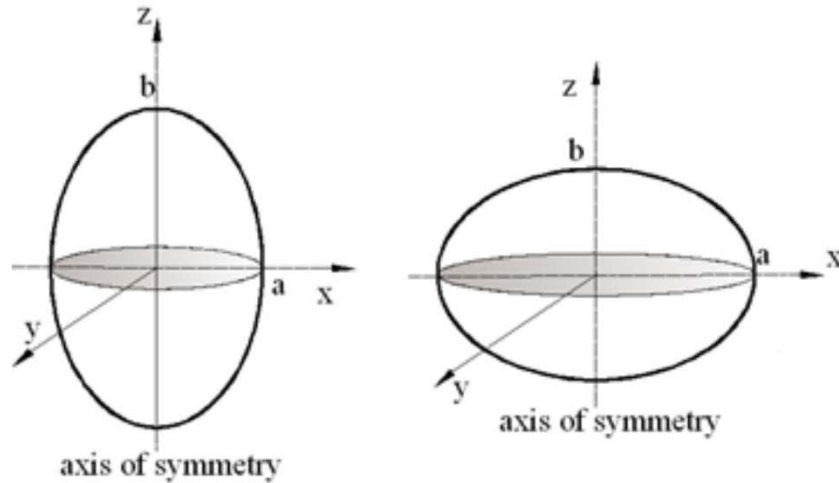


Figure 2-12. Schematic of (a) prolate ($b > a$) and (b) oblate ($b < a$) ellipsoidal particles (picture from Gan, 2015)

2.3.3 The Role of Particles Shape on Fluidizations

As it was mentioned above, since the effects of particles shape on fluidizations are the main aim of this part of the project, the literature survey on gas-solid fluidized beds and solid-liquid fluidized beds are presented as follows. Note that the particles shape influence on the fluidized beds are categorized into experiential works and numerical simulations.

2.3.3.1 Particle Shape Effects in Gas-Solid Fluidized Beds

2.3.3.1.1 Experimental works

As it is found that the particles shape is an important factor on the fluidization systems, some experimental works have been performed to discover the effects of particle shape on fluidizations. Liu and Lister (1991) conducted experiments to study the effects of particle shape on the minimum spouting velocity and fountain height in a spouted fluidized bed. They used thirteen different particles shapes, as displayed in Figure 2-13. They concluded that the predicted fountain

Chapter 2 Literature Review

heights were much lower than the experimental values when the particle shape factor was ignored. Liu et al. (2008) investigated the characteristics of fluidized beds of non-spherical particles with eight different morphologies. They observed that non-spherical particles exhibit a smaller minimum fluidization velocity than spherical particles. As the sphericity decreased, the minimum fluidization velocity also decreased. This resulted in poorer fluidizing quality in terms of pressure drop, minimum fluidization velocity, etc. A relationship between the minimum fluidization velocity of non-spherical particles and that of spherical particles was found and presented in Figure 2-14. Overall, they concluded that particle morphology has an obvious effect on fluidizing quality.

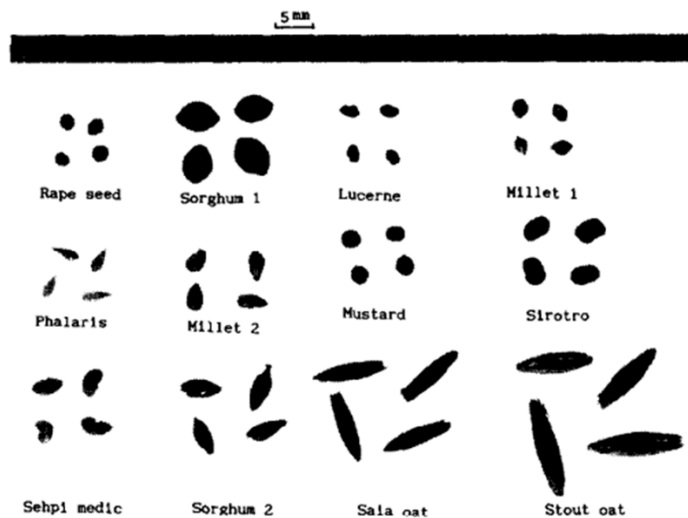


Figure 2-13. Photographs of the seed particles used (Liu and Litster, 1991).

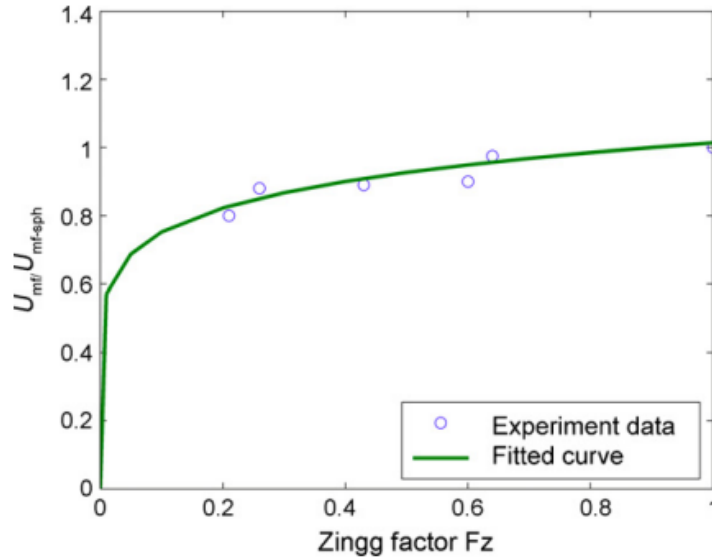


Figure 2-14. U_{mf} / U_{mf-sph} of plate-like particles vs. Zingg factor (Liu et al., 2008).

Shao et al. (2013) carried out experiments to characterize the solid waste fluidized bed containing non-spherical particles. Silica sand was selected as a fluidization medium and four different particles, as displayed in Figure 2-15, as simulative solid waste. They reported that the pressure drop curve as a function of fluid velocity was clearly fluctuant and it always underestimated the minimum fluidization velocity when the fluid velocity was increased; while the pressure drop curve for decreasing the fluid velocity was smooth and the minimum fluidization velocity was more reliable. The static bed height was found to have to influence on the minimum fluidization velocity, whereas the minimum fluidization velocity increased with the increase of the volume fraction of irregular particles. They also developed a correlation to predict the minimum fluidization velocity of any particle system from a single kind of particle system to the multi-component irregular particle mixtures.

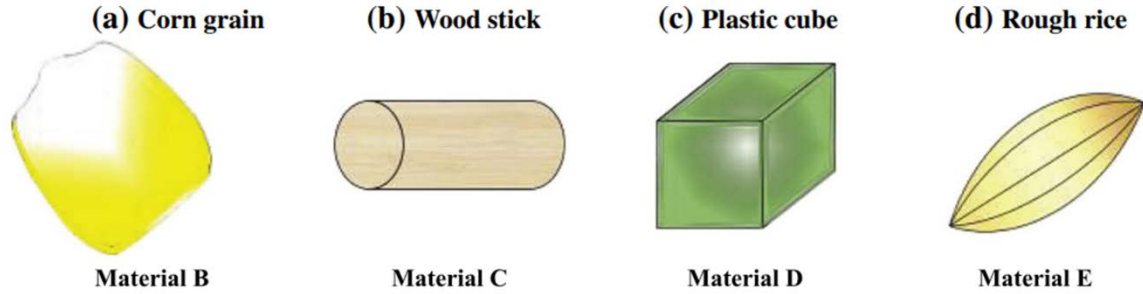


Figure 2-15. Physical properties of irregular particles used in Shao et al., 2013.

Some investigators also addressed the importance of particle shape on the macroscopic behaviour of fluidizations such as pressure drop (Allen et al., 2013; Einfeld and Schnitzlein, 2001; Nemeč and Levec, 2005; Rangel et al., 2001; Singh et al., 2006). They proposed various correlations to predict the pressure drop of beds containing non-spherical particles. For example, Dolejš and Machac (1995) proposed a new method for calculating the pressure drop of Newtonian fluid flow through

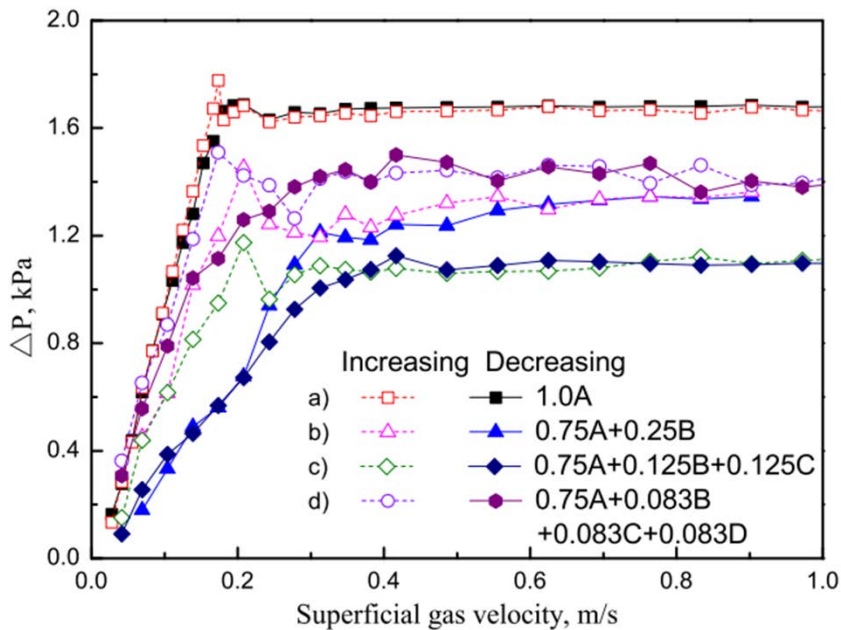


Figure 2-16. Pressure drop versus superficial gas velocity in the bed (Shao et al., 2013).

Chapter 2 Literature Review

fixed beds of spherical and non-spherical particles. Ozahi et al. (2008) planned an experimental study to figure out the applicability of the well-known Ergun correlation on the prediction of pressure drop for beds containing non-spherical particles. In the experiments, two different shapes of cylindrical particles were used. The results showed that the well-known Ergun correlation could predict the pressure drop with $\pm 20\%$ error. However, they modified the Ergun equation so that the new correlation predicted the pressure drop of non-spherical materials with $\pm 4\%$.

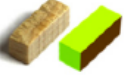
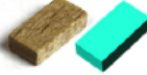
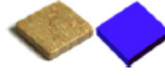
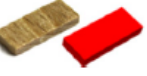
Allen et al. (2013) compared their own measured pressure drops from experiments with those from the Ergun equations for non-spherical particles and found that the Ergun equation should not be used to calculate the pressure drop of packed beds of non-spherical particles and it could over predict the pressure drop by as much as 100%. They also observed that recent correlations calculate the pressure drop of non-spherical particles different from the measured values. They recommended that in order to propose a correlation to calculate pressure drop of a packed bed of irregular particles, a sample of the particles with given packing arrangement must be used. Vollmari et al. (2016) examined the pressure drop of 13 different shape particles, shown in

Table 2-1, in a fluidized bed. They employed Particle Tracking Velocimetry (PTV) technique to detect particles and determine their orientations and heights. Channels at low superficial velocities were observed for a particle with a low sphericity; which resulted in lower pressure drops because all particles were not suspended. It was observed that equidimensional particles like cubes and ideal cylinder can accumulate in the corners of the fluidized beds. Particles orientations were found to have a great effect on the pressure drop and the difference between pressure drops of same height beds was attributed to the orientation of the particles. In

Chapter 2 Literature Review

addition, elongated particles intended to become vertically oriented with increasing the superficial velocities. Other investigators (Ku and Lin, 2008; Zhang et al., 2005) also observed such a phenomenon.

Table 2-1. Particle properties used in Vollmari et al., 2016.

Shape	Sphere		Sphere		Ideal Cylinder		Cube			Cube		
												
d_c -class [mm]	7		5		7		5			7		
Size [mm]	7.2		5		6.1 6.2		4.2 4.3 4.5			5.2 6.3 6.3		
ϕ [-]	1.00		1.00		0.87		0.81			0.80		
ρ_p [kg/m ³]	772.5		823.0		708.5		639.7			746.9		
l_{vb} [mm]/ $\bar{\epsilon}$ [-]	95 0.40		88 0.40		98 0.36		98 0.37			103 0.43		
Shape	Elongated Cylinder		Elongated Cuboid		Elongated Cuboid		Plate			Elongated Plate		
												
d_c -class [mm]	7		5		7		5			5		
Size [mm]	3.9 14.0		3.0 3.0 7.1		4.2 4.2 11.4		2.0 4.9 6.0			2.0 4.0 8.0		
ϕ [-]	0.75		0.75		0.73		0.71			0.69		
ρ_p [kg/m ³]	764.4		745.6		639.7		754.1			756.6		
l_{vb} [mm]/ $\bar{\epsilon}$ [-]	103 0.44		103 0.42		115 0.40		102 0.43			108 0.46		
Shape	Elongated Cuboid		Plate		Elongated Plate							
												
d_c -class [mm]	5		7		7							
Size [mm]	2.0 3.0 11.0		2.2 9.0 9.8		2.0 6.0 14.9							
ϕ [-]	0.64		0.63		0.58							
ρ_p [kg/m ³]	728.1		672.8		721.7							
l_{vb} [mm]/ $\bar{\epsilon}$ [-]	117 0.48		121 0.46		124 0.51							

Recently, Shao et al. (2016) extended their previous work (Shao et al., 2013) to the study of mixing behaviour of binary and multi-component mixtures of particles in waste fluidized beds. In this work, they selected 9 types of non-spherical particles to present solid wastes and used silica sand as fluidization medium. They formed binaries by mixing silica sand and one kind of non-spherical particles and multi-component by mixing silica sand and two or more types of non-spherical particles. For the analysis, they described the mixing quality with a self-defined mixing index M and they also investigated the flow patterns using a fluidization number N which is defined as the ratio of gas superficial velocity to the minimum fluidization velocity. It was found that for a specific binary mixture, a stable mixing state was reached when the fluidization number

was greater than 1 ($N > 1$), and the mixing time $t > 12$ s (see Figure 2-17). The authors found the good mixing condition when the density of non-spherical particles is similar to that of fluidization medium in the binary of multi-component mixtures.

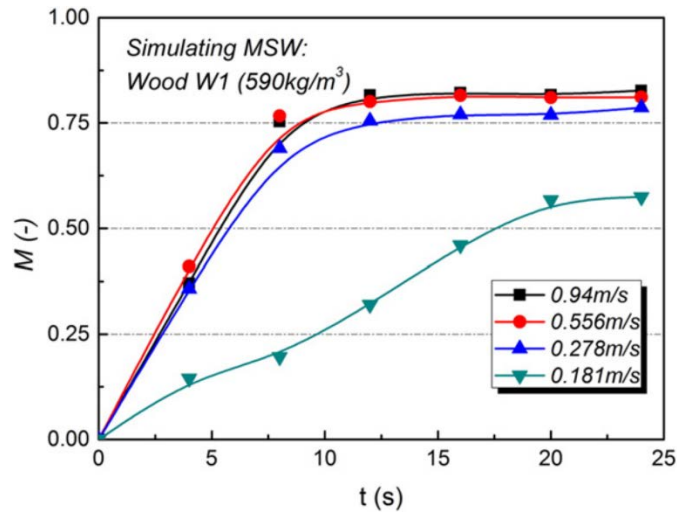


Figure 2-17. Mixing behaviour of wood pellet W1 at different superficial gas velocities (Shao et al., 2016).

Most recently, Vollmari et al. (2017) conducted experiments to study the mixing processes in mono- and disperse system under influence of particle shape. They examined the mixing quality of four different shaped particles types in a laboratory scale gas-fluidized beds. By analysing the results using the Lacey mixing index (Lacey, 1954), they found that adding plate shape particles to a mixture generally increase the mixing rates. This was attributed to the role of particles orientation. The fastest monodisperse was observed for plates followed by cubes and elongated cuboids while the slowest mixing rate was achieved for spherical particles. In addition, surprisingly, the mixing of disperse systems was found to be slower than those of monodisperse ones.

2.3.3.1.2 Numerical Simulations

Generally speaking, there are two approaches to model fluidized beds: continuum approach (e.g., so-called Eulerian-Eulerian approach or two-fluid model (Anderson and Jackson, 1967; Enwald et al., 1996; Gidaspow, 1994)) and discrete approach (e.g., so-called Lagrangian-Eulerian or discrete element method (Feng and Yu, 2004; Hoomans et al., 1996; Kafui et al., 2002)). Note that continuum approaches are more desirable in terms of computing time, they have been reported to be less accurate in prediction of mixing and segregation process (Fan and Fox, 2008; Sun et al., 2009) and even in generating of basic flow characteristics (Pirker et al., 2010). Alternatively, discrete approach such as the combination of Computational Fluid Dynamics (CFD) and Discrete Element Method (DEM) (CFD-DEM) has been widely employed to study the fundamental behavior of granular materials (Rong and Zhan, 2010; Zhu et al., 2007, 2008), and fluidized beds of spherical particles (Beetstra et al., 2007; Munjiza et al., 2011; Rong and Zhan, 2010; Di Renzo et al., 2008; Feng et al., 2004; Feng and Yu, 2007; Norouzi et al., 2011; Olaofe et al., 2014). For example, Olaofe et al. (2014) investigated the mixing and segregation phenomenon of disperse systems of spherical glass beads with the same density and different size. It was found that the CFD-DEM model with appropriate drag model for polydispersity systems was able to successfully predict the mixing quality observed in experiments, and it was concluded that the role of drag force in the prediction of hydrodynamics of particles in gas-fluidized beds is important. Di Renzo et al. (2008) utilized CFD-DEM simulation data to propose a model for the mixing process. In their work, they changed particles density ratio and the excess velocity and kept other parameters including particles size constant to develop a mixing map which was claimed to be extensible to a more complex system with different size and density. Feng and Yu (2004) observed that good mixing of spherical particles of different size occurred at high gas velocities, while at lower velocities segregation took place. More comprehensive review

Chapter 2 Literature Review

of the application of CFD-DEM on the study of fluidized beds was given by Zhu et al. (2007, 2008). However, all of those studies focused on the simulations of the spherical particles while non-spherical particles can be found in various parts of industries such as refuse-derived fuel and biomass (Wiinikka and Gebart, 2005), drying applications (Perré, 2010), food processing (Kozanoglu et al., 2002), and bulk solid handling (Qian and Yan, 2012). Therefore, in recent years, researchers put their efforts to consider complexly shaped particles in the simulations.

Zhong et al. (2009) were the first investigators who employed CFD-DEM model to simulate the flow of cylinder-shaped particles in a gas-solid fluidized. A cylinder-shaped particle was approximated by clustered spheres. In the model, Tran Cong et al. (2004) drag model was implemented. They found that simulated flow patterns and pressure drops at different superficial gas velocities were in good agreement with the experimental results from a visual fluidized bed (see Figure 2-18). However, this approach might not be recommended for dense flows as the effects of the void fraction were not appropriately considered (Vollmari et al., 2016). Hilton et al. (2010) used a drag force model (Hölzer and Sommerfeld, 2008) that considers the particles shape and orientation to study gas fluidizations of non-spherical particles, e.g., cuboid and ellipsoid (see

Table 2-2), by CFD-DEM model. They claimed that particles shape had significant effects on the fluidized beds dynamics. The non-spherical particles exhibited greater pressure gradients than spherical ones (Figure 2-19) and the traditional Ergun equation could not predict the pressure drop of the beds comprising of non-spherical particles. On the other hand, non-spherical particles reduced the fluidization velocities in comparison to the case of spherical particles.

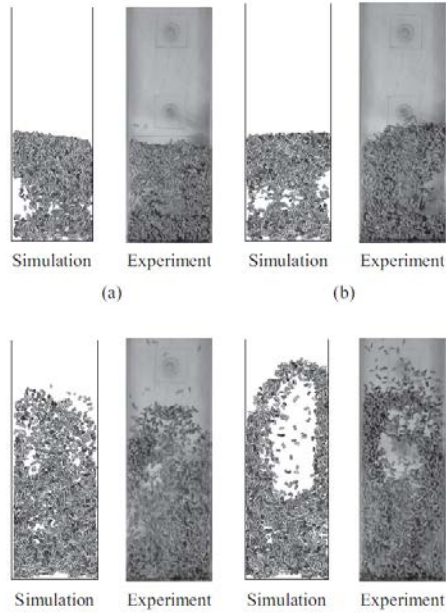


Figure 2-18. Comparison of simulated flow patterns with experiments at different superficial gas velocity: (a) $U_f = 0.5$ m/s, (b) $U_f = 1.0$ m/s, (c) $U_f = 1.5$ m/s, and (d) $U_f = 2.0$ m/s (Zhong et al., 2009).

Table 2-2. Size and shapes of particles used in Hilton et al., 2010.

Shape	Sphere	Cuboid	Prolate ellipsoid 1	Prolate ellipsoid 2	Oblate ellipsoid
					
Shape exponent q	1	0.5	1	1	1
Aspect ratio	$1 \times 1 \times 1$	$1 \times 1 \times 1$	$0.4 \times 1 \times 0.4$	$0.8 \times 1 \times 0.8$	$1 \times 0.4 \times 1$
Sphericity Φ	1	0.9559	0.8852	0.9915	0.8523
Case A					
a_x	4.00 mm	3.46 mm	2.95 mm	3.71 mm	5.43 mm
a_y	4.00 mm	3.46 mm	7.37 mm	4.64 mm	2.17 mm
a_z	4.00 mm	3.46 mm	2.95 mm	3.71 mm	5.43 mm
N	3388	3664	3588	3626	3694
Case B					
a_x	2.00 mm	1.73 mm	1.47 mm	1.86 mm	2.72 mm
a_y	2.00 mm	1.73 mm	3.68 mm	2.32 mm	1.09 mm
a_z	2.00 mm	1.73 mm	1.47 mm	1.86 mm	2.72 mm
N	6730	7944	7344	7332	7330

Zhou et al. (2011) developed a CFD-DEM model for ellipsoid particles to investigate the effects of particles shape in gas-fluidized beds. Their model presented a good consistency with experiments in terms of particle flow pattern (Figure 2-20). It was found that particle shape significantly affects bed permeability and the minimum fluidization velocity. The minimum

fluidization velocity decreased with decreasing in aspect ratio from 1.0 to 0.25, while for aspect ratio larger than one, the minimum fluidization velocity decreased first, and then it increased (Figure 2-21).

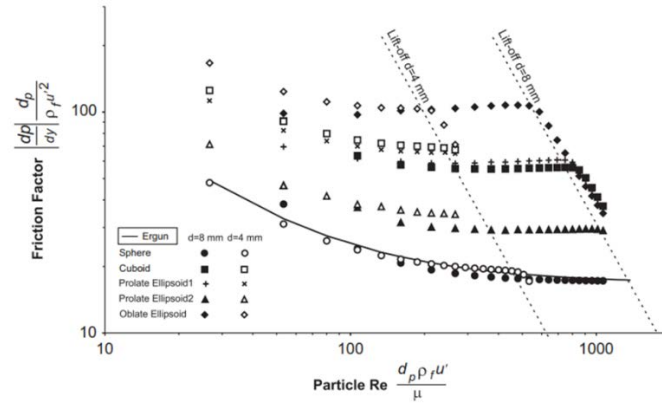


Figure 2-19. Non-dimensionalised friction factor against Reynolds number for 4 and 8 mm volume equivalent diameter particles. Lift-off pressures are shown by the dotted diagonal lines. Post-fluidisation the average friction factor follows this line, as expected. The Ergun curve, shown as a solid black line, shows excellent agreement with our spherical simulations (Hilton et al., 2010).

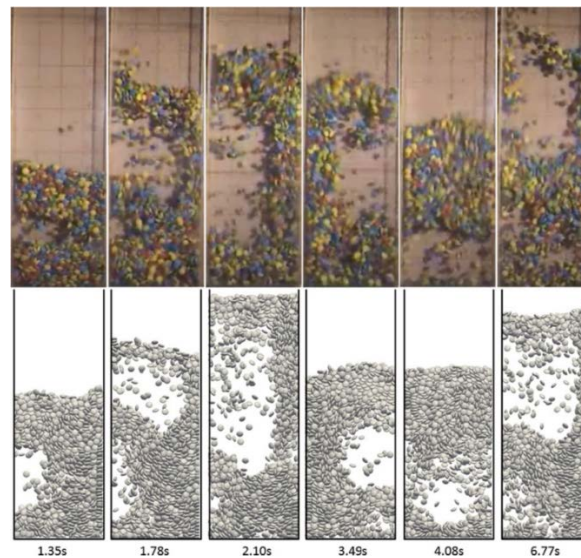


Figure 2-20. Comparison of snapshots of solid flow patterns observed in the experiments (the top figures) and CFD-DEM simulations (the bottom figures) when the gas superficial velocity is 3.0 m/s (Zhou et al., 2011).

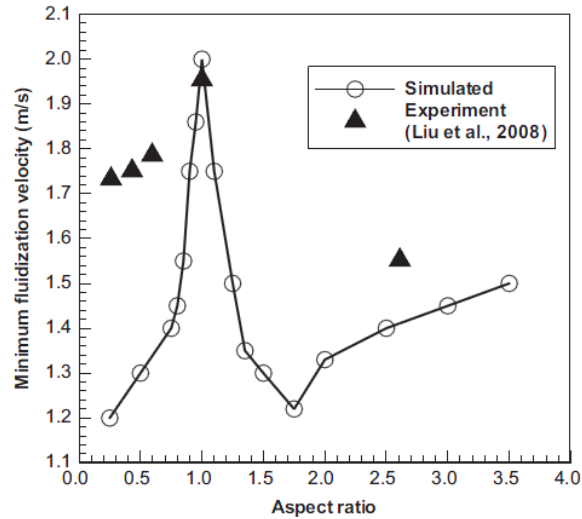


Figure 2-21. Effect of aspect ratio on the minimum fluidization velocity (Figure 2-21).

Ren et al. (2012) simulated corn shaped particle using clustered particles. They found that spherical particles mix more evenly and faster than corn-shaped particles. Oschmann et al. (2014) observed that mixtures of spheres and complex shaped with same equivalent volume displayed some segregations, which were attributed to variations of cross-sectional area and consequently different particle-fluid forces. Vollmari et al. (2017) investigated the mixing quality of mixtures with four different shapes both experimentally and numerically. The mixing speed and quality predicted by CFD-DEM coupled model were generally found in good agreement with their experiments for various mixtures. However, as it was discussed by the authors, there were found some significant discrepancies between the mixing index predicted by CFD-DEM and that of experiments for the mixtures of spheres and elongated cuboids as well as spheres and plates (Figure 2-21). They attributed such discrepancies to the lack of drag force model for polydispersity systems of spherical and non-spherical particles.

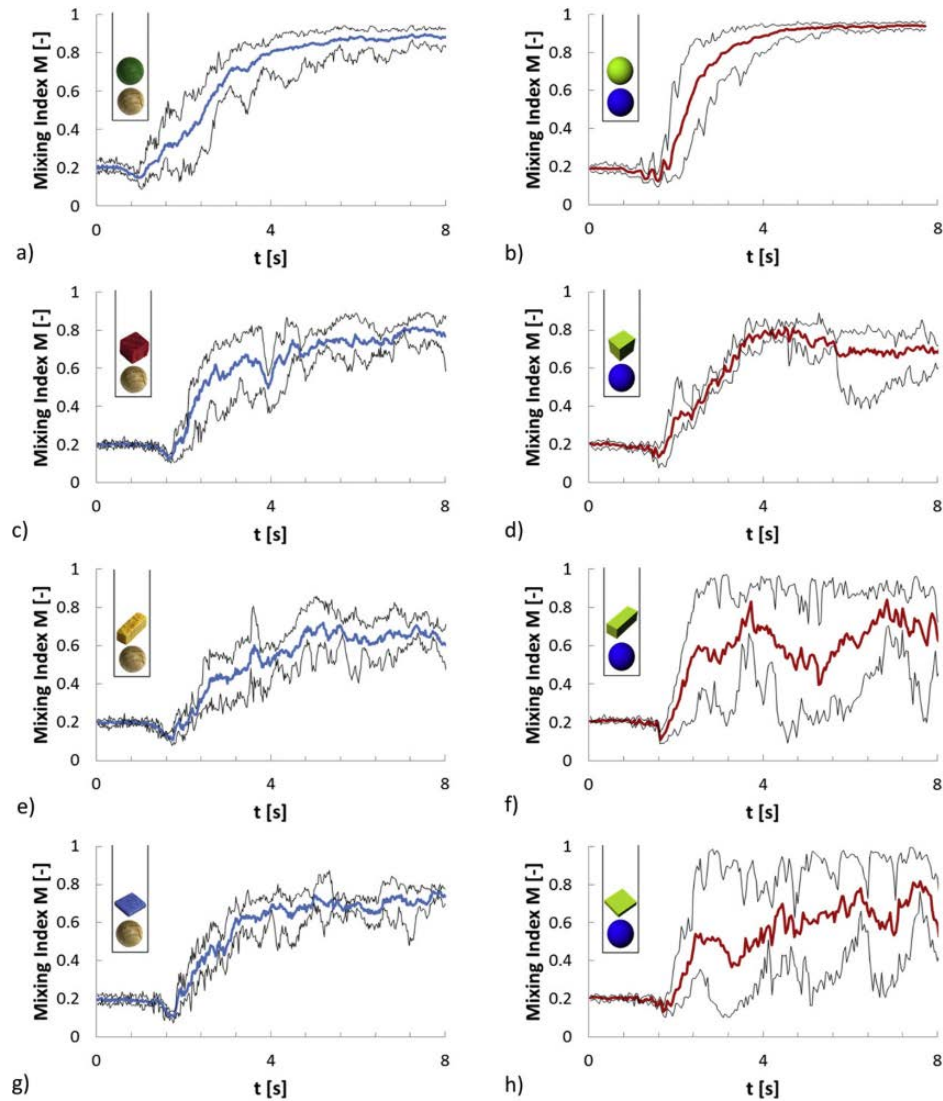


Figure 2-22. Experimental (left column) and numerical results (right column) for mixtures of 7mm spheres as the bottom component and 7mm spheres (a-b), 5mm× 6mm× 6mmcubes (cd), 4 mm × 4 mm × 11 mm elongated cuboids (e-f) or 2 mm × 9 mm × 10 mm plates (g-h) as the top component (Vollmari et al., 2017).

2.3.3.2 Particle Shape Effects in Liquid-Solid Fluidized Beds

Contrary to the relatively extensive works on the study of particles shape effects in gas-solid fluidized beds, up to now, only two experimental research (Barghi et al., 2003; Escudié et al., 2006a) have been carried out to examine the particles shape in liquid-solid fluidized beds, and no

simulations has been performed in this area. Barghi et al. (2003) observed that cylindrical particles with the length/diameter ratio $L/D = 1$ were mixed well with spherical particles, but elongated cylindrical particles with $L/D = 2$ segregated from spherical particles. Escudié et al. (2006a) carried out experiments in water-fluidized binary mixtures of Teflon spheres, discs, and rods. All the particles in the experiments had the same volume and density. In monocomponent systems, they observed that pressure gradients variations of spherical particles with height are uniform while for discs and rods, the pressure gradient exhibited a maximum in a specific height (Figure 2-23). They also found that that differences in particles shape can result in segregation/mixing phenomenon in binary mixtures of particles with same volume and density, and serial model (Epstein et al., 1981) was able to predict bed expansions for binary and ternary mixtures of different particles shapes.

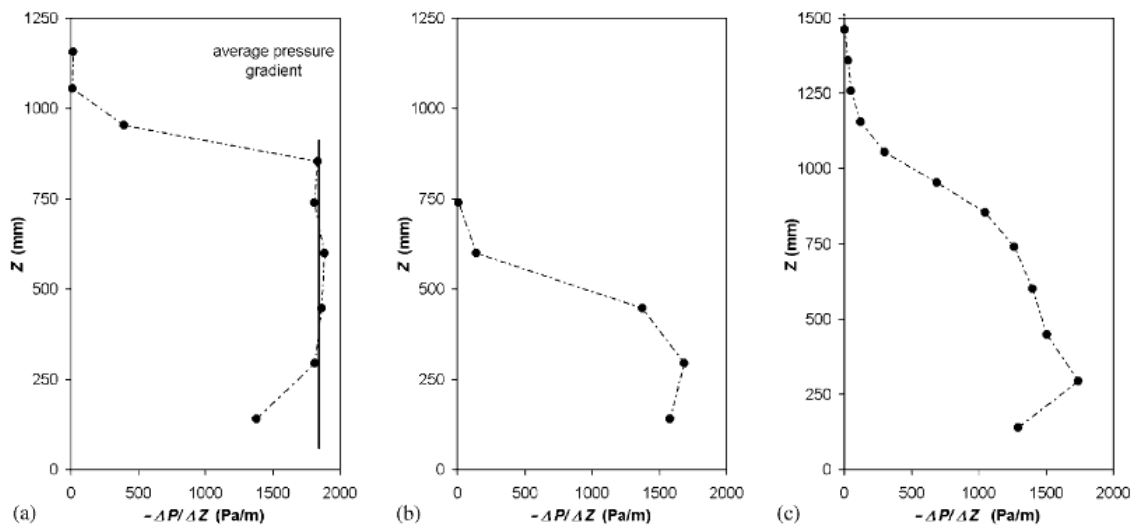


Figure 2-23. Dynamic pressure gradient profiles for the three particle shapes: (a) Spheres, $U = 0.316\text{m/s}$, (b) discs, $U = 0.251\text{m/s}$, (c) rods, $U = 0.316\text{m/s}$ (Escudié et al., 2006a).

2.4 Computational Modleing of Fluidized Beds

There are two general approaches to model particle-fluid systems: Continuum (Eulerian-Eulerian) and Discrete (Lagrangian-Eulerian) approaches. In the continuum approach (i.e., Two-

Chapter 2 Literature Review

Fluid Model), the particle flow is considered as a fluid with specific properties such as density and viscosity, which are described by some closure equations. Therefore, this approach depends on some constitutive equations that determine the momentum exchange between particles. Many efforts have been made to define appropriate constitutive or closure equations, but there is not any general continuum theory valid to any flow. On the other hand, in the discrete approach (i.e., CFD-DEM) each particle is tracked and the equation of motion is considered for any individual particle, so there is no need to constitute or closure equations.

TFM, which employs a Eulerian approach for both particles and fluid phases, is mostly applied on process modeling and various particulate systems (Chang and Zhou, 2003; Lan et al., 2009; Gan et al., 2011). The fluid and the solid phases are considered as interacting continua. Continuity and locally averaged Navier-Stokes momentum equations are written for each phase, and interphase interaction is accounted through appropriate correlations in momentum equations. This approach requires constitutive equations for the solid phase to relate the solids stress tensor to the velocity field. The interphase interaction terms typically involve empirical relationships for drag, heat transfer and other exchanges.

Without no generation or destruction within the phases, the continuity equations for the fluid phase and particle phase are given as:

fluid phase:

$$\frac{\partial(\rho_f \varepsilon_f)}{\partial t} + \nabla \cdot (\rho_f \varepsilon_f u_f) = 0 \quad (2-6)$$

particle phase:

$$\frac{\partial(\rho_p \varepsilon_p)}{\partial t} + \nabla \cdot (\rho_p \varepsilon_p v_p) = 0 \quad (2-7)$$

The volume fractions are related as:

Chapter 2 Literature Review

$$\varepsilon_p + \varepsilon_f = 1 \quad (2-8)$$

where:

$\varepsilon = \text{volume fraction}$

$\rho = \text{density}$

$u = \text{fluid velocity vector}$

$v = \text{particle velocity vector}$

and subscripts f and p stand for fluid and particle, respectively.

The momentum equations for the fluid and the particle phases are written as:

Momentum conservation:

fluid phase:

$$\frac{\partial(\rho_f \varepsilon_f u_f)}{\partial t} + \nabla \cdot (\rho_f \varepsilon_f u_f u_f) = -\varepsilon_f \nabla p - F_{pf} + \nabla \cdot \tau_f + \rho_f \varepsilon_f g \quad (2-9)$$

particle phase:

$$\frac{\partial(\rho_p \varepsilon_p v_p)}{\partial t} + \nabla \cdot (\rho_p \varepsilon_p v_p v_p) = -\varepsilon_p \nabla p - \nabla p_p + F_{pf} + \nabla \cdot \tau_p + \rho_p \varepsilon_p g \quad (2-10)$$

$\nabla \cdot \tau_i = \text{Viscous force}$

$\rho_i \varepsilon_i g = \text{Gravitational force}$

$\varepsilon_p \nabla p = \text{Static pressure force}$

$\nabla p_p = \text{Solid pressure force}$

$F_{pf} = \text{Interphase force}$

where:

In the recent years, the continuum approach in the study of liquid fluidized beds has been employed much more than the discrete approach because it needs less computational time, but it is also less accurate than discrete approach. In other words, continuum model sometimes would not be able to predict the particle flows satisfactorily due to some assumptions made in this approach for particle flows such as considering the particle phase as a continuum media, and

Chapter 2 Literature Review

definitions of non-realistic parameters such as particles viscosity and pressure. However, discrete approach such as discrete element model (DEM) provides some fundamental concepts of the flow helping better understanding of underlying mechanisms in granular flows.

The particle-particle, particles-wall, and particle-fluid interactions determine the macroscopic behaviour of particle-fluid flow. Therefore, having a deep understanding of these particle scale interaction forces results in evolving better approaches for process control. In the recent years, the rapid development of computers with high computational power along with better understanding of the physical mechanisms in particle scale has led to developing several discrete modeling techniques including the Discrete Element Model (DEM) (Zhou, 2007). Discrete Element Model approach provides information in microscopic scale that is extremely difficult or even impossible to be measured experimentally.

The CFD models can be coupled with DEM to determine the particle-fluid flows. Many investigators have used these models such as LB-DEM (Cook et al., 2004), PPM-DEM (Ge and Li, 2003a, b, DNS-DEM Hu, 1996; Pan et al., 2002), and LES-DEM (Zhou et al., 2004a; Zhou et al., 2004b). Therefore, based on the time and length scales of fluid flow, different fluid-solid models can be made from discrete and continuum approach. Nonetheless, the CFD-DEM model has been used more commonly in the study of particle-fluid flows.

Yu and Xu (2003) discussed the merits/demerits of the three popular numerical models used in particulate systems in details including TFM, DNS-DEM, and DEM-CFD. As mentioned above, in the two-fluid model (TFM), the particle and fluid phases are considered as interpenetrating continuum media, and two phases are coupled together with momentum exchange and volume fraction equations. In this approach, the numbers of equations are extremely reduced because for both particle and fluid phase one computational cell is applied that

Chapter 2 Literature Review

this cell and it is much bigger than particle size, but it still is enough small relative to the whole system. However, as discussed above, the accuracy of TFM method is highly dependent on constitutive or closure relations for the solid phase and the momentum exchange.

In DNS-DEM, the computational cell for fluid is considered as small as possible to be comparable with the particle spacing, while particles are treated as discrete moving boundaries Hu, 1996. In this model, the particle–fluid system is treated implicitly by using a combined weak formulation. DNS yields detailed results of hydrodynamic interactions between fluid and particles in a system (Pan et al., 2002). Nevertheless, it has one main flaw, which is its ability in controlling particle collisions.

In DEM-CFD coupling approach, solving of Newton’s equations of motion give the solids velocities and positions while CFD determines the fluid flow properties in a computational cell scale (Hoomans et al., 1996; Tsuji et al., 1993; Xu and Yu, 1997; Xu and Yu, 1998). The DEM and MDS differ from each other due to different length scale, and the implementation of inter-particle forces.

Yu and Xu (2003) commented that in particle-fluid flow modeling the most difficulty is due to trouble in solid phase modeling rather than fluid phase. Therefore, the DEM-CFD is more demanded because it is more convenience than DNS- or LB-DEM model in terms of computational, and it provides more details in particle scale than TFM. Therefore, in this work, the main focus is on the DEM-CFD coupling method.

In CFD-DEM coupled approach, proposed firstly by Tsuji et al. (1992,1993), the particle flow is determined based on Newton’s equations of motion by DEM approach, and the fluid flow is described by CFD model on the basis of local-averaged Navier-Stokes equations.

2.4.1 Governing Equations for Solid Particles in CFD-DEM

Particles in particle-fluid flow systems generally have two motions: translational and rotational. According to Newton's second law of motion, the governing equations are given by:

$$\frac{m_i d\mathbf{v}_i}{dt} = \sum_j (\mathbf{f}_{e,ij} + \mathbf{f}_{d,ij}) + \mathbf{f}_{pf,i} + m_i \mathbf{g} \quad (2-11)$$

$$I_i \frac{d\boldsymbol{\omega}_i}{dt} = \sum_j (\mathbf{T}_{t,ij} + \mathbf{T}_{r,ij}) \quad (2-12)$$

where m_i is the mass of particle i , \mathbf{v}_i and $\boldsymbol{\omega}_i$ are the translational and angular velocities of particle i , I_i is the moment of inertia of particle i , $\mathbf{f}_{e,ij}$ and $\mathbf{f}_{d,ij}$ are the elastic contact force and damping force, respectively, $\mathbf{f}_{pf,i}$ is the interaction force between particle and fluid, and $m_i \mathbf{g}$ is the gravitational force. The torque acting on the particle i by particle j includes two components: $\mathbf{T}_{t,ij}$ which is generated by tangential force and causes particle i to rotate, and $\mathbf{T}_{r,ij}$ commonly known as the rolling friction torque. The required equations to calculate these forces have been well established and can be found elsewhere (Zhu et al., 2007). Generally, particles contact forces can be divided in two approaches: linear and non-linear approaches.

Table 2-3. Equations to calculate forces and torques acting on the particle i .

Forces or torques	Equations
Normal elastic force, $\mathbf{f}_{en,ij}$	$-\left(\frac{4}{3}\right)E^* \sqrt{R^*} \delta_n^{3/2} \mathbf{n}$
Normal damping force, $\mathbf{f}_{dn,ij}$	$-c_n \left(6m_{ij} E^* \sqrt{R^*} \delta_n\right)^{1/2} \mathbf{v}_{n,ij}$
Tangential elastic force, $\mathbf{f}_{et,ij}$	$-\mu_s \left \mathbf{f}_{cn,ij} \right \left[1 - \left(1 - \min \left\{ \left \delta_{t,ij} \right , \delta_{t,ij,max} \right\} / \delta_{t,ij,max} \right)^{3/2} \right] \boldsymbol{\delta}_t$
Tangential damping force, $\mathbf{f}_{dt,ij}$	$-\gamma_t \left(6\mu_s m_{ij} \left \mathbf{f}_{cn,ij} \right \sqrt{1 - \delta_{t,ij} / \delta_{t,ij,max}} / \delta_{t,ij,max} \right)^{1/2} \mathbf{v}_{t,ij} (\delta_{t,ij} / \delta_{t,ij,max})$
Coulomb friction force, $\mathbf{f}_{t,ij}$	$-\mu_s \left \mathbf{f}_{en,ij} \right \boldsymbol{\delta}_t$
Torque by tangential forces,	$\mathbf{R}_{ij} \times (\mathbf{f}_{et,ij} + \mathbf{f}_{dt,ij})$

Chapter 2 Literature Review

$\mathbf{T}_{r,ij}$

Rolling friction torque, $\mathbf{T}_{r,ij} = \mu_{r,ij} |\mathbf{f}_{en,ij}| \boldsymbol{\omega}_{ij}^n$

Pressure gradient force, $\mathbf{f}_{pg,i} = -V_i \nabla p$

where $\frac{1}{m_{ij}} = \frac{1}{m_i} + \frac{1}{m_j}$, $\frac{1}{R^*} = \frac{1}{R_i} + \frac{1}{R_j}$, $E^* = \frac{E}{2(1-\nu^2)}$, $\mathbf{n} = \frac{\mathbf{R}_i}{|\mathbf{R}_i|}$, $\boldsymbol{\omega}_{ij}^n = \frac{\boldsymbol{\omega}_{ij}^n}{|\boldsymbol{\omega}_{ij}^n|}$, $\delta_t = \frac{\delta_t}{|\delta_t|}$,
 $\delta_{t,ij,max} = \mu_s \frac{2-\nu}{2(1-\nu)} \delta_n$, $R_{ij} = \frac{R_i(r_i - r_j)}{R_i + R_j}$, $v_{n,ij} = (\mathbf{v}_{ij} \cdot \mathbf{n}) \cdot \mathbf{n}$, $v_{t,ij} = v_{ij} - v_{n,ij}$

Note that the tangential force ($\mathbf{f}_{ct,ij} + \mathbf{f}_{dt,ij}$) should be replaced by $\mathbf{f}_{t,ij}$ when $\delta_t \geq \delta_{t,max}$.

- The Linear approach

The most common linear model, which is developed by Cundall and Strack (1979), is called linear-spring-dashpot model in which the spring considers the elastic deformation and the dashpot is used for viscous dissipation, as shown in Figure 2-24.

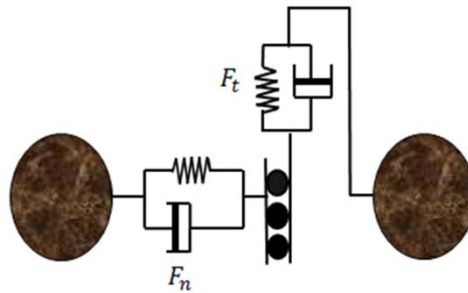


Figure 2-24. The linear-spring-dashpot contact force model.

- The non-linear models:

The non-linear models have been mainly derived centered on Hertz and Mindlin-Deresiewicz 's theories (Hertz, 1882; Mindlin and Deresiewicz, 1953). These kinds of models take too long time for DEM simulations of granular flows. Therefore, the simplified models have been developed based on Hertz and Mindlin-Deresiewicz 's theories to be practical in DEM simulation such as the semi-latched spring for-displacement model (Walton and Braun, 1986), the simplified

Chapter 2 Literature Review

tangential force model (Thornton and Yin, 1991), and the direct force-displacement tangential force model (Langston et al., 1995a). The Langston's model has been applied commonly in the study of the behaviour of granular flows, owing to its simplicity and intuitiveness (Langston et al., 1995a, b; Zhou et al., 1999; Zhou et al., 2002; Zhu and Yu, 2002). The equations used to calculate the particle-particle interaction forces and torques are listed in Table 2-3.

The inter-particle forces acting on the contact point cause a torque resulting in particles rotation. Calculation of normal component of torque, which is often called rolling friction torque, is very difficult compared to that of tangential one (Brilliantov and Pöschel, 1998; Greenwood et al., 1961; Johnson, 1985; Kondic, 1999). The normal component of torque is assumed negligible in many DEM techniques. However, many researchers have observed that the torque have important effects in some cases such as the formations of shear band (Iwashita and Oda, 1998 and heaping Zhou et al., 1999), and movement of a single particle on a plane (Zhou et al., 1999; Zhu and Yu, 2006).

The non-contact forces, which normally include the van der Waals force, capillary force, electrostatic force, ligand-receptor binding of biological cells, and liquid bridging due to a thin liquid film about a particle in a gas and sintering forces, also have important effect on the particle-fluid flow behaviour, particularly in flows with fine of moist particle system. In DEM approach, there is a capability to apply these forces directly and quantitatively in equations. As depicted in Figure 2-25, Zhu et al. (2007) studied the importance of some most common non-contact forces.

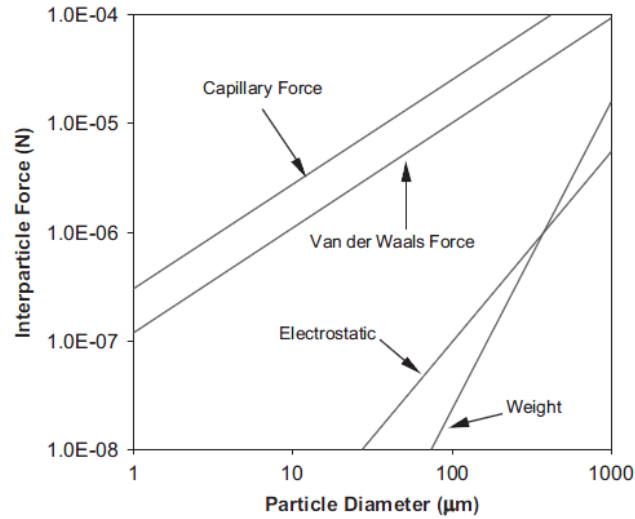


Figure 2-25: The comparison of the non-contact force (Zhu et al., 2007).

In the literature, various drag models are available to calculate the drag force for mono-sized spherical particles (Di Felice, 1994; Ergun, 1952; Gidaspow, 1994; Rong et al., 2013; Syamlal and O'Brien, 1988; Wen and Yu, 1966), binary mixtures of spherical particles (Cello et al., 2010; Rong et al., 2014; Van der Hoef et al., 2005; Yin and Sundaresan, 2009), and mono-sized non-spherical particles (Ganser, 1993; Haider and Levenspiel, 1989; Hölzer and Sommerfeld, 2008; Rong et al., 2015).

2.4.2 Governing Equations for Fluid Phase in CFD-DEM

In the CFD-DEM model, the liquid flow is described by CFD model on the basis of locally-averaged Navier-Stokes equations (Anderson and Jackson, 1967; Gidaspow, 1994). Therefore, the mass and momentum conservation equations governing liquid phase are respectively described as:

$$\frac{\partial(\varepsilon_f)}{\partial t} + \nabla \cdot (\varepsilon_f \mathbf{u}) = 0 \quad (2-13)$$

$$\frac{\partial(\rho_f \varepsilon_f \mathbf{u})}{\partial t} + \nabla \cdot (\rho_f \varepsilon_f \mathbf{u} \mathbf{u}) = -\nabla p - \sum_{i=1}^{k_v} \frac{\mathbf{f}_{d,i} + \mathbf{f}_{pg,i}}{\Delta V} + \nabla \cdot (\varepsilon_f \boldsymbol{\tau}) + \rho_f \varepsilon_f \mathbf{g} \quad (2-14)$$

where \mathbf{u} , ρ_f , and p are the fluid velocity, fluid density, and pressure, respectively; $\boldsymbol{\tau}$ and ε_f are the fluid viscous stress tensor and porosity which are given as $\boldsymbol{\tau} = \mu_f [(\nabla \mathbf{u}) + (\nabla \mathbf{u})^\dagger]$ and $\varepsilon_f = 1 - \sum_{i=1}^{k_v} V_i / \Delta V$, where V_i is the volume of the particle i , k_v is the number of particles in the computational cell, and ΔV is the cell volume. $\mathbf{f}_{d,i}$ is the drag force and $\mathbf{f}_{pg,i}$ is the pressure gradient force which is listed in Table 2-3.

A full description of CFD-DEM coupled approach for non-spherical (ellipsoidal) particles is presented in section 4.3, chapter 4.

2.5 Summary and objectives

Regarding the first part of the thesis (component 1), the layer inversion phenomenon in liquid fluidized beds has been found to be a complex phenomenon and the reasons behind the phenomenon have not been well understood. Only limited efforts have been made to explain the segregation mechanisms behind this peculiar phenomenon. Therefore, in this thesis, CFD-DEM model which provides details in particle scale is first used to explain the underlying the mechanism behind the inversion phenomenon. Then, different drag force capabilities in reproducing of layer inversion phenomenon is examined. The third objective of this part is to perform a systematic study on the effects of particles and liquid properties on this phenomenon. Finally, a mathematical model is proposed in order to predict the inversion velocity.

Chapter 2 Literature Review

In the second part of the project, the particles shape effects on the fluidized beds are investigated using CFD-DEM model. The ellipsoids are employed in order to consider particles shape. According to the literature, a little is known about the influence of particles shape on the behaviour of fluidized beds, particularly liquid fluidized beds. Thus, the second part of the thesis is classified into three stages to get a better understanding of the particle shape effects. In the first stage (component 2), the aim is to examine the effects of particle shape on the flow characteristics in liquid fluidizations of mono-sized particles. The particles shape effects are analysed mainly in terms of particle flow patterns, pressure drop, and bed expansion. In addition, force and particle orientation analysis are also conducted to examine the effect of particle shape and explain the occurrence of entrainment phenomenon. In the second stage (component 3), a modified drag force correlation applicable to multicomponent systems of non-spherical particles are proposed. The reason is that up to now, there is no such a drag correlation. In the last stage (component 4), the modified drag force proposed in the previous stage is used in order to perform a systematic study on the mixing/segregation characteristics of liquid fluidizations under influence of particles shape. The results are mainly analysed in terms of pressure drop variations, minimum fluidization velocity, mixing index, and particle scale forces.

Chapter 3 Investigation of Causes of Layer Inversion and Prediction of Inversion Velocity in Liquid Fluidizations of Binary Particle Mixtures

3.1 Overview

In this chapter, the layer inversion phenomenon is successfully reproduced by CFD-DEM, and the underlying segregation mechanisms are analysed in terms of particle-fluid interaction forces. The results reveal that the layer inversion is caused by the relative change of particle-fluid interaction forces on particles. For large particles, the reduction of the pressure gradient force cannot be compensated by the increased drag force, resulting in the downward flow. Meanwhile, small particles tend to move upward because the increased drag force exceeds the decreased pressure gradient force. In addition, the effects of particle and liquid properties on layer inversion are examined, and different drag force models in predicting the layer inversion are also assessed. It indicates that Rong et al. (2014)'s drag model represents the layer inversion with the best accuracy. Finally, a model based on the force balance criterion is proposed to predict the inversion velocity showing a better accuracy.

3.2 Introduction

Segregation is a popular phenomenon for granular materials, and can be observed in various particulate systems due to the property differences of particles in size, density, shape, and/or other characteristics such as surface roughness, resilience, and electrostatic properties

Chapter 3 Investigation of Causes of Layer Inversion and Prediction of Inversion Velocity in Liquid Fluidizations of Binary Particle Mixtures

(Caulkin et al., 2010; Lozano et al., 2015; Ottino and Khakhar, 2000). Segregation can significantly affect the quality of manufactured products, but it can also be used to separate materials. It represents a challenging research area in granular research, and many efforts have been made either experimentally (Mobius et al., 2001) or theoretically (Schröter et al., 2006). This chapter is focused on an important segregation phenomenon called layer inversion in liquid fluidization, which plays an important role in fluidized beds solid classifiers or biological reactors (Di Renzo et al., 2011).

In layer inversion, the fluidization system contains a binary mixture of particles in which small particles are denser than large particles. At low liquid velocities, the two species form distinct layers with the smaller and denser particles at the bottom while the larger and lighter particles at the top. At high liquid velocities, however, the two layers are inverted. Smaller particles move to the top, and larger particles are located at the bottom. This peculiar phenomenon plays an important role in fluidized bed solid classifiers or biological reactors (Di Renzo et al., 2011). Layer inversion was reported for the first time by Hancock (1936), then it quickly attracted extensive investigations (Escudié et al., 2006b; Gibilaro et al., 1986; Jean and Fan, 1986; Moritomi et al., 1982; Patwardhan and Tien, 1985; Syamlal and O'Brien, 1988; Van Duijn and Rietema, 1982). Substantial studies have revealed that the inversion velocity depends on many variables such as mixture compositions, size/density ratio, and fluid properties (Escudié et al., 2006b). Some investigators (Epstein and LeClair, 1985; Hancock, 1936) assumed that for a specific binary, the inversion velocity did not depend on the overall compositions of the two species. However, Moritomi et al. (1982) experimentally found that the layer inversion can be achieved by not only varying liquid superficial velocity but also changing proportions of a binary mixture in a constant velocity. These observations have made a clear picture of layer inversion for later investigators (Gibilaro et al., 1986; Jean and Fan, 1986).

Chapter 3 Investigation of Causes of Layer Inversion and Prediction of Inversion Velocity in Liquid Fluidizations of Binary Particle Mixtures

More than 20 models have been proposed in the literature to predict the layer inversion phenomenon behaviour in liquid-solid fluidized beds (for example, Epstein, 2005; Gibilaro et al., 1986; Patwardhan and Tien, 1985; Funamizu and Takakuwa, 1995; Moritomi et al., 1986; Jean and Fan, 1986; Gibilaro et al., 1986). Escudié et al. (2006b) compared these models using available experimental data and classified the models into five distinct groups based on mechanisms and approaches adopted. It was found that there were uncertainties in their comparisons because in some experimental cases the temperature had not been reported or specified exactly. Nonetheless, the best model could calculate the inversion phenomenon properties within $\pm 14\%$ error. Some studies provided some data in large liquid fluidized bed (210 mm semi-cylindrical column (Chun et al., 2011) and 190 mm cylindrical column (Vivacqua et al., 2012)). Layer inversion phenomenon in gas-liquid fluidized beds was also studied experimentally by Rim et al. (2013, 2014).

Despite a large number of experimental investigations on layer inversion in liquid fluidized beds, only a few researchers have put their efforts to numerically study this phenomenon. Generally speaking, there are two approaches to model liquid fluidized beds: continuum approach (e.g. so-called Eulerian-Eulerian approach or two-fluid model (A. Howley and J. Glasser, 2002; Reddy and Joshi, 2009; Syamlal and O'Brien, 1988)) and discrete approach (e.g. so-called Lagrangian-Eulerian or discrete element method (Di Renzo et al., 2011; Malone et al., 2007; Mukherjee and Mishra, 2007; Vivacqua et al., 2012; Zhou and Yu, 2009)). Particularly, as discrete approach such as CFD-DEM can provide some fundamental concepts of the flow at a particle scale, it has been verified as one of the most effective approaches to study the fundamental behaviour of particle-fluid systems (Zhu et al., 2007, 2008). Such an approach has been used by some investigators to study layer inversion phenomenon (for example, Di Renzo et al., 2011; Mukherjee and Mishra, 2007; Vivacqua et al., 2012; Zhou and Yu, 2009; Malone et al., 2007).

Chapter 3 Investigation of Causes of Layer Inversion and Prediction of Inversion Velocity in Liquid Fluidizations of Binary Particle Mixtures

Mukherjee and Mishra (2007) combined DEM approach with a simplified fluid model to investigate the layer inversion, but they just qualitatively observed this phenomenon. Zhou and Yu (2009) used the combined CFD-DEM approach reproduced the layer inversion behaviour, but they applied a method to adapt the monodisperse (Di Felice, 1994) drag force model for the binary mixtures. Di Renzo et al. (2011) utilized a new drag force model which was developed for polydisperse systems (Cello et al., 2010), and found that the comparison between experimental data from literature and their simulation results were satisfactory. Experimental and numerical studies were also conducted by Vivacqua et al. (2012) to analyze the factors such as temperature, bed aspect ratio on inversion phenomenon in a binary liquid fluidized bed. The results were found in a reasonable agreement with experimental measurements.

Even though substantial studies have been conducted, limited efforts are made to explain the segregation mechanisms behind this peculiar phenomenon. Therefore, there is a need to elucidate the fundamentals for the occurrence of layer inversion. In principle, the motion of particles is governed by forces acting on them, including particle-particle, particle-wall, and particle-fluid interaction forces (Zhu et al., 2007 and 2008). Thus, the layer inversion must be controlled by these interactions, and quantifying these interaction forces is crucial to reveal the segregation mechanism. Unfortunately, these interaction forces are difficult to measure experimentally. This difficulty, however, can be overcome by the CFD-DEM. Therefore, the aim of this chapter is to use this approach to address what causes layer inversion and provide a thorough explanation of this phenomenon. Different drag models are also compared to examine their applicability in generating layer inversion phenomenon. In addition, parametric studies are conducted to figure out the impacts of particle and liquid properties on the inversion velocity. Finally, a mathematical model based on force balance criterion is proposed to predict the inversion velocity.

3.3 Model descriptions

The combined CFD-DEM has been well developed and documented in the literature (for example, Feng et al., 2004; Xu and Yu, 1997; Zhou et al., 2010). Here, it is extended to liquid fluidizations with some modifications in the calculation of particle-fluid interaction force. For convenience, the model is briefly described below.

3.3.1 Governing equations for particle phase

Particles in particle-fluid flow systems generally have two motions: translational and rotational. According to Newton's second law of motion, the governing equations are given by:

$$\frac{m_i d\mathbf{v}_i}{dt} = \sum_j (\mathbf{f}_{e,ij} + \mathbf{f}_{d,ij}) + \mathbf{f}_{pf,i} + m_i \mathbf{g} \quad (3-1)$$

$$I_i \frac{d\boldsymbol{\omega}_i}{dt} = \sum_j (\mathbf{T}_{t,ij} + \mathbf{T}_{r,ij}) \quad (3-2)$$

where m_i is the mass of particle i , \mathbf{v}_i and $\boldsymbol{\omega}_i$ are the translational and angular velocities of particle i , I_i is the moment of inertia of particle i , $\mathbf{f}_{e,ij}$ and $\mathbf{f}_{d,ij}$ are the elastic contact force and damping force, respectively, $\mathbf{f}_{pf,i}$ is the interaction force between particle and fluid, and $m_i \mathbf{g}$ is the gravitational force. The torque acting on the particle i by particle j includes two components: $\mathbf{T}_{t,ij}$ which is generated by tangential force and causes particle i to rotate, and $\mathbf{T}_{r,ij}$ commonly known as the rolling friction torque. The required equations to calculate these forces have been well established and can be found elsewhere (Zhu et al., 2007).

Table 3-1 lists the equations used to calculate the particle-particle, particle-wall, and particle-fluid interaction forces and torques.

Chapter 3 Investigation of Causes of Layer Inversion and Prediction of Inversion Velocity in Liquid Fluidizations of Binary Particle Mixtures

Note that particle-fluid interaction force consists of many types of forces, including drag force, pressure gradient force, virtual mass force, Basset force, Saffman force, and Magnus force (Zhu et al., 2007). According to Di Renzo et al. (2007), the drag force and the pressure gradient force are two dominant forces, and other types of particle-fluid interaction forces can be ignored in the CFD-DEM simulations of liquid fluidizations. This is because the equations of these forces were developed mainly from simplified flow conditions, hence their applicability to liquid fluidizations is not clear. Moreover, such forces have been ignored in many literature studies, but the simulations still can produce consistent results with experiments (Cornelissen et al., 2007; Di Renzo et al., 2011; Di Renzo and Di Maio, 2007; Ehsani et al., 2016; Ghatage et al., 2014; Lettieri et al., 2006; Peng et al., 2016; Reddy and Joshi, 2009; Yang and Duan, 2013). Hence, in this work, only the drag force and the pressure gradient force are considered and included in the present CFD-DEM model.

Table 3-1. Equations to calculate forces and torques acting on the particle i .

Forces or torques	Equations
Normal elastic force, $\mathbf{f}_{en,ij}$	$-\left(\frac{4}{3}\right)E^* \sqrt{R^* \delta_n^{3/2}} \mathbf{n}$
Normal damping force, $\mathbf{f}_{dn,ij}$	$-c_n \left(6m_{ij} E^* \sqrt{R^* \delta_n}\right)^{\frac{1}{2}} \mathbf{v}_{n,ij}$
Tangential elastic force, $\mathbf{f}_{et,ij}$	$-\mu_s \left \mathbf{f}_{cn,ij} \right \left[1 - \left(1 - \min \left\{ \left \delta_{t,ij} \right , \delta_{t,ij,max} \right\} / \delta_{t,ij,max} \right)^{3/2} \right] \delta_t$
Tangential damping force, $\mathbf{f}_{dt,ij}$	$-\gamma_t \left(6\mu_s m_{ij} \left \mathbf{f}_{cn,ij} \right \sqrt{1 - \delta_{t,ij} / \delta_{t,ij,max}} / \delta_{t,ij,max} \right)^{1/2} \mathbf{v}_{t,ij} \left(\delta_{t,ij} / \delta_{t,ij,max} \right)$
Coulomb friction force, $\mathbf{f}_{t,ij}$	$-\mu_s \left \mathbf{f}_{en,ij} \right \delta_t$
Torque by tangential forces, $\mathbf{T}_{t,ij}$	$\mathbf{R}_{ij} \times (\mathbf{f}_{et,ij} + \mathbf{f}_{dt,ij})$

Chapter 3 Investigation of Causes of Layer Inversion and Prediction of Inversion Velocity in Liquid Fluidizations of Binary Particle Mixtures

Rolling friction torque, $\mathbf{T}_{r,ij}$	$\mu_{r,ij} \mathbf{f}_{en,ij} \boldsymbol{\omega}_{ij}^n$
Drag force, $\mathbf{f}_{d,i}$	Rong et al. (2014)'s model (see Table 2)
Pressure gradient force, $\mathbf{f}_{pg,i}$	$-V_i \nabla p$

where $\frac{1}{m_{ij}} = \frac{1}{m_i} + \frac{1}{m_j}$, $\frac{1}{R^*} = \frac{1}{R_i} + \frac{1}{R_j}$, $E^* = \frac{E}{2(1-\nu^2)}$, $\mathbf{n} = \frac{\mathbf{R}_i}{|\mathbf{R}_i|}$, $\boldsymbol{\omega}_{ij}^n = \frac{\boldsymbol{\omega}_{ij}^n}{|\boldsymbol{\omega}_{ij}^n|}$, $\delta_t = \frac{\delta_t}{|\delta_t|}$,

$\delta_{t,ij,max} = \mu_s \frac{2-\nu}{2(1-\nu)} \delta_n$, $R_{ij} = \frac{R_i(r_i - r_j)}{R_i + R_j}$, $v_{n,ij} = (v_{ij} \cdot \mathbf{n}) \cdot \mathbf{n}$, $v_{t,ij} = v_{ij} - v_{n,ij}$

Note that the tangential force ($\mathbf{f}_{cr,ij} + \mathbf{f}_{dr,ij}$) should be replaced by $\mathbf{f}_{t,ij}$ when $\delta_t \geq \delta_{t,max}$.

Drag force can be calculated by different drag models (for example, Di Felice, 1994; Ergun, 1952; Gidaspow, 1994; Koch and Hill, 2001; Syamlal and O'Brien, 1988). Note that the drag models developed for mono-sized particles should not be employed for multi-sized systems. Therefore, some investigators attempted to propose new correlations for multicomponent systems (for example, Cello et al., 2010; Rong et al., 2014; Van der Hoef et al., 2005; Yin and Sundaresan, 2009; Zhou and Yu, 2009). In this work, Rong et al. (2014)'s drag model is applied, but the applicability of other drag models shown in Table 3-2 are also assessed and given in Section 3.5.3.

Table 3-2. Drag force models assessed in the present work

Correlations	References
$\mathbf{f}_{d,i} = \varepsilon_f^{-\alpha}$ $\alpha = 3.7 - 0.65 \exp[-(1.5 - \log_{10} \mathbf{Re}_i)^2 / 2]$; $\mathbf{Re}_i = \frac{\varepsilon_f d_i \mathbf{u} - \mathbf{v}_i }{\nu_f}$	Di Felice, 1994
$\mathbf{f}_{D,i} = \left\{ \frac{1}{1-\phi} + \left(F_D^* - \frac{1}{1-\phi} \right) [ay_i + (1-a)y_i^2] \right\} 3\pi\mu d_i (1-\phi)\Delta U$ $F_D^* = 10 \frac{\phi}{(1-\phi)^2} + (1-\phi)^2 (1 + 1.5\sqrt{\phi})$ $a(\phi) = 1 - 2.66\phi + 9.096\phi^2 - 11.338\phi^3$; $y_i = \frac{d_i}{\langle d \rangle}$; $\langle d \rangle = \left[\sum_{i=1}^c \frac{x_i}{d_i} \right]^{-1}$	Yin and Sundaresan, 2009

$\mathbf{f}_{D,i} = \beta_i \bar{\mathbf{f}} 3\pi\mu D_i \mathbf{u}$ $\bar{\mathbf{f}} = K_1 + K_2 \varepsilon^4 + K_3 (1 - \varepsilon^4)$ $\beta_i = y_i + \frac{(1 - \varepsilon)}{\varepsilon} \left(\frac{1 - \varepsilon - 0.27}{1 - 0.27} \right) \left(\frac{y_i^2 - y_i}{\sum_k x_k y_k} \right),$ $\bar{D} = \left[\sum_{i=1}^{M_s} \frac{x_i}{d_i} \right]^{-1}; \mathbf{Re} = \frac{\rho_f \mathbf{u} \bar{D}}{\mu_f}; y_i = \frac{D_i}{\bar{D}}$ <p>Where K_1, K_2, and K_3 are dependent on ε and \mathbf{Re}, and these coefficients can be found in Cello et al., 2010).</p>	Cello et al., 2010
$\mathbf{f}_{d,i} = \frac{1}{8} C_{D0} \pi \rho_f \alpha(d_i, x_i, \varepsilon_f) \langle d \rangle^2 \mathbf{u} - \mathbf{v}_i (\mathbf{u} - \mathbf{v}_i) \varepsilon_f^{2 - \beta(\varepsilon_f, \langle \mathbf{Re} \rangle)}$ $C_{D0} = \left(0.63 + \frac{4.8}{\sqrt{\langle \mathbf{Re} \rangle}} \right)^2, \alpha(d_i, x_i, \varepsilon_f) = \frac{1 - A - B}{\sum_{i=1}^N \frac{x_i}{y_i}} + A y_i^2 + B y_i$ $A(\varepsilon_f) = 0.5(1 - \varepsilon_f); B = 0.5, \quad y_i = \frac{d_i}{\langle d \rangle}; \langle d \rangle = \left[\sum_{i=1}^N \frac{x_i}{d_i} \right]^{-1},$ $\langle \mathbf{Re} \rangle = \frac{\varepsilon_f \langle d \rangle \mathbf{u} - \mathbf{v}_i }{\nu_f}$ $\beta(\varepsilon_f, \langle \mathbf{Re} \rangle) = 2.65(\varepsilon_f + 1) - (5.3 - 3.5\varepsilon_f) \varepsilon_f^2 \exp \left[-\frac{1}{2} (1.5 - \log_{10} \langle \mathbf{Re} \rangle)^2 \right]$	Rong et al., 2014

3.3.2 Governing equations for liquid flow

In the CFD-DEM model, the liquid flow is described by CFD model on the basis of local-averaged Navier-Stokes equations (Anderson and Jackson, 1967; Gidaspow, 1994). Therefore, the mass and momentum conservation equations governing liquid phase are respectively described as:

$$\frac{\partial(\varepsilon_f)}{\partial t} + \nabla \cdot (\varepsilon_f \mathbf{u}) = 0 \quad (3-3)$$

$$\frac{\partial(\rho_f \varepsilon_f \mathbf{u})}{\partial t} + \nabla \cdot (\rho_f \varepsilon_f \mathbf{u} \mathbf{u}) = -\nabla p - \sum_{i=1}^{k_v} \frac{\mathbf{f}_{d,i} + \mathbf{f}_{pg,i}}{\Delta V} + \nabla \cdot (\varepsilon_f \boldsymbol{\tau}) + \rho_f \varepsilon_f \mathbf{g} \quad (3-4)$$

where \mathbf{u} , ρ_f , and p are the fluid velocity, fluid density, and pressure, respectively;

$\boldsymbol{\tau}$ and ε_f are the fluid viscous stress tensor and porosity which are given as

$\boldsymbol{\tau} = \mu_f [(\nabla \mathbf{u}) + (\nabla \mathbf{u})^\dagger]$ and $\varepsilon_f = 1 - \sum_{i=1}^{k_v} V_i / \Delta V$, where V_i is the volume of the particle i , k_v is

the number of particles in the computational cell, and ΔV is the cell volume. $\mathbf{f}_{d,i}$ is the drag force and $\mathbf{f}_{pg,i}$ is the pressure gradient force which are listed in

Table 3-1 and Table 3-2.

3.3.3 Coupling methodology

The coupling methodology of CFD and DEM has been well established (Feng et al., 2004; Xu and Yu, 1997), and hence is only briefly described here. In principle, at each time step, DEM gives the positions and velocities of individual particles, so the porosity and volumetric particle-fluid forces in a computational cell are evaluated. CFD will then use this information to calculate the fluid flow field. The fluid flow data will be used in the next time step to determine the particle-fluid interaction forces acting on the individual particle, resulting in the determination of new position and velocity of solids for the next time step.

3.4 Simulation conditions

The physical and geometrical parameters implemented in the present simulations are listed in Table 3-3. The simulation conditions are set similar to the experimental work performed by Jean and Fan (1986). To reduce the number of particles in the simulation, the cylindrical column utilized in their experiments is replaced by a slot with 10 mm (width) \times 1.556 mm (thickness) \times 180 mm (height). The binary mixture of

Table 3-3. Parameters used in the present simulations.

Parameters	Values
Particle size (μm), d_p	small particles: 193; large particles: 778
Particle density ($\text{kg}\cdot\text{m}^{-3}$), ρ_p	small particles: 2,510; large particles: 1,509
Volume fraction of large particles (-), X_L	0.48
Young's modulus (E), $\text{N}\cdot\text{m}^{-2}$	1.0×10^8

Chapter 3 Investigation of Causes of Layer Inversion and Prediction of Inversion Velocity in Liquid Fluidizations of Binary Particle Mixtures

Poisson's ratio (ν), $N.m^{-2}$	0.4
Sliding friction coefficient (μ),-	0.3
Damping Coefficient (c_n),-	0.3
Liquid (water) viscosity ($Pa.s$), μ_f	0.001
Liquid (water) density ($kg.m^{-3}$), ρ_f	1,000
Liquid superficial velocity ($cm.s^{-1}$), (U_0)	0.34-1.7
Time step (s), Δt	4.455×10^{-6}
Bed geometry	
Width (W), mm	10
Height (H), mm	180
Thickness (D), mm	1.556
Number of CFD cells ($n_x \times n_z$)	8×144
Bed distributor	Uniform

particles composes species 1 with 193 μm glass beads (GB), and species 2 with 778 μm activated carbon (AC), where the volume fraction of AC is 48%, based on mixture I in the work of Jean and Fan (1986). For this geometry, 2-D CFD and 3-D model are used. For boundary conditions, no-slip boundary conditions are applied to the interaction between wall and liquid phase. For collisions between particles and walls, walls are considered as a particle with infinite diameter. Periodic boundary conditions are applied to the front and rear direction of the slot to eliminate the wall effect. The inlet fluid velocity is constant; however, in the output atmospheric pressure is assumed. In the simulations, well-mixed particles are first generated randomly and settled down to form a packed bed under gravity. Then, the liquid is uniformly introduced from the bottom at a pre-set superficial velocities (U_0) to fluidize the packed bed. During the simulation, different types of interaction forces including particle-particle, particle-wall and particle-fluid interactions (including the drag force and the pressure gradient force) are recorded for further analysis.

3.5 Results and discussion

3.5.1 Layer inversion phenomenon

Figure 3-1 shows the flow patterns of small and large particles in liquid fluidized beds at different U_0 . The initial bed configuration for all cases is shown in Figure 3-1(a), where large particles (in red) and small particles (in green) are well mixed. At $U_0 = 0.34$ cm/s, larger particles move to the top (Figure 3-1(b)); however small ones pile up at the bottom. At $U_0 = 0.6$ cm/s, the bed height expands a little bit, but small particles begin to percolate into larger particles, forming a mixed region of small and large particles at the upper part; simultaneously, some large particles also move downward to form a mixed region at the bottom section. At $U_0 = 1.0$ cm/s, a well-mixed bed is formed both in the upper and bottom parts (Figure 3-1 (d)). With the further increase of U_0 , the layer inversion starts to occur (Figure 3-1 (e)). At high $U_0 = 1.7$ cm/s (Figure 3-1(f)), two species are almost completely separated to form two discrete layers. This visual analysis demonstrates that the inversion velocity, in which two species are well mixed throughout the whole bed, is around 1.0 cm/s, which is consistent with that reported (Jean and Fan, 1986). The results confirm that the current CFD-DEM approach is able to reproduce the layer inversion satisfactorily, consistent with the experimental observations (Di Renzo et al., 2011; Jean and Fan, 1986; Moritomi et al., 1982; Rasul et al., 2000; Vivacqua et al., 2012).

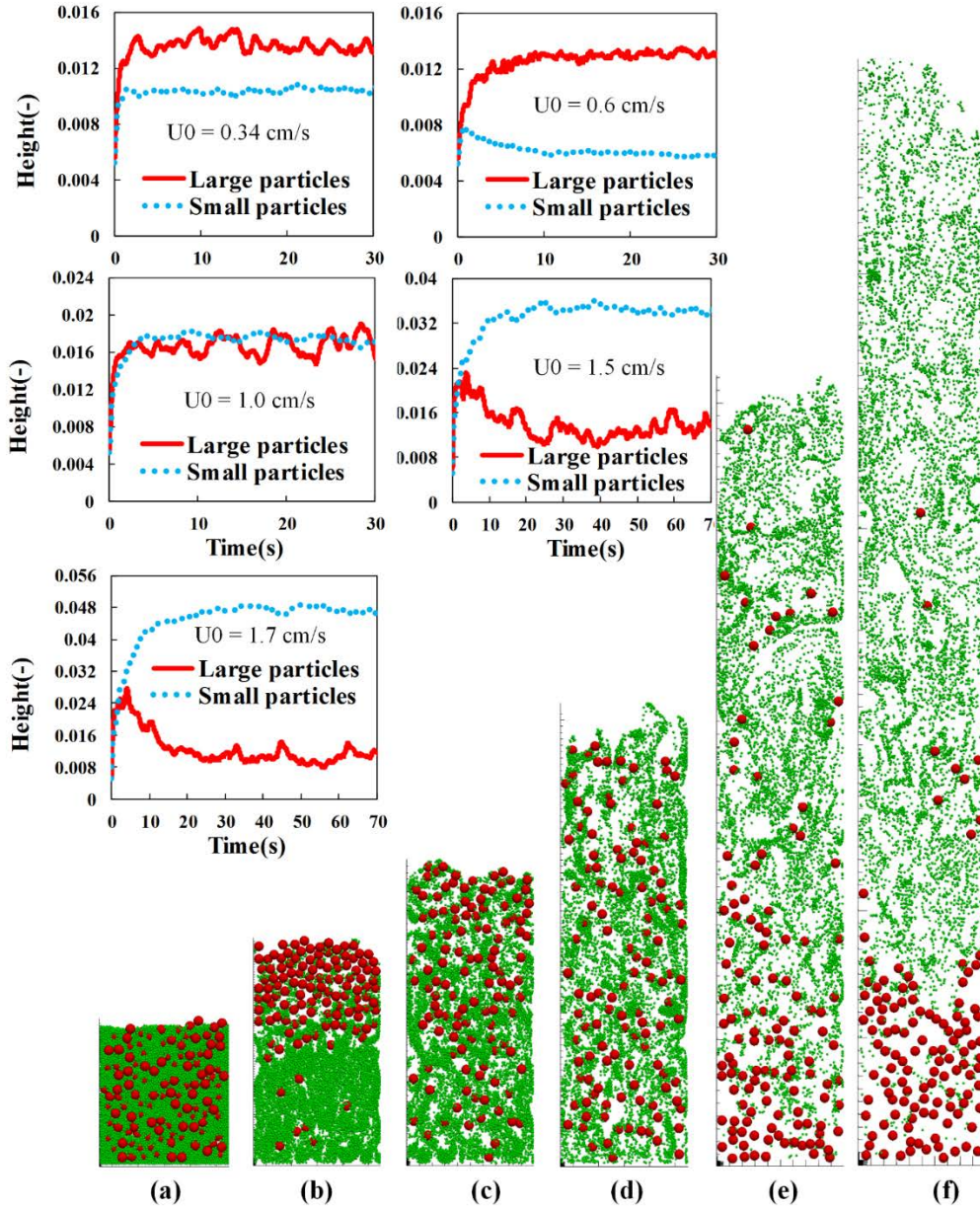


Figure 3-1. Snapshots (a-f) of flow patterns in liquid fluidized beds at different liquid superficial velocities U_0 : (a) 0 cm/s; (b) 0.34 cm/s; (c) 0.6 cm/s; (d) 1.0 cm/s; (e) 1.5 cm/s; and (f): 1.7 cm/s. Six inset figures at the left top: temporal variations of the mean height of each of the species at different liquid superficial velocities.

The formation process of flow patterns shown in Figure 3-1(b)-(f) can be illustrated by the temporal variations of mean height of particles (see inset figures in Figure 3-1). Here, the spatial mean height is calculated by $\langle \bar{H}_i \rangle = (1/\Delta t) \sum_{\Delta t} \left(\sum_{j=1}^{N_i} H_{j,i} / N_i \right)$, where N_i denotes the total number of species i (small or large) and $H_{j,i}$ is the height of particle j of species i . It can be observed that from the time ($t=0$) when liquid is injected from the bed bottom to the

Chapter 3 Investigation of Causes of Layer Inversion and Prediction of Inversion Velocity in Liquid Fluidizations of Binary Particle Mixtures

time when each species reaches to the stable conditions, two stages can be identified: transient and steady-state. During the transient stage, bed height experiences expansion and particles move upward under the particle-fluid driving forces. Depending on U_0 , the binary mixture intends to segregate or mix partially (or completely). At the stable stage, particles reach their macroscopically equilibrium conditions resulting from the transient stage and their mean height fluctuates around a mean value.

At inversion velocity at which two species are well mixed throughout the bed, the average height of two components should be equal. The local-averaged height is averaged over the period of simulation time, and calculated by $\langle \overline{H}_i \rangle = (1 / \Delta t) \sum_{\Delta t} \left(\sum_{j=1}^{N_i} H_{j,i} / N_i \right)$. Figure 3-2 (a) shows the local-time averaged height of small and large particles which is normalized by the maximum bed height in each case. This figure demonstrates that the increase of the inlet velocity causes small particles to move toward the top of the bed, while large ones decrease their heights. This continues until at the inversion velocity of 1.0 cm/s, small and large particles are blended uniformly resulting in the same mean height. Further increasing the velocity changes the position of the two species, so small particles have a higher height and large ones move to the lower part of the bed. Jean and Fan (1986) examined the variations of different bed heights as defined in the inset in Figure 3-2(b) (for example, h_T - the total bed height of the binary mixture, h_{BN} - the height of the bottom layer, and h_{TP} - the height of the top layer). This figure shows the height of the bottom layer which is normalized by h_T . It can be seen that it not only demonstrates the layer inversion process, but also confirms that the inversion velocity of this binary species is 1.0 cm/s which is consistent with the value reported by Jean and Fan (1986).

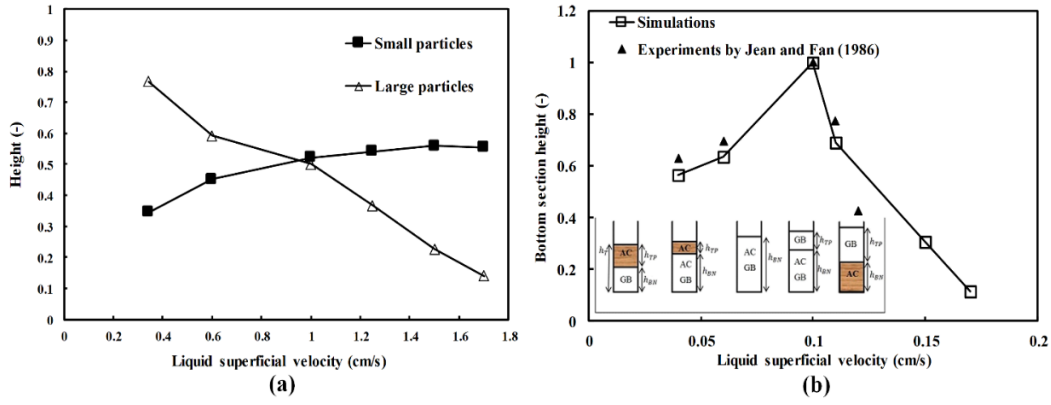


Figure 3-2. Variations of the mean-normalized height of each component with liquid velocity; (b) variations of normalized bottom layer height with liquid velocity (the left-bottom inset is a schematic diagram of the definition of different bed heights introduced by Jean and Fan (1986)).

3.5.2 Force analysis

The solids behaviour in fluidized beds is determined by particle-fluid, particle-particle, particle-wall interaction forces, and gravitational force. Hence, the analysis of these forces can reveal what causes the layer inversion. Note that as the layer inversion takes place in the vertical direction, only the forces in this direction are analysed. It also should be noted that all the forces in this work are normalized by the particle weight. The spatial and time-averaged forces are respectively given by $\overline{F}_i = \left(\sum_{j=1}^{N_i} F_{j,i} \right) / N_i$ and $\langle \overline{F}_i \rangle = (1 / \Delta t) \sum_{\Delta t} \left(\sum_{j=1}^{N_i} F_{j,i} / N_i \right)$, where F can be the drag force, the pressure gradient force, the total particle-fluid interaction force, and particle-particle or particle-wall interaction forces.

Chapter 3 Investigation of Causes of Layer Inversion and Prediction of Inversion Velocity in Liquid Fluidizations of Binary Particle Mixtures

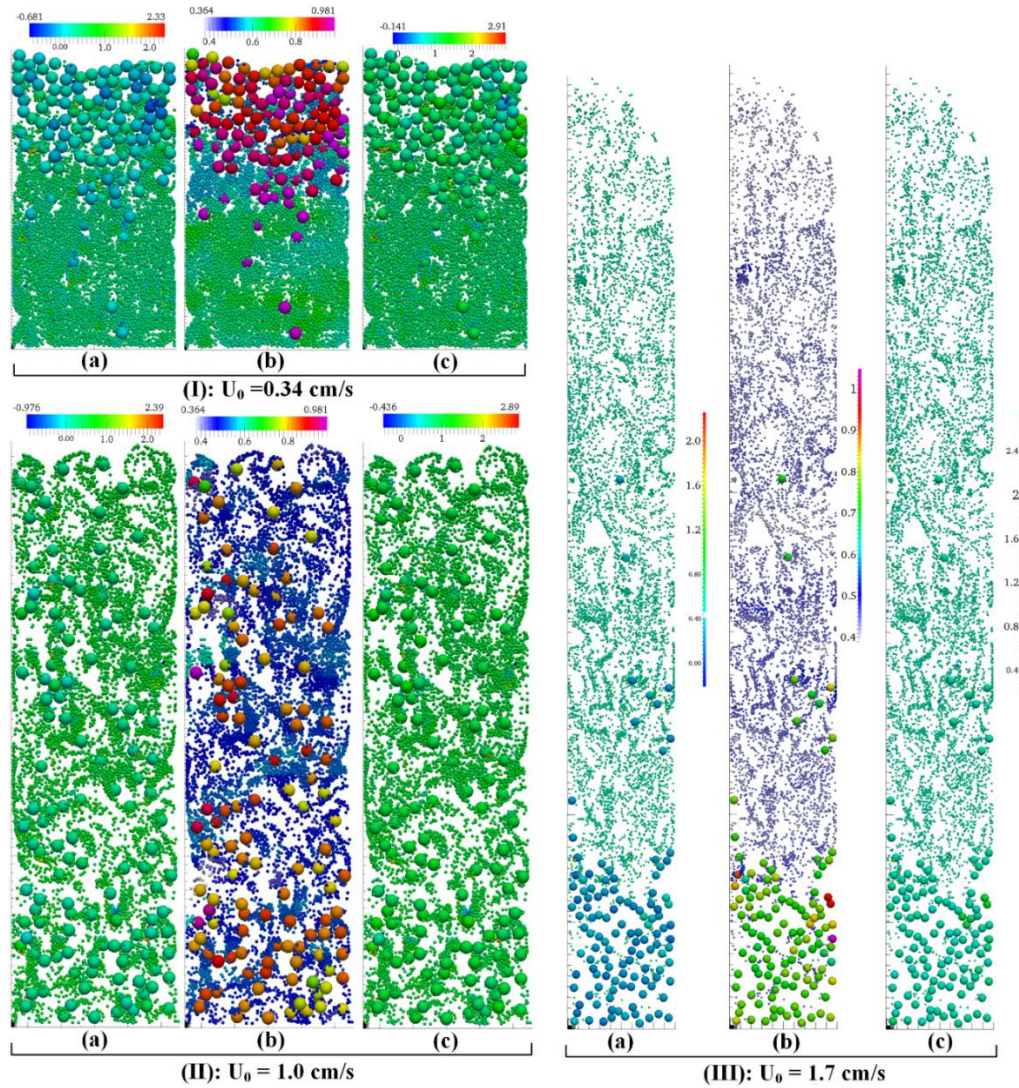


Figure 3-3. Snapshots displaying the spatial distribution of particle-fluid interaction forces at steady state conditions at different liquid superficial velocities: (a) drag force, (b) pressure gradient force, and (c) total particle-fluid interaction force.

Figure 3-3 illustrates the spatial distributions of the drag force, the pressure gradient force, and the total particle-fluid interaction force acting on particles at three different velocities of 0.34 cm/s (below the inversion velocity), 1.0 cm/s (at the inversion velocity), and 1.7 cm/s (above the inversion velocity). It can be observed that at $U_0 = 0.34 \text{ m/s}$ (Figure 3-3 (I)), large particles have smaller drag force but much larger pressure gradient

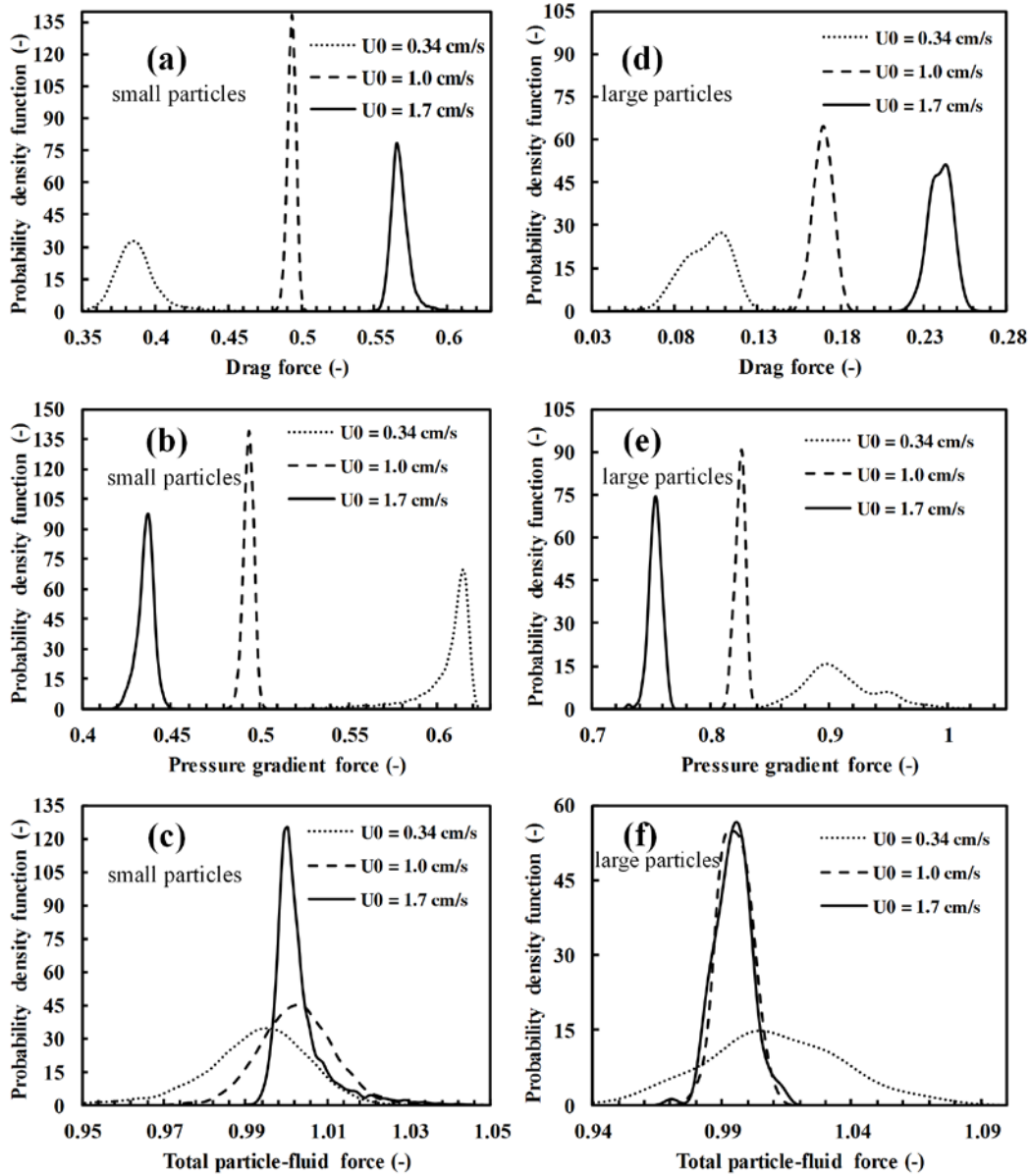


Figure 3-4. Probability density function of normalized forces on particles at different liquid superficial velocities on small particles ((a), (b), (c)); and large particles ((d), (e), (f)).

force than small particles. Therefore, according to Figure 3-3 (I-c), which is the summation of Figure 3-3(I-a) and Figure 3-3(I-b), large particles are located at the top of the bed. At the critical velocity (1.0 m/s) shown in Figure 3-3 (II), the particle-fluid interaction forces on both small and large particles are almost the same (Figure 3-3 (II-c)). Thus, two components are mixed well along the height of the bed. Figure 3-3 (III) illustrates the particle-fluid force distribution at the velocity of 1.7 cm/s. From Figure 3-3 (III-c), it can be observed that smaller

Chapter 3 Investigation of Causes of Layer Inversion and Prediction of Inversion Velocity in Liquid Fluidizations of Binary Particle Mixtures

particle-fluid interaction forces are exerted on large particles resulting in staying in the lower part of the bed.

Figure 3-4 quantitatively demonstrates the probability density distribution of the drag force, the pressure gradient force and the total particle-fluid interaction force exerted on large and small particles at different liquid velocities. It can be observed that the increase in velocity causes both large and small particles to receive larger drag force (Figure 3-4(a) and (d)), and smaller pressure gradient force (Figure 3-4(b) and (e)), which results in increasing the particle-fluid interaction force on small particles, but decreasing on large ones. Therefore, small particles may intend to rise to the top at high liquid velocities. In addition, all the forces are distributed more uniformly in a narrower range at the inversion velocity of 1.0 cm/s, but the distributions are wider for high and low liquid velocities.

To explore the mechanisms responsible for the occurrence of layer inversion, the temporal variations of different interaction forces are plotted and shown in Figure 3-4. Here, the spatial mean forces are used, and defined as follows. For large particles, the particle-particle, particle-wall and particle-fluid interaction forces are defined as

$$\langle |\mathbf{f}_{pp,L}| \rangle = \sum_{i=1}^{N_L} \left[\left(\sum_{j=1}^{k_{c,i}} \mathbf{f}_{pp,ij} / (m_L \mathbf{g}) \right) \right] / N_L \quad , \quad \langle |\mathbf{f}_{pw,L}| \rangle = \sum_{i=1}^{N_L} \left[\left(\mathbf{f}_{pw,i} / (m_L \mathbf{g}) \right) \right] / N_L \quad , \quad \text{and}$$

$$\langle |\mathbf{f}_{pf,L}| \rangle = \sum_{i=1}^{N_L} \left[\left(\mathbf{f}_{pf,i} / (m_L \mathbf{g}) \right) \right] / N_L \quad , \quad \text{respectively, where } N_L \text{ is the number of large particles,}$$

$k_{c,i}$ is the number of particles contacting with particle i , $\mathbf{f}_{pp,ij}$ is the particle-particle interaction force between particles i and j , $\mathbf{f}_{pw,i}$ is the particle-wall interaction force

between particle i and the wall, and $m_L \mathbf{g}$ is the weight of large particles. Note that the

notations $| |$ and $\langle \rangle$ stand for the magnitude and average of the variable, respectively.

Forces acting on small particles can be calculated in the same manner. Figure 3-5 clearly shows that compared to the particle-fluid interaction force, inter-particle and particle-wall

Chapter 3 Investigation of Causes of Layer Inversion and Prediction of Inversion Velocity in Liquid Fluidizations of Binary Particle Mixtures

interaction forces are very small. However, the interactions between small and large particles contribute the force balance for each species. It has been checked and confirmed that the entire bed weight is balanced by the total particle-fluid interaction force, and the particle-wall interaction force can be safely ignored. For each species, its weight is balanced by not only the particle-fluid interaction force but also the interaction forces between small and large particles. For example, at a low velocity of $U_0 = 0.34$ cm/s, the particle-fluid interaction force on small particles is less than 1.0, and the particle-particle interaction force from large particles to small particles is upward to support the partial weight. However, for large particles, the particle-fluid interaction force on large particles is larger than 1.0, so downward negative particle-particle interaction force is required to balance the weight of large particles. Such a force balance can be found at other velocities as well (Figure 3-5 (b) and (c)), proving a macroscopic equilibrium of forces in the bed.

The driving force for the movement of particles is the particle-fluid interaction force. As clearly shown in Figure 3-5, the particle-fluid interaction force is dominant, and their values vary around 1.0. Notably, a slight difference exists for large and small particles at different velocities. At $U_0 = 0.34$ cm/s (Figure 3-5 (a)), the particle-fluid interaction force acting on large particles is larger than 1.0; the value on small particles less than 1.0. At $U_0 = 1.0$ cm/s (Figure 3-5 (b)), the particle-fluid interaction forces acting on both particles are similar. At $U_0 = 1.7$ cm/s (Figure 3-5 (c)), the particle-fluid interaction force on small particles is larger than 1.0, but less than 1.0 on large particles. It is believed that such a slight difference of particle-fluid interaction forces acting on different particles is responsible for the layer inversion. To further demonstrate this, the average values of particle-fluid interaction forces against U_0 is calculated and plotted in Figure 3-6 (a).

Chapter 3 Investigation of Causes of Layer Inversion and Prediction of Inversion Velocity in Liquid Fluidizations of Binary Particle Mixtures

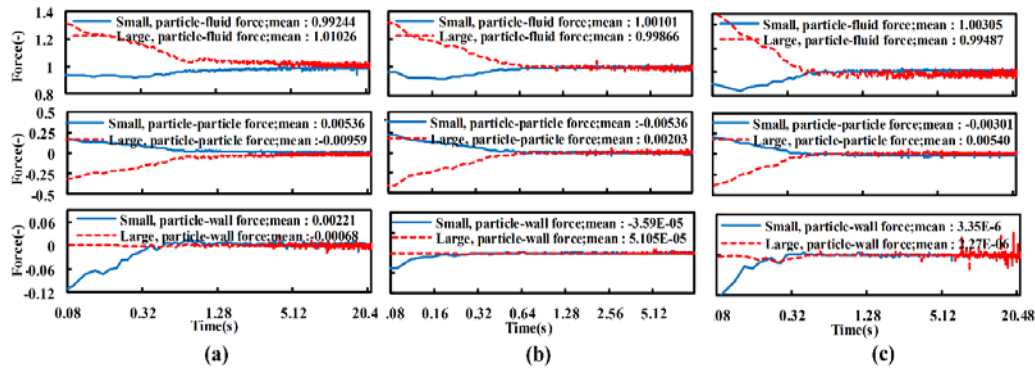


Figure 3-5. The variation of the mean forces on both large and small particles in the vertical direction: the top row is particle-fluid interaction force; the middle row is the particle-particle interaction force; and the bottom row is the particle-wall (including side and bottom walls) interaction force. Figures from the left to the right are corresponding to different liquid velocities: (a) 0.34 cm/s, (b) 1.0 cm/s, and (c) 1.7 cm/s. Note that the time-axis in the figures is on a logarithmic scale.

Figure 3-6 (a) shows that with increasing U_0 , the particle-fluid interaction force acting on large particles gradually decreases, but the force acting on small particles increases. At a low U_0 , the mean particle-fluid interaction force on large particles is larger than small particles, hence large particles incline to depart from the bottom toward the top of the bed; while small particles accumulate at the bottom because they have low particle-fluid interaction force. Hence, increasing U_0 results in a lower driving force for segregation of two species. Hence, at $U_0 = 0.6$ cm/s, mixed regions of particles are observed at the bottom (dominated by large particles) and the top (dominated by small particles). At $U_0 = 1.0$ cm/s, the particle-fluid interaction forces on both species are equal; thus, there is no driving force to separate large and small particles. When U_0 is larger than 1.0 cm/s (the inversion point), e.g., 1.5 cm/s, small particles receive large particle-fluid interaction force from the flowing fluid and move toward to the top part of the bed; large particles, on the other hand, intend to be at the bottom section. At this velocity, as the driving force is not large enough, a mixture of large and small particles is still observed between the top part which is dominated by small ones and the bottom part which is prevailed by large ones. With U_0 increasing further, e.g., at $U_0 = 1.7$ cm/s, the particle-fluid interaction force on small particles is much higher than large particles, resulting in the disappearance of mixed regions and the generation of two distinct layers:

small particles being at the top part of the bed, and large ones accumulating at the bottom section.

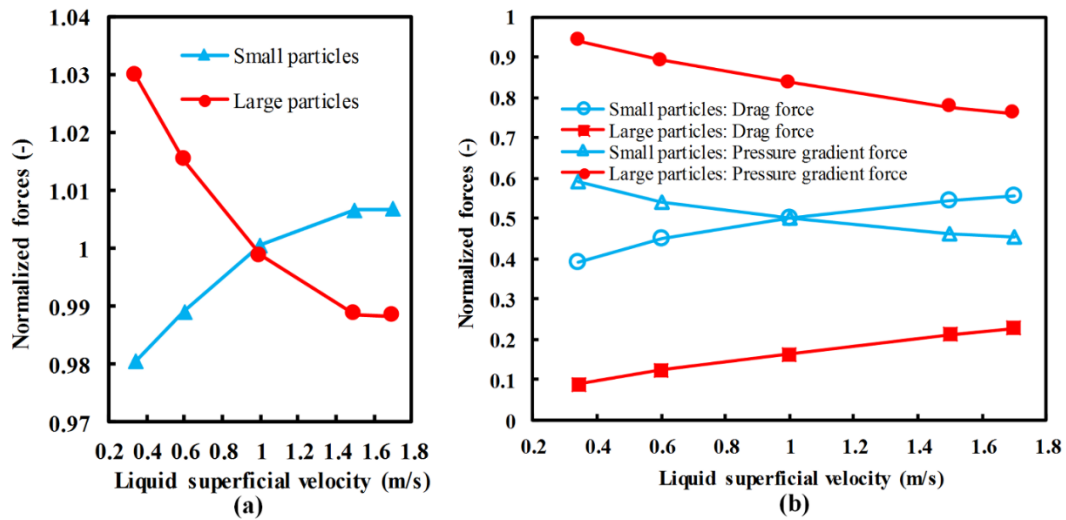


Figure 3-6. Variations of temporal-spatial mean forces with liquid superficial velocity for both large (represented by circles) and small particles (represented by triangles): (a) the total particle-fluid interaction force, and (b) the drag force and pressure gradient force.

Therefore, the driving force for the layer inversion is the difference of particle-fluid interaction forces acting on large and small particles. However, the variation trend of particle-fluid interaction force against U_0 is the result of counteractions of drag force and pressure gradient force. As observed from Figure 3-6(b), the drag force on both small and large particles increases with U_0 increasing, which is consistent with the general understanding of the nature of the drag force. But interestingly, the pressure gradient force acting on both species reduces. However, for large particles, the pressure gradient force contributes more to the total particle-fluid interaction force than the drag force. The increasing rate in the drag force is not sufficient to compensate the loss in the pressure gradient force, hence the total particle-fluid interaction force exerting on large particles reduces with U_0 , causing large particles gradually fall down. On the other hand, the pressure gradient force and drag force acting on small particles almost have equivalent values in the whole range of velocities. More importantly, the increasing rate of the drag force on small particles not only compensates but also exceeds the decreasing rate of the pressure gradient force. Hence, the total particle-fluid

interaction force acting on small particles increases with U_0 , driving small particles to move upward.

3.5.3 Comparison of different drag force models

Several drag force models have been adopted in the literature to calculate the momentum transfer between particles and fluid phases in multiphase systems. In this section, the widely used drag models developed for multicomponent systems (Cello et al., 2010; Rong et al., 2014; Yin and Sundaresan, 2009) as well as the most commonly used drag model for mono-component systems (Di Felice, 1994) are compared with respect to the prediction of layer inversion. In particular, the comparisons are made on the basis of the fact that the actual inversion velocity for the binary mixture is 0.99 cm/s (Jean and Fan, 1986). The simulation conditions are the same as explained in Section 3.4 for all cases. A summary of drag models assessed is given in Table 3-2.

Figure 3-7 display snapshots of particle positions for the different drag force models at three different velocities of 0.34 cm/s, 1.0 cm/s, and 1.7 cm/s. Figure 3-7 (I-b) shows that Di Felice (1994) model fails to represent expected flow pattern at low velocities in which large particles should be at the top of the bed. This is mainly due to the fact that this model was developed for mono-sized particle systems. Figure 3-7 (I-c) shows that Rong et al. (2014)'s model predicts the segregation patterns well in low liquid velocity. The other two drag models (Cello et al., 2010; Yin and Sundaresan, 2009) also can produce similar segregation pattern. Note that the bed expansion is quite similar to different drag laws except for Yin and Sundaresan (2009)'s model which predicts a slightly larger expansion.

Chapter 3 Investigation of Causes of Layer Inversion and Prediction of Inversion Velocity in Liquid Fluidizations of Binary Particle Mixtures

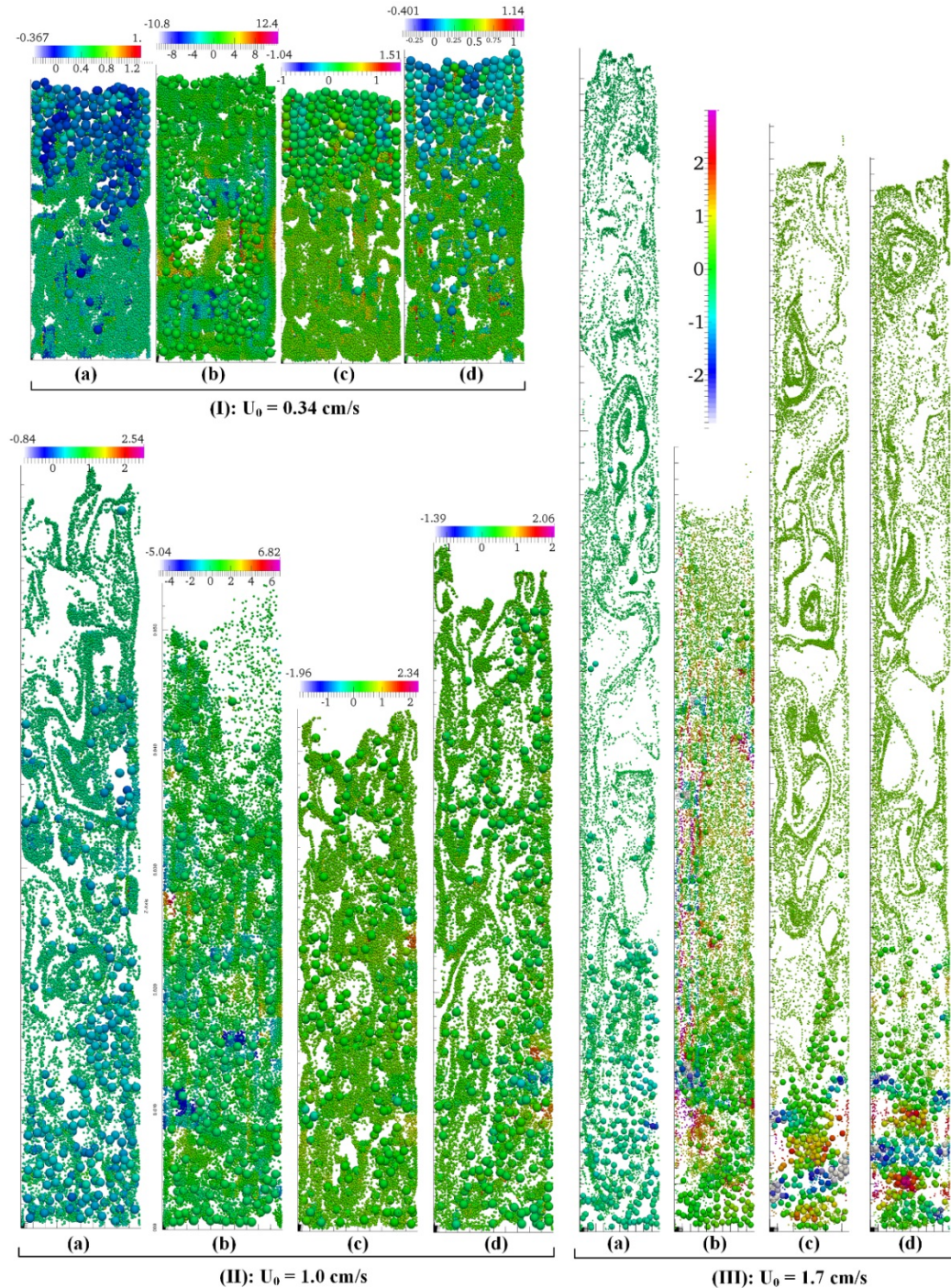


Figure 3-7. Snapshots of flow patterns in solid-liquid fluidized beds for different drag force models at different liquid superficial velocities: (a) Cello et al. (2010); (b) Di Felice (1994); (c) Rong et al. (2014); and (d) Yin and Sundaresan (2009). All snapshots are coloured based on drag force values.

Figure 3-7 (II) illustrates the particle flow patterns at the inversion velocity (1.0 cm/s) for different drag models. Similarly, Di Felice (1994)'s model cannot generate well-mixed flow patterns at this velocity. Yin and Sundaresan (2009) and Rong et al. (2014) models predict a fairly uniform distribution of particles in the bed. However, less large particles accumulate at

Chapter 3 Investigation of Causes of Layer Inversion and Prediction of Inversion Velocity in Liquid Fluidizations of Binary Particle Mixtures

the bottom for Cello et al. (2010)'s model. Both Yin and Sundaresan (2009) and Cello et al. (2010)'s models represent higher bed expansion than other models. At high liquid velocities (Figure 3-7 (III)), it is anticipated that small particles move toward the top of the bed and large ones locate at the bed lower part. It can be seen that all drag force models can produce such flow patterns, although still some discrepancies in the prediction of bed expansion.

Figure 3-7 also depicts the spatial distribution of normalized drag force predicted by different drag models. It can be observed for all cases, the drag forces acting on small particles are reasonably larger than those on large particles, and this matter is quite obvious in Rong et al. (2014)'s drag model. The probability density functions of the drag forces predicted by different drag models are plotted in Figure 2-1. It can be observed that Di Felice (1994)'s model predicts the wide distribution of the drag force and pressure gradient force compared to other models. However, the drag forces calculated by Rong et al. (2014)'s model have the narrowest distribution and largest peak values.

In terms of the capability of the drag models to predict the inversion velocity, the inversion velocities predicted are presented in Table 3-4 and compared with the inversion velocity reported in experiments by Jean and Fan (1986), which is 0.99 cm/s. It can be seen that some disagreements are found for this specific binary mixture. Di Felice (1994)'s model fails to predict the segregation patterns hence the inversion velocity. Both Yin and Sundaresan (2009)'s drag model and Cello et al. (2010)'s drag model underestimate the inversion velocity with errors at 20% and 13 %, respectively. The inversion velocity predicted by Rong et al. (2014) model has the best agreement with the one measured in physical experiments.

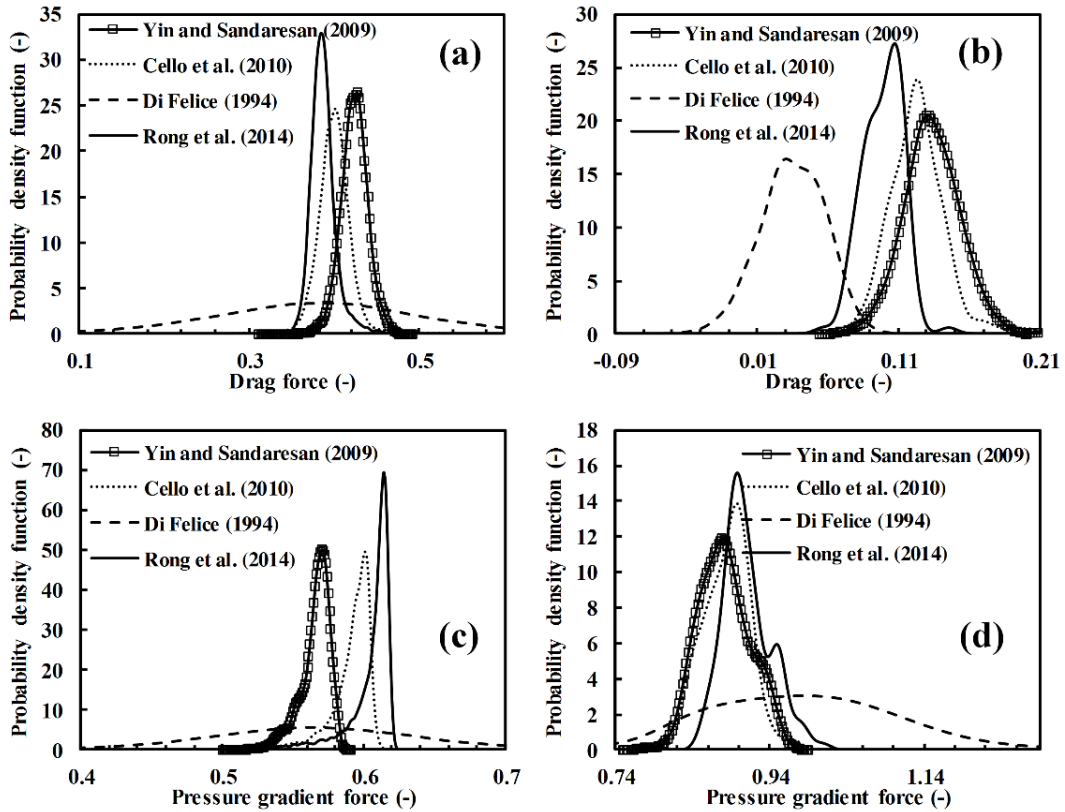


Figure 3-8. Probability density function of the drag force and the pressure gradient force predicted by different drag models ($U_0 = 0.34\text{m/s}$): (a) and (c) for small particles; (b) and (d) for large particles.

Table 3-4. Inversion velocities predicted by different drag force models.

Drag models	Di Felice (1994)	Yin and Sundaesan (2009)	Cello et al. (2010)	Rong et al. (2014)
Inversion velocity (cm/s)	fail	0.79	0.86	1.0
Error (%)	fail	-20.20	-13.13	1.01

3.5.4 Effects of particle and fluid properties on inversion velocity

The inversion velocity is affected by particle and liquid properties. In this section, the influences of particle size ratio and density ratio, and fluid properties such as viscosity, density, and density are examined to perform a systematic analysis of the impacts of these parameters on the inversion velocity. Figure 3-9 (a) and Figure 3-9 (b) displays the effects of particle size ratio and density ratio on the inversion velocity, respectively. It can be observed that the inversion velocity decreases with increasing particle size ratio and density ratio. Fitted

Chapter 3 Investigation of Causes of Layer Inversion and Prediction of Inversion Velocity in Liquid Fluidizations of Binary Particle Mixtures

curves are also plotted for each figure. It shows that the rate of decreasing for the case of particles size ratio is sharper than the linear falling trend of particles density ratio effect. This implies that the influence of particles size ratio is more significant than the effects of particle density ratio. In addition, reducing the inversion velocity with increasing particles size and density ratio indicates that small and large particle get well-mixed at lower velocities. In the range of size and density ratios examined, no layer inversion is observed when particle size ratio is less than 2.85 and particles density ratio is less than 0.19 or larger than 0.52.

The effect of particle size and density ratio can be explained by the particle-fluid interaction force ratio as a function of liquid superficial velocities, and shown in Figure 3-9 (c) and (d). Note that the particle-fluid force ratio is defined as the ratio of mean particle-fluid force on large particles to mean particle-fluid force on small particles. It can be found from Figure 3-9 (c) that at a specific size ratio such as 3.7 (the base case similar to work of Jean and Fan (1986)), the particle-fluid force ratio declines with increasing liquid superficial velocities and at inversion velocity, the force ratio becomes 1.0 as previously explained in Section 3.5.2 and Figure 3-6. Figure 3-9 (c) illustrates that with increasing the particle size ratio, the force ratio trend becomes sharper and it intersects with the dashed line (ratio = 1.0) at a lower velocity, so the inversion velocity decreases. Nonetheless, at the size ratio of 2.85, the particle-fluid force ratio for the whole range of velocities are larger than one, which means that large particles at different liquid velocities have higher mean heights than small particles, and the layer inversion cannot happen for this size ratio and less. Note that the further increase in liquid velocity causes particles to be entrained to freeboard, and the fluidized bed becomes hydraulic conveyor.

In the case of the effect of particles density ratio, similar behaviour can be found (Figure 3-9(a)). For the density ratio of 0.19, for instance, since the force ratio is always bigger than one, even at high velocities, large particles are exposed to higher particle-fluid

Chapter 3 Investigation of Causes of Layer Inversion and Prediction of Inversion Velocity in Liquid Fluidizations of Binary Particle Mixtures

interaction force resulting in staying at the top of the small particles at the entire range of liquid velocity. Hence, layer inversion does not occur. On the other hand, when the density ratio is 0.52, the force ratio value is less than one which causes large particle have less mean height than small particles at the operating velocities, and again no layer inversion happens.

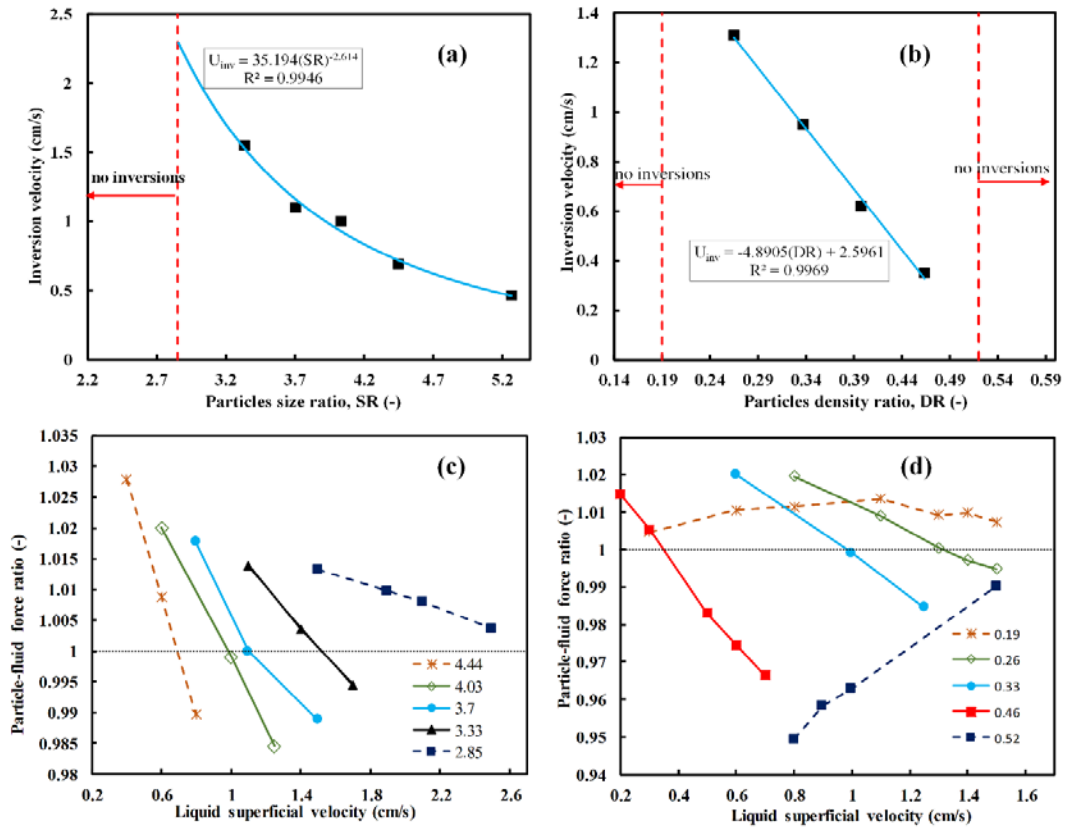


Figure 3-9. (a) The effect of particles size ratio on the inversion velocity; (b) the effect of density size ratio on the inversion velocity; (c) variations of particle-fluid force ratio with liquid superficial velocities at different particles size ratio; and (d) variations of particle-fluid force ratio with liquid superficial velocities at different particle density ratio.

Chapter 3 Investigation of Causes of Layer Inversion and Prediction of Inversion Velocity in Liquid Fluidizations of Binary Particle Mixtures

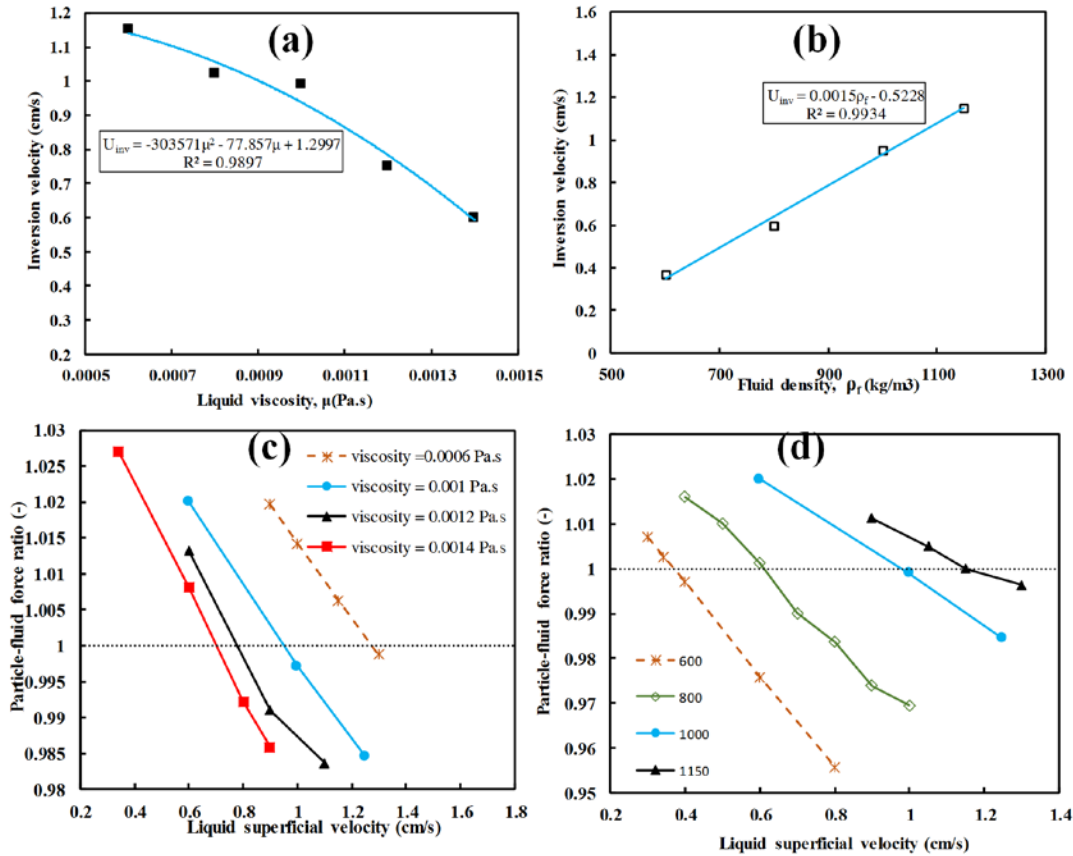


Figure 3-10. (a) The effect of liquid viscosity on the inversion velocity; (b) the effect of liquid density size ratio on the inversion velocity; (c) variations of particle-fluid force ratio with liquid superficial velocities at different liquid viscosity; and (d) variations of particle-fluid force ratio with liquid superficial velocities at different liquid density.

Figure 3-10 demonstrates the effects of liquid density and viscosity on the inversion velocity. From Figure 3-10 (a), it can be seen that when the liquid becomes more viscous, the layer inversion happens at a lower velocity. This implies that the more the viscous the liquid, the less liquid velocity is required to reach a well-mixed condition. The fitted curve shows that the relationship between the inversion velocity and liquid viscosity is polynomial. On the other hand, increasing liquid density increases the inversion velocity which shows a linear relationship (Figure 3-10(b)). To figure out the reason for such effects, the particle-fluid force ratio against liquid velocity is also examined and shown in Figure 3-10(c) and (d). Figure 3-10 (c) shows the particle-fluid force ratio at different liquid viscosity, indicating that increasing liquid viscosity shifts the force ratio curve to a lower value. This causes the force

Chapter 3 Investigation of Causes of Layer Inversion and Prediction of Inversion Velocity in Liquid Fluidizations of Binary Particle Mixtures

ratio intersects with the dashed line (the ratio =1.0) at lower liquid velocity, which implies that the particle-fluid force on small and large particles approach to the same value at a lower velocity (inversion velocity). The opposite trend happens when liquid density increases (Figure 3-10 (d)). In this case, the particle-fluid force on small and large particles meet each other at a higher velocity when heavier liquid is used.

Figure 3-11 illustrates the impact of operating temperature on the inversion velocity. In this case, it is assumed that all particles and liquid are at the same temperature when the temperature is increased, so there is no heat transfer between particles and liquid. With the temperature increasing, liquid viscosity and density are affected while particle properties are assumed to be independent of temperature. From Figure 3-11, it can be found that the inversion velocity increases with increasing the temperature. Such an influence was also observed by previous researchers (Escudié et al., 2006b; Vivacqua et al., 2012). This can be attributed to the counteraction effects of liquid density and viscosity when the temperature changes. With the temperature increasing, the density and viscosity decrease. According to Figure 3-11, the inversion velocity increases with reducing liquid viscosity but decreases with reducing liquid density.

Therefore, the effect of liquid temperature can be regarded as the simultaneous effects of liquid viscosity and liquid density. However, as the temperature varies in the range of 5 to 35 °C, and hence has little impact on the water density (e.g. water density decreases from 0.999 to 0.992 in this range), the effect of the temperature is mostly determined by the liquid viscosity which is sensitive to liquid temperature. The inversion values in Figure 3-11 (a) for different viscosities are also plotted in Figure 3-11. It can be observed that the trends of temperature effect and viscosity effect are similar.

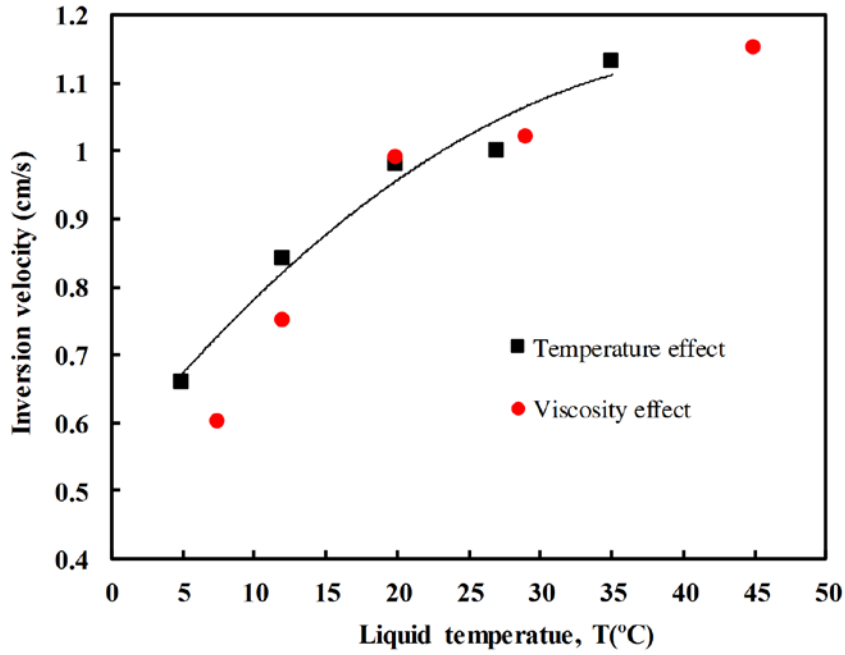


Figure 3-11. The effects of operating temperature on the inversion velocity.

3.5.5 A new mathematical model for prediction of inversion velocity

From above discussions (Figure 3-6, Figure 3-9, and Figure 3-10), it has been found that at the inversion point, the dimensionless particle-fluid interaction force ratio of large particle to that of small particles is equal to one. This is the criterion for this new mathematical model which can be written as:

$$\frac{(f_{d,L} + f_{pg,L}) / W_L}{(f_{d,S} + f_{pg,S}) / W_S} = 1 \quad (3-5)$$

where “pg” is the abbreviation of pressure gradient, “L” stands for large particles, “S” stands for small particles, “d” stands for drag force, and “W” is the particle weight. The pressure gradient force can be calculated by $f_{pg,i} = V_i(-dp/dz)$; where “V” is the particle volume.

Therefore, Eq. (3-5) can be rearranged as:

Chapter 3 Investigation of Causes of Layer Inversion and Prediction of Inversion Velocity in Liquid Fluidizations of Binary Particle Mixtures

$$\frac{f_{d,L} - V_L \left(\frac{dp}{dz} \right)}{f_{d,S} - V_S \left(\frac{dp}{dz} \right)} = \frac{W_L}{W_S} \quad (3-6)$$

The drag force in Eq. (3-6) can be determined by Rong et al.'s model (2014) as given in Table 3-2. On the other hand, there is a need to have an equation for the pressure gradient calculation. Based on the fact that the total pressure drop is equal to the total bed weight per unit cross-sectional area in fluidized beds, the pressure gradient along the bed height can be determined by:

$$-\frac{dp}{dz} = [\varepsilon \rho_f + (1 - \varepsilon)(x_L \rho_L + x_S \rho_S)] \quad (3-7)$$

By substituting Eq. (3-7) and the drag force from Table 1 into Eq. (3-6), there would be one non-linear equation with two unknown variables (ε, U_0). Therefore, another equation is required to find two unknown variables. This equation can be derived from the condition that the particle-fluid interaction force on small or large particles is equal to the particle weight at the inversion point (Figure 3-6), and given by:

$$f_{d,L} - V_L \left(\frac{dp}{dz} \right) = W_L g \quad (3-8)$$

or

$$f_{d,S} - V_S \left(\frac{dp}{dz} \right) = W_S g \quad (3-9)$$

Eq. (3-6) and one of the Eq. (3-8) or Eq. (3-9), which represent two non-linear equations with two unknown variables (ε, U_0), can be solved with any numerical methods such as the Newton-Raphson method. Therefore, for a specific binary mixture, once the particle properties such as diameter, density and volume fractions and liquid properties (viscosity and

Chapter 3 Investigation of Causes of Layer Inversion and Prediction of Inversion Velocity in Liquid Fluidizations of Binary Particle Mixtures

density) are known, the inversion velocity can be determined by solving of Eq. (3-6) and Eq. (3-8) or Eq. (3-9).

In order to verify the capability of the current model, 29 different mixtures with reported experimental inversion velocity are chosen. The 29 selected binary mixtures cover a wide range of particles size (0.091-3.15 mm), particle density (1,170-11,330 kg/m³), liquid density (1,000-1,070 kg/m³), and liquid viscosity (0.001-0.14 Pa s). Figure 3-12 compares the inversion velocities predicted by the proposed model and those of measured values from experiments, generally showing a good agreement.

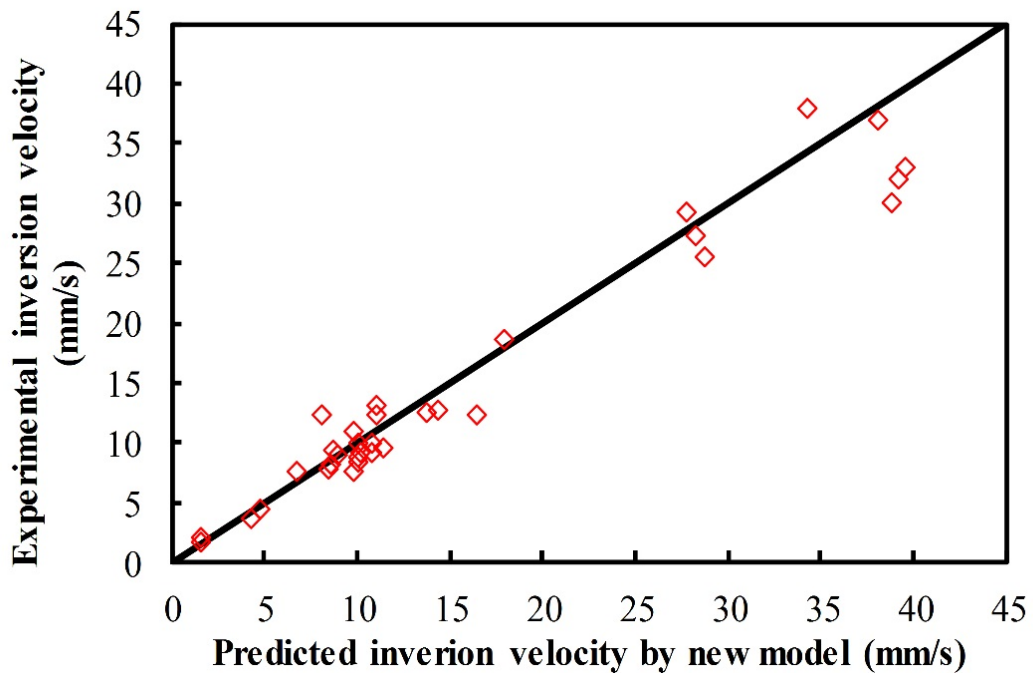


Figure 3-12. The comparison of inversion velocity predicted by the model and measured experimentally.

Table 3-5. Different mathematical model for prediction of the inversion velocity.

Chapter 3 Investigation of Causes of Layer Inversion and Prediction of Inversion Velocity in Liquid Fluidizations of Binary Particle Mixtures

No.	Researchers	Model type
Model 1	Epstein and LeClair, 1985	Bulk density equivalence model
Model 2	Hu, 2002	Bulk density equivalence model
Model 3	Patwardhan and Tien, 1985	Apparent porosity model
Model 4	Escudié et al., 2006b	Modified apparent porosity model
Model 5	Bhattacharya and Dutta, 2002	Effective voidage model
Model 6	Moritomi et al., 1986	Unit cell model
Model 7	Funamizu and Takakuwa, 1995	Force balance model
Model 8	Jean and Fan, 1986	Segregation velocity model
Model 9	Escudié et al., 2006b	Segregation velocity model +packing model 1
Model 10	Escudié et al., 2006b	Segregation velocity model +packing model 2
Model 11	Escudié et al., 2006b	Segregation velocity model + serial model
Model 12	Escudié et al., 2006b	Pseudofluid segregation velocity model Asif (1998b) +packing model 1
Model 13	Escudié et al., 2006b	Pseudofluid segregation velocity model Asif (1998b) +packing model 2
Model 14	Escudié et al., 2006b	Pseudofluid segregation velocity model Asif (1998b) +prop. avg. model
Model 15	Escudié et al., 2006b	Corrected pseudofluid segregation velocity model + serial model
Model 16	Escudié et al., 2006b	Corrected pseudofluid segregation velocity model +packing model 1
Model 17	Escudié et al., 2006b	Corrected pseudofluid segregation velocity model +packing model 2
Model 18	Escudié et al., 2006b	Corrected pseudofluid segregation velocity model + prop. avg. model
Model 19	Gibilaro et al., 1986	Complete segregation model
Model 20	Epstein, 2005	Modified complete segregation model
Model 21	Asif, 1998	Property-averaging model
Model 22	Escudié et al., 2006b	Property averaging model
Model 23	Asif, 2002	Packing model 1
Model 24	Asif, 2002	Packing model 2
Model 25	Asif, 2004	Hybrid model
Model 26	Escudié et al., 2006b	Hybrid model: property-averaging and packing model 1
Model 27	Escudié et al., 2006b	Hybrid model: property-averaging and packing model 2

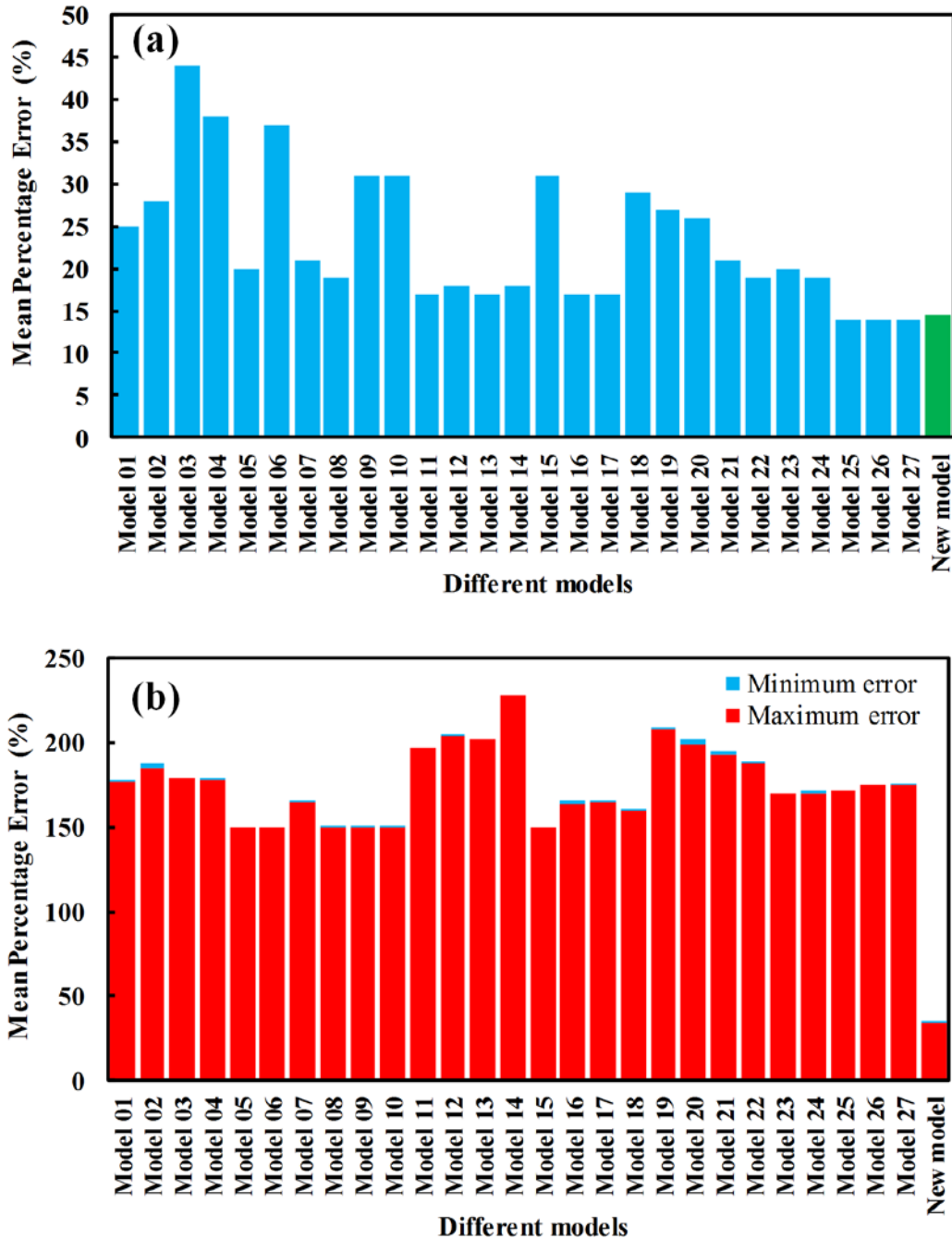


Figure 3-13. (a) Comparison of the mean errors of different models; and (b) comparison of the maximum and minimum mean errors of different models.

The prediction errors by the current model are also compared with those by other models as given in Table 3-5. The models are named from 1 to 27 in Table 3-5. Here, the prediction error is defined as $Error = |U_{inv}^{experimental} - U_{inv}^{model}| / U_{inv}^{experimental} \times 100$. Figure 3-13 (a) shows the comparison of the average error by the current model with the average errors of other 27 models. It can be found that the highest mean error is from Patwardhan and Tien (1985)'s

model, and the lowest mean error is 14% predicted by models 25, 26 and 27. The current model prediction error is 14.4 % which is inconsistent with the best available models in the literature. As shown in Figure 3-13 (b), previous models predict the inversion velocity in a wider range with maximum error at least 150% while the maximum error by the current model is 34.1%. Therefore, the current model's error distribution is narrower than previous models. This can be attributed to the fact that the current model does not need any empirical correlations for terminal velocity, void fraction, or Richardson and Zaki indexes as required in previous models. In addition, the current model can consider the effect of particle properties (size, density, and volume fraction) and liquid properties (density and viscosity). Therefore, the current model is more comprehensive with a better accuracy and reliability in predicting the inversion velocity than other models shown in Table 3-5.

3.6 Summary

In Summary, the CFD-DEM approach is applied to liquid-solid fluidized beds to investigate the layer inversion phenomenon. The force analysis revealed that the particle-fluid interaction force is responsible for the occurrence of layer inversion. When the liquid superficial velocity increases, the pressure gradient force decreases while the drag force decreases. However, for large particles, the rate of increasing the drag force cannot compensate the rate of decrease in pressure gradient force. Thus large particles move to the bottom of the bed at high velocity. At the inversion velocity, the amount of particle-fluid forces on the small and large particle are equal. Thus, there is no driving force for segregation and at this velocity two components are mixed uniformly. We also performed systematic studies to figure out how particle and liquid properties affect the inversion phenomenon. It was found that increasing in particles size and density ratios lead to a delay in layer inversion and in some cases no layer inversion happens. By increasing in liquid viscosity, the inversion velocity decreases while denser and hotter liquid increases the inversion point. It is found that

Chapter 3 Investigation of Causes of Layer Inversion and Prediction of Inversion Velocity in Liquid Fluidizations of Binary Particle Mixtures

the changes in inversion velocity due to changes in particles and liquid properties can be directly related to particle-fluid force on small and large particles.

The comparisons of different drag force correlations (Cello et al., 2010; Di Felice, 1994; Rong et al., 2014; Yin and Sundaresan, 2009) revealed that Di Felice model fails to reproduce this phenomenon, but Rong et al. (2014)'s model predicts the inversion velocity with better accuracy than other drag models. Nonetheless, Cello et al. (2010) and Yin and Sundaresan (2009) drag models also can reproduce the layer inversion with good agreements. A new mathematical model was proposed in this chapter in order to predict the inversion velocity. The model is based on the criterion that the ratio of dimensionless particle-fluid force on large particles to the dimensionless particle-fluid force on small particles is 1.0. The major advantage of this model is that it does not require correlations such as those needed to estimate terminal velocity, void fraction, and Richardson and Zaki indexes in previous models. The proposed model predicts the inversion velocity with the mean accuracy of 14.4 % which is the same of the best available model in the literature. In addition, the maximum error by the current model is just 34% which is much less than others.

Chapter 4 **CFD-DEM Modelling of Solid Flow Characteristics in Liquid Fluidizations of Ellipsoidal Particles**

4.1 Overview

In this chapter, CFD-DEM approach is used to investigate the hydrodynamics of non-spherical particles (ellipsoids in particular) in liquid fluidisations. The non-uniformity distributions of pressure gradient and porosity with bed height are successfully captured for ellipsoids at high liquid superficial velocities, consistent with those reported in the literature. The results also show that ellipsoids intend to enter the freeboard region and entrainment may occur. Disc-shape particles expand more significantly than spherical and elongated particles. The force analysis indicates that with particle aspect ratio deviating from 1.0, the drag force acting on ellipsoids increases while pressure gradient force reduces. Particle shape effects shown above are closely related to particle orientations which can significantly affect particle-fluid interaction force and particle terminal velocities.

4.2 Introduction

In most of the multiphase operations in liquid fluidized beds, particle properties such as size, density and shape may experience significant changes during the process because of attrition, coalescence, comminution or chemical reactions. The difference in particle properties can result in significant segregation problem in liquid fluidized beds.

Chapter 4 CFD-DEM Modelling of Solid Flow Characteristics in Liquid Fluidizations of Ellipsoidal Particles

To gain an understanding of liquid fluidisation behaviour, most studies, either experimentally or numerically, have focused on solid flow behaviour with mono-sized particles or mixtures with different particle sizes or densities. Mono-sized spherical particles make homogenous fluidized beds (Johnson, 1949; Wilhelm and Kwauk, 1948), and the bed expansion can be described by Richardson and Zaki (1954) correlation. Apart from homogenous/particulate flow regimes, other flow regimes such as wavy (Didwania and Homsy, 1981), aggregative/turbulent (Didwania and Homsy, 1981; Wilhelm and Kwauk, 1948), slugging (Lettieri et al., 2006), and bubbly (Didwania and Homsy, 1981) regimes can also be observed in liquid fluidized beds. Moreover, introducing a second or third components with a different size or density causes more complicated flow structures. Extensive efforts have been made in this direction to understand the principles of liquid fluidized beds of multicomponent mixtures of spherical particles (Di Felice, 1995; Didwania and Homsy, 1981; Escudié et al., 2006b; Gibilaro et al., 1986; Moritomi et al., 1982; Van Duijn and Rietema, 1982). As a result, various models have been proposed to quantify the solid-liquid fluidized bed characteristics (Asif, 2004; Escudié et al., 2006b; Moritomi et al., 1982).

In spite of substantial studies on the hydrodynamics of liquid fluidized beds, the effects of particles shape on the solid-liquid flow behaviour are still less reported. Except for two physical experiments (Barghi et al., 2003; Escudié et al., 2006a), the previous studies considered particles as spheres, and few studies have been remarked on liquid fluidization of non-spherical particles. However, particles are generally irregular in most of processes (Escudié et al., 2006a) such as ore beneficiations using liquid-solid fluidized beds separator (Tripathy et al., 2017). Barghi et al (2003) observed that cylindrical particles with the length/diameter ratio $L/D = 1$ were mixed well with spherical particles, but elongated cylindrical particles with $L/D = 2$ segregated from spherical particles. Escudie et al. (2006a) reported that differences in particle shape can result in segregation for binary mixtures of particles with the same volume and density. Epstein et al.

(1981) demonstrated that the serial model (Epstein et al., 1981) was able to predict bed expansions for binary and ternary mixtures of different particle shapes. These observations show that particle shape can cause different flow behaviour in liquid fluidizations rather than that observed for ideal spherical particles. However, the answers to some fundamental questions such as how and why particle shape affects flow phenomena are not clear, and hence still poorly understood.

In recent years, mathematical modelling, typically based on the CFD-DEM approach, has increasingly become an efficient tool to study fluidisations. CFD-DEM has been verified as one of the most effective approaches to study the fundamentals of granular materials (Zhu et al., 2007), and it provides some fundamental concepts of flow regimes in fluidized beds. Therefore, in this chapter, CFD-DEM is used to examine the effects of particle shape on the flow characteristics in liquid fluidizations. In the simulations, ellipsoidal particles are used as they can represent a wide range of particle shapes from oblate to prolate particles. Different aspect ratios varying from 0.28 to 5.33 are employed, and results are analysed mainly in terms of particle flow patterns, pressure drop, and bed expansion. In addition, force and particle orientation analysis are also conducted to examine the effect of particle shape and explain the occurrence of entrainment phenomenon.

4.3 Model Descriptions

The CFD-DEM approach has been well developed and documented in the literature (Feng et al., 2004; Xu and Yu, 1997; Zhou et al., 2010), and its extension to coarse (Zhou et al., 2011; Zhou et al., 2009) and fine (Gan et al., 2016; Gan et al., 2017) ellipsoidal particles has been presented for gas fluidizations. In this work, it is further extended to liquid fluidizations. For convenience, the model is briefly given below.

4.3.1 CFD-DEM governing equations for ellipsoids

The particle phase in the particle-fluid flow is considered as a discrete phase. According to the DEM (Cundall and Strack, 1979), a particle can have two types of motions: translational and rotational, which are determined by Newton's second law of motion. The governing equations for the translational and rotational motion of particle i with radius R_i , mass m_i , and moment of inertia I_i can be written as:

$$\frac{m_i d\mathbf{v}_i}{dt} = \sum_{j=1}^{k_i} (\mathbf{f}_{c,ij} + \mathbf{f}_{d,ij}) + \mathbf{f}_{pf,i} + m_i \mathbf{g} \quad (4-1)$$

and

$$I_i \frac{d\boldsymbol{\omega}_i}{dt} = \sum_{j=1}^{k_i} (\mathbf{M}_{t,ij} + \mathbf{M}_{r,ij} + \mathbf{M}_{n,ij}) \quad (4-2)$$

where m_i is the mass of the particle i , \mathbf{v}_i and $\boldsymbol{\omega}_i$ are translational and angular velocities of the particle i , k_i is the number of particles interacting with the particle i , $\mathbf{f}_{c,ij}$ and $\mathbf{f}_{d,ij}$ are elastic contact force and damping force, respectively. $\mathbf{f}_{pf,i}$ is the interaction force between particle and fluid, and $m_i \mathbf{g}$ is the gravitational force. I_i is the moment of inertia of particle i , and the torque acting on the particle i by particle j includes three components: $\mathbf{M}_{t,ij}$ which is generated by tangential force and causes the particle i to rotate, $\mathbf{M}_{r,ij}$ commonly known as the rolling friction torque, and $\mathbf{M}_{n,ij}$ is the torque generated by normal force when the normal force does not pass through the particle centre.

The liquid flow field is described by CFD on the basis of local-averaged Navier-Stokes equations (Anderson and Jackson, 1967; Gidaspow, 1994). Therefore, the mass and momentum conservation equations governing the liquid phase are respectively described as:

$$\frac{\partial(\varepsilon_f)}{\partial t} + \nabla \cdot (\varepsilon_f \mathbf{u}) = 0 \quad (4-3)$$

$$\frac{\partial(\rho_f \varepsilon_f \mathbf{u})}{\partial t} + \nabla \cdot (\rho_f \varepsilon_f \mathbf{u} \mathbf{u}) = -\nabla p - \mathbf{F}_{pf} + \nabla \cdot (\varepsilon_f \boldsymbol{\tau}) + \rho_f \varepsilon_f \mathbf{g} \quad (4-4)$$

where \mathbf{u} , ρ_f , p , and \mathbf{F}_{pf} are the fluid velocity, fluid density, pressure, and volumetric fluid-particle interaction force, respectively; $\boldsymbol{\tau}$ and ε_f are the fluid viscous stress tensor and porosity which are given as $\boldsymbol{\tau} = \mu_e [(\nabla \mathbf{u}) + (\nabla \mathbf{u})^{-1}]$ and $\varepsilon_f = 1 - \sum_{i=1}^{k_i} V_i / \Delta V$, where V_i is the volume of particle i (or part of the volume if particle is not fully in the CFD cell), k_i is the number of particles in the computational cell. μ_e is the fluid effective viscosity determined by $k-\varepsilon$ the model (Launder and Spalding, 1974) which has been used in our previous work (Gan et al., 2017; Zhou et al., 2011; Zhou et al., 2009). The volumetric fluid-particle interaction force in a computational cell volume of ΔV is calculated by $\mathbf{F}_{pf} = (\sum_{i=1}^{k_i} \mathbf{f}_{pf,i}) / \Delta V$, where $\mathbf{f}_{pf,i}$ is the particle-fluid interaction force on the particle i .

4.3.2 Particle-particle and particle-fluid interaction forces

The equations to calculate contact forces and torques between two spheres have been well established (Zhu et al., 2007), and also extended to ellipsoidal particles (Gan et al., 2016; Zhou et al., 2011). Zheng et al. (2013) proved that the normal and tangential contact force models used for spheres are also valid for ellipsoids. In addition, since ellipsoids provide smooth/continuous surfaces, the same Coulomb condition or sliding/rolling friction models as used for spheres can

also be applied. The equations used in this work to calculate the inter-particle forces and torques are listed in Table 4-1.

Table 4-1. Equations to calculate forces and torques acting on the particle i .

Forces or torques	Equations
Normal elastic force, $\mathbf{f}_{cn,ij}$	$-4/3E^* \sqrt{R^*} \delta_n^{3/2} \mathbf{n}$
Normal damping force, $\mathbf{f}_{dn,ij}$	$-c_n (8m_{ij} E^* \sqrt{R^*} \delta_n)^{1/2} \mathbf{v}_{n,ij}$
Tangential elastic force, $\mathbf{f}_{ct,ij}$	$-\mu_s \mathbf{f}_{cn,ij} (1 - (\delta_t / \delta_{t,max})^{3/2}) \hat{\delta}_t$
Tangential damping force, $\mathbf{f}_{dt,ij}$	$-c_t (6\mu_s m_{ij} \mathbf{f}_{cn,ij} \sqrt{1 - \delta_t / \delta_{t,max}} / \delta_{t,max})^{1/2} \mathbf{v}_{t,ij}$
Coulomb friction force, $\mathbf{f}_{t,ij}$	$-\mu_s \mathbf{f}_{cn,ij} \hat{\delta}_t$
Torque by tangential forces, $\mathbf{M}_{t,ij}$	$\mathbf{R}_{c,ij} \times (\mathbf{f}_{ct,ij} + \mathbf{f}_{dt,ij})$
Torque by normal forces, $\mathbf{M}_{n,ij}$	$\mathbf{R}_{c,ij} \times (\mathbf{f}_{cn,ij} + \mathbf{f}_{dn,ij})$
Rolling friction torque, $\mathbf{M}_{r,ij}$	$\mu_{r,ij} \mathbf{f}_{n,ij} \hat{\omega}_{ij}^n$

Where $1/m_{ij} = 1/m_i + 1/m_j$, $R^* = 1/(2\sqrt{A'B'})$, $E^* = E/(2(1-\nu^2))$, $\hat{\omega}_{ij}^n = \omega_{ij}^n / |\omega_{ij}^n|$, $\hat{\delta}_t = \delta_t / |\delta_t|$,
 $\delta_{t,max} = \mu_s(2-\nu) / 2(1-\nu)\delta_n$, $\mathbf{v}_{ij} = \mathbf{v}_j - \mathbf{v}_i + \omega_j \mathbf{R}_{c,ji} - \omega_i \mathbf{R}_{c,ij}$, $\mathbf{v}_{n,ij} = (\mathbf{v}_{ij} \cdot \mathbf{n}) \mathbf{n}$, $\mathbf{v}_{t,ij} = (\mathbf{v}_{ij} \times \mathbf{n}) \times \mathbf{n}$.
 Note that tangential force ($\mathbf{f}_{ct,ij} + \mathbf{f}_{dt,ij}$) should be replaced by $\mathbf{f}_{t,ij}$ when $\delta_t \geq \delta_{t,max}$.

Various forces have been identified to determine interactions between particles and liquid, including the drag force, the pressure gradient force, the virtual mass force, the Basset force, the Saffman force, and the Magnus force (Zhu et al., 2007). Comprehensive discussions have been made by Di Renzo et al. (2007) that except for the drag force and the pressure gradient force, other types of particle-fluid interaction forces can be ignored in the simulations of liquid fluidizations. This is due to the fact that the equations of these forces were developed mainly

Chapter 4 CFD-DEM Modelling of Solid Flow Characteristics in Liquid Fluidizations of Ellipsoidal Particles

based on single-particle/dilute systems or under simplified fluid flow conditions (e.g., creeping flow), hence their applicability is questionable (Clift et al., 1978). Moreover, such forces have been ignored in many studies in the literature, demonstrating that the reliable and consistent results with experiments can be generated (Cornelissen et al., 2007; Di Renzo et al., 2011; Di Renzo and Di Maio, 2007; Ehsani et al., 2016; Ghatage et al., 2014; Lettieri et al., 2006; Peng et al., 2016; Reddy and Joshi, 2009; Yang and Duan, 2013). Hence, in this work, only the drag force $\mathbf{f}_{d,i}$ and the pressure gradient force ($\mathbf{f}_{pg,i} = -V_i \nabla P$) are considered and included in the present CFD-DEM model.

Different correlations have been proposed to calculate the drag force on spheres (Zhu et al., 2007). In particular, the approach proposed by Di Felice (1994) is one of the most popular ones (Feng et al., 2004; Xu and Yu, 1997; Zhou et al., 2011), and also suitable for ellipsoids as demonstrated in our previous work (Zhou et al., 2011). Therefore, this method is still used, and the equation is written as (Di Felice, 1994):

$$\mathbf{f}_{d,i} = 0.5 \times C_D \rho_f A_{\perp} \varepsilon_f^2 |\mathbf{u}_i - \mathbf{v}_i| (\mathbf{u}_i - \mathbf{v}_i) \varepsilon_f^{-\gamma} \quad (4-5)$$

where $\gamma = 3.7 - 0.65 \exp[-(1.5 - \log_{10} \text{Re}_i)^2 / 2]$, A_{\perp} is the cross-sectional area perpendicular to the fluid flow, Re_i is the relative Reynolds number, which is defined as $\text{Re}_i = \rho_f d_v \varepsilon_f |\mathbf{u}_i - \mathbf{v}_i| / \mu_f$, where d_v is the equivalent diameter defined as the diameter of a sphere with the same volume as the ellipsoid particle. C_D is the drag coefficient, which can be calculated by different models as briefly discussed below.

Considerable investigations have been made to determine the drag coefficient C_D for non-spherical particles, with shapes varying from cubes and cylinders to ellipsoids and more generally

irregular shapes (Ganser, 1993; Haider and Levenspiel, 1989; Hölzer and Sommerfeld, 2008; Militzer et al., 1989; Ouchene et al., 2016; Richter and Nikrityuk, 2012; Yow et al., 2005). Based on the work by Sommerfeld and Lain (2008) that Ganser's (1993) correlation over-predicts the particle average velocity, Holzer and Sommerfeld (2008) used a large number of experimental data from literature and performed numerical study as well to propose a correlation for C_D which is applicable over a wide range of Re numbers, and also considers the effects of both particle shape and orientation. This has been verified by Hilton et al. (2010), Zhou et al. (2011), and Rong et al. (2015). Therefore, this correlation (Hölzer and Sommerfeld, 2008) is used in this work to calculate the drag coefficient expression C_D on an ellipsoidal particle, and given as:

$$C_D = \frac{8}{\text{Re}_{p,i}} \frac{1}{\sqrt{\phi_{\perp}}} + \frac{16}{\text{Re}_{p,i}} \frac{1}{\sqrt{\phi}} + \frac{16}{\sqrt{\text{Re}_{p,i}}} \frac{1}{\phi^{3/4}} + 0.42 \times 10^{0.4(-\log \phi)^{0.2}} \frac{1}{\phi_{\perp}} \quad (4-6)$$

where ϕ is the sphericity of an ellipsoid which is defined as the ratio of surface area of a sphere being equivalent volume of the ellipsoid to the surface area of the ellipsoid. ϕ_{\perp} is the crosswise sphericity, defined as the ratio between the cross-sectional area of the volume equivalent sphere and the projected cross-sectional area (A_{\perp}) of the considered particle.

4.3.3 Particle-particle contact detection and particle orientation

The particle-particle contact point detection for non-spherical particles is much more complicated and time-consuming than spheres. Different analytical methods can be found in the literature (Dziugys and Peters, 2001; Lu et al., 2015) to determine the contact points of ellipses or ellipsoids, including intersection algorithm, geometric potential algorithm, and common normal algorithm. Dziugys and Peters (2001) reported that geometric potential algorithm provides more accuracy as well as efficiency, so it has been employed in the most of the previous work

(Džiugys and Peters, 2001; Lin and Ng, 1997; Zhou et al., 2011) and also in this work. It is worth mentioning that the algorithm to detect one contact point involves the numerical solutions of a sixth-order polynomial equation. Thus, the computational time required to determine all detection points is huge.

Besides, particle orientation is one of the main differences in the modeling of spherical and non-spherical particles and must be considered. It can be generally described by the three Euler angles (ϕ, θ, ψ) (Goldstein, 1980). To determine the inertia tensor I_i of an ellipsoid conveniently, at each time step, the rotational equation given by Eq. (2) in the space-fixed coordinate system (x, y, z) is converted to the body-fixed coordinate system (x', y', z') , which is a moving Cartesian coordinate system fixed with the particle and whose axes are superposed by the principal axes of inertia. Therefore, the calculation of angular velocities ω'_i of particles would be the same as spheres. They are then used to determine the new three Euler angles on the basis of the so-called quaternion method (for more details see the refs: Džiugys and Peters, 2001; Goldstein, 1980).

4.3.4 CFD-DEM coupling methodology

In the CFD-DEM coupling technique, the particle motions are determined by Newton's second law of motion at a particle scale, and the continuum fluid flow is described on the basis of local-averaged Navier-Stokes equations at a CFD computational cell level. The coupling methodology of two phases at different scales has been well established and documented in the literature for spheres (Feng et al., 2004; Xu and Yu, 1997) and extended to ellipsoids (Gan et al., 2017; Zhou et al., 2011), and hence still used in the current work. In this coupling method, at each time step, DEM gives positions and velocities of individual particles, so the porosity and volumetric particle-fluid forces in a computational cell are evaluated. CFD will then use this

information to calculate the fluid flow field. The fluid flow data will be used in the next time step to determine the particle-fluid forces acting on an individual particle, resulting in the determination of new position and velocity of solids for the next time step.

4.4 Simulation Conditions

For the comparison purpose, the simulation conditions are set similar to the experimental work conducted by Escudie et al. (2006a). To reduce the number of particles, the cylindrical column is replaced by a slot with periodic boundary conditions applied to the front and rear walls to eliminate wall effect. For this geometry, 2-D CFD and 3-D DEM are used, which was successfully employed in the previous studies (Feng et al., 2004; Zhou et al., 2011). The poured packing method (Zhang et al., 2001) is used to generate the fixed bed. In this method, random velocities and orientation are assigned to each ellipsoid, and then particles fall from a certain height under gravity. The settling process continues until all particle velocity approaches to zero. Then, the packed bed is used to inject liquid uniformly from the bottom of the bed. The steady state condition is achieved when the pressure drop and bed voidage fluctuates around their mean values. No-slip boundary condition is applied to the interaction between wall and liquid phase. For the collisions between particles and side walls, walls are considered as a particle with infinite diameter. The physical and geometrical parameters implemented in the present simulations are listed in Table 4-2.

Particles with different shapes from oblate to prolate are generated with varying aspect ratio of spheroids. Spheroids, as shown in Figure 4-1, are composed of three radii: a is assigned to the radius in the polar direction, and b and c are considered as the radii in the equatorial plane. Therefore, the particle aspect ratio (AR) is defined as: $AR = c/a$. Consequently, $AR > 1$

Chapter 4 CFD-DEM Modelling of Solid Flow Characteristics in Liquid Fluidizations of Ellipsoidal Particles

corresponds to prolate spheroids, $AR=1$ stands for spheres, and $AR<1$ is for oblate spheroids. Two key variables are examined in this work to make qualitative and quantitative comparisons with physical experiments. One is particle aspect ratio which varies from 0.28 to 5.33 (see Table 2), and the other is liquid superficial velocities (U_0) which are from 0.055 to 0.316 m/s, similar to the physical experiments (Escudié et al., 2006a).

Table 4-2. Parameters used in the present simulations.

Particle phase	
Density (ρ_p), $kg.m^{-3}$	2160.3
Equivalent diameter (d_p), mm	9.525, 9.461
Particle shape	Oblate, sphere, and prolate
Particle Aspect Ratio (AR), -	0.28, 0.5, 0.75, 1.0, 1.5, 2.5, 3.5, 5.33
Number of particles (N), -	4500
Young's modulus (E), $N.m^{-2}$	1.0×10^8
Poisson's ratio (ν), $N.m^{-2}$	0.3
Sliding friction coefficient (μ), -	0.1
Damping Coefficient (c_n), -	0.3
Time step (Δt), s	2.5×10^{-6}
Liquid phase	
Viscosity (μ_f), $kg.m^{-1}.s^{-1}$	0.001
Density (ρ_f), $kg.m^{-3}$	1000
Bed geometry	
Width (W), m	0.127
Height (H), m	3.0
Thickness (D), m	$4d_p$
Number of CFD cells ($n_x \times n_z$)	9×216
Bed distributor	Uniform
Time step (Δt), s	2.5×10^{-6}

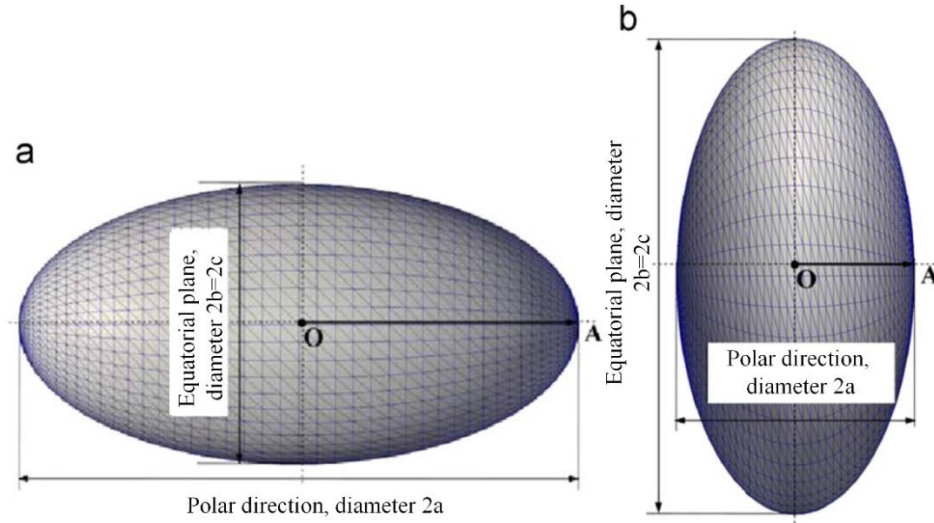


Figure 4-1. Illustrations of spheroids with different aspect ratios (AR): (a) oblate spheroid with $AR = 0.5$, and (b) prolate spheroid with $AR = 2$. The vector OA is used to represent particle orientation (O - particle mass centre; A - polar apex).

4.5 Results and Discussions

4.5.1 Flow patterns

Figure 4-2 shows the particle flow patterns in the beds containing oblate ($AR = 0.28$), spherical ($AR = 1$), and prolate ($AR = 3.5$) particles at different liquid superficial velocities. As an inherent characteristic of liquid fluidizations (Didwania and Homsy, 1981; Wilhelm and Kwauk, 1948), it can be seen that spherical particles expand homogeneously regardless of liquid superficial velocities (Figure 4-2(II)). In addition, the interface between the bed and the freeboard is clear, and no particles are entrained to the freeboard region. On the other hand, oblate and prolate particles (Figure 4-2(I) & (III)) intend to expand to higher heights compared to spheres. The interface is clear when liquid velocities are low. But it becomes difficult to distinguish the interface at high liquid velocities as some particles are carried to the freeboard. The entrainment phenomenon of disc-shaped particles captured is consistent with the observations by Escudie et al.

(2006a). In their experiments, however, they did not mention the entrainment of prolate particles (rod-like shape). The reason might be due to the fact that the maximum velocity used in their work was less than the terminal velocity that prolate particles need to enter the freeboard region.

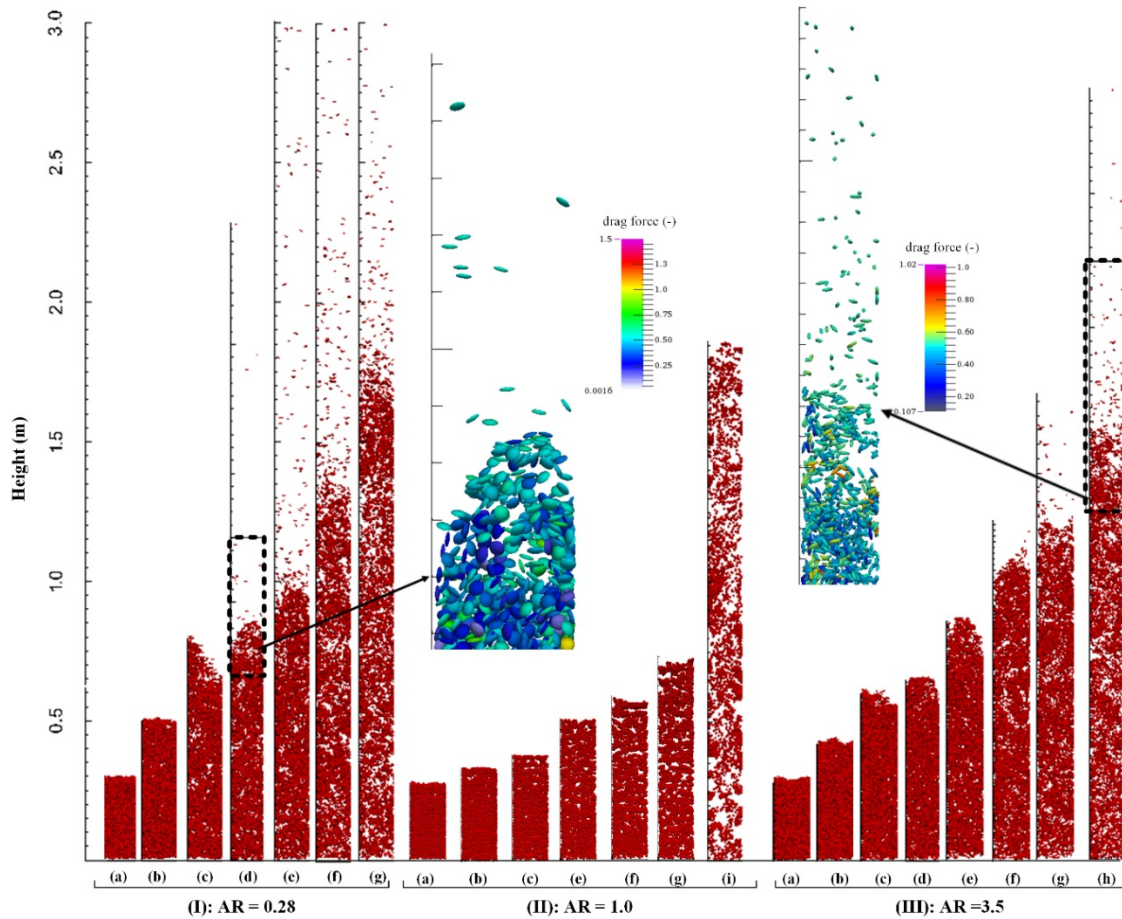


Figure 4-2. Particle configurations for different aspect ratios: (I) AR = 0.28, (II) AR = 1.0, and (III) AR = 3.5. For each aspect ratio, liquid superficial velocities used are: (a) 0.1 m/s, (b) 0.15 m/s, (c) 0.2 m/s, (d) 0.225 m/s, (e) 0.251 m/s, (f) 0.275 m/s, (g) 0.316 m/s, (h) 0.325 m/s, and (i) 0.47 m/s.

The macroscopic flow structures shown in Figure 4-2 are inherently related to microscopic characteristics of particles such as particle-fluid interaction force, particle-particle interaction force, and particle orientations. For example, the enlarged section of beds (the insets in Figure 4-2), which shows the entrainment of particles, indicates that particles in the dense beds receive different drag forces than those in the freeboard regions. Therefore, the force and particle

orientation analysis will be presented in the later sections to explain the occurrence of entrainment phenomenon as observed in Figure 4-2.

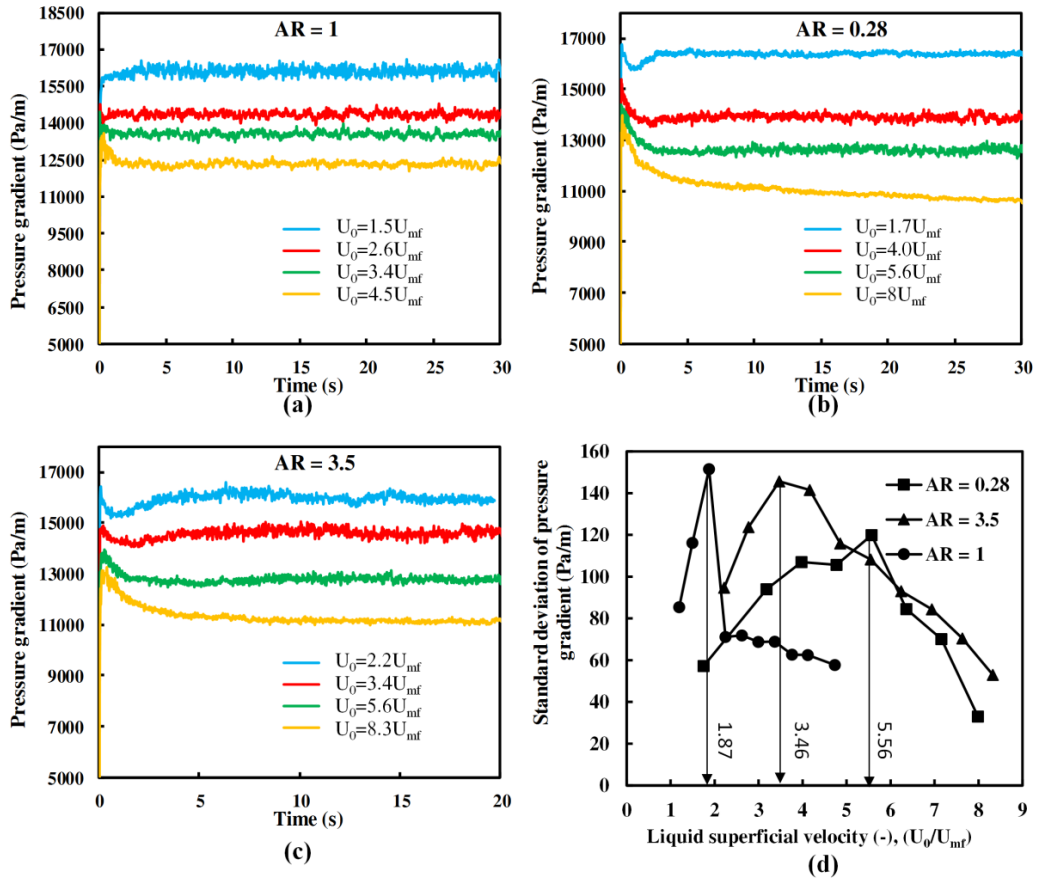


Figure 4-3. Effect of aspect ratio on the pressure drop variation with time and its corresponding standard deviation: (a) Spherical particles (AR = 1), (b) oblate particles (AR = 0.28), (c) prolate particles (AR = 3.5); and (d) variations of standard deviation with liquid superficial velocities for different particle shape.

4.5.2 Pressure drop

Pressure drop is an important characteristic of packed and fluidised beds. The pressure drop fluctuation has been employed as a tool to identify different flow regimes in fluidized beds (Fan et al., 1981; Felipe and Rocha, 2004; Trnka et al., 2000). Figure 4-3 shows the pressure gradient temporal variations for different particle shapes and liquid superficial velocities. It can be

Chapter 4 CFD-DEM Modelling of Solid Flow Characteristics in Liquid Fluidizations of Ellipsoidal Particles

observed that for spheres (Figure 4-3(a)), the pressure gradient jumps to a maximum quickly after injecting fluids and then fluctuates around a mean value. However, for oblate and prolate particles (Figure 4-3(b) and (c)), it takes a longer time to reach the stable condition, with the pressure gradient falling down gradually, and then fluctuating in a mean value.

The standard deviations of the pressure gradient as a function of liquid superficial velocities are plotted in Figure 4-3(d). It can be observed that for all aspect ratios, the standard deviation of pressure gradient firstly increases with liquid velocities to reach a maximum, and then decreases. This trend was also reported in the study of gas-solid fluidized beds (Fan et al., 1981; Gopalan et al., 2016; Ishii and Horio, 1991), and the velocity at which maximum standard deviation occurs corresponds to the velocity so-called transition velocity between slugging fluidization and turbulent fluidization (Ishii and Horio, 1991). However, the flow regimes in liquid fluidizations are quite different from that in gas-fluidized beds. Liquid fluidized beds generally present uniform bed expansion which is called smooth/particulate fluidizations (Didwania and Homsy, 1981). Depending on the particle and liquid properties, other types of regimes such as wavy, turbulent, and bubbly flow pattern might be observed (Didwania and Homsy, 1981). For the simulation conditions considered in this work (similar to those used in the experiments (Escudié et al., 2006a)), the wavy and bubbly flow regimes are not observed. Therefore, two flow regimes can be identified by the transition velocities shown in Figure 4-3 (d): particulate and turbulent fluidizations. Furthermore, Figure 4-3 (d) shows that particle aspect ratio affects the transition velocities significantly. For example, the transition velocity for spheres is $1.87U_{mf}$ (U_{mf} - minimum fluidisation velocity); however, it increases to $3.46U_{mf}$ and $5.56U_{mf}$ for prolate particles (AR = 3.5) and oblate particles (AR = 0.28), respectively. This implies that oblate and prolate particles intend to enter into the turbulent fluidization regime at higher relative velocities

Chapter 4 CFD-DEM Modelling of Solid Flow Characteristics in Liquid Fluidizations of Ellipsoidal Particles

(U_0/U_{mf}). The effect of particle aspect ratio on the transition velocity is further shown in Figure 4-4. Clearly, spheres have the lowest relative transition velocity (U_{tran}/U_{mf}). As aspect ratio deviates from 1.0, the transition point moves to relatively higher velocities, and this effect is more significant for oblate particles.

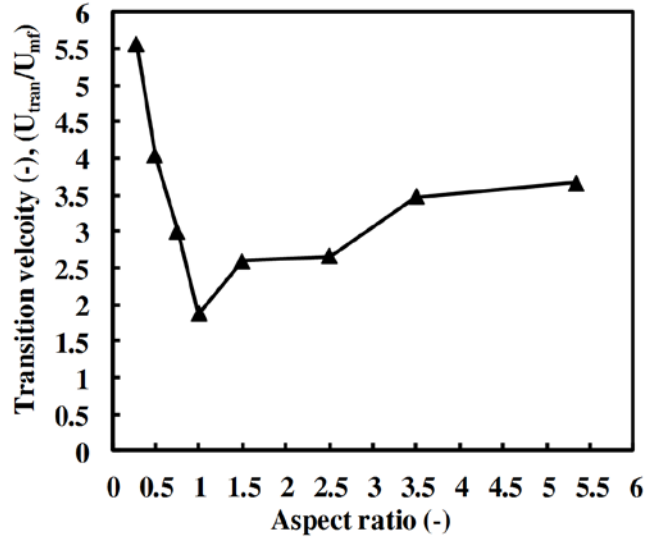


Figure 4-4. The effect of aspect ratio on the transition velocities from particulate fluidisation to turbulent fluidisation.

The pressure drop-liquid superficial velocity curves are plotted in Figure 4-5 for different particle aspect ratio. Note that the pressure drop is non-dimensionalised by bed weight. Generally, with increasing the liquid velocity, the pressure drop increases. After the U_{mf} , the pressure drop fluctuates around 1.0, balancing the bed weight. The figure also shows that at the same liquid velocity, spheres generate less pressure drop in packed beds than oblate and prolate particles. This indicates that spheres exhibit high permeability, which also was reported in the literature (Gan et al., 2016). Figure 4-6 shows the effect of aspect ratio on U_{mf} , indicating that with decreasing aspect ratio from 1, U_{mf} decreases significantly. For prolate particles, U_{mf} decreases sharply first with aspect ratio, and then slightly. Spheres have the highest U_{mf} . This could be due

to the enhanced projected area of ellipsoids in packed beds, and consequently larger particle-fluid interaction force on ellipsoids when particles distort from the spherical shape.

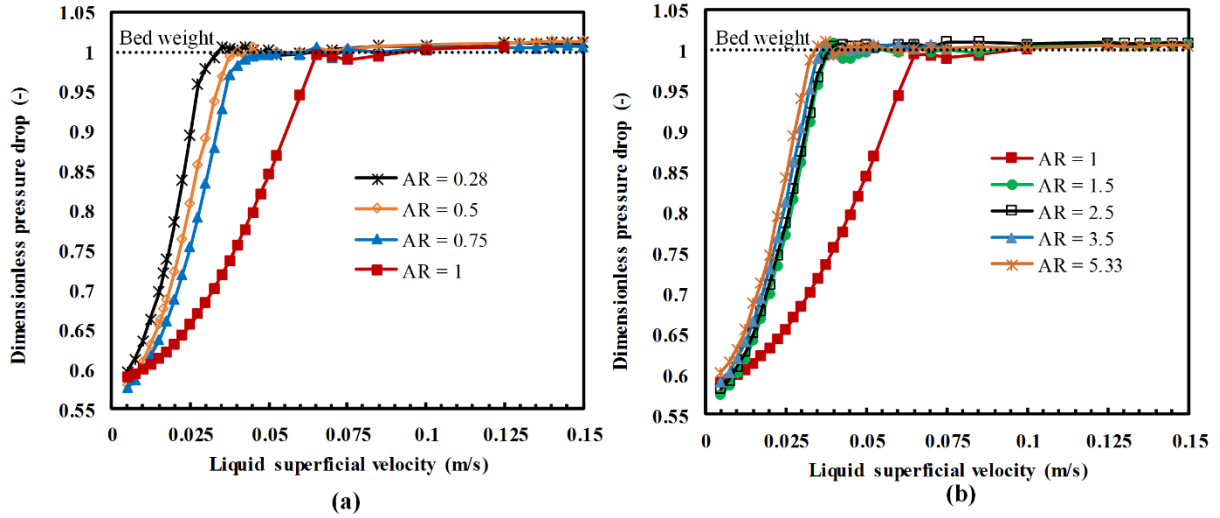


Figure 4-5. Dimensionless pressure drop variations as a function of liquid superficial velocities: (a) Oblate spheroids ($AR \leq 1.0$), and (b) prolate spheroids ($AR \geq 1.0$).

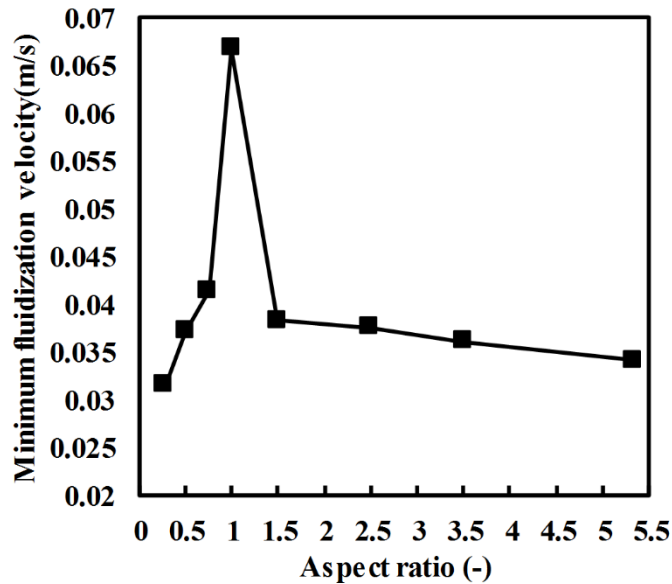


Figure 4-6. Effect of particle aspect ratio on the minimum fluidization velocity.

Figure 4-7 demonstrates the time-averaged pressure gradient variations with bed height for different particle shapes at two different liquid velocities ($U_0 = 0.1$ m/s and 0.251 m/s). Note that the pressure gradient used here does not include the hydrostatic pressure gradient. At low U_0 (Figure 4-7 (a-c)), except the bed surface region, the pressure gradients along the bed height are largely uniform which denotes the homogenous distribution of particles. However, at high U_0 (Figure 4-7 (e-f)), particle shape affects the pressure gradient distributions significantly. For spheres, the pressure gradient still stays constant along the bed height. But for oblate and prolate particles, parentheses-shape relations can be observed, consistent with those reported (Escudié et al., 2006b). As shown in Figure 4-7 (d) and (f), the pressure gradient increases with the bed height to reach a maximum and then decreases. These parenthesis-shape pressure gradient profile for ellipsoids could be due to the simultaneous effect of liquid injection and the significant effect of particle shape on particle motions. Liquid injection from the bed bottom increases the local bed porosity but decreases the energy dissipations due to flowing liquid through the particles. Consequently, the pressure gradient is low near the bed bottom. However, as the liquid injection power is not strong enough to overcome particle interlocks due to non-sphericity of particles, particles are accumulated and locked in some regions above the distributor which results in high-pressure gradients. It is worth mentioning that the pressure gradient trends for oblate (Figure 4-7(d)) and prolate (Figure 4-7(f)) particles are similar which implies that particle distributions and pressure gradients are independent of particle shape types.

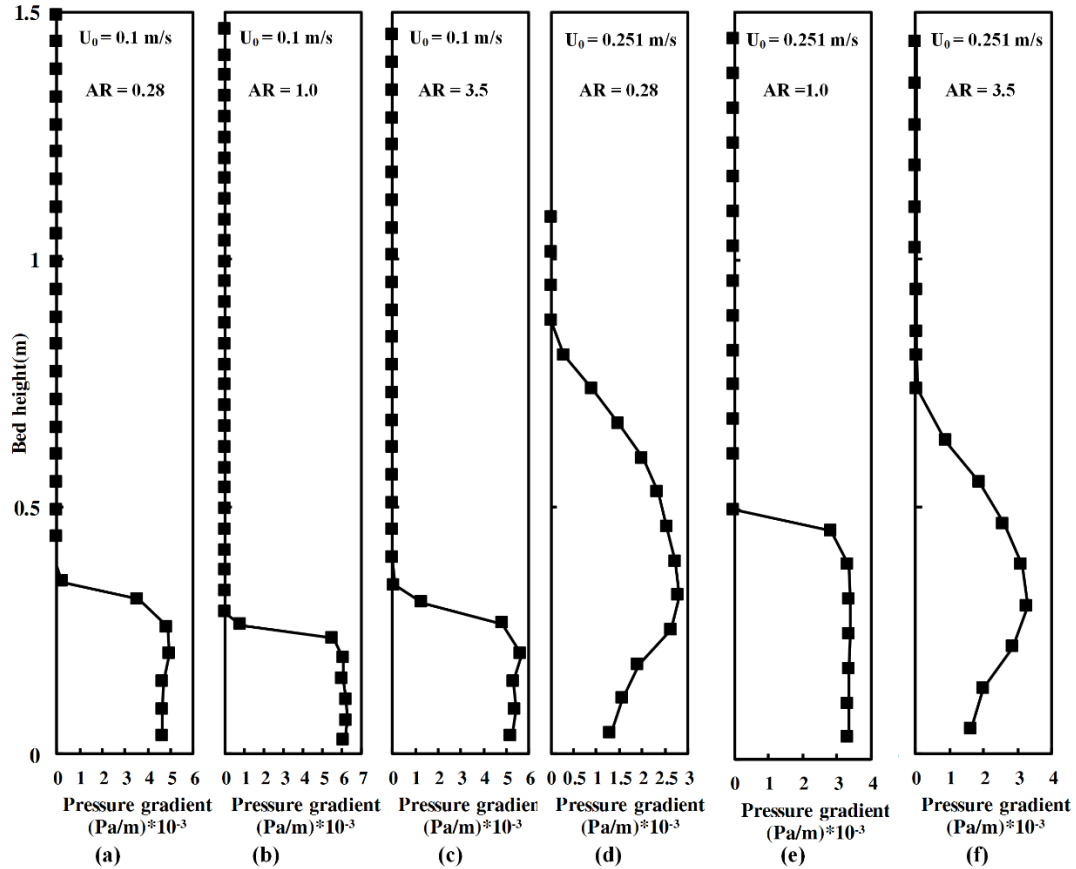


Figure 4-7. Time-averaged pressure gradient variations along the bed height for oblate (a, d), spherical (b, e), and prolate (c, f) particles at two different liquid superficial velocities: (a-c) 0.1 m/s, and (d-f) 0.251 m/s.

4.5.3 Bed expansion

The macroscopic behaviour of liquid fluidised beds can also be examined by the bed expansion analysis, which can provide useful information to understand the behaviour of binary mixtures, as shown by many investigators (Epstein and LeClair, 1985; Moritomi et al., 1982; Patwardhan and Tien, 1985). Figure 4-8 displays the bed porosity temporal variations for oblate (AR = 0.28), spherical (AR = 1), and prolate (AR = 3.5) particles at low ($U_0 = 0.1$ m/s) and high ($U_0 = 0.251$ m/s) liquid superficial velocities. At low U_0 , compared with spheres, oblate and prolate particles take a longer time to expand to a maximal height and then descend into a lower

height. This is caused by the fact that the interlock of ellipsoids increases and particles need more time to break the interlocks and expand. Once the bed becomes loose, the local voidage increases resulting in the deduction of the particle-fluid interaction force on particles. Finally, particles fall into their final steady condition. This behaviour was also reported by Ma et al. (2016) for fluidizing rod-shaped particles. However, at high U_0 (Figure 4-8(b)), such maximal bed height peak does not appear during the expansion process. This is because at a high liquid flow rate, the particle-fluid interaction force is strong enough to overcome the interlocks between particles at the early stage of bed expansion, and the beds can expand freely.

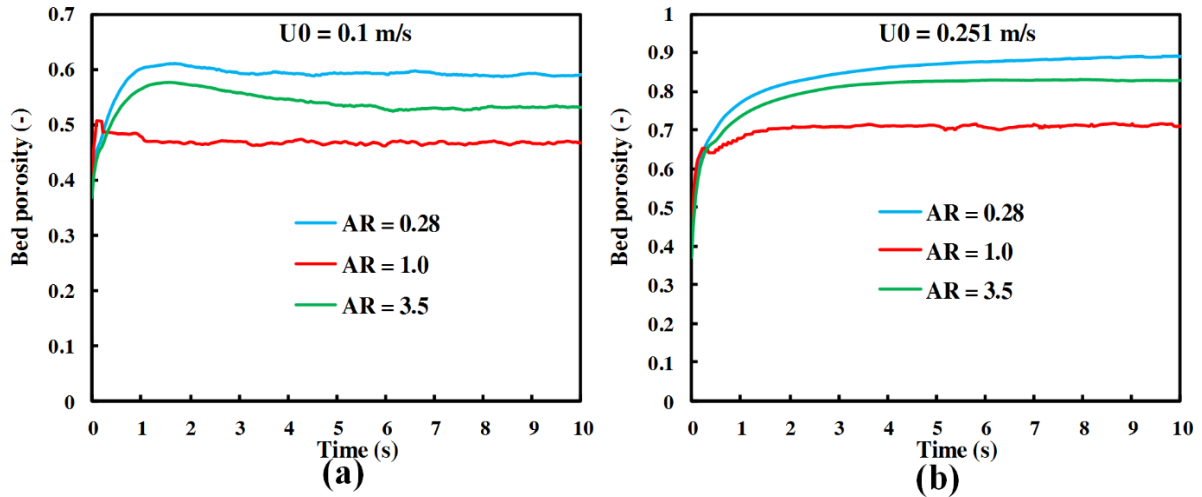


Figure 4-8. Transient bed expansion for different particle aspect ratios at two different liquid superficial velocities: (a) 0.1 m/s, and (b) 0.251 m/s.

The time-averaged bed voidage variations with bed height for different particle aspect ratio and liquid velocities are displayed in Figure 4-9, showing similar feature to the pressure gradient distribution. At low liquid velocities, porosity is almost constant for each aspect ratio, indicating that particles are distributed uniformly along the bed height (Figure 4-9(a-c)).

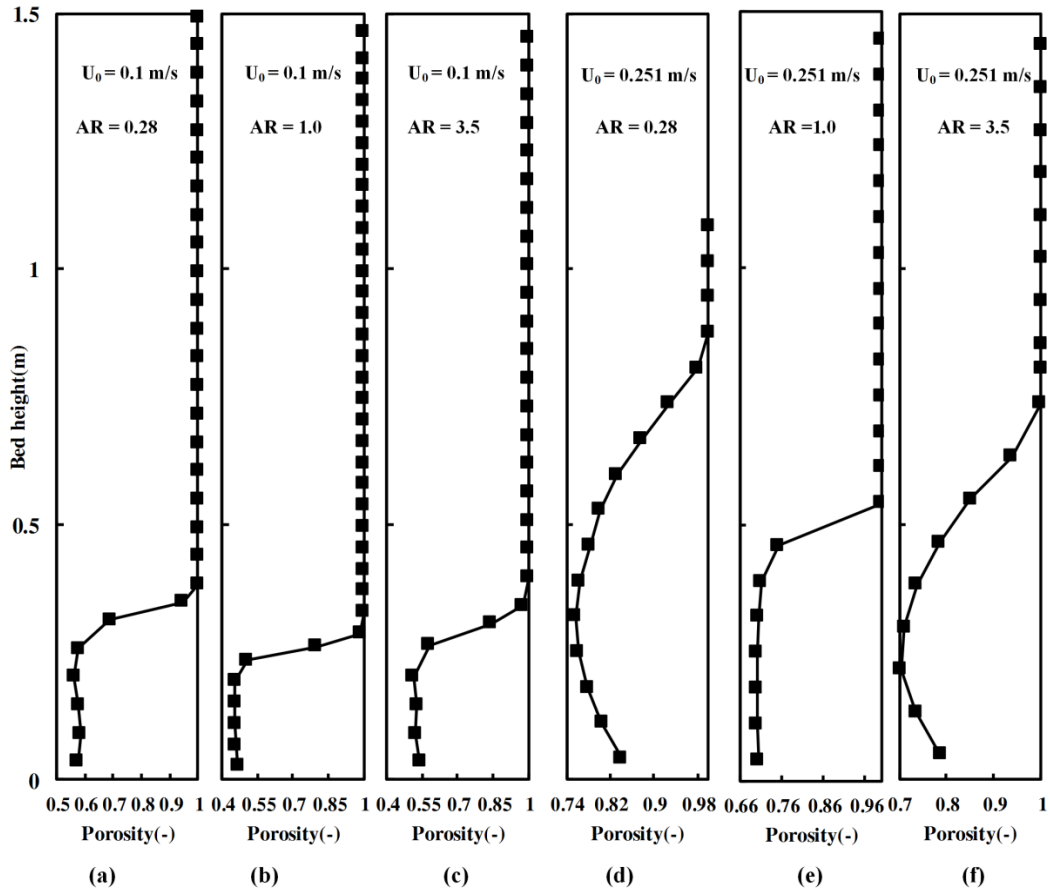


Figure 4-9. Time-averaged local voidage variations along the bed height for oblate (a, d), spherical (b, e), and prolate (c, f) particles at two different liquid superficial velocities: (a-c) 0.1 m/s, and (d-f) 0.251 m/s.

However, at a higher U_0 (Figure 4-9 (d-f)), the porosity distributions are strongly affected by aspect ratio. For spheres (Figure 4-9 (e)), the porosity does not vary with bed height. But for ellipsoids with aspect ratio at 3.5 (Figure 4-9 (f)), the porosity distribution changes to distorted parentheses-shape. The minimum porosity appears at the level of one-third of the bed height, which indicates that prolate particles are inclined to form clusters here. These clusters are mainly due to the interlocks among prolate particles. The high porosity at the bed bottom section indicates that due to liquid injection from the bed bottom, fewer particles rest at the distributor resulting in a higher void fraction. Oblate particles at the aspect ratio of 0.28 show the similar porosity distribution as prolate particles (Figure 4-9 (d)).

Chapter 4 CFD-DEM Modelling of Solid Flow Characteristics in Liquid Fluidizations of Ellipsoidal Particles

The time-averaged overall bed void fractions under different conditions are plotted in Figure 4-10. Figure 4-10 (a-c) show that the bed voidage predicted is in a good consistency with the experimental data reported by Escudie et al. (2006a). In Figure 4-10 (d), the effect of aspect ratio on porosity is presented at different liquid velocities. It is found that the porosity-AR relation shows ‘V’ shape in which minimum void fraction corresponds to spheres. When aspect ratio deviates from 1.0, the bed experiences large expansion with the bed voidage increasing gradually.

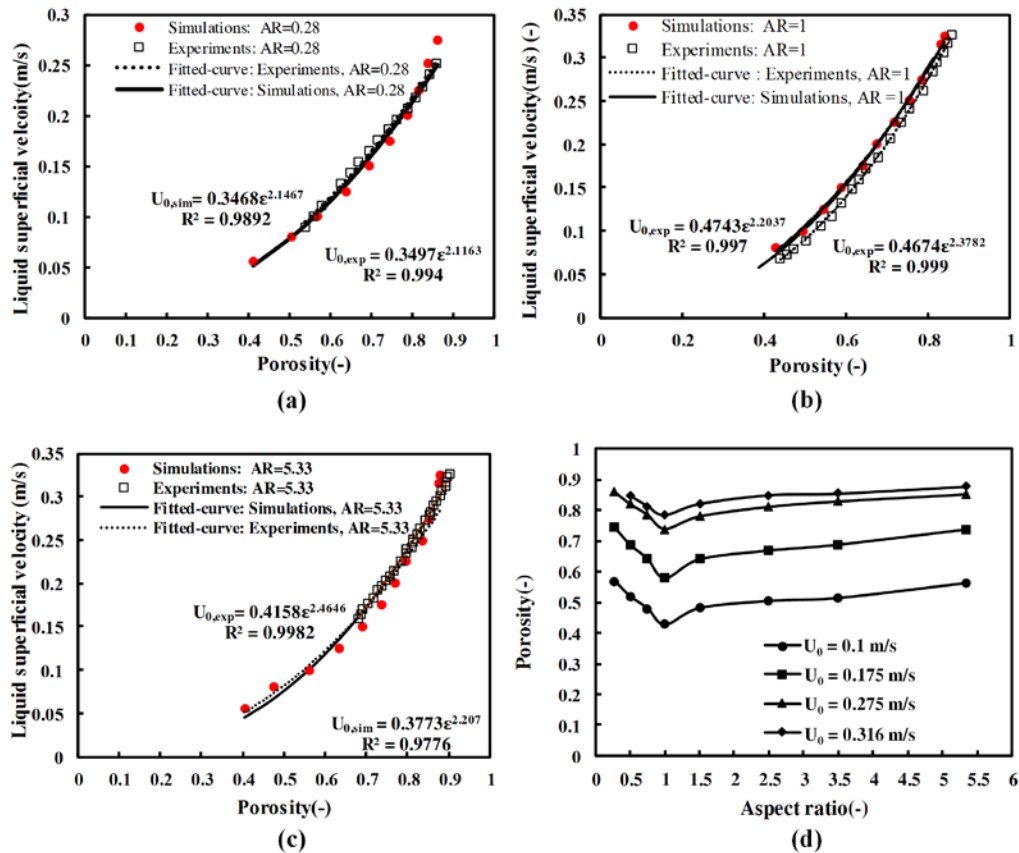


Figure 4-10. Bed expansion variations with liquid superficial velocities and aspect ratios: (a) oblate particles (AR=0.28), (b) spherical particles (AR=1), (c) prolate particles (AR=5.33), and (d) effects of aspect ratio on the bed expansion at different liquid superficial velocities.

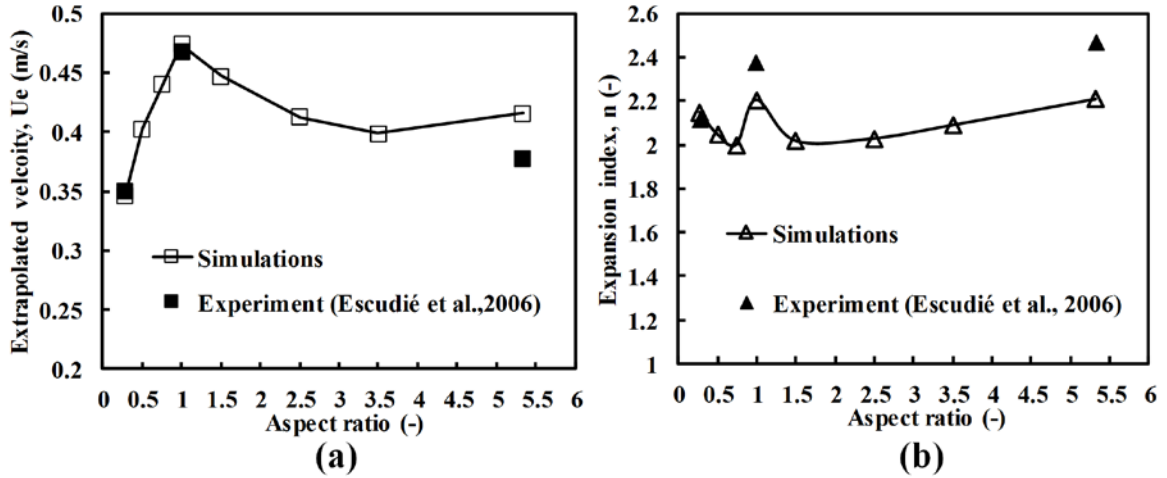


Figure 4-11. Richardson-Zaki's equation parameters as a function of aspect ratio: (a) extrapolated velocity U_e , and (b) expansion index (n).

In liquid fluidized beds of mono-sized spherical particles, the beds expand homogeneously. The bed expansion can be estimated by the well-known Richardson and Zaki (1954) equation $U_0/U_e = \varepsilon^n$, where U_e is the extrapolated value of U_0 in $\log(U_0)$ vs. $\log(\varepsilon)$ diagram when voidage approaches one, and n is the expansion index. The unknown variables of U_e and n can be calculated by fitting a power-law equation ($Y = aX^b$) on the data points of U_0 as a function of ε . These fitted curves are shown in Figure 4-10 (a-c) for both experimental data (Escudié et al., 2006a) and simulation results, and the calculated values of U_e and n are plotted in Figure 4-11. From this figure, it can be seen that the effects of particles shape on U_e and n are significant. The maximum U_e corresponds to spherical particles. With decreasing aspect ratio from 1.0 to 0.28, U_e decreases. On the other hand, prolate particles show a minimum at the aspect ratio of 3.5. Figure 4-11(b) also illustrates that the effect of particle aspect ratio on the expansion index is complicated. The simulation results have a good agreement with experiments in the prediction of

n for the aspect ratio of 0.28. But the model underestimates the values of n for spherical and prolate particles. However, the curve provides the general trend on how particle aspect ratio affects the expansion, providing useful information for understanding.

4.5.4 Force analysis

In essence, the beds behaviour for different shapes of the particle is determined by forces acting on particles, for example, the gravitational force, and interaction forces among particles, particles and fluid, and particles and walls. The analysis of these forces is helpful to understand the bed expansion and entrainment phenomenon under the influence of particle shape. Figure 4-12 shows the probability density distributions of various forces at $U_0 = 0.251 \text{ m/s}$ for different particle shapes. It can be found that the common characteristics of the force distributions is that most of them demonstrate unimodal distributions. For instance, Figure 4-12 (a) and (d) display that particles present normal distribution of drag force with the skewness is almost zero. For oblate particles (Figure 4-12 (a)), with decreasing aspect ratio from 1.0 to 0.5, the drag force distribution profile is not affected much by aspect ratio, but the magnitude increases significantly. With the further decrease in aspect ratio to 0.28, the distribution not only shifts to the right but also becomes wider with a lower peak. This implies that particles with lower aspect ratio intend to have a wide range of drag force. This could be due to the fact that more random orientations of particles generate a wide range of projected area, which affects the magnitude of drag force. For prolate particles (Figure 4-12 (d)), the similar trend can be observed.

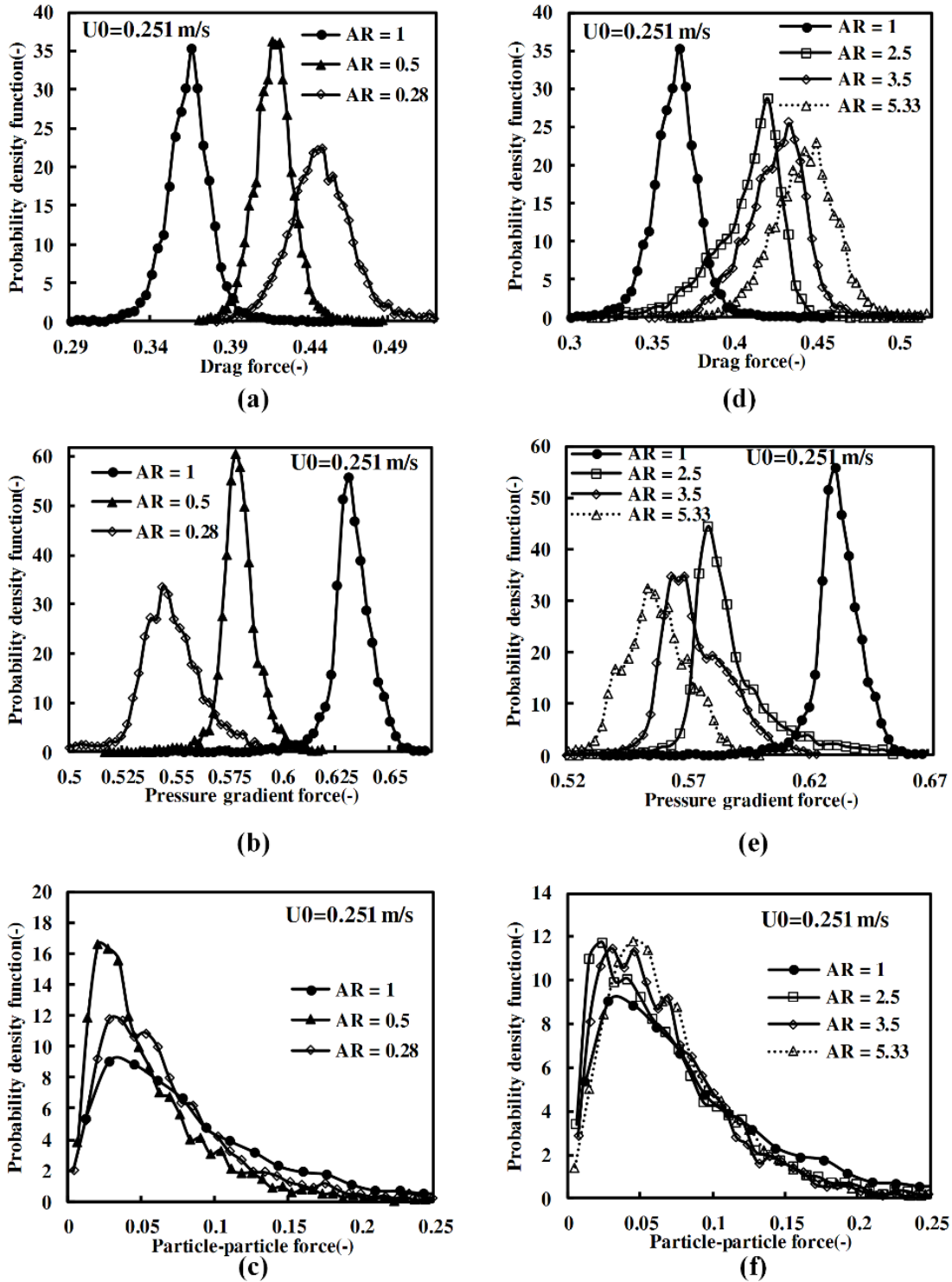


Figure 4-12. Effects of particle aspect ratio on the force probability density distribution at liquid superficial velocity of 0.251m/s: top two figures - drag force, middle two figures - pressure gradient force, and bottom two figures - particle-particle interaction force. Note that in the left column (a-c) are oblate particles, and in the right column (d-f) are prolate particles.

The pressure gradient force distributions in Figure 4-12 (b) and (e) illustrate that the pressure gradient force on spherical particles are more uniform than oblate and prolate particles. In addition, with increasing (Figure 4-12(b)) and decreasing (Figure 4-12(e)) aspect ratio, the pressure gradient force distributions shift to the left, indicating the decreased pressure gradient force, and particles experience a wider range of pressure gradient force. For particle-particle interaction force distributions, Figure 4-12 (c) and (f) show that all particle shapes express a non-symmetric distributions with long right-hand tails and maximum peak near the y-axis. This illustrates that most of the particles experience the low magnitude of particle-particle interaction force. For both oblate and prolate particles, the curves slightly shift to the left side and the peak values increases. This means that at the same liquid velocity, the beds of ellipsoids can expand more significantly and particles have more free space to move without severe interactions.

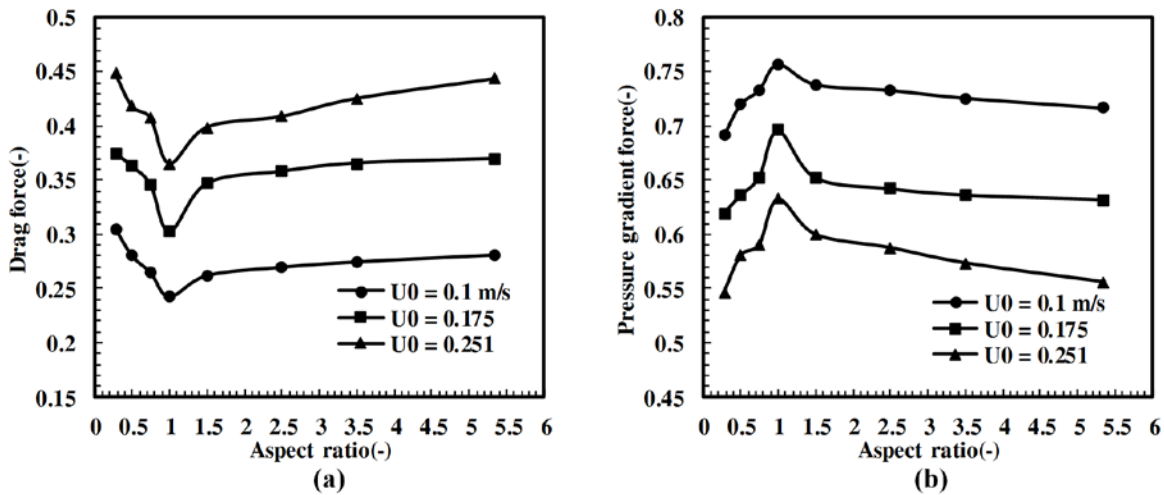


Figure 4-13. Effect of particle aspect ratio and liquid superficial velocities on spatial-temporal averaged forces: (a) drag force and (b) pressure gradient force.

The average values of drag force and pressure gradient force as a function of particle aspect ratio and liquid superficial velocity are shown in Figure 4-13. At a given U_0 , with increasing particle aspect ratio from 0.28 to 5.33, the drag force declines first and then increases with a

Chapter 4 CFD-DEM Modelling of Solid Flow Characteristics in Liquid Fluidizations of Ellipsoidal Particles

minimum occurring at $AR = 1$. Spheres have the minimum drag force. This is because the projected area increases when particles changes to oblate or prolate shapes. However, the projected area is also affected by particles orientations which will be discussed in the next section. The pressure gradient force curve shown in Figure 4-13(a) is opposite to drag force variations. The maximum pressure gradient force can be observed for spheres. This is because that at the given U_0 , spherical particles have a lower bed height and hence larger bed density than oblate and prolate particles.

The time-averaged force variations with bed height are examined at $U_0 = 0.251 \text{ m/s}$ and shown in Figure 4-14. For oblate particles ($AR = 0.28$), Figure 4-14 (a) shows that the mean drag force on an oblate particle along the bed height fluctuates smoothly around a mean value from the bed bottom to the height near the bed interface (displayed by vertical red dashed-line). But starting from the bed interface to higher heights, the mean drag force increases (this increasing trend has been found to be attributed to the particle orientation which will be discussed in the next section). On the other hand, the mean pressure gradient force on an oblate particle varies slightly with the bed height and it falls to lower values as it passes the bed interface (Figure 4-14 (b)). The growing trend of mean drag force and declining tendency of mean pressure gradient force on oblate particles passing the bed interface result in sufficient particle-fluid interaction force to balance the particle weight (Figure 4-14 (c)). This causes particles which have positive velocities and have passed the bed interface (Figure 4-14 (d)) to flee from the dense bed and enter the freeboard region. Hence, the entrainment occurs. The particle-particle (Figure 4-14 (e)) and particle-wall (Figure 4-14 (f)) interaction forces become zero as the freeboard region is dilute.

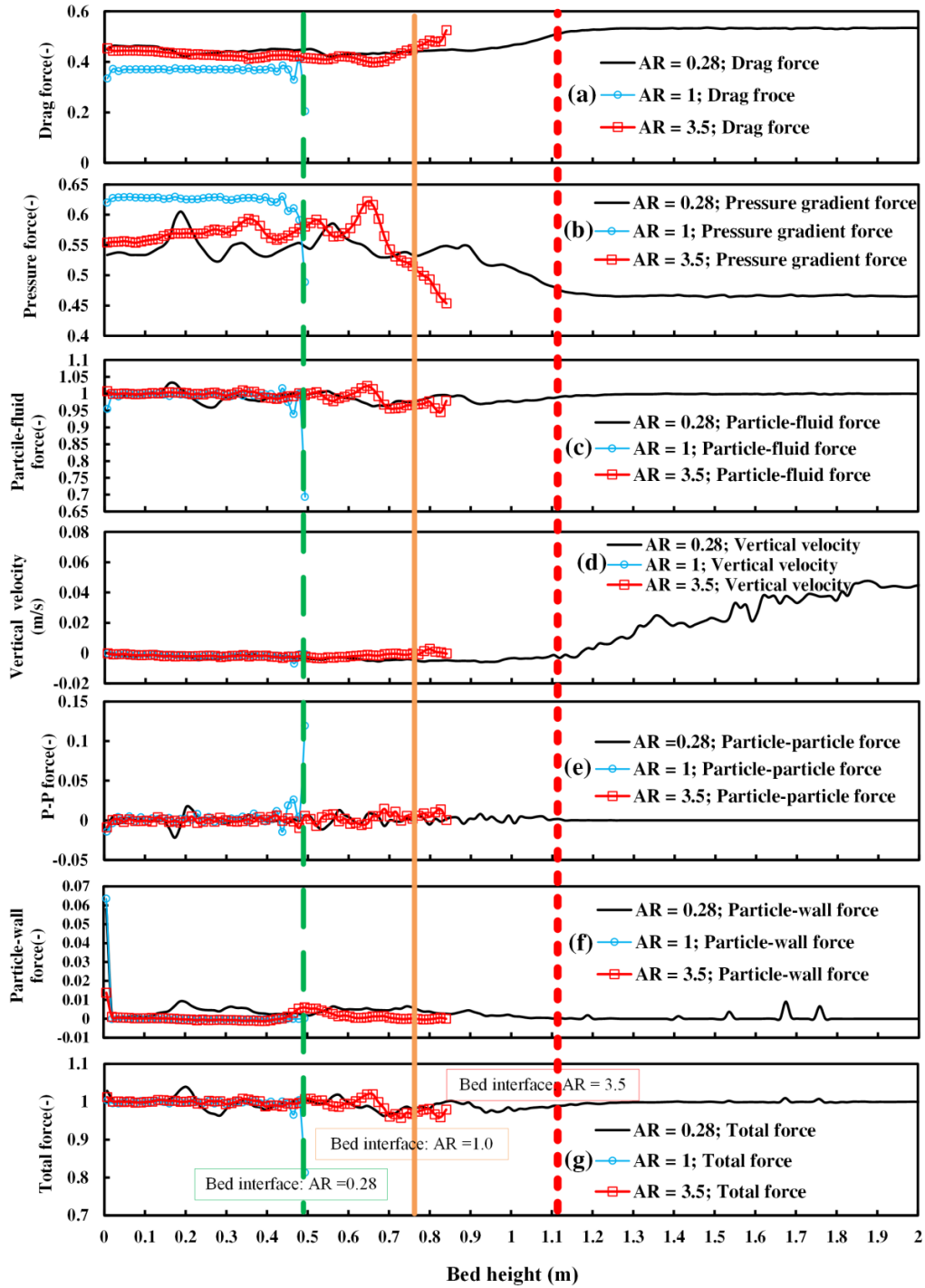


Figure 4-14. Time-averaged variations of different variables with bed height at liquid superficial velocity of 0.251 m/s: (a) drag force, (b) pressure gradient force, (c) particle-fluid interaction force, (d) particle vertical velocity, (e) particle-particle interaction force, (f) particle-wall interaction force, and (g) total force acting on particles. The red dash line – bed interface height for ellipsoids at AR = 3.5, brown dash line – bed interface height for spheres, and green dash line – bed interface for ellipsoids at AR = 0.28.

However, spherical and prolate particles ($AR = 3.5$) show quite a different behaviour at the same fluidization velocity. When a sphere approaches the bed interface, the mean drag force (Figure 4-14 (a)) rises slightly and pressure gradient force (Figure 4-14 (b)) decreases remarkably. As the declined pressure gradient force cannot be compensated by the slight increase in the drag force, spheres which cross the bed interface encounters a sharp decline in particle-fluid interaction force (Figure 4-14 (c)) which is the main driving force for the particle motion. Thus, these particles begin to deaccelerate and reduce the velocities (Figure 4-14 (d)) to zero and then negative values which lead them to return to the dense bed. An analysis of the mean force variations for prolate particles ($AR = 3.5$) also clearly reveals the similar phenomenon. Under this condition, the particle-fluid interaction force acting on the particle cannot be large enough to overcome the particle weight, so particles which have just passed the bed interface would return to the bed under the influence of gravitational force.

4.5.5 Particle orientation analysis

One key difference between spheres and ellipsoids is the particle orientation. Spheres do not present orientation due to the isotopic feature. However, ellipsoids can exhibit a wide range of orientation, which makes significant influences on the fluidization behaviour. Therefore, an analysis of particle orientation can provide information to explain the flow structures of ellipsoids. In this work, the angle between the vertical z-axis and **OA** shown in Figure 4-1 is defined as particle orientation angle (α). Note that **OA** is the vector from particle centre to the polar apex. Therefore, the orientation angle of 0° indicates that **OA** is parallel to the z-axis, and 90° indicates that **OA** is perpendicular to the z-axis. For convenience, all orientation angles varying from $90^\circ - 360^\circ$ are transformed to the angles between 0° to 90° . The angles can be calculated as $180^\circ - \alpha$ if $\alpha \in (90^\circ, 180^\circ)$, or $\alpha - 180^\circ$ if $\alpha \in (180^\circ, 270^\circ)$, or $360^\circ - \alpha$ if $\alpha \in (270^\circ, 360^\circ)$.

Chapter 4 CFD-DEM Modelling of Solid Flow Characteristics in Liquid Fluidizations of Ellipsoidal Particles

Figure 4-15 shows the temporal variations of the mean orientation angle of particles as a function of particle aspect ratio and liquid superficial velocity. At $U_0 = 0.1 \text{ m/s}$ (Figure 4-15 (a)), as expected, the orientation angle for spheres fluctuates around 45° due to the isotropic nature; however, this is not the case for oblate and prolate particles. Oblate particles ($AR = 0.28$) intend to increase the orientation angle from 27° at the early stage to reach a stable condition in which the mean angle oscillates around a mean value (36.7°). This implies that due to the interaction from the fluid, the disc-shaped particles become more inclined to its horizontal orientation. On the other hand, prolate particles ($AR = 3.5$) are more likely to be in the horizontal direction before introducing the liquid, then the mean angle decreases to a low constant value. This indicates that prolate particles intend to align their long axis direction parallel to the vertical z-axis. With the increase of U_0 to 0.251 m/s , prolate particles ($AR = 3.5$) have a larger mean angle (around 48° shown in Figure 4-15 (b)), indicating the tendency to become horizontally orientated. The mean orientation angle of oblate particles increases slightly with U_0 , indicating a slightly more random orientation.

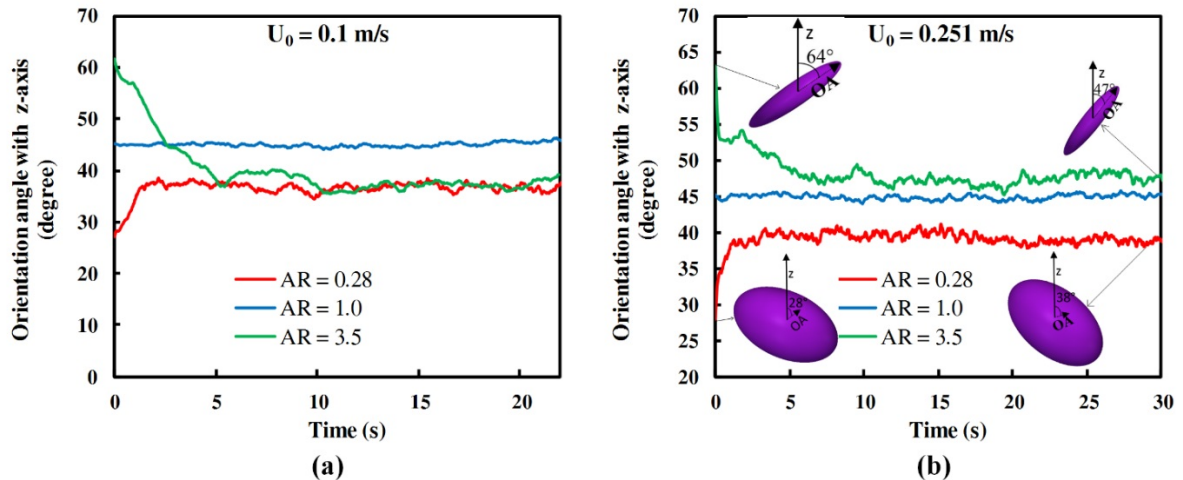


Figure 4-15. Variations of particle orientation with time for various aspect ratios at two different liquid superficial velocities: (a) 0.1 m/s , and (b) 0.251 m/s .

Figure 4-16 illustrates the mean orientation angle variations with particle aspect ratio at different liquid superficial velocities. At low U_0 (e.g., $U_0 = 0.1 \text{ m/s}$), with increasing aspect ratio from 0.28 to 1, the angle declines first and then increases with the minimum at $AR = 0.5$. But the minimum disappears gradually with increasing U_0 . Therefore, the less the aspect ratio, the more tendency for oblate particles to be in the horizontal position. On the other hand, with increasing aspect ratio to the values larger than 1.0, the orientation angle decreases which indicates that when particles get more elongated, they intend to be in the vertically-orientated direction. As U_0 increases, the beds expand and particles have more space to orient to their stable positions which is the horizontally orientated direction; thus the orientation angle grows. At $U_0 = 0.251 \text{ m/s}$, the orientation angle of prolate particles is apparently independent of aspect ratio.

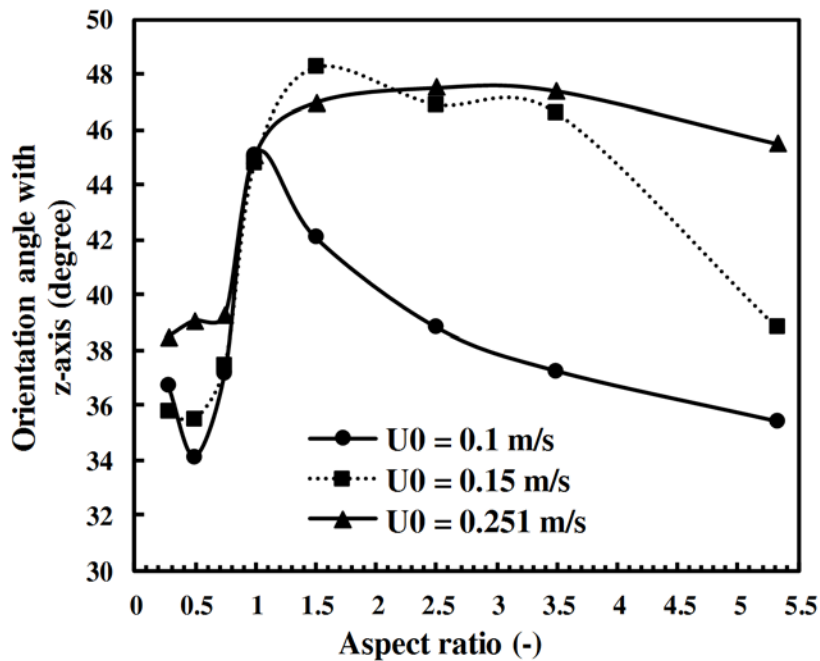


Figure 4-16. Effects of particle aspect ratio and liquid superficial velocities on the bed average orientation angle.

Figure 4-17 displays the mean orientation angle along the bed height for different aspect ratios. As shown in Figure 4-17 (a), the mean angle of oblate particles ($AR = 0.28$) in the bed

Chapter 4 CFD-DEM Modelling of Solid Flow Characteristics in Liquid Fluidizations of Ellipsoidal Particles

dense region is almost constant, fluctuating around a fixed value. However, when particles approach the bed interface, the angle decays sharply. This indicates that oblate particles move towards the top of the bed in a horizontally-oriented position. This is the reason that when oblate particles reach the region near the bed interface, they encounter high magnitude of drag force from the liquid (Figure 4-14 (a)). This indicates that how particle orientation can affect particle motions significantly. For spheres (Figure 4-17(b)), as expected, orientation angle is constant at different heights. For prolate particles, Figure 4-17 (c) shows that the orientation angle increases in the bed interface region, indicating that prolate particles prefer to orient horizontally.

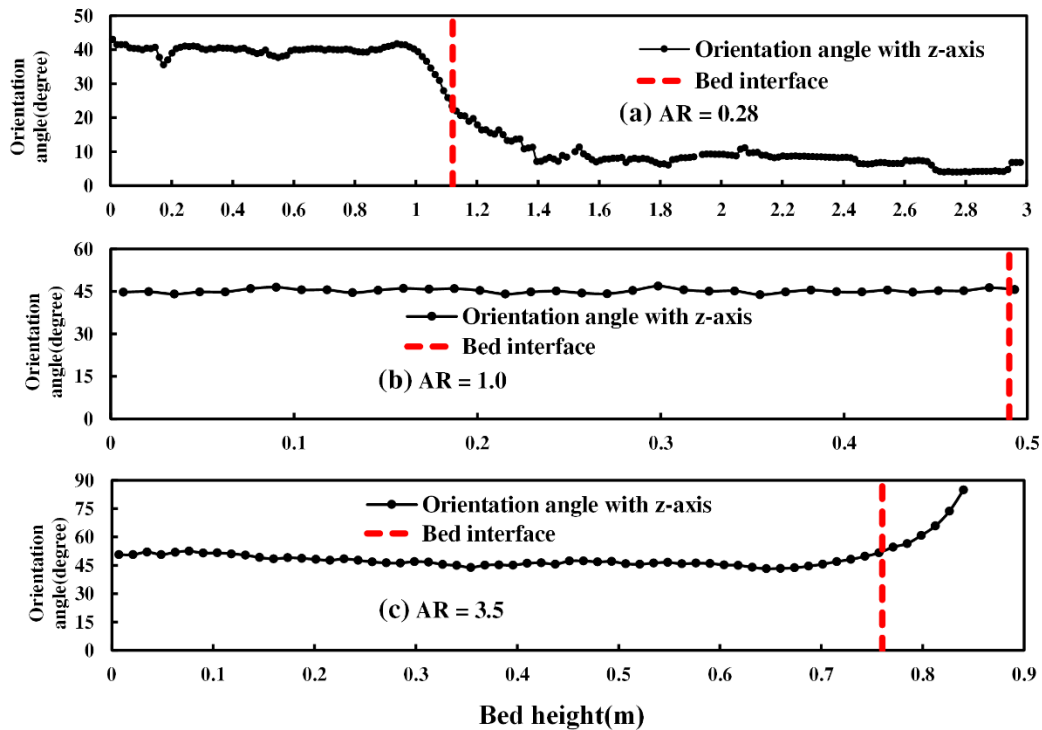


Figure 4-17. Effect of liquid superficial velocities on the particle orientation angle distributions with bed height when $U_0 = 0.251$ m/s: (a) AR = 0.28, (b) AR = 1.0, and (c) AR = 3.5.

Note that when particles with different shapes approach and pass the bed interface at same liquid superficial velocity $U_0 = 0.251$ m/s, they undergo different phenomena. Oblate particles are

Chapter 4 CFD-DEM Modelling of Solid Flow Characteristics in Liquid Fluidizations of Ellipsoidal Particles

entrained by fluid, but spherical and prolate particles return to the dense bed. This phenomenon can be explained by the terminal velocities of particles. It is the particle orientation that changes the projected area of particles and hence the magnitude of drag force and pressure gradient force. The changes of forces significantly affect the terminal velocities of particles. The terminal velocity of particles at different orientation angles can be calculated based on the general force balance on a single particle falling in a stagnant liquid. The calculated terminal velocities of the oblate ($AR = 0.28$), spherical ($AR = 1.0$), and prolate ($AR = 3.5$) particles at different orientation angles are plotted in Fig. 18.

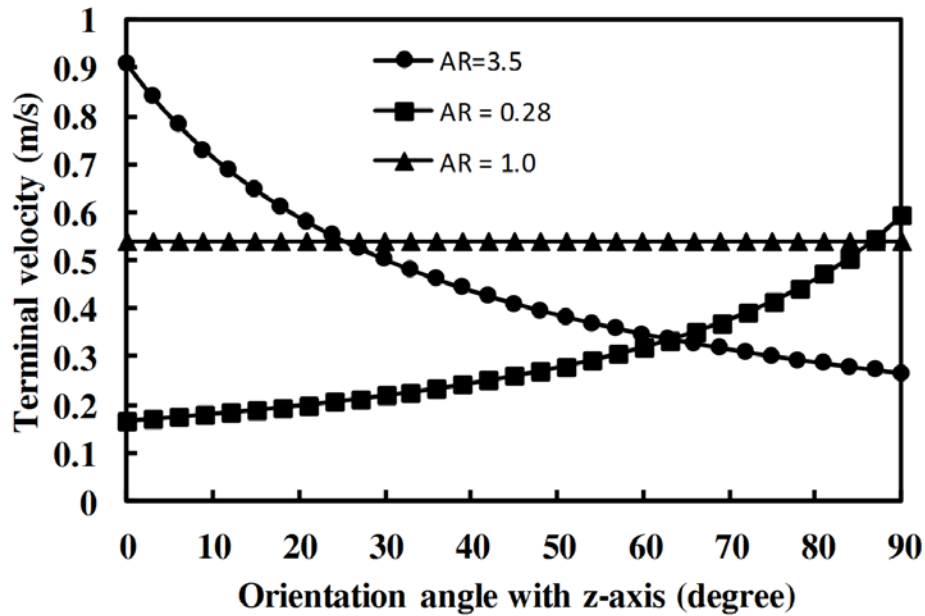


Figure 4-18. Effect of particle orientation on the terminal velocity of ellipsoidal particles.

Figure 4-18 reveals the significant effect of particle orientation on the terminal velocities of particles. It can be observed that generally, spheres have larger terminal velocities than oblate and prolate particles except for some ranges of orientation angle (e.g., particularly for prolate particles with the orientation angle less than $\sim 24^\circ$, but note that prolate particles preferably have an angle larger than 24° as shown in Figure 4-16). Prolate and oblate particles can have the same

terminal velocity at the angle of around 63° . Hence, according to Figure 4-18, the occurrence of entrainment phenomenon for different shapes of particles strongly depends on the orientation angle and also the operational liquid superficial velocity. This can be used to explain the difference of flow patterns as observed in Figure 4-2. For example, at $U_0 = 0.251$ m/s, the terminal velocities of spheres and prolate particles in the entire range of particle orientation angles are larger than 0.251 m/s. As a result, no entrainment occurs at this velocity. However, for oblate particles, the terminal velocity at a certain range of orientation angles is less than 0.251 m/s, hence oblate particles with the angle in this range would enter the freeboard region. When liquid superficial velocity is increased to 0.325 m/s (Figure 4-2 (h)), prolate particles which reach the interface with orientation angles more than 60° can be entrained to the freeboard region. However, the significant increase in liquid velocity to 0.47 m/s for spheres still do not cause any entrainment as shown in Figure 4-2 (i). This is because the terminal velocity of spheres is high (e.g., 0.54 m/s as shown in Figure 4-18), and independent of orientation angle. Hence, the entrainment phenomenon does not occur.

4.5.6 Summary

In summary, we employed CFD-DEM to investigate the effect of particle shape on the hydrodynamics of liquid fluidizations. Spheroids are used in this work to represent non-spherical particles. It was found that particles shape significantly affects the solid flow behaviour in liquid fluidizations. The entrainment phenomenon was observed for oblate particles, but spheres and prolate particles did not enter to the freeboard regions at the same velocity. Spheres exhibit the uniform distributions of pressure gradient and porosity along the bed height, independence of liquid superficial velocity. However, at high liquid velocities, non-symmetric parentheses-shape profiles are observed for ellipsoids with maximum pressure gradient and porosity happening at a

Chapter 4 CFD-DEM Modelling of Solid Flow Characteristics in Liquid Fluidizations of Ellipsoidal Particles

certain height. This is mainly caused by particle interlocks due to non-sphericity of particles. Elongated or platy particles are easily accumulated at high liquid velocities and locked in some regions above the distributor which results in high-pressure gradient and low porosity. Besides, bed permeability decreases remarkably for ellipsoids, and spheres have the largest minimum fluidization velocity. Finally, the changes of particle orientations have been found to be responsible for the entrainment phenomenon.

Chapter 5 A modified drag model for multicomponent mixtures of non-spherical particles

5.1 Overview

In this chapter, CFD-DEM is used to investigate the effects of particle shape on the mixing process. A modified drag model suitable for multicomponent mixtures of non-spherical particles is proposed first, and its validity is then verified by comparison to experimental data. In addition, the results show that adding a second component (oblate or prolate particles) to spheres results in reducing the minimum fluidization velocity of the mixtures; however, oblate particles in decreasing the minimum fluidization velocity is more significant than prolate particles. The mixing index increases with increasing gas velocity while after a specific gas velocity, the mixing index becomes constant. The results also show that with the added component changing from spheres to oblate/prolate particles, clear segregation happens in the bed. It is found that the effect of particle shape on the particle-fluid interaction force is responsible for the occurrence of particle segregation.

5.2 Introduction

Different numerical methods were used to study mixing process in the fluidized bed by either continuum approach (Fan and Fox, 2008; Pirker et al., 2010; Sun et al., 2009) or discrete approach (Di Renzo et al., 2008; Feng et al., 2004; Feng and Yu, 2007; Norouzi et al., 2011;

Olaofe et al., 2014; Zhu et al., 2007, 2008). Note that continuum approaches are more desirable in terms of computing time, but the results are less accurate in prediction of mixing and segregation process (Fan and Fox, 2008; Sun et al., 2009) and even in generating basic flow characteristics (Pirker et al., 2010). Alternatively, discrete approach such as CFD-DEM has been widely employed to study the fundamental behaviour of granular materials (Zhu et al., 2007, 2008), and the mixing/segregation process in fluidized beds (Di Renzo et al., 2008; Feng et al., 2004; Feng and Yu, 2007; Norouzi et al., 2011; Olaofe et al., 2014). For example, Olaofe et al. (2014) investigated the mixing and segregation phenomenon of disperse systems of spherical glass beads with the same density and different sizes. It was found that the CFD-DEM model with appropriate drag model for polydispersity systems was able to successfully predict the mixing quality as observed in experiments, and concluded that the role of drag force in the prediction of hydrodynamics of particles in gas-fluidized beds is important. Di Renzo et al. (2008) utilized CFD-DEM simulation data to propose a model for the mixing process, and a mixing map was developed which was claimed to be extensible to more complex systems with different particle sizes and densities. Feng and Yu (2004) observed that good mixing of spherical particles of different sizes and densities occurred at high gas velocities, while at lower velocities segregation took place.

However, all the aforementioned studies considered particles as ideal spherical particles. In practice such as biomass particles in gasification or combustion process (Cui and Grace, 2007), coating of tablets in fluidized beds (Li et al., 2015), food processing (Kozanoglu et al., 2002), and bulk solid handling (Qian and Yan, 2012), particle shapes are complex, either regular or irregular. Particle shape can affect particle behaviour significantly, as demonstrated in mono-sized fluidizations (Cai et al., 2016; Chen et al., 2017; Gan et al., 2016; Hilton et al., 2010; Ma et al.,

2016; Vollmari et al., 2016; Zhou et al., 2011). However, it is still little known about fluidizations of multicomponent mixtures of non-spherical particles and how particle shape affects the mixing and segregation. Some efforts have been made in this direction (Alobaid et al., 2013; Barghi et al., 2003; Escudié et al., 2006a; Oschmann et al., 2014; Ren et al., 2012; Shao et al., 2016). For example, observations from Escudié et al. (2006a) showed that particles shape can significantly cause segregation in binary mixtures with particles having the same size and density. Experimental work of Shao et al. (2016) examined the mixing behaviour of non-spherical particles in a waste fluidized bed, showing that high particles mixing index can be achieved when the density of non-spherical particles is similar to the density of fluidization medium in multi-component mixtures. Ren et al. (2012) found that spherical particles mix more evenly and faster than corn-shaped particles. Mixtures of spheres and complex shaped particles with same equivalent volume displayed some segregations, which were attributed to variations of cross-sectional area and consequently different particle-fluid interaction forces (Oschmann et al., 2014). Vollmari et al. (2017) investigated the mixing quality of mixtures with four different shapes both experimentally and numerically. The mixing speed and quality predicted by CFD-DEM coupled model were found in good agreement with their experiments. Adding plates to mixtures resulted in faster mixing rates. However, in cases of adding cubes and elongated particles to other complex shaped particles, the mixing was not affected significantly.

So far, only limited studies have been conducted to use CFD-DEM approach for the mixing behaviour of multi-component mixtures of non-spherical particles in fluidized beds. One main reason is that a proper drag force model for a multi-component mixture of non-spherical particles is not available. Many drag models so far are proposed for a binary mixture of spherical particles and systems with mono-sized non-spherical particles. These drag models are not recommended

Chapter 5 A modified drag model for multicomponent mixtures of non-spherical particles for mixtures of non-spherical particles. This fact was also highlighted by Vollmari et al. (2017) who found noticeable differences between experimental and numerical predictions of mixing index for mixtures of spheres and elongated cuboids as well as spheres and plates. They attributed such discrepancies to the lack of drag model for polydispersity systems of spherical and non-spherical particles.

Therefore, in this chapter, an effort is made to propose a drag model for mixtures of different shapes by the combination of drag models of Rong et al. (2014), Hölzer and Sommerfeld (2008) and Rong et al. (2015). In addition, it is not well understood that when particle shapes change from one shape to other shapes, how this affects the mixing quality. Ellipsoidal particles are able to overcome this as they can represent a wide range of particle shapes from oblate (disc-like) to prolate (elongated) particles. Thus, a systematic analysis of effects of particle aspect ratio, which varies from 0.25 to 3.5, on the mixing of binary mixtures is carried out.

5.3 Model Descriptions

The CFD-DEM model used in this chapter is the same as the model which was explained in the sections of 4.3 of Chapter 4. The only difference is in using a new correlation for the drag force correlation of mixture of non-spherical particles, which is described in the next section.

5.3.1 Drag model for mixtures of non-spherical particles

In the literature, various drag models are available to calculate the drag force for mono-sized spherical particles (Di Felice, 1994; Ergun, 1952; Gidaspow, 1994; Rong et al., 2013; Syamlal and O'Brien, 1988; Wen and Yu, 1966), binary mixtures of spherical particles (Cello et al., 2010; Rong et al., 2014; Van der Hoef et al., 2005; Yin and Sundaresan, 2009), and mono-sized non-spherical particles (Ganser, 1993; Haider and Levenspiel, 1989; Hölzer and Sommerfeld, 2008;

Rong et al., 2015). However, so far there has been no drag models for mixtures of non-spherical particles. The extension of drag models developed based on mono-sized particles to binaries of non-spherical particles can result in discrepancies between simulations and experiments (Vollmari et al., 2017). Therefore, in order to develop a drag model that is suitable for multicomponent mixtures of non-spherical particles, three drag models of Rong et al. (2014), Holzer and Sommerfeld (2008), and Rong et al. (2015) are combined in this work to formulate a drag model for binary mixtures of non-spherical particles, and details are given below.

Rong et al. (2014) employed Lattice Boltzmann method to propose a drag model for mixtures of spherical particles. Extensive discussion of the drag model's advantages over other drag models can be found in Rong et al. (2014). The general equation of this drag model, which is similar to the general format of Di Felice (1994) model used in the literature, is given by Eq. (5-1):

$$\mathbf{f}_{d,i} = 0.5C_{D0}\rho_f A_{\perp} \varepsilon_f^2 \alpha(d_i, x_i, \varepsilon_f) |\mathbf{u} - \mathbf{v}_i| (\mathbf{u} - \mathbf{v}_i) \varepsilon_f^{-\beta(\varepsilon_f, \langle \text{Re} \rangle)} \quad (5-1)$$

where C_{D0} is the drag coefficient of an isolated sphere which is determined by

$$C_{D0} = \left(0.63 + 4.8 / \sqrt{\langle \text{Re} \rangle}\right)^2 \quad (\text{DallaValle, 1948}),$$

ρ_f is the liquid density, A_{\perp} is the projected area of particles in the fluid flow direction (for spheres, it is $\pi \langle d \rangle^2 / 4$ and $\langle d \rangle$ is the harmonic mean

diameter of a mixture and determined by $\langle d \rangle = \left[\sum_{i=1}^N x_i / d_i \right]^{-1}$, d_i is the particle size of

component i , N is the total number of components (for binary mixtures, $N=2$), x_i is the volume

fraction of a component in a mixture, α is the coefficient which determines the fraction of total

drag force based on the mean particle size should be allocated to each component, and calculated

by $\alpha(d_i, x_i, \varepsilon_f) = (1 - A - B) / \left(\sum_{i=1}^N (x_i / y_i^2) \right) + Ay_i^2 + By_i$, the parameters A and B are, respectively,

given by $A(\varepsilon_f) = 0.5(1 - \varepsilon_f)$ and $B = 0.5$, y_i is the diameter ratio of i th component given by

$y_i = d_i / \langle d \rangle$, β is the corrective exponent and defined as

$\beta(\varepsilon_f, \langle \text{Re} \rangle) = 2.65(\varepsilon_f + 1) - (5.3 - 3.5\varepsilon_f)\varepsilon_f^2 \exp[-0.5(1.5 - \log_{10} \langle \text{Re} \rangle)^2]$, $\langle \text{Re} \rangle$ is the Reynolds number based

on mean particles size and defined as $\langle \text{Re} \rangle = \varepsilon_f \langle d \rangle |\mathbf{u} - \mathbf{v}_i| / \nu$, ε_f is the voidage, \mathbf{u} is the local

fluid velocity vector, \mathbf{v}_i is particle velocity, and ν is the fluid kinetic viscosity.

Note that Eq. (5-1) only applies to binary mixtures of spherical particles. In this work, Eq. (5-1) is still used but modified for binary mixtures of non-spherical particles. The details of the modification of Eq. (5-1) includes:

(i) The drag coefficient C_{D0} in Eq. (5-1) is determined by Holzer and Sommerfeld (2008)'s drag model. This coefficient was proposed based on a large number of literature experimental data and performed numerical studies, and hence is applicable over a wide range of the Reynolds numbers. One important advantage of this coefficient is that it considers the effects of both particle shape and orientation. The reliability of the drag coefficient has been verified by (Hilton et al. Hilton et al., 2010, Zhou et al. Zhou et al., 2011, and Rong et al. Rong et al., 2015). Therefore, this correlation (Hölzer and Sommerfeld, 2008) is used in this work to calculate the drag coefficient C_{D0} on an ellipsoidal particle, which is given as:

$$C_{D0} = \frac{8}{\text{Re}_{p,i}} \frac{1}{\sqrt{\phi_{\perp}}} + \frac{16}{\text{Re}_{p,i}} \frac{1}{\sqrt{\phi}} + \frac{16}{\sqrt{\text{Re}_{p,i}}} \frac{1}{\phi^{3/4}} + 0.42 \times 10^{0.4(-\log \phi)^{0.2}} \frac{1}{\phi_{\perp}} \quad (5-2)$$

where ϕ_{\perp} is the crosswise sphericity, defined as the ratio between the cross-sectional area of the volume equivalent sphere and the projected cross-sectional area (A_{\perp}) of the considered particle.

(ii) The particle diameter d_i in the modified drag model is replaced by the volume equivalent diameter which is given as $d_i = (6V_i / \pi)^{1/3}$ where V_i is the volume of the ellipsoid i . However, when two ellipsoids have different shapes but the same volume, their equivalent particle diameters are equal to each other. As a result, the parameter α approaches one and the equation (Eq. (5-1)) would be simplified to the case for mono-sized particles. Therefore, there is a need to modify the definition of particle equivalent diameter (d_i) to overcome the problem. Here, we use another equivalent particle diameter in terms of the projected area of particles, which are also used in many studies of drag coefficient (Heiss and Coull, 1952; Rodrigue et al., 1994; Singh and Roychowdhury, 1969; Unnikrishnan and Chhabra, 1991). The projected area-based equivalent diameter is determined by $d_i^p = (4A_p / \pi)^{1/2}$ where A_p is the projected area of the particle normal to the direction of its motion.

(iii) Add a corrective function to Eq (5-1) to consider the effect of particle shape. The corrective function, which is proposed by Rong et al. (2015) for mono-sized ellipsoidal particles, is used here and defined as $J(\varepsilon, \phi, \text{Re}) = \varepsilon_f^{-\lambda(\phi, \langle \text{Re} \rangle)}$. Clearly, J is a function of local porosity, particle sphericity of ellipsoids, and Reynolds number. Hence, the modified drag equation can be written as:

$$\mathbf{f}_{d,i} = 0.5C_{D0}\rho_f A_{\perp} \varepsilon_f^2 \alpha(d_i, x_i, \varepsilon_f) |\mathbf{u} - \mathbf{v}_i| (\mathbf{u} - \mathbf{v}_i) \varepsilon_f^{-\lambda(\varepsilon_f, \langle \text{Re} \rangle) + \lambda(\phi, \langle \text{Re} \rangle)} \quad (5-3)$$

where the sphericity ϕ is to represent particle shape factor, and defined as the ratio of surface area of a sphere having the same volume of the non-spherical particle to the surface area of the particle. The exponential term in the corrective function J is defined as

$\lambda(\phi, \langle \text{Re} \rangle) = (1 - \phi)\{C - D \exp[-0.5(3.5 - \log \langle \text{Re} \rangle)^2]\}$, where the parameters of C and D are respectively given by $C(\phi) = 39\phi - 20.6$ and $D(\phi) = 101.8(\phi - 0.81)^2 + 2.4$.

The three steps above should be applied to Eq. (5-1), hence the new equation (Eq. (5-3)) can be considered as a modified drag model which considers not only particle shape and size but also particle volume fraction.

5.4 Simulation conditions

The CFD-DEM simulations are conducted in a rectangular slot with periodic boundary conditions applied to the front and rear walls to eliminate wall effects. For this geometry, 2-D CFD and 3-D DEM are used, which was also successfully employed in the previous studies (Feng et al., 2004; Zhou et al., 2011). The poured packing method (Zhang et al., 2001) is used to generate the fixed bed. In this method, random velocities and orientation are assigned to each ellipsoid, and then particles fall from certain height under gravity force. The settling process continues until all particle velocity approaches to zero. Then, the packed bed is used to inject liquid uniformly from the bottom of the bed. The steady state condition is achieved when the pressure drop and bed voidage fluctuates around their mean values. No-slip boundary condition is applied to the interaction between wall and liquid phase. For the collisions between particles and side walls, walls are considered as a particle with infinite diameter. The physical and geometrical parameters implemented in the present simulations are listed in Table 5-1.

Table 5-1. Parameters used in the present simulations.

Particle phase	
Density (ρ_p), $kg.m^{-3}$	772.5
Equivalent diameter (d_p), mm	7

Chapter 5 A modified drag model for multicomponent mixtures of non-spherical particles

Particle shape	Oblate, sphere, and prolate
Particle Aspect Ratio (AR), -	0.25, 0.5, 1, 1.5, 2, 3.5
Number of particles (N), -	6000
Young's modulus (E), $N.m^{-2}$	1.0×10^8
Poisson's ratio (ν), $N.m^{-2}$	0.4
Sliding friction coefficient (μ), -	0.3
Damping Coefficient (c_n), -	0.3
Time step (Δt), s	2.5×10^{-6}
<hr/>	
Gas phase	
<hr/>	
Viscosity (μ_f), $kg.m^{-1}.s^{-1}$	1.83e-005
Density (ρ_f), $kg.m^{-3}$	1.168
Bed geometry	
Width (W), m	0.2
Height (H), m	1.0
Thickness (D), m	$4d_p$
Size of CFD cells	$2d_p \times 2d_p$
Bed distributor	Uniform
Time step (Δt), s	2.5×10^{-6}
<hr/>	

Particles with different shapes from oblate to prolate are generated with varying aspect ratio of spheroids. Spheroids are composed of three radii: a is assigned to the radius in the polar direction, and b and c are considered as the radii in the equatorial plane. Therefore, the particle aspect ratio (AR) is defined as $AR = c/a$. Consequently, $AR > 1$ corresponds to prolate spheroids, $AR = 1$ stands for spheres, and $AR < 1$ is for oblate spheroids. In order to perform a systematic analysis of the effects of particles shape on the mixing quality of binary mixtures, all properties of particles (i.e., volume and density) except shape and the volume fraction of each component (50 % by volume) remain constant in all simulation cases. Each binary mixture is generated by a combination of spherical particles and spheroids with a specific aspect ratio (i.e., $AR = 0.25, 0.5, 1, 1.5, 2, 3.5$). Therefore, in this work, six different binaries are studied to figure out that when

particles shape gradually change from flat shape to a sphere and then elongated shape how this affects the mixing quality of mixtures. Each binary is made by adding a second component in ellipsoidal shape to the spheres with the equal volume fraction of 50%. Note that a mixture of spheres and ellipsoids is presented in the format of AR(ψ_1 , ψ_2), where AR stands for Aspect Ratio, ψ_1 is the aspect ratio of component 1 (mono-sized spheres), and ψ_2 is the aspect ratio of component 2 (added mono-sized ellipsoids).

The mixing quality of a mixture can be quantified by calculating mixing index. Various methods have been proposed in the literature to quantify the mixing/segregation quality in fluidized beds (Hemati et al., 1990; Lacey, 1954; Nienow et al., 1978; Rice and Brainovich, 1986). Among them, the well-known Lacy mixing index (Lacey, 1954) is used in this work. The Lacy mixing index can be given by $M = (S_0^2 - S^2) / (S_0^2 - S_R^2)$, where S^2 is the actual variance, S_0^2 and S_R^2 are the variances of the completely segregated and well-mixed states, and respectively given by $S_0^2 = p \times q$ and $S_R^2 = (p \times q) / N$, where p and q are the volume fraction of spheres and added ellipsoids in a mixture, and N is the number of particles in the samples. Note that due to the presence of bubbles in the beds, the weight of each sample can be significantly different from each other and this can affect the mixing index calculation. To avoid this problem, some researchers (Feng et al., 2004; Rhodes et al., 2001) proposed different approaches. Here, the method proposed by Feng et al. (2004) is used to handle this problem. Feng et al. (2004) discretized the bed to fixed sample sizes and the contribution of each sample to the total mixing index calculation is considered with a weighting factor. Thus, the actual variance S^2 is expressed as:

$$S^2 = \frac{1}{k_t} \sum_{i=1}^n k_{wvf} (X_i - \bar{X})^2 \quad (5-4)$$

where $k_t = \sum k_{wvf}$ and k_{wvf} is a weighting factor, equal to N/N_{\max} (N is the number of equivalent particles in the i^{th} sample, and N_{\max} is the maximum number of equivalent particles among all the samples at a considered time step). n is the number of samples, X_i is the volume fraction of spheres in the i^{th} sample, and \bar{X} is the volume fraction of spheres in the whole bed which in this work is equal to p .

Another important parameter for mixing index calculation is the selection of the sample size (Fan et al., 1970; Feng et al., 2004). Therefore, for each binary mixture, the effect of sampling size on the mixing index is firstly investigated for a well-mixed bed and a fully segregated bed, and then an optimum range of sample size is chosen. Figure 5-1, for example, displays the effect of sample size on the mixing index for the two extreme configurations of well-mixed beds and fully segregated beds containing different binary mixtures of AR(1, 0.25), AR(1,1) and AR(1,3.5). It can be seen from Figure 5-1(a) that with a sample size of 0.016-0.027 m, the mixing index of well-mixed bed is close to one, and at the same time the mixing index of fully segregated beds is close to zero. Therefore, the middle value (0.0215 m) of this range is selected to calculate the mixing index for all the cases of binary mixtures of spheres and oblate particles with AR=0.25. On this basis, a similar analysis is performed for other binary mixtures to find a reasonable sample size. Hence, the sample size of 0.018 m is chosen for the mixture AR (1, 1) (Figure 5-1 (b)), and the sample size of 0.028 m for the mixture AR (1, 3.5) (Figure 5-1 (c)).

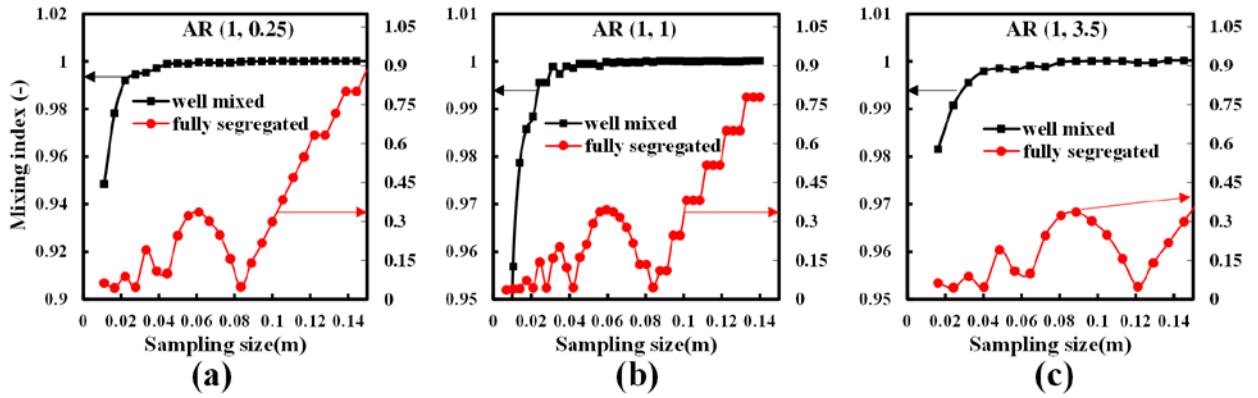


Figure 5-1. Sampling size effects on mixing index for two extreme conditions of well-mixed bed and fully segregated bed; (a) binaries of oblate ($AR=0.25$) and spheres, (b) binaries of two identical spheres, (c) binaries of prolate ($AR=3.5$) and spheres.

5.5 Results and discussion

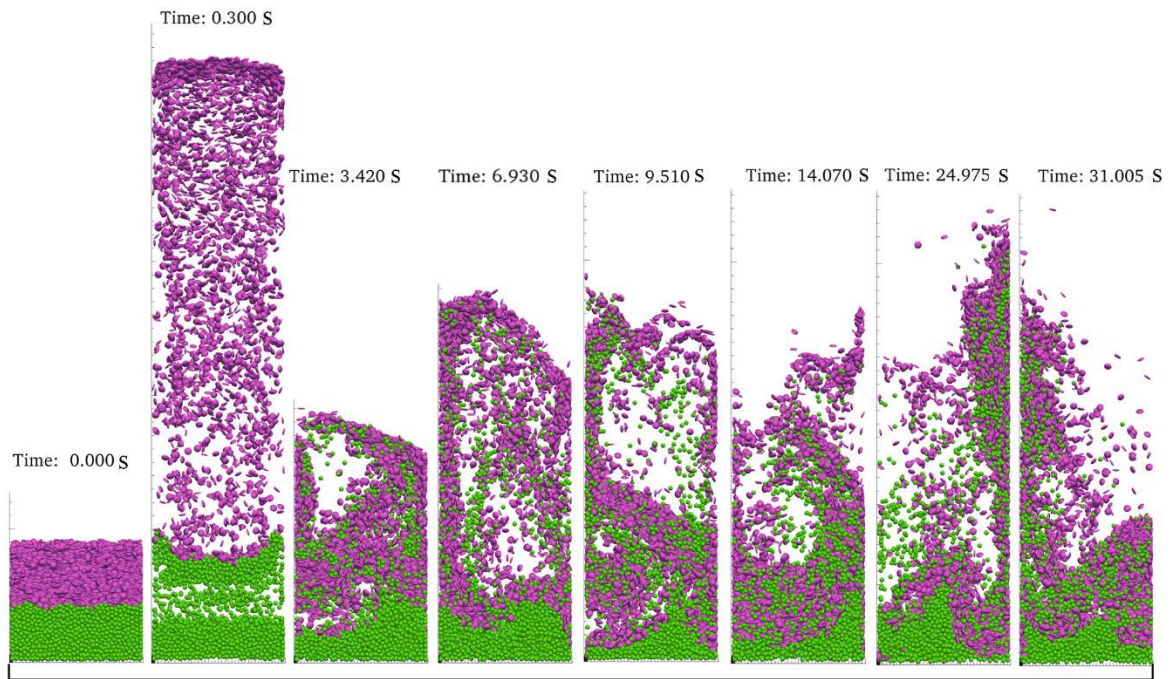
5.5.1 Validations of the modified drag model

The modified drag model can be validated by comparisons with other drag models and physical experiments. In particular, since limited experimental data for binary mixtures of ellipsoids are available to quantitatively validate the modified drag model, the experimental work of Vollmari et al. (2017) is selected to verify the modified drag model's capabilities in the modeling of binary mixtures of spherical and non-spherical particles. In the work of Vollmari et al. (2017), the mixing quality of four different shapes (sphere, cube, elongated cuboid, and plate) are analyzed experimentally and numerically. Here, the experimental results of the binary mixture of plates and spheres are chosen to compare with the simulated results by the present model. Note that plate-like particles can be estimated by ellipsoids with very low aspect ratio.

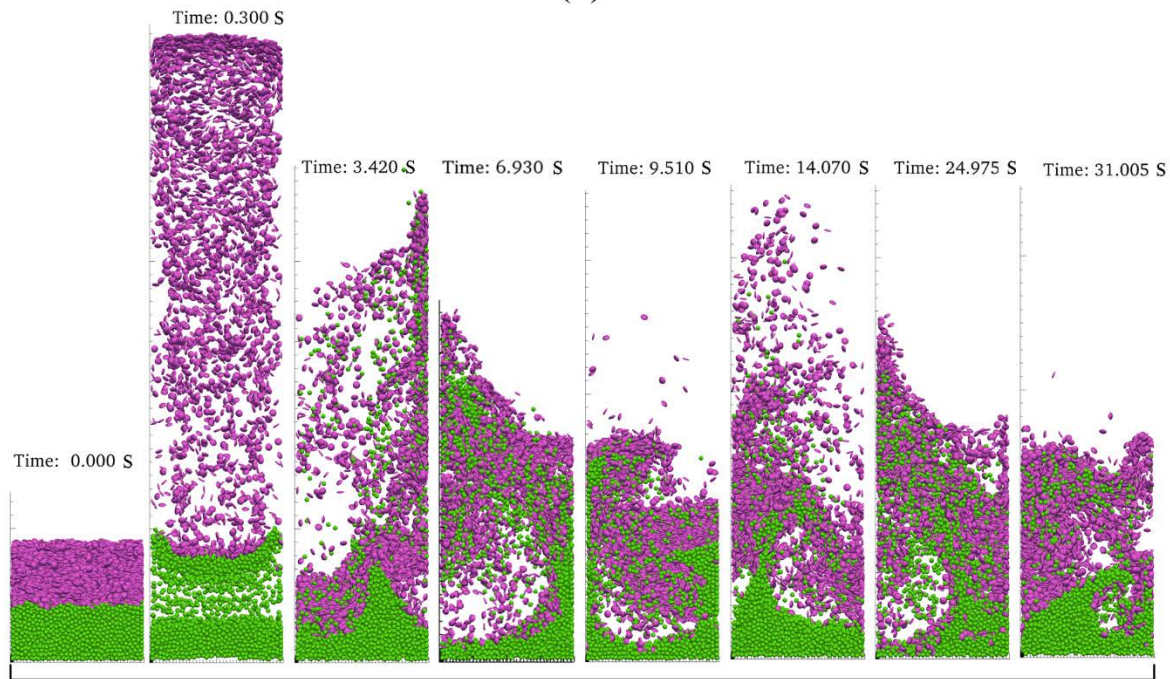
The comparisons of the CFD-DEM results in two different cases are carried out first. In the first case, the modified drag force model (Eq. (5-3)) is implemented into the CFD-DEM model and in the second case, the drag force model developed based on mono-sized non-spherical

particles is used in the model. Note that the drag force on the basis of mono-sized drag coefficient is calculated by $\mathbf{f}_{d,i} = 0.5 \times C_D \rho_f A_{\perp} \varepsilon_f^2 |\mathbf{u}_i - \mathbf{v}_i| (\mathbf{u}_i - \mathbf{v}_i) \varepsilon_f^{-\gamma}$, where $\gamma = 3.7 - 0.65 \exp[-(1.5 - \log_{10} \text{Re}_i)^2 / 2]$, A_{\perp} is the cross-sectional area perpendicular to the fluid flow, Re_i is the relative Reynolds number, which is defined as $\text{Re}_i = \rho_f d_v \varepsilon_f |\mathbf{u}_i - \mathbf{v}_i| / \mu_f$, where d_v is the equivalent diameter defined as the diameter of a sphere with the same volume as the ellipsoid particle. C_D is the drag coefficient given by Eq. (5-2). This drag force equation was also used in previous works (Gan et al., 2016; Oschmann et al., 2014; Vollmari et al., 2017; Zhou et al., 2011) to calculate the drag force on non-spherical particles in fluidized beds.

Figure 5-2 compares the particle flow patterns predicted by the two drag models at different times, indicating no significant difference. Generally speaking, from both Figure 5-2 (a) and (b), it can be observed that when the gas is injected into the bed, the oblate particles (pink colour particles at the top in intimal stage) expands remarkably to a maximum a maximum height while spherical particles slightly move towards to the top. The mixing process happens gradually in both cases. While oblate particles at the top part of the bed are mixed with some spheres, some spheres are fully segregated at the bottom of the bed. Obvious bubbles can be seen in the top layer of the bed, which can be the cause of mixing process of spheres with oblate particles. It is can be seen that when the modified drag model is implemented into the model (Figure 5-2 (a)), a smaller number of spherical particles (in green) is accumulated at the bottom. This implies more mixing of spheres into oblate particles.



(a)



(b)

Figure 5-2. Particles configurations predicted with (a) modified drag force model (Eq. (5-3)) (b) drag model for mono-sized drag model at different times and at the gas velocity of 2.4 m/s.

In order to quantify the difference of the results predicted by the two different drag models, the mixing indices of a binary mixture of spheres AR(1,1), and the mixture of AR(1,0.25) corresponding to Figure 5-2 (a) and (b) are plotted in Figure 5-3. For the case of AR(1,1), when the modified drag model is applied, it is anticipated that the particles flow pattern as well as mixing index become similar to the case simulated with mono-size drag model. This verification can be seen in Figure 5-3 (a) where mixing index of two different drag models become identical for mixtures of identical spheres. However, as shown in Figure 5-3 (b), a noticeable difference is observed between mixing indices calculated for two cases of binaries of spheres and oblate particles (aspect ratio AR= 0.25). From Figure 5-3 (b), it can be observed that when the mono-size drag model is used, the mixing index of the mixture is unstable and change in the shape of a wave. Such an unstable mixing index variations with time for the binary mixtures of spheres and plates were also reported in the numerical simulations by Vollmari et al. (2017). However, the experimental mixing index for this binary mixture was observed more stable at the steady-state condition (see Fig. 3 in Vollmari et al. (2017)). The mixing index predicted by the modified drag model in this work shown in Figure 5-3 (b) demonstrates more stable mixing index which is similar to the observations in Vollmari et al. (2017). In addition, the mean mixing index with the modified drag model is fluctuating around the mean experimental value while there is a big difference between the mean experimental mixing index and the case with mono-sized drag model. This further validates the capabilities of the new modified drag model in simulating the binary mixtures of non-spherical particles. Therefore, for all simulations, the modified drag model as presented in Eq. (5-3) is employed.

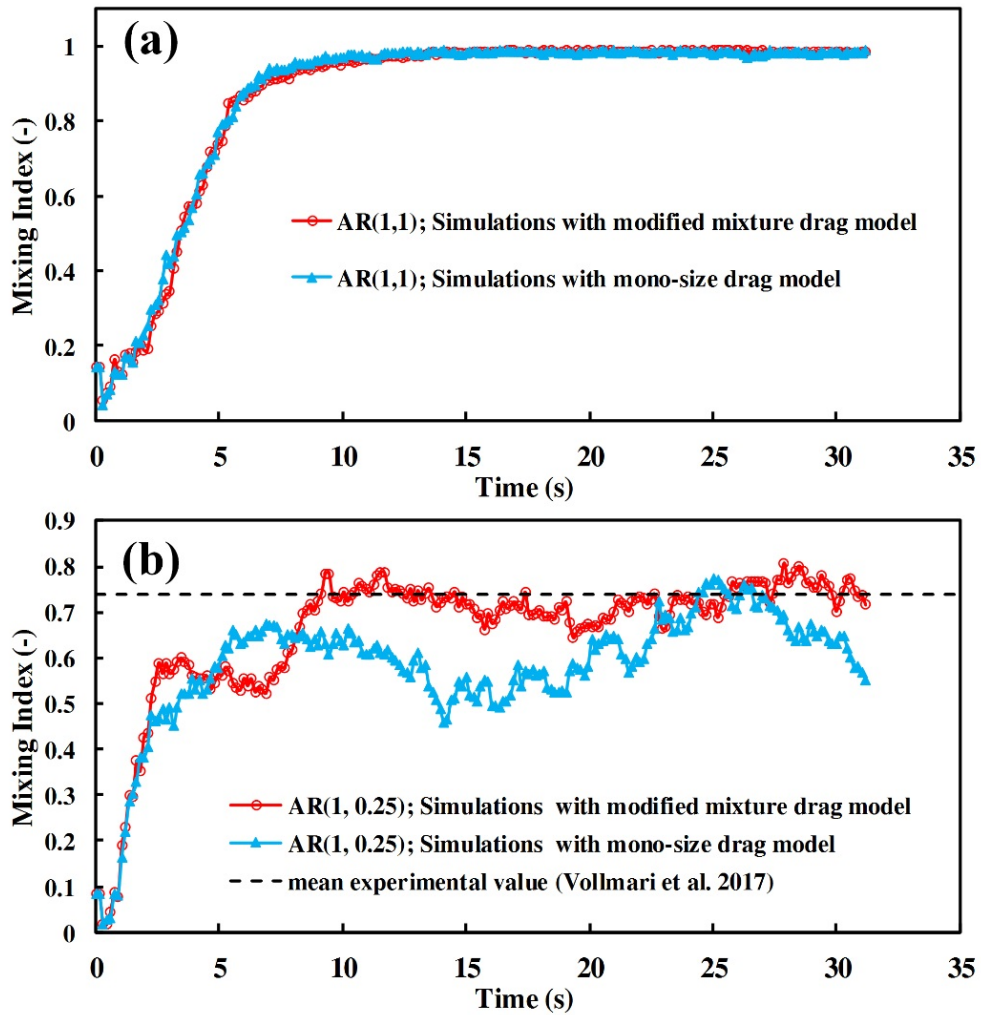


Figure 5-3. Comparison between the mixing index of beds simulated by modified drag model (Eq. (7)) and drag model for mono-size particles (Eq. (12)); (a) binaries of two spheres with the same size and density, (b) binaries of oblate particles (AR=0.25) and spheres.

Note that with the addition of the second component of ellipsoids to spheres, the bed performance changes correspondingly, particularly the relationships of the pressure drop and gas velocity as plotted in Figure 5-4. This figure shows the curves for mono-sized particles (spheres or ellipsoids) and their binary mixtures. The pressure drop variations with gas velocity for spheres is compared with Ergun equation (Ergun, 1952) and shown in Figure 5-4 (a). It can be

seen that the prediction of CFD-DEM model with the modified drag model is consistent with Ergun predictions of pressure drop with gas velocity, further confirming the validity of the modified drag model. Figure 5-4 (a) also shows that spheres generate less pressure drop than oblate and prolate particles in packed beds of mono-sized particles. This indicates that spheres exhibit high permeability, which also was reported in the literature (Zhou et al., 2011). This figure also illustrates the cases of mono-sized oblate and prolate particle with aspect ratios of 0.25, 0.5, and 2. With increasing the liquid velocity, the pressure drop increases and after the minimum fluidization point (U_{mf}), the pressure drop fluctuates around mean value which is equal to bed weight per unit area. Figure 5-4 (b), (c), and (d) show the pressure drop-gas velocity variations of binary mixtures of oblate and prolate particles with spheres. Generally, the pressure drop variations of binary mixtures locate between the two curves for the two mono-sized particles. This indicates that adding non-spherical particles to spheres increase the pressure drop at a specific velocity, leading to lower permeability.

Figure 5-4 also demonstrates that the highest minimum fluidization velocity of mono-components belongs to spheres while changing the particles shape to oblate or prolate significantly decreases the minimum fluidization velocity. This could be due to the enhanced projected area of ellipsoids in packed beds, and consequently larger particle-fluid interaction force on ellipsoids when particles distort from the spherical shape. When the second component - ellipsoidal particles- is added to the spheres to make binary mixtures of spheres and ellipsoids, the U_{mf} of mixtures generally increases compared to the U_{mf} of added ellipsoids. From this figure, it can be found that when the second component (ellipsoids) with a specific aspect ratio is added to spherical particles, the minimum fluidization velocity reduces remarkably. This indicates that

spherical particles can start to fluidize at lower gas velocity by adding some prolate or oblate particles to the spheres.

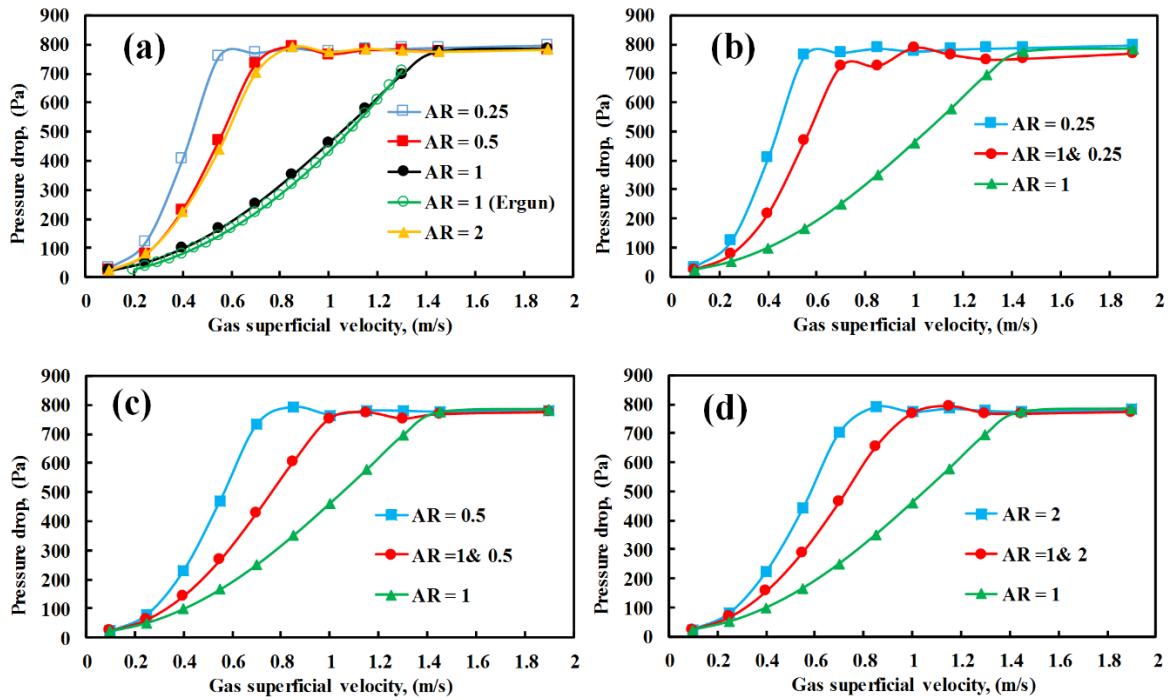


Figure 5-4. The pressure drop variations as a function of liquid superficial velocities: (a) mono particles with different aspect ratios, (b) binaries with AR (1, 0.25), (c) binaries with AR (1, 0.5), (d) binaries with AR (1, 2).

5.5.2 Mixing behaviour under influence of particles shape

Figure 5-5 demonstrates snapshots of particles flow pattern for different mixtures of spheres and ellipsoids at the steady state condition at the gas velocity of 2.4 m/s. The mixtures of identical spheres (Figure 5-5 (c)) exhibits a well-mixed mixture. However, when the aspect ratio of the added ellipsoids is decreased or increased, two components intend to segregate. For the mixture of oblate particles and spheres, with decreasing the particle aspect ratio the segregation

degree increases. A similar effect can be observed by adding prolate particles to spheres; mixtures of prolate particles with greater aspect ratio with spheres reduce the mixing quality.

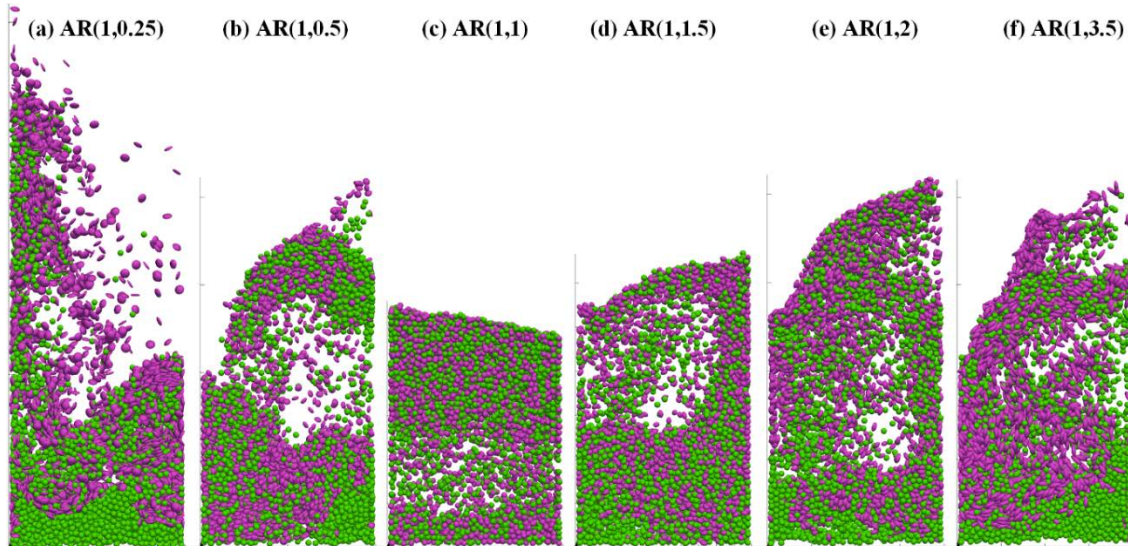


Figure 5-5. Particles configurations predicted for different binaries at an equilibrium state at the gas velocity of 2.4 m/s.

Fig. 6 shows the effects of gas superficial velocity on the mixing index for different binary mixtures of spheres and ellipsoids. Starting from binary mixtures of spheres and oblate particles (AR(1, 0.25)) (Fig. 6 (a)), the mixing index fluctuates with high amplitude at lower velocities (1.6 and 1.9 m/s). This can be due to particles interlocks which requires strong forces, from fluid or other particles to be broken down. On the other hand, with increasing the gas velocity, the variations of mixing index at the dynamic equilibrium state with time becomes smoother. This implies that the mixing quality enhances with increasing the gas velocity for the mixtures of spheres and oblate particles as the high gas velocity can exert a greater drag force on particles,

leading to more vigorous particles motions which prevent particles from interlocking, and hence more uniform mixing quality over the time can be achieved.

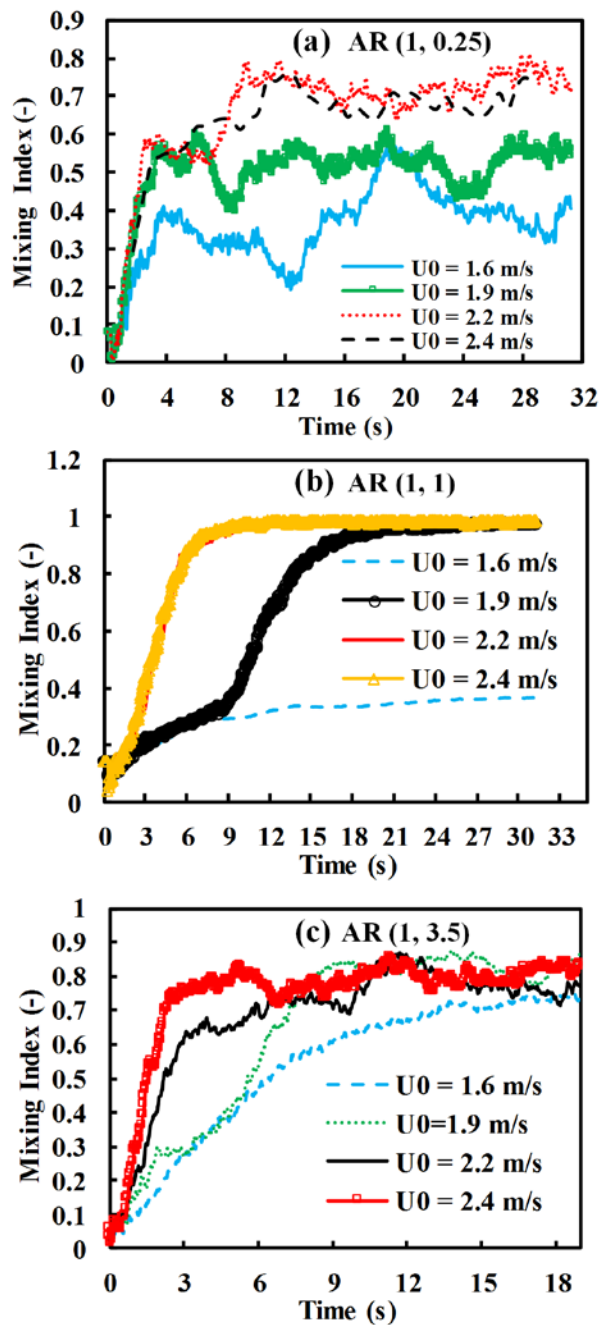


Figure 5-6. The effects of gas velocity on the mixing behavior of different mixtures: (a) AR(1, 0.25), (c) AR(1,1), and (e) AR(1,3.5); The required time to reach steady-state mixed condition as a function of gas velocity for different mixtures: (b) AR(1, 0.25), (d) AR(1,1), and (f) AR(1,3.5).

For the case of binary mixtures of identical particles (Figure 5-6 (b)), on the other hand, it is found that the identical spheres cannot get fully mixed ($MI=1$) at lower velocity, while with increasing the velocity over 1.6 m/s, particles reach to fully mixed state. Increase in gas velocity from 1.6 m/s to 2.2 m/s reduces the required time to reach the equilibrium state, while further increase in gas velocity to 2.2 m/s does not affect the required time to reach stable mix condition. Figure 5-6 (c) illustrates that time variations of mixing index for binaries of prolate particles ($AR=3.5$) and spheres exhibit fewer fluctuations compared to mixtures of spheres and oblate particles (Figure 5-6 (a)). This further emphasizes the significance of particles shape on the mixing quality. Even though different gas velocities result in different transition time to reach a stable mixed condition, the final mixing degree is not much affected by gas velocity.

5.5.3 Relations of mixing index to forces acting on particles

Figure 5-8 displays the mixing index as a function of the aspect ratio of the added component to the spheres. This figure shows that a clear segregation occurs when the shape of the added component is changed from spherical to oblate or prolate ones. Oblate particles decrease the mixing index more sharply compared to the oblate particles. Reducing the aspect ratio of the second added component from 1 to 0.5, for example, drops the mixing index by 17%, while increasing the aspect ratio from 1 to 1.5, reduces the mixing index only 8%. This effect and the overall effect of aspect ratio on the mixing index shown in Figure 5-8 can be related to the effects of particles aspect ratio on a number of particles scale forces.

The spatial mean forces are defined as follows to elucidate the influence of particles shape on the mixing index. For one component with larger aspect ratio, the particle-particle, particle-wall

and particle-fluid interaction forces are defined as $\langle |\mathbf{f}_{pp,L}| \rangle = \sum_{i=1}^{N_L} \left[\left(\sum_{j=1}^{k_{c,i}} \mathbf{f}_{pp,ij} / (m_L \mathbf{g}) \right) \right] / N_L$, $\langle |\mathbf{f}_{pw,L}| \rangle = \sum_{i=1}^{N_L} \left[\left(\mathbf{f}_{pw,i} / (m_L \mathbf{g}) \right) \right] / N_L$, and $\langle |\mathbf{f}_{pf,L}| \rangle = \sum_{i=1}^{N_L} \left[\left(\mathbf{f}_{pf,i} / (m_L \mathbf{g}) \right) \right] / N_L$, respectively, where N_L is the number of particles with larger aspect ratio, $k_{c,i}$ is the number of particles contacting with particle i , $\mathbf{f}_{pp,ij}$ is the particle-particle interaction force between particles i and j , $\mathbf{f}_{pw,i}$ is the particle-wall interaction force between particle i and the wall, and $m_L \mathbf{g}$ is the weight of the particle with larger aspect ratio. Note that the notations $| \cdot |$ and $\langle \cdot \rangle$ stand for the magnitude and average of the variable, respectively. The spatial-temporal mean forces are also calculated by averaging the spatial mean forces over the steady-state time period. Spatial-temporal mean forces acting on another component- with smaller aspect ratio - can be calculated in the same manner.

Figure 5-7 illustrates the spatial distribution of the total particle-fluid force at a steady state condition in three different mixtures of spherical and ellipsoidal particles. From Figure 5-7(a), it can be seen that the particle-fluid force value distribution on oblate particles (disk-shape) is in large range than those on spherical particles. As a result, spherical particles intend to stay in the lower part of the bed and disk-shaped particles are observed mostly in the upper part of the bed. This leads to bad mixing and segregation under influence of particles shape occur. However, when two identical spherical particles are mixed (Figure 5-7(b)), all particles almost receive the same amount of particle-fluid force and well mixing occurs with no sign of segregation. The particle-fluid force distributions for the mixture of spherical particles and prolate particles (Figure 5-7(c)) show non-uniform force distributions which cause the segregation in the bed.

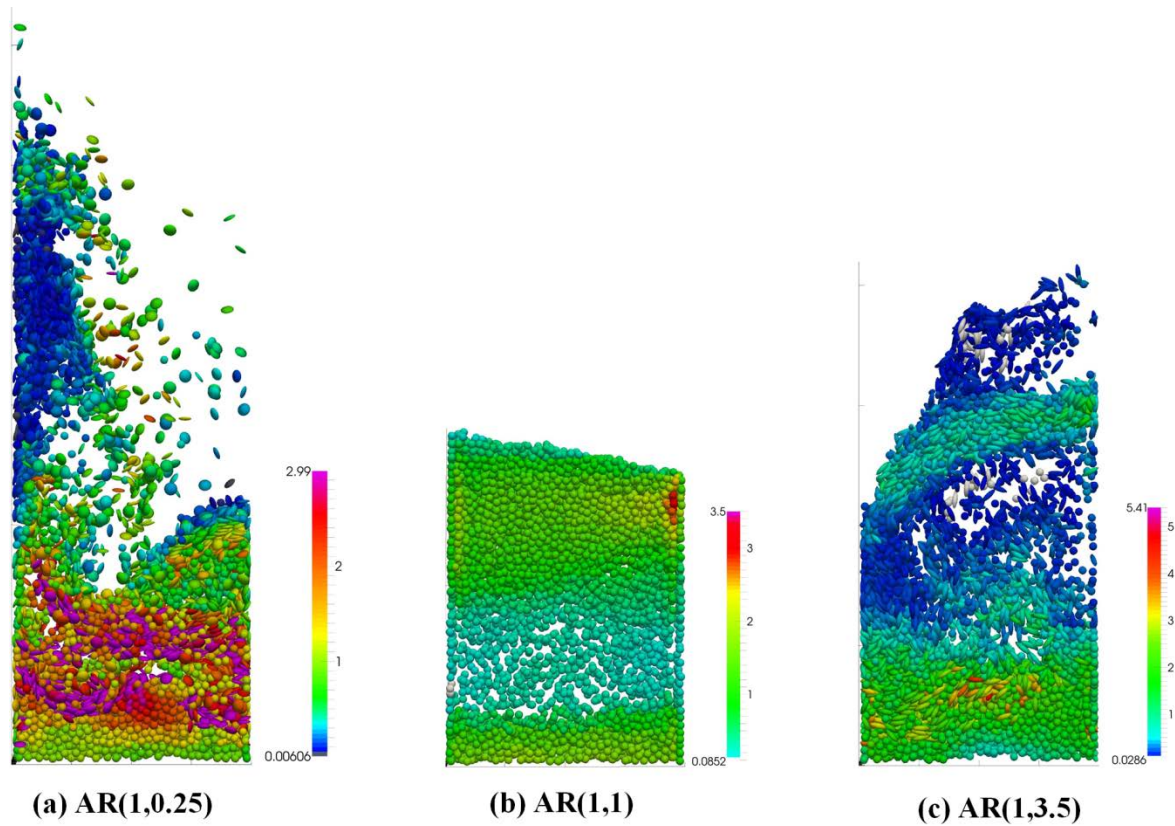


Figure 5-7. The total particle-fluid force distributions in three different mixtures: (a) AR(1,0.25), (b) AR(1,1), (c) AR(1,3.5); $U_0 = 2.4$ m/s.

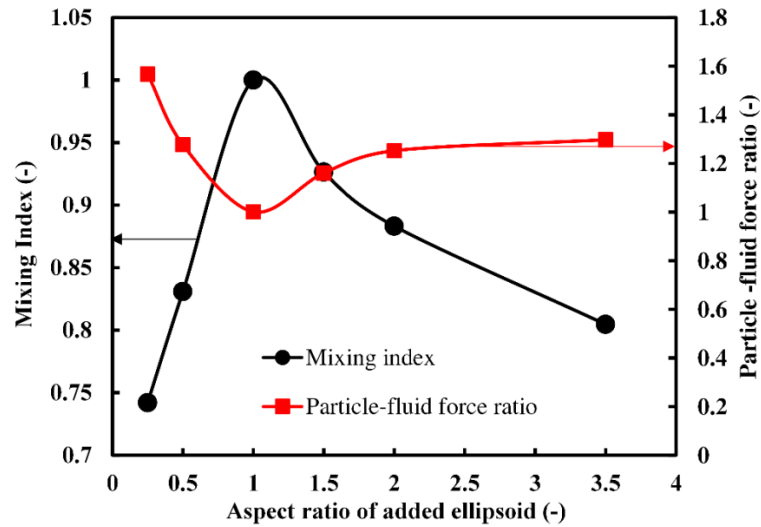
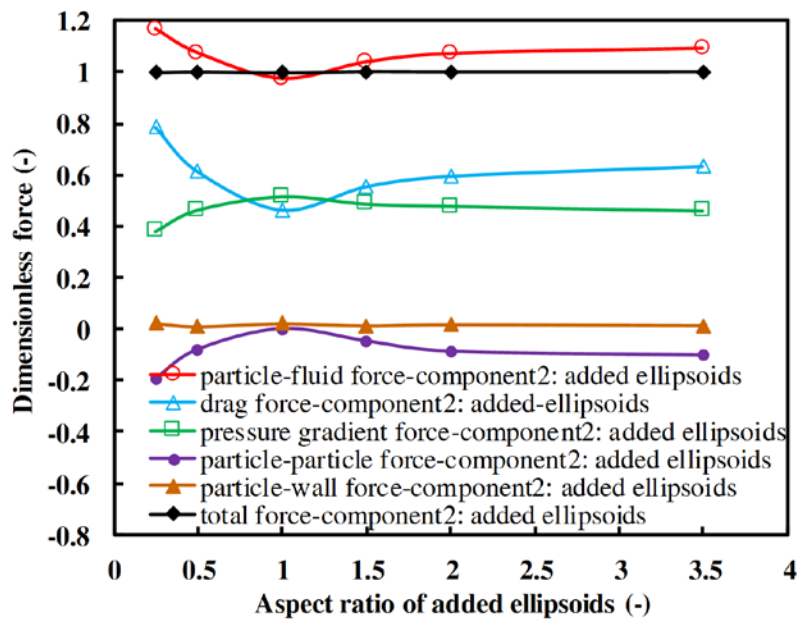
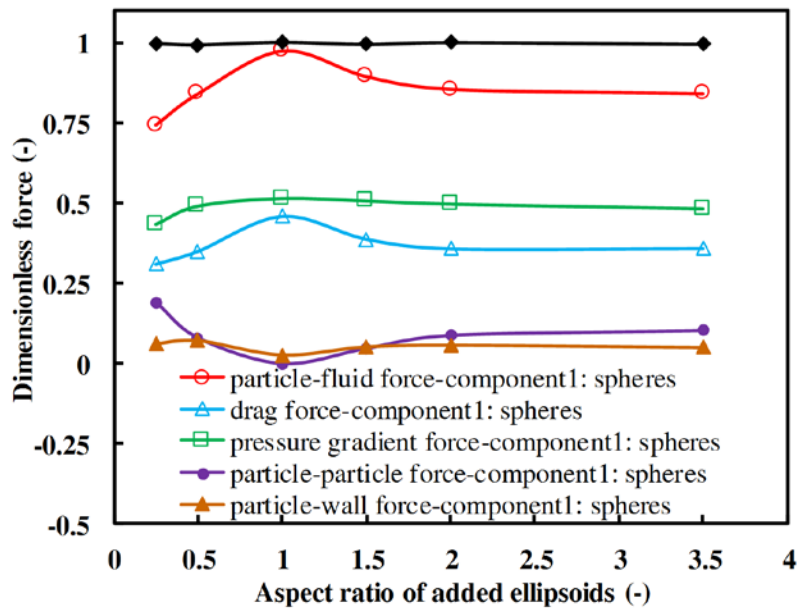


Figure 5-8. The effects of the aspect ratio of the added component to the spheres on the mixing index and particle-fluid force ratio at $U_0 = 2.4$ m/s.



(a)



(b)

Figure 5-9. Variations of temporal-spatial mean forces with the aspect ratio of the added component for both components: (a) added component (ellipsoids), and (b) spheres at $U_0=2.4$ m/s.

The ratio of the spatial-temporal mean particle-fluid interaction force on the added ellipsoids to the spatial-temporal mean particle-fluid interaction force on spheres is plotted in Figure 5-8. As it can be seen from this figure, when the added ellipsoid is a sphere, the particle-fluid force ratio is equal to one. This is because, in this situation, all particles have same characteristics, i.e., size, density, and shape. Thus, the mixing index for this binary of AR(1,1) becomes one and a perfect mixing is achieved. This further verifies the capability of the new modified drag model. On the other hand, when the shape of the added component to the spheres changes from spherical (AR=1) to prolate (AR<1) or oblate (AR>1) particles, the amount of upward particle-fluid force exerted on the oblate or prolate particles exceeds the amount of upward particle-fluid force exerted on spheres. This provides a driving force for segregation and as a result, the mixing index of binaries of spheres and oblate particles or spheres and prolate particles tends to be less than one. Figure 5-9 shows different force variations as a function of the aspect ratio of added ellipsoids for both spheres and added ellipsoids. It can be found that the effect of particles shape on the pressure gradient force is much less than the effect of particles aspect ratio on the drag force for both spheres and added ellipsoids. With decreasing the aspect ratio from 1 to 0.25 and increasing the aspect ratio from 1 to 3.5, the drag force on the added ellipsoids (Figure 5-9 (a)) increases while the drag force on the spheres decreases (Figure 5-9 (b)). The increasing the drag force for the case of added ellipsoids is because of the fact that changing the aspect ratio increases the projected area, and hence the drag force increases. This increase in the drag force leads to increase in particle-fluid force to over one. On the other hand, the drag force on spheres decreases with adding ellipsoids, and this reduces the particle-fluid force to under one. A segregation occurs as a result of the difference in particle-fluid force. This segregation is mostly affected by the effects of particles aspect ratio on the drag force. Since the upward particle-fluid

force on the added ellipsoids (Figure 5-9 (a)) is larger than one for oblate and prolate particles, the negative value of particle-particle interaction force hinders the particles to continuously move upward, and makes the total force equal force; note that the particle-wall force on added ellipsoids is almost zero. On the other hand, the particle-fluid force on spheres (Figure 5-9 (b)) is less than one for binaries including oblate and prolate as added ellipsoids. Thus, the particle-fluid force is not big enough to balance the particle weight, and the positive value of particle-particle and particle-wall force must contribute to the total force balance to make the spheres suspended in the beds. Therefore, the overall force on the whole bed is also balanced for both spheres and added ellipsoids.

5.6 Summary

A CFD-DEM model is developed to study the effects of particles shape in the binary mixtures of non-spherical particles. Spheroids are used in this work to represent non-spherical particles by varying aspect ratio from 0.25 to 3.5. A modified drag model was proposed to be implemented in CFD-DEM model. The proposed drag model can not only consider the particles shape and orientations but also the volume fraction of each component. The modified drag force presents more consistent results with experiments in comparison to drag model which was developed for mono-sized particles. This implies the significance of proper selection of drag force in the simulation of binary mixtures of non-spherical particles. In addition, it was found that adding ellipsoids to spheres causes segregation phenomenon, and it reduces the mixing index and the reason behind the bad quality of mixing under influence of particles aspect ratio is found to be the fact the drag force on the oblate and prolate particles added to spheres are greater than that on spheres, thus it causes a driving force for segregation.

Chapter 6 Mixing and Segregation Characteristics of Binary Mixtures of Ellipsoidal Particles in Liquid Fluidizations

6.1 Overview

In this chapter, CFD-DEM approach is employed to perform a systematic analysis of the effects of particle shape on the particle intermixing and segregation phenomenon in liquid fluidization systems. The modified drag model proposed in chapter 5 is used to calculate the drag force. Different particle shape from oblate to prolate particles are produced by varying aspect ratio of ellipsoids from 0.25 to 3, and eight binary mixtures of spheres and ellipsoids are examined. The results show that when particles with oblate or prolate shapes but having the same volume and density of spherical particles are added to spheres, they cause obvious segregation. The segregation becomes more significant with increasing or decreasing particle aspect ratio from 1.0 and liquid superficial velocity. The relationship of mixing index with aspect ratio under different liquid velocities is established, and a detailed explanation is given. It is revealed that increasing the projected area and hence the drag force results in the separation of ellipsoidal particles from spheres.

6.2 Introduction

As discussed in the section 2.3.3.2 of Chapter 2, the particle shape effects have not been well studied. From literature survey, it is found that except two experiments (Barghi et al., 2003; Escudié et al., 2006a), most of the previous works considered particles as spherical. Up to date, no numerical studies on the liquid fluidizations of non-spherical particles has been conducted in the literature. Note that particles are highly irregular in the most of practical processes (Escudié et al., 2006a) such as ore beneficiations using liquid-solid fluidized beds separator (Tripathy et al., 2017). The observations show that particles shape can have an influence on the mixing of particles in liquid fluidizations. However, the understanding of the underlying mechanisms is little known and there is a need to investigate the effect of particle shape on the mixing and segregation of particle mixtures in liquid fluidizations. To achieve this goal, numerical modelling is used in this chapter. The CFD-DEM model is used to investigate the role of particles shape on the mixing and segregation in liquid fluidizations. In the simulations, ellipsoid particles are used to study the shape factor since they can present a wide range of particles shape from oblate to prolate shapes. Different ellipsoids are generated by varying the particle aspect ratio (varying from 0.25 to 3). Eight binary mixtures of spheres and ellipsoids are produced and examined, and the mixing quality is quantified by means of the Lacy mixing index.

6.3 Model descriptions and Simulation Conditions

Please refer to the section of 5.3 of chapter 5 for the descriptions of CFD-DEM model. The physical and geometrical parameters implemented in the present simulations are listed in Table 6-1. A rectangular slot that the thickness is much less than the width and height is used to

Chapter 6 Mixing and Segregation Characteristics of Binary Mixtures of Ellipsoidal Particles in Liquid Fluidizations

carry out the simulations. For this geometry, 2-D CFD and 3-D DEM are used, which was also successfully employed in the previous studies (Feng et al., 2004; Zhou et al., 2011). In this work,

Table 6-1. Parameters used in the present simulations.

Particle phase	
Density (ρ_p), $kg.m^{-3}$	2000
Equivalent diameter (d_p), mm	7
Particle shape	Oblate, sphere, and prolate
Particle Aspect Ratio (AR), -	0.25, 0.5, 0.65, 0.8, 1, 1.13, 1.5, 2, 3
Number of particles (N), -	6000
Young's modulus (E), $N.m^{-2}$	1.0×10^8
Poisson's ratio (ν), $N.m^{-2}$	0.4
Sliding friction coefficient (μ), -	0.3
Damping Coefficient (c_n), -	0.3
Time step (Δt), s	2.5×10^{-6}
Liquid phase	
Viscosity (μ_f), $kg.m^{-1}.s^{-1}$	0.001
Density (ρ_f), $kg.m^{-3}$	1000
Bed geometry	
Width (W), m	0.2
Height (H), m	1.0
Thickness (D), m	$4d_p$
Size of CFD cells	$2d_p \times 2d_p$
Bed distributor	Uniform
Time step (Δt), s	2.5×10^{-6}

spheroids are used to generate particles with different shapes from oblate (disc-shaped) to prolate (elongated) particles. Spheroids are composed of three radii: a is assigned to the radius in the polar direction, and b and c are considered as the radii in the equatorial plane. In order to perform a systematic analysis of the effects of particles shape on the mixing quality of binary mixtures, all

Chapter 6 Mixing and Segregation Characteristics of Binary Mixtures of Ellipsoidal Particles in Liquid Fluidizations

properties of particles (i.e., volume and density) except shape and the volume fraction of each component (50 % by volume) remain constant in all simulation cases. Each binary mixture is generated by a combination of spherical particles (50% by volume) and spheroids (50% by volume) with a specific aspect ratio (i.e., $AR = 0.25, 0.5, 0.65, 0.8, 1, 1.13, 1.5, 2, 3$). Each spheroid has the same volume and density as spherical particles. Note that a mixture of spheres and ellipsoids is presented in the format of $AR(\psi_1, \psi_2)$, where AR stands for Aspect Ratio, ψ_1 is the aspect ratio of component 1 - spheres, and ψ_2 is the aspect ratio of component 2 - added ellipsoids. In this work, eight different binary mixtures are studied to figure out that when particles shapes gradually change from oblate shape to a sphere and then elongated shape, how this change affects the mixing quality of mixtures.

In this chapter, the mixing quality of a mixture is quantified by Lacy mixing index (Lacey, 1954) as given explained in the section of 5.4 of chapter 5.

6.4 Results and discussion

6.4.1 Flow patterns and mixing quality

Figure 6-1 shows the particles flow pattern for binary mixtures of spheres and oblate particles at different liquid superficial velocities. Note that the initial bed configurations before injecting the liquid is fully segregated (Figure 6-1 (a)). It can be observed that for the mixture of $AR(1, 0.5)$, the bottom region of the bed is occupied by spherical particles for the whole range of velocities, which is consistent with the observations by Escudié et al. (2006a). However, this region becomes more distinct at higher velocities. At $U_0=0.09$ m/s, some spherical particles percolate into the top part and make a partially mixed region, and no region with only oblate

Chapter 6 Mixing and Segregation Characteristics of Binary Mixtures of Ellipsoidal Particles in Liquid Fluidizations

particles can be differentiated. As the liquid velocity increases, two components intend to segregate more noticeably. As a result, a clearer interface is created between two layers at higher velocities. With aspect ratio increasing to $AR=0.8$ (case II in Figure 6-1), the mixture presents different behavior. At $U_0=0.09$ m/s, a partial mixing can be seen in the whole bed with the bottom section rich in spherical particles and the top section rich in oblate particles. With increasing the velocity, these sections become richer in one component. Yet, the degree of segregation is not as high as that of the mixture $AR(1,0.5)$. It is due to the fact that oblate particles with $AR=0.8$ are closer to spherical particles than those with $AR=0.5$, and this causes the segregation more difficult. Hence, particles intend to mix and this is further shown in Figure 6-2.

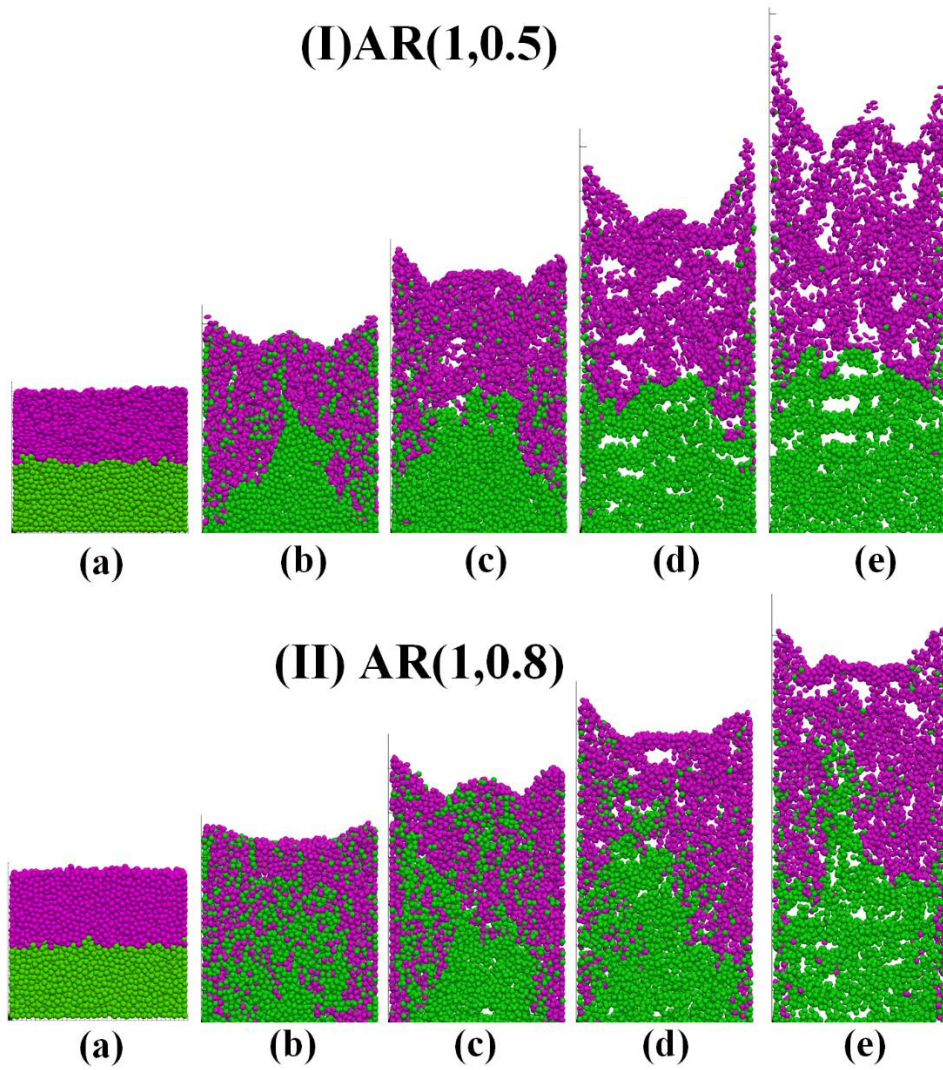


Figure 6-1. Solids configurations for binary mixtures of oblate particles and spheres: (I) AR(1,0.25), (II) AR(1,0.8) at different liquid velocities: (a) 0 m/s; (b) 0.09 m/s; (c) 0.13 m/s; (d) 0.16 m/s; (e) 0.19 m/s.

Chapter 6 Mixing and Segregation Characteristics of Binary Mixtures of Ellipsoidal Particles in Liquid Fluidizations

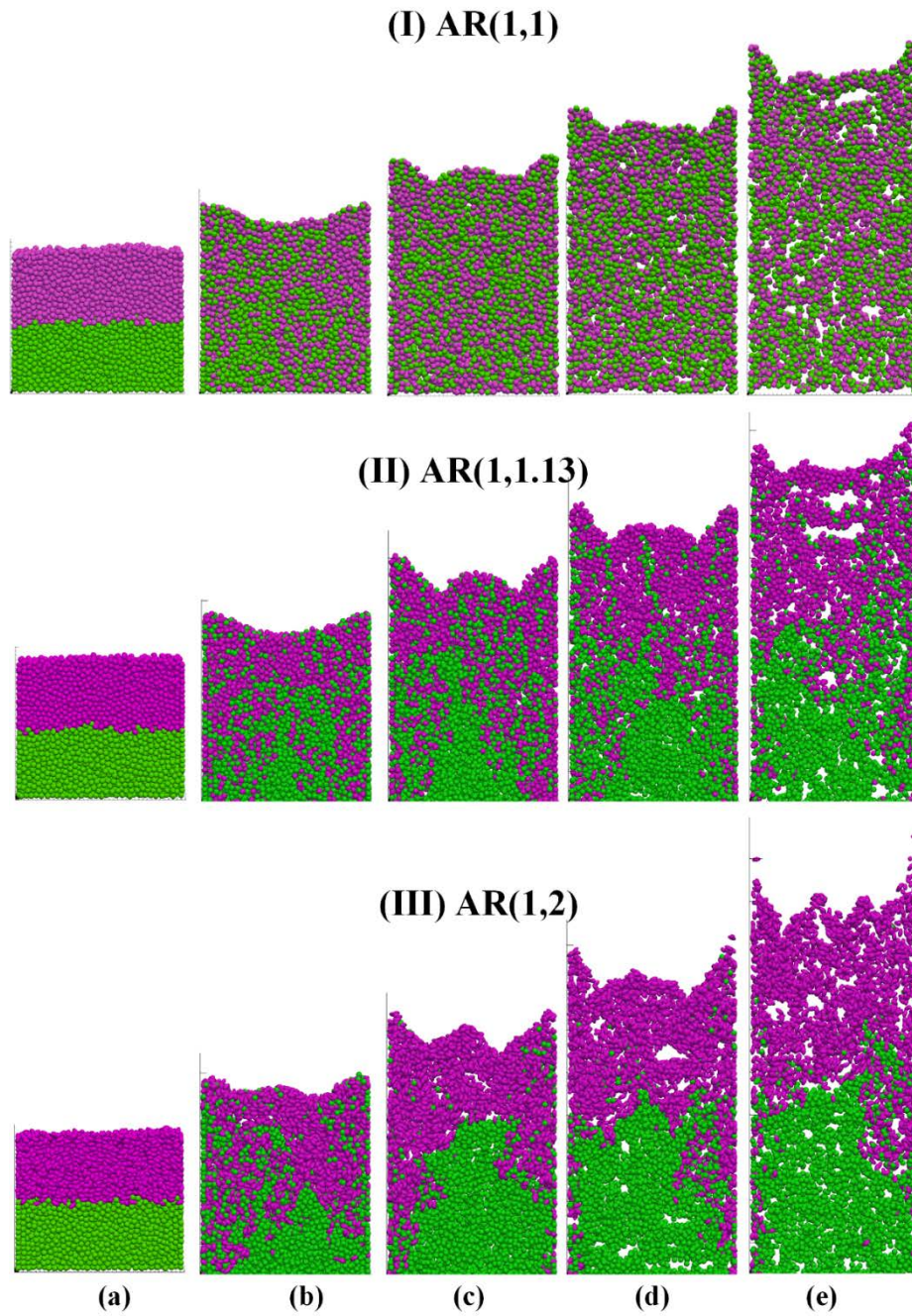


Figure 6-2. Solids configurations for different binary mixtures: (I) AR(1, 1), (II) AR(1, 1.13), and (III) AR(1, 2) at different liquid velocities: (a) 0 m/s; (b) 0.09 m/s; (c) 0.13 m/s; (d) 0.16 m/s; (e) 0.19 m/s.

Chapter 6 Mixing and Segregation Characteristics of Binary Mixtures of Ellipsoidal Particles in Liquid Fluidizations

Figure 6-2 displays the particle flow patterns of binary mixtures of spheres and prolate particles at different liquid velocities. It can be observed that as expected, the mixture of spheres demonstrates a well-mixed particle configurations at different liquid velocities (Figure 6-2 (I)). This is because for the mixture of AR(1, 1), all particles have the same properties such as size, density and shape. However, changing the added ellipsoids from spherical to prolate with AR=1.13 (Figure 6-2 (II)) prevents particles from good mixing. At $U_0=0.09$ m/s for the mixture of AR(1, 1.13), partial segregation can be seen with spheres rich in the bottom section and prolate particles rich in the top. At $U_0=0.13$ m/s and higher velocities, spherical particles mostly accumulate at the bottom of the bed while they also present at the top of the bed and mix with prolate particles. As a result, two distinct regions similar to the case observed for the mixture of AR(1, 0.8) cannot be generated. For the mixture of AR(1, 2), except at $U_0=0.09$ m/s, spheres and prolate particles are segregated more significantly at higher velocities.

To further confirm whether the initial bed structures affects the final flow pattern of particles. Figure 6-3 compares the variations of mixing index with time for two mixtures of AR(1,1) and AR(1,0.8) under different initial bed conditions: well-mixed and fully-segregated. As seen from Figure 6-3 (a), the particle flow pattern and the mixing index are similar to each other at the equilibrium state. This not only confirms the validity of the model but also confirms that the initial bed configurations do not affect the particle segregation patterns at the equilibrium state. Figure 6-3 (b) also shows that for the case of initially segregated particles, the spheres and oblate particles start to intermix to each other until they reach to the mixing index of 0.75. On the other hand, when the initial bed configuration is well-mixed, two components segregate as time elapses until the mixing index approaches to the case with the fully-segregated initial bed condition.

Therefore, this further confirms the independence of the final mixing index to the initial bed configuration.

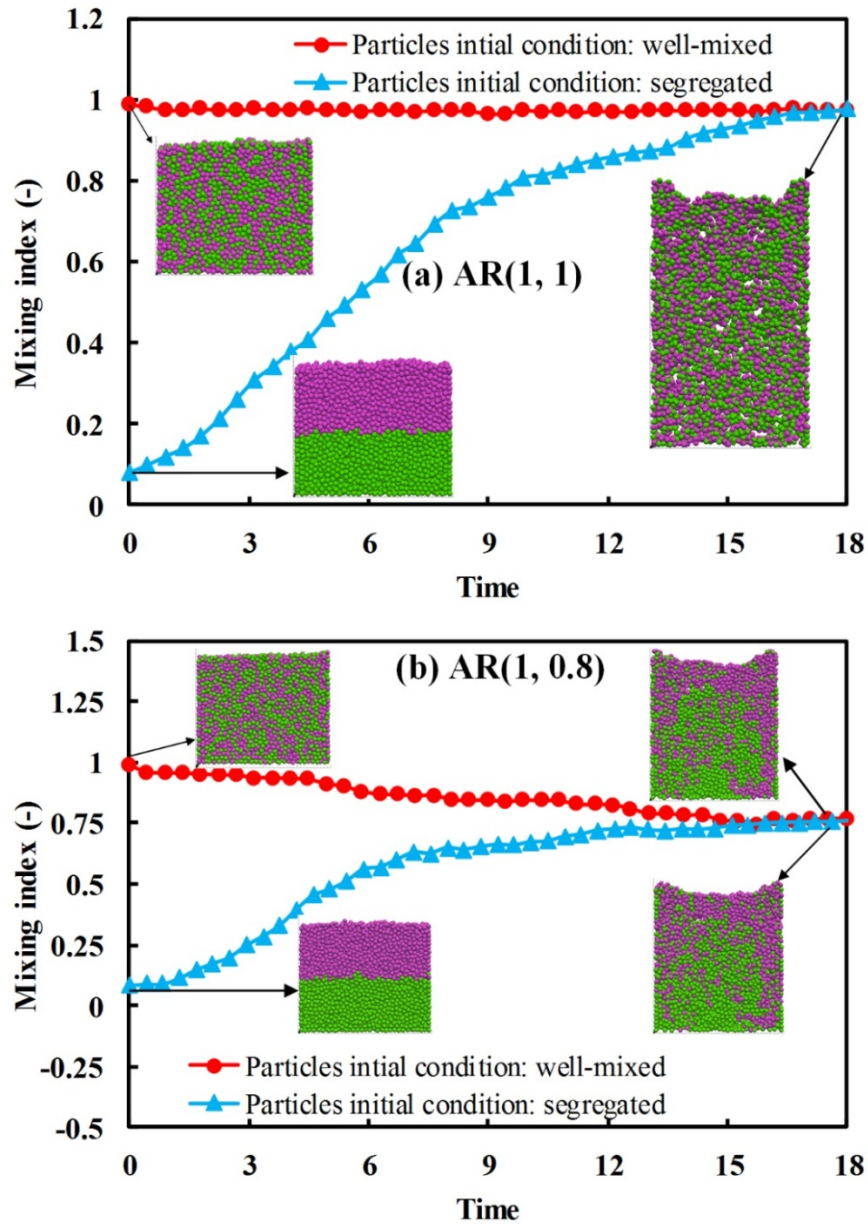


Figure 6-3. Effects of particle initial configurations on the mixing index of binary mixtures: (a) mixture of AR(1, 1); and (b) mixture of AR(1, 0.8).

The segregation under influence of particle shape for different binary mixtures can be further quantified by the vertical distribution of volume fraction of spheres. The volume fractions of

Chapter 6 Mixing and Segregation Characteristics of Binary Mixtures of Ellipsoidal Particles in Liquid Fluidizations

spheres along the bed height are recorded every 0.015 seconds in simulations, then the time-averaged volume fraction of spheres is plotted in Figure 6-4. Figure 6-4(a) shows that the binary mixture of spheres and oblate particles with $AR=0.25$ displays two distinct layers at different velocities. For example, from the bottom of the bed to the height of 0.13 m, spheres are located at the bottom with the volume fraction of almost 1.0, and then the volume fraction of spheres reduces sharply to 0.08 and then becomes zero above the height of 0.2 m. On the other hand, other binary mixtures (Figure 6-4 (b-d)) do not generate such a sudden variation in the volume fraction of spheres along the bed height, demonstrating less clear interface between spheres and ellipsoids.

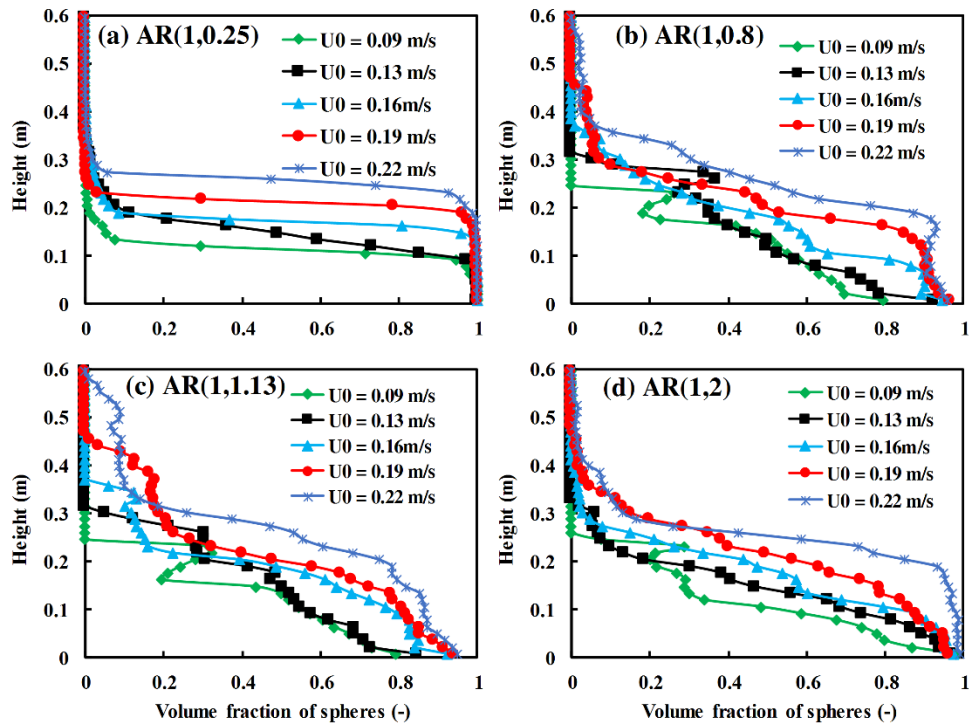


Figure 6-4. Variation of the volume fraction of spheres along the bed height for different binaries at different liquid superficial velocities.

Chapter 6 Mixing and Segregation Characteristics of Binary Mixtures of Ellipsoidal Particles in Liquid Fluidizations

Figure 6-4 (b) shows that the volume fraction of spheres at the bottom cannot reach 1.0 even at higher velocities. This implies that the mixture of AR(1,0.8) has less tendency to segregate than the mixture of AR(1,0.25). From Figure 6-4 (c-d), it also can be found that increasing the liquid velocity increases the volume fraction of spheres at the bottom section, facilitating the segregation. Sharper changes in variations of spheres volume fractions with height can be observed for the mixture of AR(1,2) than the mixture of AR(1,1.13). This indicates that as the added ellipsoids become more elongated, the mixing region between two distinct layers, which are rich in each component, becomes narrower.

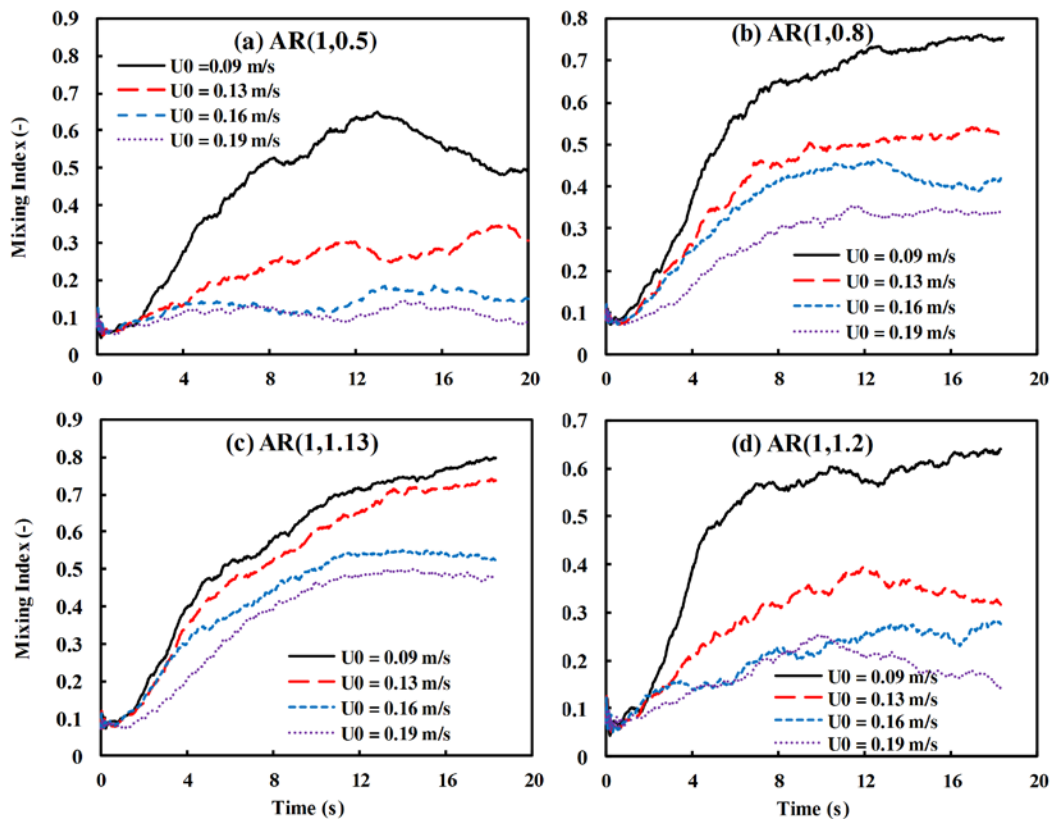


Figure 6-5. Mixing index variations with time for different liquid superficial velocities and different mixtures: (a) AR(1, 0.5); (b) AR(1, 0.8); (c) AR(1, 1.13); and (d) AR(1, 1.2).

6.4.2 Mixing index

The variation of mixing index with time for different binary mixtures of spheres and added ellipsoids at different liquid velocities are presented in Figure 6-5. Note that the non-zero value of mixing index at the initial stage, where particles are segregated, is a result of the sampling cell locations as some samples could include two different shaped particles; hence binary mixtures with the mixing indices less than 0.13 (the initial mixing index) are considered as fully segregated. Generally speaking, the mixing index increases with time, indicating that the bed gradually changes from full segregated to partially mixed, and the final state depends on the liquid velocity and aspect ratio of added ellipsoids. Increasing the liquid velocity not only decreases the final mixing index but also reduce the time to reach a stable condition.

The spatial-temporal averaged mixing indices as a function of liquid superficial velocities for different binary mixtures are plotted in Figure 6-6. Generally, the mixing index decreases with increasing the liquid superficial velocities. This implies that the higher liquid velocities cause two types of particles to become more segregated. The declining trend of mixing index for different mixtures of spheres and oblate particles are similar to each other except for the mixture of AR(1,0.25). The mixing index drops until $U_0=0.19$ m/s and then almost becomes constant, indicating the independence of mixing index after a specific velocity. Note that the mixing index for the mixture of AR(1,0.25) is less than 0.13 - the mixing index value for fully segregated bed, it can be concluded that no mixing happens for this mixture. Spheres and oblate particles with AR=0.25 intend to segregate completely. On the other hand, it can be observed that the mixing index for the mixture AR(1,1.13) decreases with increasing velocity from 0.09 m/s to 0.16 m/s and then it almost remains constant (Figure 6-6 (b)). This shows that further increase in liquid

Chapter 6 Mixing and Segregation Characteristics of Binary Mixtures of Ellipsoidal Particles in Liquid Fluidizations

velocity does not result in more segregation. The mixing index of the mixtures of AR(1,2) and AR(1,3), however, drops at higher velocities until a complete segregation is achieved.

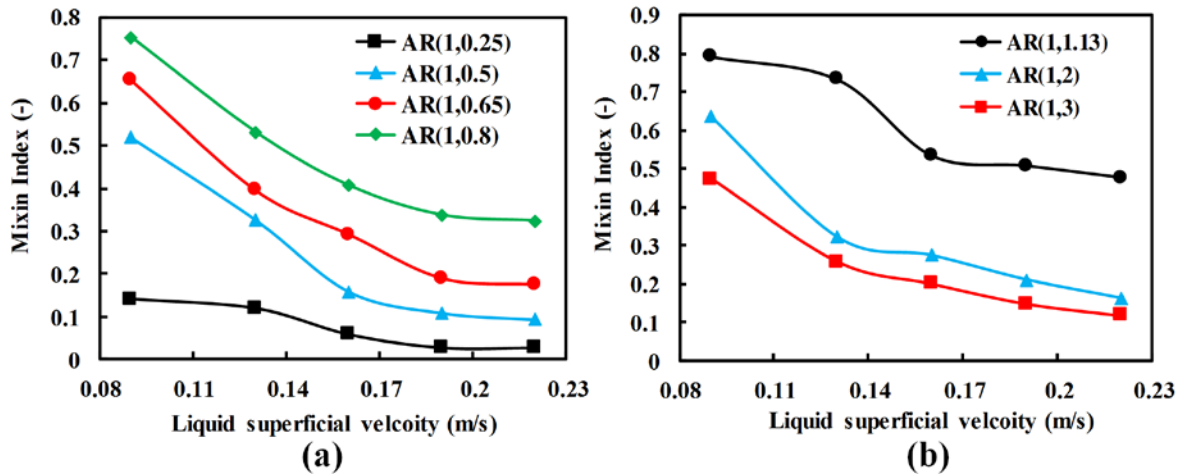


Figure 6-6. The effects of liquid superficial velocity on the temporal-spatial averaged mixing index of different binaries of ellipsoids and spheres: (a) binaries of oblate particles and spheres, (b) binaries of prolate particles and spheres.

Figure 6-7 illustrates the effect of aspect ratio of added ellipsoids on the mixing index at different velocities. It can be seen that as expected, the maximum mixing index happens when the aspect ratio of added ellipsoids is 1.0 which are spheres. When the aspect ratio of added ellipsoids is decreased from 1 to 0.25 (oblate particles), the mixing index declines significantly. The similar phenomena can be observed when the aspect ratio is increased from 1.0 to 3 (prolate particles), but the decreasing trend is smoother than oblate particles. With increasing the liquid velocity, the mixing index drops sharply with changing the aspect ratio from 1.0 to below or above one.

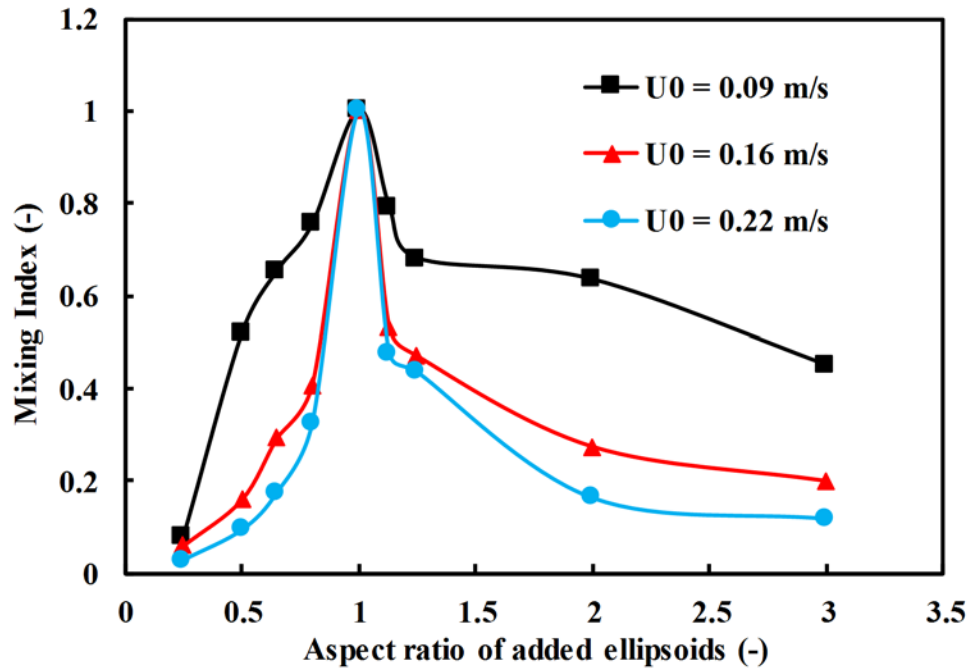


Figure 6-7. Mixing index variation with respect to the aspect ratio of added ellipsoids to spheres at different liquid velocities.

6.4.3 Force Analysis

The segregation of binary mixtures can be explained by the forces acting particles, including particle-particle and particle-fluid interaction force. Therefore, analyzing these forces can help in a better understanding of the segregation occurring due to particle shape effects. Figure 6-8 shows the distributions of the drag force, the pressure gradient force, the particle-particle interaction force, and particles velocity in the bed for three binary mixtures of AR(1,0.8), AR(1,1) and AR(1,2) when $U_0=0.09$ m/s. Starting from the mixture of AR(1,0.8), the drag force distribution on added ellipsoids is mostly coloured by green while the drag force on spheres is generally coloured by light blue. This indicates that the added ellipsoids have higher drag forces than spheres. The pressure gradient force distribution (Figure 6-8(b), top row) shows that in some

Chapter 6 Mixing and Segregation Characteristics of Binary Mixtures of Ellipsoidal Particles in Liquid Fluidizations

regions the pressure gradient force is higher than other regions. These regions can correspond to the regions with high particle-particle contacts (Figure 6-8(c), top row) or dense regions. Nonetheless, no significant pressure gradient force difference on spheres and added prolate particles can be observed. The particle velocity field for this mixture demonstrates six particle circulation loops in the bed. The two loops at the bottom of the bed are responsible for the circulation of spherical particles, while the two loops in the middle mostly cause a mixing of spheres and prolate particles which are mostly found at the top of the bed. Two side loops also convey prolate particles to the bottom and take some spherical particles to the top, resulting in a mixed region near the side walls.

For the mixture of AR(1,1), the drag and pressure gradient forces are more uniform than the mixture of AR(1,0.8). It can be observed that for the bed containing identical spherical particles, two symmetric vortices are generated in the middle and two near the side walls. Particles can ascend from the side wall region or from the middle of the bed. These four circulation loops generate a good mixing in the bed. When the aspect ratio of added ellipsoids increases to 2, the symmetric circulation loops are altered into arbitrary circulation patterns with different sizes (Figure 6-8 (d), bottom row). These small vorticities only cause local mixing and most of the spheres located in the bottom section of the bed are not involved in the mixing process. This might be due to the fact that the drag force distribution on added prolate particles displays greater values than spheres (Figure 6-8 (a), bottom row), considering the similarity of pressure gradient force distribution on spheres and prolate particles (Figure 6-8(b), bottom row).

Chapter 6 Mixing and Segregation Characteristics of Binary Mixtures of Ellipsoidal Particles in Liquid Fluidizations

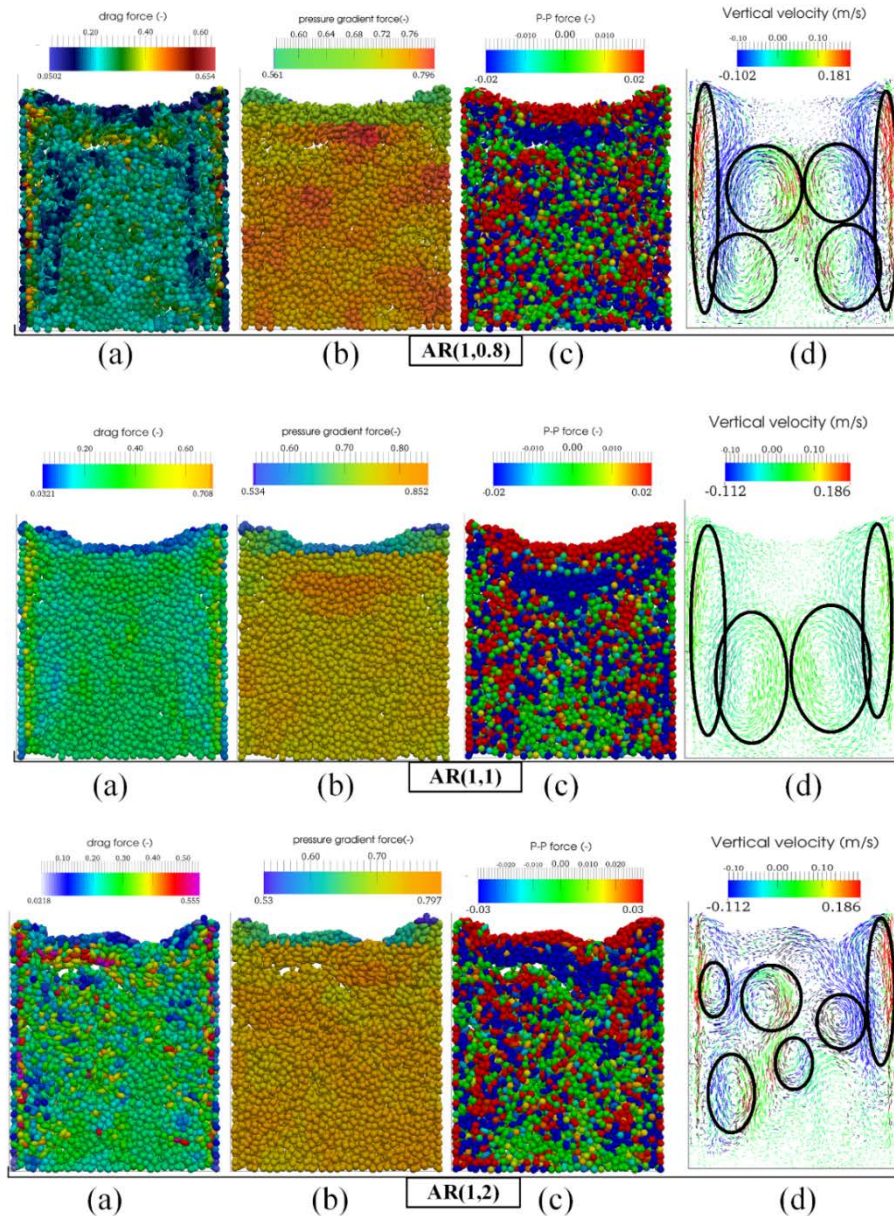


Figure 6-8. The snapshots of particles configuration at steady state conditions coloured by different forces when $U_0=0.09$ m/s: (a) drag force, (b) pressure gradient force, and (c) particle-particle force; (d) particles velocity field coloured and sized by vertical velocity. Note that the top row is for the mixture of AR (1, 0.8), the middle row is for the mixture of AR(1,1) and the bottom row is for the mixture of AR(1,2).

Regarding the above discussion, it is believed that the segregation phenomenon due to particle shape dissimilarity is inherited in the role of particle-particle and particle-fluid (the drag and the pressure gradient) interaction forces. Thus, it is essential to perform quantitative force

Chapter 6 Mixing and Segregation Characteristics of Binary Mixtures of Ellipsoidal Particles in Liquid Fluidizations

analysis. Note that segregation mostly happens in the vertical direction, the forces in the vertical direction are only analyzed in this work. The spatial mean forces are defined as follows. For the component with larger aspect ratio, the particle-particle, particle-wall and particle-fluid interaction forces are respectively defined as $\langle |\mathbf{f}_{pp,L}| \rangle = \sum_{i=1}^{N_L} \left[\left(\sum_{j=1}^{k_{c,i}} \mathbf{f}_{pp,ij} / (m_L \mathbf{g}) \right) \right] / N_L$, $\langle |\mathbf{f}_{pw,L}| \rangle = \sum_{i=1}^{N_L} \left[\left(\mathbf{f}_{pw,i} / (m_L \mathbf{g}) \right) \right] / N_L$, and $\langle |\mathbf{f}_{pf,L}| \rangle = \sum_{i=1}^{N_L} \left[\left(\mathbf{f}_{pf,i} / (m_L \mathbf{g}) \right) \right] / N_L$, where N_L is the number of particles with larger aspect ratio, $k_{c,i}$ is the number of particles contacting with particle i , $\mathbf{f}_{pp,ij}$ is the particle-particle interaction force between particles i and j , $\mathbf{f}_{pw,i}$ is the particle-wall interaction force between particle i and the wall, and $m_L \mathbf{g}$ is the weight of the particle with larger aspect ratio. Note that the notations $||$ and $\langle \rangle$ stand for the magnitude and average of the variable, respectively. The spatial-temporal mean forces are also calculated by averaging the spatial mean forces over the steady-state time period. Spatial-temporal mean forces acting on another component- with smaller aspect ratio - can be calculated in the same manner.

Here the force analysis is carried out for three selected binary mixtures at a specific velocity in order to avoid repetition. The spatial-averaged forces as a function of time for binary mixtures of AR(1, 0.8), AR (1, 1), and AR (1, 2) at $U_0=0.09$ m/s are plotted in Figure 6-9. For the mixture of AR(1,0.8), it can be seen that the pressure gradient force on the spheres and oblate particles are almost identical. However, the drag force on oblate particles is greater than that of spheres. This produces a larger total particle-fluid interaction force on oblate particles than that of spheres. As a result, this driving force causes segregation among spheres and added oblate particles. The particle-fluid interaction force on spheres is bigger than one, so the negative value of particle-particle interaction force prevent particles to leave the bed and it also balances the total force to

Chapter 6 Mixing and Segregation Characteristics of Binary Mixtures of Ellipsoidal Particles in Liquid Fluidizations

be one. On the other hand, the particle-fluid interaction force on the spheres is less than one, which indicates that in order to make the spheres suspended in the bed the positive particle-particle interaction force from added oblate particles are required. The particle-wall interaction forces on both components are negligible. When the aspect ratio of the added ellipsoid is one (Figure 6-9 (b)), all forces on the two components are equal as expected, this is because the two types of particles are identical in this binary mixture. Hence, there is no driving force between the two components to separate, and a good mixing is observed in this case. On the other hand, similar to the case of AR(1,0.8), the drag force on the added prolate particles is bigger than that of spheres and this leads to separation of spheres and prolate particles (AR=2).

The effects of the aspect ratio of added ellipsoids on the mixing index as demonstrated in Figure 6-7 can be clarified by analyzing the drag force (note that the pressure gradient force acting on two types of particles are almost identical as demonstrated in Figure 6-9). Figure 6-10 shows the variations of mixing index, the drag force ratio, and the projected area ratio as a function of the aspect ratio of the added ellipsoids. Here, the drag force ratio is defined as the ratio of the drag force on added ellipsoids to the drag force on spheres, and the projected area ratio is similarly defined. It can be seen that when the aspect ratio of added ellipsoids is equal to one, the drag force ratio is also equal to one and there is no driving force for segregation. However, when the aspect ratio distorts from one, the drag force ratio on the added ellipsoids become larger than one. This implies that two types of particles receive a different amount of drag force and this leads to separation of the two components. The reason behind such a variation of drag force with aspect ratio can be found in the variation of the projected area ratio with changing the aspect ratio. Changing the particles shape from spherical to oblate or prolate ones

Chapter 6 Mixing and Segregation Characteristics of Binary Mixtures of Ellipsoidal Particles in Liquid Fluidizations

generates larger projected area and consequently larger drag force. Therefore, the mixing quality under influence of particles shape is explicitly related to the particle scale force variations, particularly the drag force.

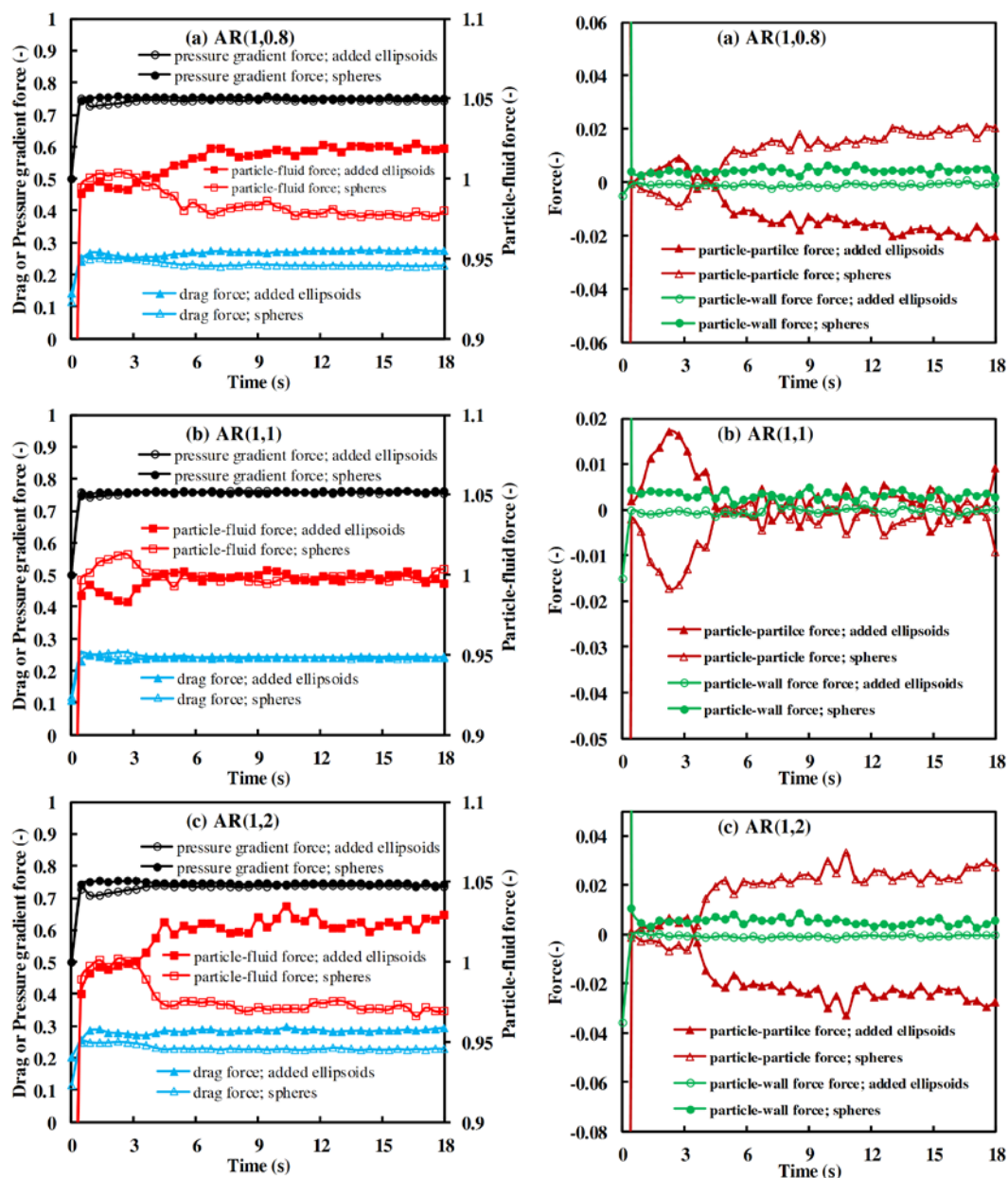


Figure 6-9. Spatial-averaged forces variations with time for different binaries: first row: binary of oblate particles (AR=0.8) and spheres, second row: binary of identical spheres, binary of oblate particles (AR=0.8) and spheres, binary of prolate particles (AR=2) and spheres. Note that right

column presents the drag force, pressure gradient force, and particle-fluid force and left column shows the particle-particle interaction force and the particle-wall interaction force.

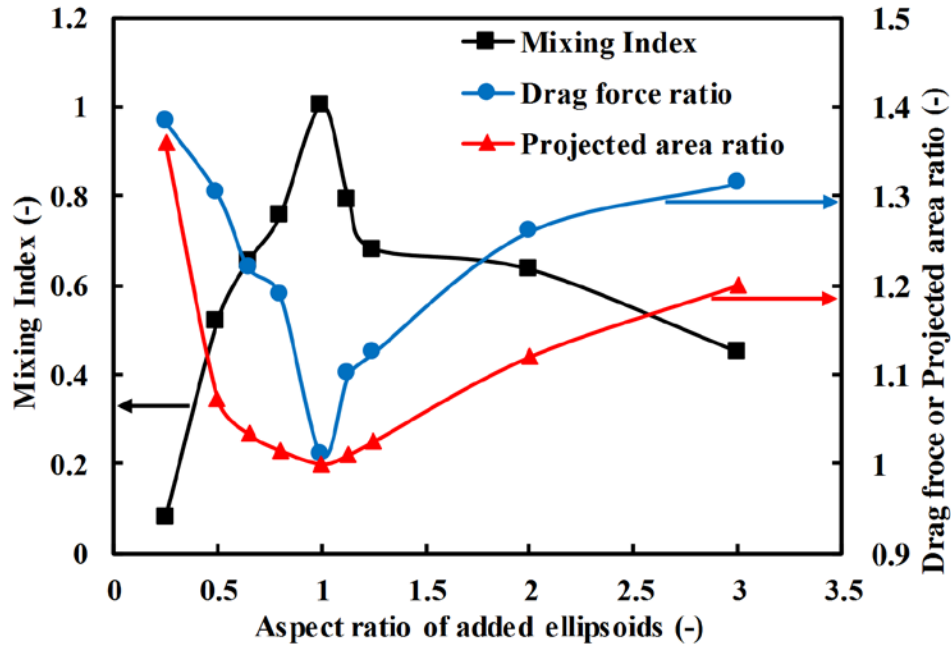


Figure 6-10. Mixing index, drag force ratio, and projected area ratio as a function of the aspect ratio of the added ellipsoids when $U_0 = 0.09$ cm/s.

6.5 Summary

In summary, we used CFD-DEM model to study the mixing and segregation phenomenon under influence of particle shape in solid-liquid fluidized beds. Eight binary mixtures of spheres and ellipsoids are examined. The special cases for the mixture of AR (1, 1) and the different initial bed configures are also included in the discussion to support the results simulated. We found that particles shape clearly affects the mixing and segregation phenomenon in liquid fluidized beds. When the aspect ratio of the added ellipsoids changes from one to above or below one, a transient segregation phenomenon is observed. In addition, increase in liquid superficial velocity results in decreasing the mixing index. Thus, more clear segregation occurs at higher liquid velocity. The reason behind the segregation due to particle shape effect is found to be the

Chapter 6 Mixing and Segregation Characteristics of Binary Mixtures of Ellipsoidal Particles in Liquid Fluidizations

role of the particles shape on the amount of the drag force that a particle receives when particle shape varies.

Chapter 7 Conclusions and Recommendations for Future Work

7.1 Conclusions

This thesis aims to investigate the underlying mechanism behind the mixing and segregation phenomenon in a particle scale in fluidized beds. This aim has been achieved with the help of an advanced combination of Computational Fluid Dynamics and Discrete Element Method (CFD-DEM). Two specific types of segregation have been studied: The first one is called layer inversion phenomenon and the other one is the segregation under influence of particles shape. In the latter case, ellipsoidal particles, which can represent a wide variety of shape from disc-shaped particles to elongate-shaped particles, are used in order to consider particles shape in the model. The key findings are briefly summarized below:

In chapter 3, layer inversion phenomenon in solid-liquid fluidized beds was comprehensively studied using CFD-DEM. It is revealed that the layer inversion is caused by the differences of particle-fluid interaction forces acting on large and small particles. When liquid velocity increases, the pressure gradient decreases and the fluid drag force increases. For large particles, the decreasing rate of the pressure gradient force exceeds the increasing rate of drag force, causing the total particle-fluid interaction force on large particles to decrease from above 1.0 to below 1.0. Hence, large particles move downward. But for small particles, the decreasing rate of the pressure gradient force is less than the increasing rate of the drag force, causing the total particle-fluid interaction force on small particles to increase from below 1.0 to above 1.0 and driving small particles to move upward. When the particle-fluid forces for both types of particles are 1.0, it corresponds to the well-mixed state or the layer inversion point.

Chapter 7 Conclusions and Recommendations for Future Work

The parametric studies on the layer inversion show that particles and liquid properties have significant influences on this phenomenon. Increasing in particles size and density ratios lead to a delay in layer inversion and in some cases no layer inversion happens. With increasing in liquid viscosity, the inversion velocity decreases while denser and hotter liquid increases the inversion point. It is found that the changes in inversion velocity due to changes in particles and liquid properties can be directly related to particle-fluid force on small and large particles.

Comparisons of different drag models (Cello et al., 2010; Di Felice, 1994; Rong et al., 2014; Yin and Sundaresan, 2009) have been made to figure out how different drag laws could predict the layer inversion. The results show that Di Felice (1994) model fails to regenerate the layer inversion, but Rong et al. (2014)'s model predicts the inversion velocity with better accuracy than other drag models. Nonetheless, Cello et al. (2010) and Yin and Sundaresan (2009) drag models also can reproduce the layer inversion with good agreements.

A new model has been proposed on the basis of the criterion that the ratio of dimensionless particle-fluid force on large particles to the dimensionless particle-fluid force on small particles is 1.0. The major advantage of this model is that it does not require correlations such as those needed to estimate terminal velocity, void fraction, and Richardson and Zaki indexes in previous models. The results show that the proposed model predicts the inversion velocity with a mean accuracy of 14.4 % which is the same of the best available model in the literature. Also, the maximum error by the current model is just 34% which is much less than others.

In chapter 4, the effects of particles shape on the behaviour of liquid fluidized beds of mono-sized particles were studied. It has been found that particles shape significantly affects the solid flow behaviour in liquid fluidizations. The analysis of standard deviation of pressure drop indicates that spheres have the lowest relative transition velocities (U_{cr}/U_{mf}) with bed

regimes from particulate to turbulent fluidisations, and ellipsoids have higher values. The analysis of flow patterns shows that at the same liquid velocity, oblate particles display entrainment phenomenon, but spheres and prolate particles do not. This indicates that oblate particles have low terminal velocities than spheres and prolate particles, which is found to be closely related to orientations of ellipsoids.

Particle shape also causes the non-uniformity distributions of pressure gradient and porosity along the bed height. Spheres exhibit the uniform distributions of pressure gradient and porosity, independence of liquid superficial velocity. However, at high liquid velocities, non-symmetric parentheses-shape profiles are observed for ellipsoids with maximum pressure gradient and porosity happening at a certain height. This is mainly caused by particle interlocks due to non-sphericity of particles. Elongated or platy particles are easily accumulated at high liquid velocities and locked in some regions above the distributor which results in high-pressure gradient and low porosity.

Particle shape affects the bed permeability and minimum fluidization velocity. Bed permeability decreases remarkably for ellipsoids, and spheres have the largest minimum fluidization velocity. The bed expansion can be predicted, generally showing good agreements with experiments. At the same liquid superficial velocity, spheres show minimum void fraction, and ellipsoids have more significant bed expansion. The relationships of parameters U_e and n in Richardson and Zaki's equation with aspect ratio are also discussed, illustrating the significant effect of particle shape.

Force distributions of particles along the bed height are significantly affected by particles shape. This is mainly caused by the changes of particle orientations which has been found to be responsible for the entrainment phenomenon. It is shown that the terminal velocity of prolate particles is greater than spheres at small orientation angles (e.g., 0~24 degree). However, for oblate particles, the terminal velocity is almost always less than spheres, and

also prolate particles in the range of 0~64 degrees. As a result, at the same operating liquid velocity, oblate particles intend to be entrained to the freeboard region.

In chapter 5, a modified drag force model applicable to multicomponent was proposed and it was validated against the experimental data for the case of gas-fluidized beds. The modified drag force presents more consistent results with experiments in comparison to drag model which was developed for mono-sized particles. This implies the significance of proper selection of drag force in the simulation of binary mixtures of non-spherical particles. Adding ellipsoids to spheres causes segregation phenomenon, and it reduces the mixing index. Mixtures of oblate and spheres exhibit significant segregation while adding prolate particles to spheres causes less reduction in mixing index. In addition, when ellipsoids are mixed with spheres, they decrease the minimum fluidization velocity of particles, resulting in fluidization at a lower velocity. In addition, the reason behind the bad quality of mixing under influence of particles aspect ratio is found to be the effects of particles aspect ratio on the particle-fluid interaction force, particularly the drag force. The drag force on the oblate and prolate particles added to spheres are greater than that on spheres, thus it causes a driving force for segregation.

In chapter 6, the mixing and segregation phenomenon under influence of particles shape in solid-liquid fluidized beds were investigated. It was found that particles shape clearly affects the mixing and segregation phenomenon in liquid fluidized beds. When the aspect ratio of the added ellipsoids changes from one to above or below one, a transient segregation phenomenon is observed. In all binary mixtures of spheres and ellipsoids, some spherical particles intend to accumulate at the bottom and some of them make a partial mixing with ellipsoids. This might be attributed to the effects of particle shape on the particles circulation loops. Overall, the more the aspect ratio distorts from one, the more segregation is produced in the bed. Furthermore, increase in liquid superficial velocity results in decreasing the mixing index. Thus, more clear segregation occurs at higher liquid velocity. Nonetheless, for the

mixtures of spheres and oblate particles, the mixing index remains constant after specific liquid velocity. This velocity corresponds to the maximum segregation that can be achieved under influence of particles shape. In addition, the reason behind the segregation due to particle shape effect is found to be the role of the particles shape on the amount of the drag force that a particle receives when particle shape varies. The oblate and prolate particle have larger projected area compared to spherical particles and this leads to receiving larger drag force than that of spherical and hence a driving force is created and segregation happens.

7.2 Recommendations for Future Work

The inversion phenomenon in liquid fluidized beds was investigated in particle scale, and a new mathematical model was also proposed in this thesis. Nonetheless, some works related to this topic is suggested for the future studies. The prediction of inversion velocity by conducting experiments, performing simulations, or using mathematical models can be expensive, time-consuming, and inconvenient, respectively. On the other hand, proposing a general phase diagram that inversion velocity can be directly and conveniently extract from it could be a better mean to calculate the inversion velocity. This phase diagram can be based on some dimensionless number developed from particles and fluid properties. Needless to say that an extensive set of inversion velocity data for different binaries for a wide range of particles and liquid properties is needed to develop such a phase diagram. In addition, the effects of particles shape on the inversion phenomenon have not been investigated. Thus there is a need to figure out when particles shape change from spherical to non-spherical, how that would affect the inversion phenomenon.

In terms of the effects particles shape on the flow characteristics of fluidized beds as well as on the mixing/segregation phenomenon in fluidized beds, more works need to be conducted. For example, it was reported in this thesis that the minimum fluidization velocity of mono-sized particles, decreases when particles shape changes from spherical to non-

Chapter 7 Conclusions and Recommendations for Future Work

spherical even the particle density volume and density is kept constant. However, the reason behind this effect has not been known. In addition, the role of bed width on the segregation and mixing phenomenon under influence of particles shape is not well known. Some research is recommended to be done in this direction to clarify such an effect.

A modified drag model was proposed in this project for the polydisperse systems of non-spherical particles, and until now, there is no such a drag model. The modified drag model was our best choice to be used in this work; however, it is not perfect. Therefore, it is suggested to propose a new drag force correlation for multicomponent of non-spherical particles. This could be performed by employing some direct methods such as Lattice Boltzmann Method (LBM)-DEM.

References

- A. Howley, M., J. Glasser, B., 2002. Hydrodynamics of a uniform liquid-fluidized bed containing a binary mixture of particles. *Chemical Engineering Science* 57, 4209-4226.
- Abbaspour-Fard, M.H., 2004. Theoretical Validation of a Multi-sphere, Discrete Element Model Suitable for Biomaterials Handling Simulation. *Biosystems Engineering* 88, 153-161.
- Adema, A.T., Yang, Y., Boom, R., 2010. Discrete Element Method-Computational Fluid Dynamic Simulation of the Materials Flow in an Iron-making Blast Furnace. *ISIJ International* 50, 954-961.
- Allen, K.G., von Backström, T.W., Kröger, D.G., 2013. Packed bed pressure drop dependence on particle shape, size distribution, packing arrangement and roughness. *Powder Technology* 246, 590-600.
- Alobaid, F., Ströhle, J., Epple, B., 2013. Extended CFD/DEM model for the simulation of circulating fluidized bed. *Advanced Powder Technology* 24, 403-415.
- Anderson, T.B., Jackson, R., 1967. Fluid Mechanical Description of Fluidized Beds. Equations of Motion. *Industrial & Engineering Chemistry Fundamentals* 6, 527-539.
- Asif, M., 1998. Generalized Richardson-Zaki Correlation for Liquid Fluidization of Binary Solids. *Chemical engineering & technology* 21, 77-82.
- Asif, M., 2002. Predicting binary-solid fluidized bed behavior using averaging approaches. *Powder technology* 127, 226-238.
- Asif, M., 2004. The complete segregation model for a liquid fluidized bed: formulation and related issues. *Powder Technology* 140, 21-29.
- Barghi, S., Briens, C.L., Bergougnou, M.A., 2003. Mixing and segregation of binary mixtures of particles in liquid–solid fluidized beds. *Powder Technology* 131, 223-233.
- Beetstra, R., van der Hoef, M.A., Kuipers, J.A.M., 2007. Numerical study of segregation using a new drag force correlation for polydisperse systems derived from lattice-Boltzmann simulations. *Chemical Engineering Science* 62, 246-255.
- Bhattacharya, S., Dutta, B.K., 2002. Effective Voidage Model of a Binary Solid–Liquid Fluidized Bed: Application to Solid Layer Inversion. *Industrial & Engineering Chemistry Research* 41, 5098-5108.
- Brilliantov, N.V., Pöschel, T., 1998. Rolling friction of a viscous sphere on a hard plane. *Europhysics Letters* 42, 511-516.
- Cai, J., Yuan, Z., Zhao, X., 2016. Study on two-way coupling of gas–solid two-phase flow of cylindrical particles. *Powder Technology* 300, 136-145.
- Caulkin, R., Jia, X., Fairweather, M., Williams, R.A., 2010. Geometric aspects of particle segregation. *Physical Review E* 81, 051302.
- Cello, F., Di Renzo, A., Di Maio, F.P., 2010. A semi-empirical model for the drag force and fluid–particle interaction in polydisperse suspensions. *Chemical Engineering Science* 65, 3128-3139.
- Chen, X., Zhong, W., Heindel, T.J., 2017. Fluidization of cylinder particles in a fluidized bed. *Advanced Powder Technology* 28, 820-835.
- Chun, B.-S., Lee, D.H., Epstein, N., Grace, J.R., Park, A.-H.A., Kim, S.D., Lee, J.K., 2011. Layer inversion and mixing of binary solids in two- and three-phase fluidized beds. *Chemical Engineering Science* 66, 3180-3184.
- Clift, R., Grace, J., Weber, M., 1978. Bubbles, drops and particles. Academic Press, New York.

Cook, B.K., Noble, D.R., Williams, J.R., 2004. A direct simulation method for particle-fluid systems. *Engineering Computations* 21, 151-168.

Cornelissen, J.T., Taghipour, F., Escudíe, R., Ellis, N., Grace, J.R., 2007. CFD modelling of a liquid–solid fluidized bed. *Chemical Engineering Science* 62, 6334-6348.

Cui, H., Grace, J.R., 2007. Fluidization of biomass particles: a review of experimental multiphase flow aspects. *Chemical Engineering Science* 62, 45-55.

Cundall, P.A., Strack, O.D.L., 1979. A discrete numerical model for granular assemblies. *Géotechnique* 29, 47-65.

DallaValle, J.M., 1948. *Micromeritics: the technology of fine particles*. Pitman Publishing Corporation, New York.

Delaney, G.W., Morrison, R.D., Sinnott, M.D., Cummins, S., Cleary, P.W., 2015. DEM modelling of non-spherical particle breakage and flow in an industrial scale cone crusher. *Minerals Engineering* 74, 112-122.

Di Felice, R., 1994. The voidage function for fluid-particle interaction systems. *International Journal of Multiphase Flow* 20, 153-159.

Di Felice, R., 1995. Hydrodynamics of liquid fluidisation. *Chemical Engineering Science* 50, 1213-1245.

Di Renzo, A., Cello, F., Di Maio, F.P., 2011. Simulation of the layer inversion phenomenon in binary liquid–fluidized beds by DEM–CFD with a drag law for polydisperse systems. *Chemical Engineering Science* 66, 2945-2958.

Di Renzo, A., Di Maio, F.P., 2007. Homogeneous and bubbling fluidization regimes in DEM–CFD simulations: Hydrodynamic stability of gas and liquid fluidized beds. *Chemical Engineering Science* 62, 116-130.

Di Renzo, A., Di Maio, F.P., Girimonte, R., Formisani, B., 2008. DEM simulation of the mixing equilibrium in fluidized beds of two solids differing in density. *Powder Technology* 184, 214-223.

Didwania, A.K., Homsy, G.M., 1981. Flow regimes and flow transitions in liquid fluidized beds. *International Journal of Multiphase Flow* 7, 563-580.

Dolejš, V., Machač, I., 1995. Pressure drop during the flow of a Newtonian fluid through a fixed bed of particles. *Chemical Engineering and Processing: Process Intensification* 34, 1-8.

Dźiugys, A., Peters, B., 2001. An approach to simulate the motion of spherical and non-spherical fuel particles in combustion chambers. *Granular Matter* 3, 231-266.

Ehsani, M., Movahedirad, S., Shahhosseini, S., 2016. The effect of particle properties on the heat transfer characteristics of a liquid–solid fluidized bed heat exchanger. *International Journal of Thermal Sciences* 102, 111-121.

Eisfeld, B., Schnitzlein, K., 2001. The influence of confining walls on the pressure drop in packed beds. *Chemical Engineering Science* 56, 4321-4329.

Enwald, H., Peirano, E., Almstedt, A.E., 1996. Eulerian two-phase flow theory applied to fluidization. *International Journal of Multiphase Flow* 22, 21-66.

Epstein, N., 2005. Teetering. *Powder Technology* 151, 2-14.

Epstein, N., LeClair, B.P., 1985. Liquid fluidization of binary particle mixtures—II. Bed inversion. *Chemical Engineering Science* 40, 1517-1526.

Epstein, N., Leclair, B.P., Pruden, B.B., 1981. Liquid fluidization of binary particle mixtures—I: Overall bed expansion. *Chemical Engineering Science* 36, 1803-1809.

Ergun, S., 1952. Fluid flow through packed columns. *Chem. ENG. Prog.* 48, 89-94.

Escudié, R., Epstein, N., Grace, J.R., Bi, H.T., 2006a. Effect of particle shape on liquid-fluidized beds of binary (and ternary) solids mixtures: segregation vs. mixing. *Chemical Engineering Science* 61, 1528-1539.

Escudié, R., Epstein, N., Grace, J.R., Bi, H.T., 2006b. Layer inversion phenomenon in binary-solid liquid-fluidized beds: Prediction of the inversion velocity. *Chemical Engineering Science* 61, 6667-6690.

Fan, L.T., Chen, S.J., Watson, C.A., 1970. ANNUAL REVIEW Solids Mixing. *Industrial & Engineering Chemistry* 62, 53-69.

Fan, L.T., Ho, T.-C., Hiraoka, S., Walawender, W.P., 1981. Pressure fluctuations in a fluidized bed. *AIChE Journal* 27, 388-396.

Fan, R., Fox, R.O., 2008. Segregation in polydisperse fluidized beds: Validation of a multi-fluid model. *Chemical Engineering Science* 63, 272-285.

Felipe, C.A.S., Rocha, S.C.S., 2004. Time series analysis of pressure fluctuation in gas-solid fluidized beds. *Brazilian Journal of Chemical Engineering* 21, 497-507.

Feng, Y.Q., Xu, B.H., Zhang, S.J., Yu, A.B., Zulli, P., 2004. Discrete particle simulation of gas fluidization of particle mixtures. *AIChE Journal* 50, 1713-1728.

Feng, Y.Q., Yu, A.B., 2004. Assessment of model formulations in the discrete particle simulation of gas-solid flow. American Chemical Society, Washington, DC, ETATS-UNIS.

Feng, Y.Q., Yu, A.B., 2007. Microdynamic modelling and analysis of the mixing and segregation of binary mixtures of particles in gas fluidization. *Chemical Engineering Science* 62, 256-268.

Foscolo, P.U., Gibilaro, L.G., 1984. A fully predictive criterion for the transition between particulate and aggregate fluidization. *Chemical Engineering Science* 39, 1667-1675.

Freireich, B., Ketterhagen, W.R., Wassgren, C., 2011. Intra-tablet coating variability for several pharmaceutical tablet shapes. *Chemical Engineering Science* 66, 2535-2544.

Freireich, B., Kumar, R., Ketterhagen, W., Su, K., Wassgren, C., Zeitler, J.A., 2015. Comparisons of intra-tablet coating variability using DEM simulations, asymptotic limit models, and experiments. *Chemical Engineering Science* 131, 197-212.

Funamizu, N., Takakuwa, T., 1995. An improved Richardson-Zaki formula for computing mixed layer composition in binary solid-liquid fluidized beds. *Chemical Engineering Science* 50, 3025-3032.

Gan, J., 2015. DISCRETE PARTICLE SIMULATION OF PACKING, FLUIDIZATION AND HEAT TRANSFER OF ELLIPSOIDS, Chemical Engineering. Monash University, p. 325.

Gan, J., Zhou, Z., Yu, A., 2016. CFD-DEM modeling of gas fluidization of fine ellipsoidal particles. *AIChE Journal* 62, 62-77.

Gan, J.Q., Zhou, Z.Y., Yu, A.B., 2017. Micromechanical analysis of flow behaviour of fine ellipsoids in gas fluidization. *Chemical Engineering Science* 163, 11-26.

Ganser, G.H., 1993. A rational approach to drag prediction of spherical and nonspherical particles. *Powder Technology* 77, 143-152.

Ge, W., Li, J., 2003a. Macro-scale phenomena reproduced in microscopic systems—pseudo-particle modeling of fluidization. *Chemical Engineering Science* 58, 1565-1585.

Ge, W., Li, J., 2003b. Simulation of particle-fluid systems with macro-scale pseudo-particle modeling. *Powder Technology* 137, 99-108.

Ghatage, S.V., Peng, Z., Sathe, M.J., Doroodchi, E., Padhiyar, N., Moghtaderi, B., Joshi, J.B., Evans, G.M., 2014. Stability analysis in solid–liquid fluidized beds: Experimental and computational. *Chemical Engineering Journal* 256, 169-186.

Gibilaro, L.G., Di Felice, R., Waldram, S.P., Foscolo, P.U., 1986. A predictive model for the equilibrium composition and inversion of binary-solid liquid fluidized beds. *Chemical Engineering Science* 41, 379-387.

Gibilaro, L.G., Hossain, I., Waldram, S.P., 1985. On the Kennedy and Bretton model for mixing and segregation in liquid fluidized beds. *Chemical Engineering Science* 40, 2333-2338.

Gidaspow, D., 1994. *Multiphase Flow and Fluidization: Continuum and Kinetic Theory Descriptions*. Academic Press.

Goldstein, H., 1980. *Classical Mechanics*. Addison-Wesley Publishing Company.

Gopalan, B., Shahnam, M., Panday, R., Tucker, J., Shaffer, F., Shadle, L., Mei, J., Rogers, W., Guenther, C., Syamlal, M., 2016. Measurements of pressure drop and particle velocity in a pseudo 2-D rectangular bed with Geldart Group D particles. *Powder Technology* 291, 299-310.

Greenwood, J.A., Minshall, H., Tabor, D., 1961. Hysteresis Losses in Rolling and Sliding Friction. *Proceedings of the Royal Society of London. Series A. Mathematical and Physical Sciences* 259, 480-507.

Haider, A., Levenspiel, O., 1989. Drag coefficient and terminal velocity of spherical and nonspherical particles. *Powder Technology* 58, 63-70.

Hancock, R.T., 1936. The teeter condition. *Mag* 50, 90–94.

Heiss, J.F., Coull, J., 1952. The effect of orientation and shape on the settling velocity of non-isometric particles in a viscous medium,. *Chemical Engineering Process* 48, 133-140.

Hemati, M., Spieker, K., Laguérie, C., Alvarez, R., Riera, F.A., 1990. Experimental study of sawdust and coal particle mixing in sand or catalyst fluidized beds. *The Canadian Journal of Chemical Engineering* 68, 768-772.

Hertz, H., 1882. Ueber die Berührung fester elastischer Körper. *Journal für die reine und angewandte Mathematik* 1882, 156-171.

Hidalgo, R.C., Zuriguel, I., Maza, D., Pagonabarraga, I., 2009. Role of Particle Shape on the Stress Propagation in Granular Packings. *Physical Review Letters* 103, 118001.

Hilton, J., Mason, L., Cleary, P., 2010. Dynamics of gas–solid fluidised beds with non-spherical particle geometry. *Chemical Engineering Science* 65, 1584-1596.

Hölzer, A., Sommerfeld, M., 2008. New simple correlation formula for the drag coefficient of non-spherical particles. *Powder Technology* 184, 361-365.

Hoomans, B.P.B., Kuipers, J.A.M., Briels, W.J., van Swaaij, W.P.M., 1996. Discrete particle simulation of bubble and slug formation in a two-dimensional gas-fluidised bed: A hard-sphere approach. *Chemical Engineering Science* 51, 99-118.

Hu, H.H., 1996. Direct simulation of flows of solid-liquid mixtures. *International Journal of Multiphase Flow* 22, 335-352.

Hu, X., 2002. The Segregation in the Binary-Solid Liquid Fluidized Bed. *Chemical Engineering & Technology* 25, 911-915.

Ishii, H., Horio, M., 1991. The flow structures of a circulating fluidized bed. *Advanced Powder Technology* 2, 25-36.

Iwashita, K., Oda, M., 1998. Rolling Resistance at Contacts in Simulation of Shear Band Development by DEM. *Journal of Engineering Mechanics* 124, 285-292.

Jean, R.-H., Fan, L.-S., 1986. On the criteria of solids layer inversion in a liquid-solid fluidized bed containing a binary mixture of particles. *Chemical Engineering Science* 41, 2811-2821.

Johnson, K.L., 1985. Contact Mechanics. Cambridge University Press.

Kafui, K.D., Thornton, C., Adams, M., 2002. Discrete Particle-Continuum Fluid Modelling for Gas-Solid Fluidised Beds.

Knuth, M.A., Johnson, J.B., Hopkins, M.A., Sullivan, R.J., Moore, J.M., 2012. Discrete element modeling of a Mars Exploration Rover wheel in granular material. *Journal of Terramechanics* 49, 27-36.

Koch, D., Hill, R., 2001. INERTIAL EFFECTS IN SUSPENSION AND POROUS-MEDIA FLOWS. *Annual Review of Fluid Mechanics* 33, 619-647.

Kondic, L., 1999. Dynamics of spherical particles on a surface, collision-induced sliding and other effects. *Physical Review E* 60, 751-770.

Kozanoglu, B., Chanes, J.W., Cuautle, D.G.a., Jean, J.S., 2002. Hydrodynamics of large particle fluidization in reduced pressure operations: an experimental study. *Powder technology* 125, 55-60.

Krugger-Emden, H., Sudbrock, F., Wirtz, S., Scherer, V., 2012. Experimental and numerical investigation of the bulk behavior of wood pellets on a model type grate. *Granular Matter* 14, 681-693.

Ku, X.-k., Lin, J.-z., 2008. Motion and orientation of cylindrical and cubic particles in pipe flow with high concentration and high particle to pipe size ratio. *Journal of Zhejiang University-SCIENCE A* 9, 664-671.

Lacey, P.M.C., 1954. Developments in the theory of particle mixing. *Journal of Applied Chemistry* 4, 257-268.

Langston, P.A., Tüzün, U., Heyes, D.M., 1995a. Discrete element simulation of granular flow in 2D and 3D hoppers: Dependence of discharge rate and wall stress on particle interactions. *Chemical Engineering Science* 50, 967-987.

Langston, P.A., Tüzün, U., Heyes, D.M., 1995b. Discrete element simulation of internal stress and flow fields in funnel flow hoppers. *Powder Technology* 85, 153-169.

Lauder, B.E., Spalding, D.B., 1974. The numerical computation of turbulent flows. *Computer Methods in Applied Mechanics and Engineering* 3, 269-289.

Lettieri, P., Di Felice, R., Pacciani, R., Owoyemi, O., 2006. CFD modelling of liquid fluidized beds in slugging mode. *Powder Technology* 167, 94-103.

Li, L., Rempelgas, J., van Wachem, B.G., von Corswant, C., Johansson, M., Folestad, S., Rasmuson, A., 2015. Residence time distributions of different size particles in the spray zone of a Wurster fluid bed studied using DEM-CFD. *Powder Technology* 280, 124-134.

Lin, X., Ng, T.-T., 1997. A three-dimensional discrete element model using arrays of ellipsoids. *Géotechnique* 47, 319-329.

Liu, B., Zhang, X., Wang, L., Hong, H., 2008. Fluidization of non-spherical particles: Sphericity, Zingg factor and other fluidization parameters. *Particuology* 6, 125-129.

Liu, L.X., Litster, J.D., 1991. The effect of particle shape on the spouting properties of non-spherical particles. *Powder Technology* 66, 59-67.

Loth, E., 2008. Drag of non-spherical solid particles of regular and irregular shape. *Powder Technology* 182, 342-353.

Lozano, C., Zuriguel, I., Garcimartín, A., Mullin, T., 2015. Granular Segregation Driven by Particle Interactions. *Physical Review Letters* 114, 178002.

Lu, G., Third, J.R., Müller, C.R., 2015. Discrete element models for non-spherical particle systems: From theoretical developments to applications. *Chemical Engineering Science* 127, 425-465.

Ma, H., Xu, L., Zhao, Y., 2016. CFD-DEM simulation of fluidization of rod-like particles in a fluidized bed. *Powder Technology* 314, 355-366.

Malone, K.F., Xu, B.H., Fairweather, M., 2007. Numerical Investigation of the Layer-Inversion Phenomenon in Binary Solid Liquid Fluidized Beds, Proceedings of the 12th International Conference on Fluidization, pp. 297-304.

Masliyah, J.H., 1979. Hindered settling in a multi-species particle system. *Chemical Engineering Science* 34, 1166-1168.

Matsuura, A., Akehata, T., 1985. Distribution of solid particles and bed expansion in a liquid fluidised bed containing a binary mixture of particles Presented at the 50th Annual Meeting of the Society of Chemical Engineers of Japan, Yokohama, pp. 28-30, Paper C-108.

Militzer, J., Kan, J.M., Hamdullahpur, F., Amyotte, P.R., Al Taweel, A.M., 1989. Drag coefficient for axisymmetric flow around individual spheroidal particles. *Powder Technology* 57, 193-195.

Mindlin, R.D., Deresiewicz, H., 1953. Elastic spheres in contact under varying oblique forces. *Journal of Applied Mechanics* 20, 327-344.

Mobius, M.E., Lauderdale, B.E., Nagel, S.R., Jaeger, H.M., 2001. Brazil-nut effect: Size separation of granular particles. *Nature* 414, 270-270.

Moritomi, H., Iwase, T., Chiba, T., 1982. A comprehensive interpretation of solid layer inversion in liquid fluidised beds. *Chemical Engineering Science* 37, 1751-1757.

Moritomi, H., Yamagishi, T., Chiba, T., 1986. Prediction of complete mixing of liquid-fluidized binary solid particles. *Chemical Engineering Science* 41, 297-305.

Mukherjee, A.K., Mishra, B.K., 2007. Experimental and simulation studies on the role of fluid velocity during particle separation in a liquid-solid fluidized bed. *International Journal of Mineral Processing* 82, 211-221.

Munjiza, A.A., Knight, E., Rougier, E., 2011. Computational Mechanics of Discontinua. Wiley.

Nemec, D., Levec, J., 2005. Flow through packed bed reactors: 1. Single-phase flow. *Chemical Engineering Science* 60, 6947-6957.

Nienow, A.W., Rowe, P.N., Cheung, L.Y.L., 1978. A quantitative analysis of the mixing of two segregating powders of different density in a gas-fluidised bed. *Powder Technology* 20, 89-97.

Njobuenwu, D.O., Fairweather, M., 2015. Dynamics of single, non-spherical ellipsoidal particles in a turbulent channel flow. *Chemical Engineering Science* 123, 265-282.

Norouzi, H., Mostoufi, N., Mansourpour, Z., Sotudeh-Gharebagh, R., Chaouki, J., 2011. Characterization of solids mixing patterns in bubbling fluidized beds. *Chemical Engineering Research and Design* 89, 817-826.

Olaofe, O., Patil, A., Deen, N., van der Hoef, M.A., Kuipers, J., 2014. Simulation of particle mixing and segregation in bidisperse gas fluidized beds. *Chemical engineering science* 108, 258-269.

Oschmann, T., Hold, J., Kruggel-Emden, H., 2014. Numerical investigation of mixing and orientation of non-spherical particles in a model type fluidized bed. *Powder Technology* 258, 304-323.

Ottino, J.M., Khakhar, D.V., 2000. MIXING AND SEGREGATION OF GRANULAR MATERIALS. *Annual Review of Fluid Mechanics* 32, 55-91.

Ouchene, R., Khalij, M., Arcen, B., Tanière, A., 2016. A new set of correlations of drag, lift and torque coefficients for non-spherical particles and large Reynolds numbers. *Powder Technology* 303, 33-43.

Ozahi, E., Gundogdu, M.Y., Carpinlioglu, M.Ö., 2008. A Modification on Ergun's Correlation for Use in Cylindrical Packed Beds With Non-spherical Particles. *Advanced Powder Technology* 19, 369-381.

Pan, T.W., Joseph, D.D., Bai, R., Glowinski, R., Sarin, V., 2002. Fluidization of 1204 spheres: simulation and experiment. *Journal of Fluid Mechanics* 451, 169–191.

Paterson, N., Zhuo, Y., Reed, G.P., Dugwell, D.R., Kandiyoti, R., 2004. PYROLYSIS AND GASIFICATION OF SEWAGE SLUDGE IN A SPOUTED-BED REACTOR. *Water and Environment Journal* 18, 90-95.

Patwardhan, V.S., Tien, C., 1985. Sedimentation and liquid fluidization of solid particles of different sizes and densities. *Chemical Engineering Science* 40, 1051-1060.

Peacey, J.G., 1979. The iron blast furnace : theory and practice / by J. G. Peacey and W. G. Davenport. Pergamon Press, Oxford ; New York.

Peng, Z., Joshi, J.B., Moghtaderi, B., Khan, M.S., Evans, G.M., Doroodchi, E., 2016. Segregation and dispersion of binary solids in liquid fluidised beds: A CFD-DEM study. *Chemical Engineering Science* 152, 65-83.

Perré, P., 2010. Multiscale Modeling of Drying as a Powerful Extension of the Macroscopic Approach: Application to Solid Wood and Biomass Processing. *Drying Technology* 28, 944-959.

Pirker, S., Kahrimanovic, D., Kloss, C., Popoff, B., Braun, M., 2010. Simulating coarse particle conveying by a set of Eulerian, Lagrangian and hybrid particle models. *Powder Technology* 204, 203-213.

Pourghahramani, P., Forssberg, E., 2005. REVIEW OF APPLIED PARTICLE SHAPE DESCRIPTORS AND PRODUCED PARTICLE SHAPES IN GRINDING ENVIRONMENTS. PART I: PARTICLE SHAPE DESCRIPTORS. *Mineral Processing and Extractive Metallurgy Review* 26, 145-166.

Qian, X., Yan, Y., 2012. Flow measurement of biomass and blended biomass fuels in pneumatic conveying pipelines using electrostatic sensor-arrays. *IEEE Transactions on Instrumentation and Measurement* 61, 1343-1352.

Rangel, N., Santos, A., Pinho, C., 2001. Pressure Drop in Packed Shallow Beds of Cylindrical Cork Stoppers. *Chemical Engineering Research and Design* 79, 547-552.

Rasul, M.G., Rudolph, V., Wang, F.Y., 2000. Particles separation using fluidization techniques. *International Journal of Mineral Processing* 60, 163-179.

Reddy, R.K., Joshi, J.B., 2009. CFD modeling of solid–liquid fluidized beds of mono and binary particle mixtures. *Chemical Engineering Science* 64, 3641-3658.

Ren, B., Zhong, W., Chen, Y., Chen, X., Jin, B., Yuan, Z., Lu, Y., 2012. CFD-DEM simulation of spouting of corn-shaped particles. *Particuology* 10, 562-572.

Rhodes, M.J., Wang, X.S., Nguyen, M., Stewart, P., Liffman, K., 2001. Study of mixing in gas-fluidized beds using a DEM model. *Chemical Engineering Science* 56, 2859-2866.

Rice, R.W., Brainovich, J.F., 1986. Mixing/segregation in two- and three-dimensional fluidized beds: Binary systems of equidensity spherical particles. *AIChE Journal* 32, 7-16.

Richardson, J.F., Zaki, W.N., 1954. Sedimentation and fluidization: part I. *Transactions of the Institution of Chemical Engineers* 32, 35-53.

Richter, A., Nikrityuk, P.A., 2012. Drag forces and heat transfer coefficients for spherical, cuboidal and ellipsoidal particles in cross flow at sub-critical Reynolds numbers. *International Journal of Heat and Mass Transfer* 55, 1343-1354.

Rim, G., Jeong, C., Bae, J., Lee, Y., Lee, D.H., Epstein, N., Grace, J.R., Kim, S.D., 2013. Prediction of layer inversion velocity in three-phase fluidized beds. *Chemical Engineering Science* 100, 91-97.

Rim, G.H., Kim, J.Y., Lee, D.H., Grace, J.R., Epstein, N., 2014. Data and models for liquid velocity and liquid holdup at layer inversion point in a three-phase fluidized bed of binary solids. *Chemical Engineering Science* 109, 82-84.

Rodrigue, D., Chhabra, R., De Kee, D., 1994. Drag on non-spherical particles in non-newtonian fluids. *The Canadian Journal of Chemical Engineering* 72, 588-593.

Rong, L.-w., Zhan, J.-m., 2010. Improved DEM-CFD model and validation: A conical-base spouted bed simulation study. *Journal of Hydrodynamics, Ser. B* 22, 351-359.

Rong, L., Zhou, Z., Yu, A., 2015. Lattice-Boltzmann simulation of fluid flow through packed beds of uniform ellipsoids. *Powder Technology* 285, 146-156.

Rong, L.W., Dong, K.J., Yu, A.B., 2013. Lattice-Boltzmann simulation of fluid flow through packed beds of uniform spheres: Effect of porosity. *Chemical Engineering Science* 99, 44-58.

Rong, L.W., Dong, K.J., Yu, A.B., 2014. Lattice-Boltzmann simulation of fluid flow through packed beds of spheres: Effect of particle size distribution. *Chemical Engineering Science* 116, 508-523.

Schiller, L., Naumann, A.Z., 1933. ber die grundlegenden erechnungen bei der chwerkraftaufbereitung. *Ver. Deut. Ing.* 77, 318-320.

Schröter, M., Ulrich, S., Kreft, J., Swift, J.B., Swinney, H.L., 2006. Mechanisms in the size segregation of a binary granular mixture. *Physical Review E* 74, 011307.

Shao, Y., Ren, B., Jin, B., Zhong, W., Hu, H., Chen, X., Sha, C., 2013. Experimental flow behaviors of irregular particles with silica sand in solid waste fluidized bed. *Powder Technology* 234, 67-75.

Shao, Y., Zhong, W., Chen, X., Chen, Y., Jin, B., 2014. Spouting of non-spherical particles in conical-cylindrical spouted bed. *The Canadian Journal of Chemical Engineering* 92, 742-746.

Shao, Y., Zhong, W., Yu, A., 2016. Mixing behavior of binary and multi-component mixtures of particles in waste fluidized beds. *Powder Technology* 304, 73-80.

Singh, A.N., Roychowdhury, K.C., 1969. Study of the effects of orientation and shape on the settling velocity of non-isometric particles. *Chemical Engineering Science* 24, 1185-1186.

Singh, R., Saini, R.P., Saini, J.S., 2006. Nusselt number and friction factor correlations for packed bed solar energy storage system having large sized elements of different shapes. *Solar Energy* 80, 760-771.

Sommerfeld, M., Laín Beatove, S., 2008. Transport characteristics of isometric non-spherical particles in turbulent flows.

Sun, J., Xiao, H., Gao, D., 2009. Numerical study of segregation using multiscale models. *International Journal of Computational Fluid Dynamics* 23, 81-92.

Syamlal, M., O'Brien, T.J., 1988. Simulation of granular layer inversion in liquid fluidized beds. *International Journal of Multiphase Flow* 14, 473-481.

Thornton, C., Yin, K.K., 1991. Impact of elastic spheres with and without adhesion. *Powder Technology* 65, 153-166.

- Tran-Cong, S., Gay, M., Michaelides, E.E., 2004. Drag coefficients of irregularly shaped particles. *Powder Technology* 139, 21-32.
- Tripathy, A., Bagchi, S., Biswal, S.K., Meikap, B.C., 2017. Study of particle hydrodynamics and misplacement in liquid–solid fluidized bed separator. *Chemical Engineering Research and Design* 117, 520-532.
- Trnka, O., Veselý, V., Hartman, M., Beran, Z., 2000. Identification of the state of a fluidized bed by pressure fluctuations. *AIChE Journal* 46, 509-514.
- Tsuji, Y., Kawaguchi, T., Tanaka, T., 1993. Discrete particle simulation of two-dimensional fluidized bed. *Powder Technology* 77, 79-87.
- Tsuji, Y., Tanaka, T., Ishida, T., 1992. Lagrangian numerical simulation of plug flow of cohesionless particles in a horizontal pipe. *Powder Technology* 71, 239-250.
- Unnikrishnan, A., Chhabra, R., 1991. An experimental study of motion of cylinders in Newtonian fluids: wall effects and drag coefficient. *The Canadian Journal of Chemical Engineering* 69, 729-735.
- Van der Hoef, M.A., Beetstra, R., Kuipers, J.A.M., 2005. Lattice-Boltzmann simulations of low-Reynolds-number flow past mono- and bidisperse arrays of spheres: Results for the permeability and drag force. *Journal of Fluid Mechanics* 528, 233-254.
- Van Duijn, G., Rietema, K., 1982. Segregation of liquid—fluidized solids. *Chemical Engineering Science* 37, 727-733.
- Vivacqua, V., Vashisth, S., Hébrard, G., Grace, J.R., Epstein, N., 2012. Characterization of fluidized bed layer inversion in a 191-mm-diameter column using both experimental and CPFD approaches. *Chemical Engineering Science* 80, 419-428.
- Vollmari, K., Jasevičius, R., Kruggel-Emden, H., 2016. Experimental and numerical study of fluidization and pressure drop of spherical and non-spherical particles in a model scale fluidized bed. *Powder Technology* 291, 506-521.
- Vollmari, K., Oschmann, T., Kruggel-Emden, H., 2017. Mixing quality in mono-and bidisperse systems under the influence of particle shape: A numerical and experimental study. *Powder Technology* 308, 101-113.
- Walton, O.R., Braun, R.L., 1986. Viscosity, granular-temperature, and stress calculations for shearing assemblies of inelastic, frictional disks. *Journal of Rheology (1978-present)* 30, 949-980.
- Wen, C.Y., Yu, Y.H., 1966. Mechanics of fluidization. *AIChE series* 62, 100-111.
- Wiinikka, H., Gebart, R., 2005. THE INFLUENCE OF AIR DISTRIBUTION RATE ON PARTICLE EMISSIONS IN FIXED BED COMBUSTION OF BIOMASS. *Combustion Science and Technology* 177, 1747-1766.
- Wilhelm, R.H., Kwauk, M., 1948. Fluidization of solid particles *Chemical Engineering Progress* 44, 201-218.
- Xu, B.H., Yu, A.B., 1997. Numerical simulation of the gas-solid flow in a fluidized bed by combining discrete particle method with computational fluid dynamics. *Chemical Engineering Science* 52, 2785-2809.
- Xu, B.H., Yu, A.B., 1998. Comments on the paper "Numerical simulation of the gas-solid flow in a fluidized bed by combining discrete particle method with computational fluid dynamics" - Reply. *Chemical Engineering Science* 53, 2646-2647.
- Yang, C., Duan, Y., 2013. CFD-DEM Model for Simulating Solid Exchange in a Dual-Leg Fluidized Bed. *Chemical Engineering & Technology* 36, 1907-1914.
- Yin, X., Sundaresan, S., 2009. Fluid-particle drag in low-Reynolds-number polydisperse gas–solid suspensions. *AIChE Journal* 55, 1352-1368.

- Yovanovich, M., Teertstra, P., Culham, J.R., 1995. Modeling transient conduction from isothermal convex bodies of arbitrary shape. *Journal of Thermophysics and Heat Transfer* 9, 385-390.
- Yow, H.N., Pitt, M.J., Salman, A.D., 2005. Drag correlations for particles of regular shape. *Advanced Powder Technology* 16, 363-372.
- Yu, A.B., Xu, B.H., 2003. Particle-scale modelling of gas–solid flow in fluidisation. *Journal of Chemical Technology & Biotechnology* 78, 111-121.
- Zhang, L.-X., Lin, J.-Z., Chan, T.L., 2005. Orientation distribution of cylindrical particles suspended in a turbulent pipe flow. *Physics of Fluids* 17, 093105.
- Zhang, Y., Jin, B., Zhong, W., 2009. Experimental investigation on mixing and segregation behavior of biomass particle in fluidized bed. *Chemical Engineering and Processing: Process Intensification* 48, 745-754.
- Zhang, Z.P., Liu, L.F., Yuan, Y.D., Yu, A.B., 2001. A simulation study of the effects of dynamic variables on the packing of spheres. *Powder Technology* 116, 23-32.
- Zhong, W., Yu, A., Liu, X., Tong, Z., Zhang, H., 2016. DEM/CFD-DEM Modelling of Non-spherical Particulate Systems: Theoretical Developments and Applications. *Powder Technology* 302, 108-152.
- Zhong, W.Q., Zhang, Y., Jin, B.S., Zhang, M.Y., 2009. Discrete Element Method Simulation of Cylinder-Shaped Particle Flow in a Gas-Solid Fluidized Bed. *Chemical Engineering & Technology* 32, 386-391.
- Zhou, Y.C., Wright, B.D., Yang, R.Y., Xu, B.H., Yu, A.B., 1999. Rolling friction in the dynamic simulation of sandpile formation. *Physica A: Statistical Mechanics and its Applications* 269, 536-553.
- Zhou, Y.C., Xu, B.H., Yu, A.B., Zulli, P., 2002. An experimental and numerical study of the angle of repose of coarse spheres. *Powder Technology* 125, 45-54.
- Zhou, Y.C., Yu, A.B., Stewar, R.L., Bridgwater, J., 2004a. Microdynamic analysis of the particle flow in a cylindrical bladed mixer. Elsevier, Kidlington, ROYAUME-UNI.
- Zhou, Z.Y., 2007. Mathematical Modelling of Gas-solid Flow and Thermal Behaviour in an Ironmaking Blast Furnace, School of Materials Science and Engineering. The University of New South Wales, p. 250.
- Zhou, Z.Y., Kuang, S.B., Chu, K.W., Yu, A.B., 2010. Discrete particle simulation of particle–fluid flow: model formulations and their applicability. *Journal of Fluid Mechanics* 661, 482-510
- Zhou, Z.Y., Pinson, D., Zou, R.P., Yu, A.B., 2011. Discrete particle simulation of gas fluidization of ellipsoidal particles. *Chemical Engineering Science* 66, 6128-6145.
- Zhou, Z.Y., Yu, A.B., 2009. Simulation of the Flow and Segregation of Particle Mixtures in Liquid Fluidization, AIP Conference Proceedings, pp. 993-996.
- Zhou, Z.Y., Yu, A.B., Zulli, P., 2004b. A simplified mathematical model for gas–solid flow in a blast furnace. *Progress in Computational Fluid Dynamics, an International Journal* 4, 39-45.
- Zhou, Z.Y., Yu, A.B., Zulli, P., 2009. Particle scale study of heat transfer in packed and bubbling fluidized beds. *AIChE Journal* 55, 868-884.
- Zhu, H.P., Yu, A.B., 2002. Averaging method of granular materials. *Physical Review E* 66, 021302.
- Zhu, H.P., Yu, A.B., 2006. A theoretical analysis of the force models in discrete element method. *Powder Technology* 161, 122-129.

Zhu, H.P., Zhou, Z.Y., Yang, R.Y., Yu, A.B., 2007. Discrete particle simulation of particulate systems: Theoretical developments. *Chemical Engineering Science* 62, 3378-3396.

Zhu, H.P., Zhou, Z.Y., Yang, R.Y., Yu, A.B., 2008. Discrete particle simulation of particulate systems: A review of major applications and findings. *Chemical Engineering Science* 63, 5728-5770.